Faculté des Sciences Appliquées
Génie Civil et Géologie
Département de Mécanique des matériaux et Structures
Secteur Mécanique des Solides et des Matériaux

2D½ THERMAL-MECHANICAL MODEL OF CONTINUOUS CASTING OF STEEL USING FINITE ELEMENT METHOD

–

Modèle thermo-mécanique 2D½ de la coulée continue de l'acier à l'aide de la méthode des éléments finis

Thèse présentée en vue de l'obtention du grade de
Docteur en Sciences Appliquées
par Frédéric Pascon

Année académique 2002-2003

Membres du Jury :

J. Lecomte-Beckers
Chargée de cours Université de Liège, présidente du jury

S. Cescotto
Professeur Université de Liège

A. M. Habraken
Maître de recherches FNRS à l'Université de Liège, promoteur

M. Bellet
Maître de recherche CNRS à l'Ecole des Mines de Paris (France)

B.G. Thomas
Professeur University of Illinois at Urbana-Champaign (USA)

H. Grober
Directeur Innovation, Recherche & Développement, Profil ARBED, Groupe Arcelor

L. Chefneux
Directeur Stratégie et Progrès Technique, Cockerill-Sambre, Groupe Arcelor

M. Bobadilla
Chef du Service Transformation de phase et précipitation, IRSID, Groupe Arcelor

Coordonnées de l'auteur : Pascon Frédéric
Département M&S
Université de Liège
1, chemin des Chevreuils
4000 Liège
Belgique
e-mail : F.Pascon@ULg.ac.be

Foreword

This work has been possible thanks to a significant collaboration between M&S Department and R&D teams within steel making industry: Profil Arbed Research and Direction du Développement Technique of Arcelor Group.

I would like to express my gratitude to everyone who helped me making this work interesting and especially Mrs Habraken for her advice in the thesis writing.

Today, I also have a though to my nearest and dearest who always supported me and encouraged.

Contents

I. Introduction

I. Introduction

1. *Fundamentals of continuous casting process*

1.1. Historical and industrial context

First steps in continuous casting go back to the middle of the 19th century [WOL00], when twin-roll casting has been developed by Sir Henry Bessemer as an alternative to ingot casting of nonferrous metals (Cu and Cu–alloys, 1843) as well as for steel casting a few years later (1856). Progressively and during about one hundred years, different modifications have been brought to the process in order to make it more efficient, accurate and economic and to improve the quality of the cast products.

The real takeoff of continuous casting in steel industry took place in the years sixty and seventy, first in Japan [MIY01] and some other countries such as Finland [TEK90] (even if the contribution of this country to the world production is marginal), then in other Western-Europe countries (West Germany, Great Britain, ...) and finally in United States during the eighties. The reason of this difference between countries is linked to the technical and economical situation of each one.

The worldwide 1973 petroleum crisis led occidental countries to face up to some economical difficulties: rising of energy cost, decreasing of economical activity and successive periods of recession. In this new context, steel producers had to change their politics of development in order to remain present on the international scene and to avoid an economical downfall. From the second part of the seventies up to today, steel makers have restructured many times their activity in order to reduce costs (energy, manpower savings) and to maximize yield and quality of the products.

Progressively, continuous casting of steel became the chosen way to produce crude steel because this process helps to reach the economical and technical goals above. Little by little, it has effectively replaced the older ingot casting process, which is only used nowadays for very special applications.

Like any other industrial process, continuous casting has required (and shall required) for a long time tuning, development and improvement to cure cast products of defects under some difficult casting conditions, as well as to optimise the process to reach ever higher yields. The model presented in this thesis is obviously not a global solution. However it could contribute to go a little further in the understanding of the steel behaviour during continuous casting.

1.2. Phenomenology and terminology of continuous casting

In the production of steel, continuous casting takes place after steel making and before hot rolling. It rests on a rather simple principle: it is a kind of big "heat exchanger" which handles the continuous cooling and solidification of steel. The Figure 1 is a sketch of steel making.

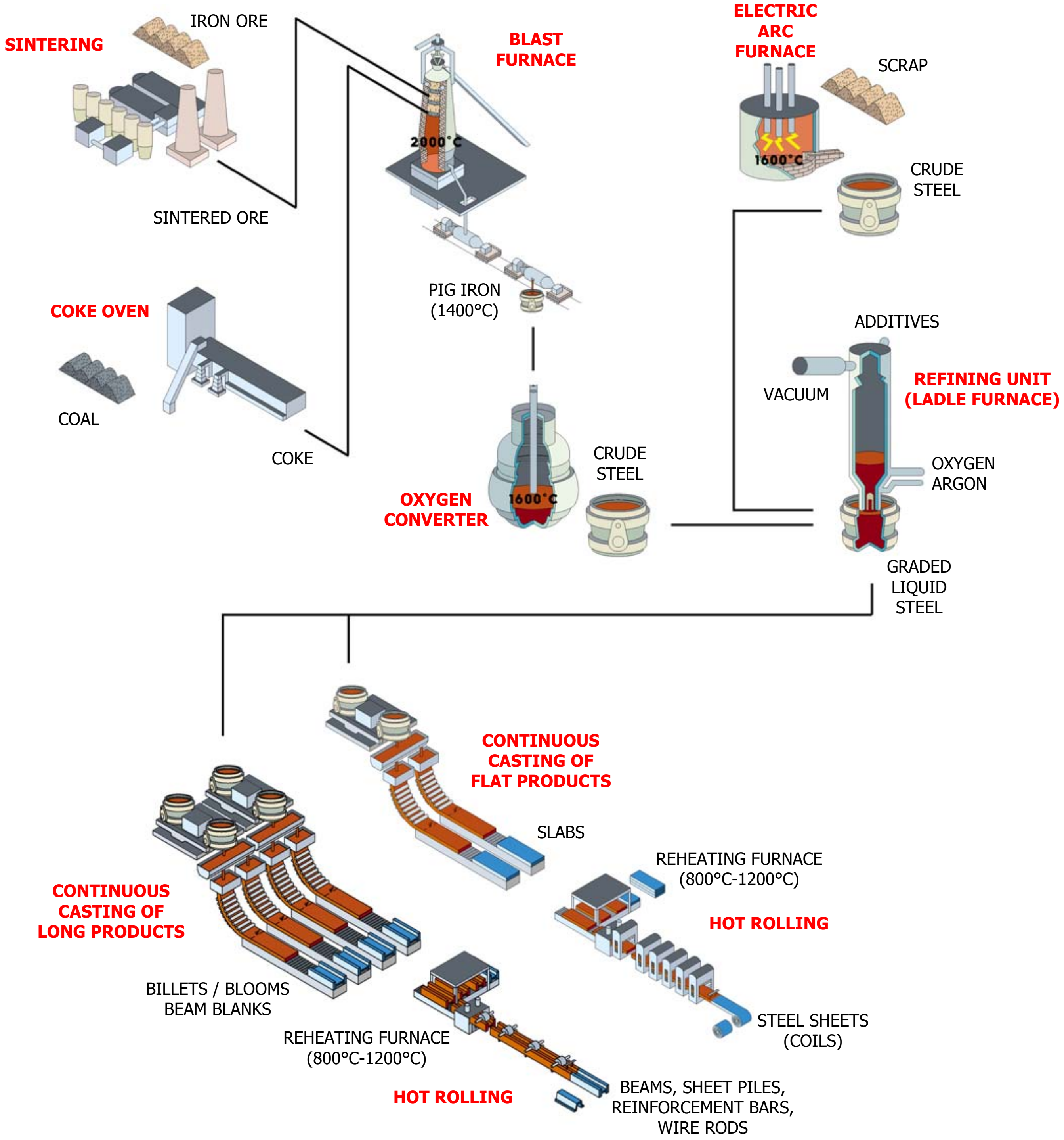

Figure 1: Sketch of steel making [ARC]

Basically, there are two different ways to produce crude steel:

1. In the first one (called smelting process), iron ore is prepared and crushed (in the sintering plant), while coal is distilled into coke (a powerful combustible, very rich in carbon). Then, the blast furnace is filled by successive layers of sintered ore and coke, while hot air (1200 °C) is blown at the bottom causing the coke to combust. The formed carbon oxides reduce the iron oxides, and thus separate iron. At the bottom of the blast furnace, an iron-based molten mixture called pig iron is obtained together with slag (which floats on pig iron because of its lower density). Pig iron is then poured onto a bed of scrap in the bottom of a giant vat. Then, it is heated at 1600°C while pure oxygen is blown in, causing unwanted elements (carbon and residues) to burn. The obtained liquid steel is called crude steel.
2. In the second way (called electric process), scrap is molten in a large furnace thanks to powerful electric arcs between electrodes. The residue is also crude steel.

Crude steel is steel, however it has to be refined by adjusting the carbon, residues and other additives content. This operation is performed in the refining unit under strongly controlled conditions: vacuum, high precision in chemical composition (steel grade). Even the temperature of graded liquid steel is highly controlled before and during its transportation to the next step: the continuous casting mill.

The Figure 2 shows the main elements of continuous casting:

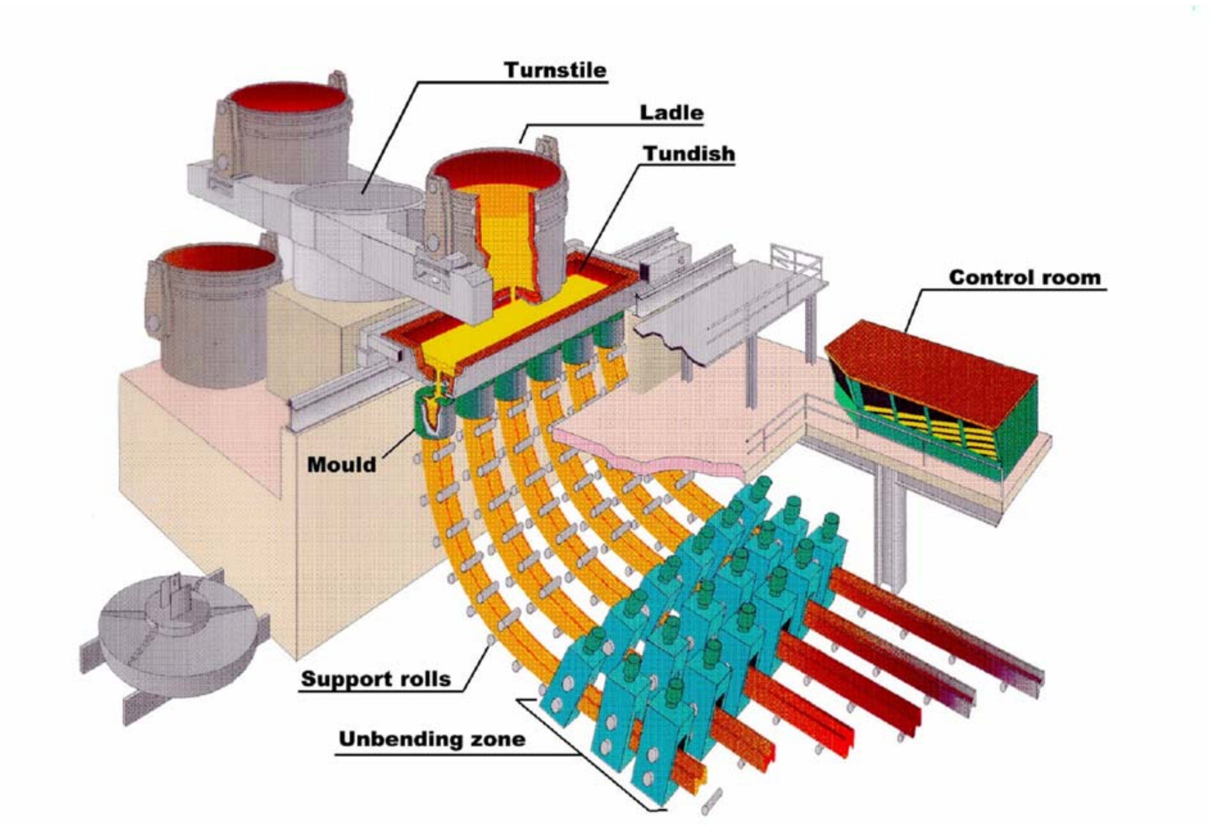

Figure 2: Continuous casting mill (6 parallel lines) [ARB]

Graded liquid steel comes from the refining unit in successive ladles, the content of which being poured into a tundish. The task of the tundish is multiple: it is of course a provider, but also a buffer of liquid steel (during ladle changes) for the continuous casting process. Moreover, the design of the tundish helps the inclusion separation and prevents reoxidation.

Liquid steel flows from the tundish to the mould trough a nozzle placed in the bottom of the tundish (see Figure 3). Orifices at the end of the nozzle are under the free level in the mould (meniscus). Note that the use of submerged entry nozzle is not systematic, free jet filling is also used in many cases. A special powder covers the free surface, its expected functions being [RIB79]:

- to protect the liquid steel against oxidation by contact with oxygen in the air;
- to insulate the free level and to avoid partial solidification at the surface;
- to absorb inclusions rising up to the surface;
- to lubricate contact between the mould and the strand;
- to allow a homogeneous thermal transfer adapted to casting conditions.

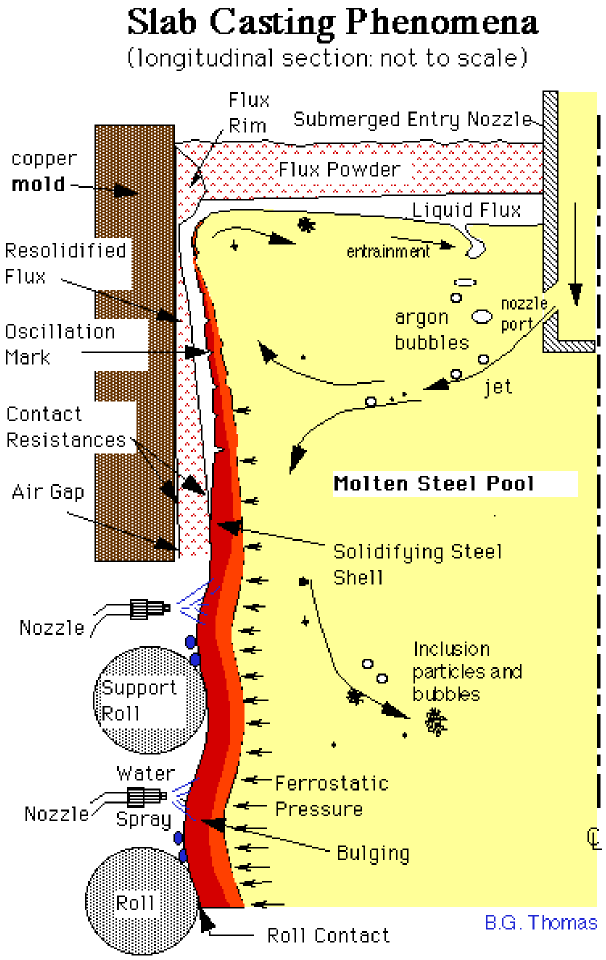

Figure 3: Filling of the mould through the nozzle [THO02]

The mould is bottomless and its internal walls are made of Cu-alloy plates or simply a Cu-alloy tube (for billet casting). An internal water-cooling circuit keeps the wall at a relatively constant and a rather low temperature range (100-200°C) during casting.

When liquid steel comes in contact with cold walls of the mould, it freezes and a solidified shell starts to form all around the perimeter of the cast product. Then, the solid shell is growing to the core.

At the same time, some extracting rolls are pulling out the forming steel strand, which is thus moving downward, and the mould must be supplied in liquid steel to insure a continuous process and a constant level in the mould. The velocity of the strand is called casting speed.

Considering a horizontal slice moving downward the mould, three areas can be recognized:

- the external solidified layer;
- the liquid core;
- an intermediate zone, partly made of liquid and solid fractions, called mushy zone.

While the slice is in progress in the mould, the solid shell is growing and it must be thick and strong enough when the slice reaches the exit at the bottom of the mould. Otherwise, some obvious problems occur such as cracks or even breakout (the liquid steel flows through the pierced shell). So the mould must extract heat from the steel at a maximum rate, allowing the solidification to reach the highest possible depth inside the strand.

To avoid the thin and fragile solid shell to stick to mould walls, which can causes cracks, a lubricant agent is usually contained in the powder. When the powder smelts in contact with steel, it forms a viscous film that flows in thin layer between the strand and the mould walls. So, there is an effective consumption of powder, which also requires a continuous providing.

In parallel to the use of lubricant powders, sticking is avoided thank to vertical oscillation of the mould. A consequence of vertical oscillation is the formation of oscillations marks at the surface of the product. These oscillation marks remain visible on the surface of the cast product. They look like short waves the frequency of which corresponds to the frequency of the mould oscillation. Moreover, they represent singularities from where transverse cracks generally initiate, even later during casting. Formation of oscillation marks is more detailed in some relevant publications [MAH91b,BRE93,BRI93].

Beneath the mould, the heat removal from the strand continues thanks to water sprays. This part is called secondary cooling as opposed to cooling in the mould region, called primary cooling. Nozzles are spraying the surface of the strand with either straight water or air mist (air + water), which is used more and more (less blocage, more uniform coverage, but more expensive [JES86,PAT00]). Globally, the temperature decreases not only at the surface, but also in the strand. The solidified shell grows until it reaches the middle of the strand. Then, the liquid pool, which is contained in the solid envelop, is closed (see Figure 4).

As long as the liquid pool is not completely closed, the liquid core of the strand is under pressure. The height of fluid column in the pool becomes in fact considerable (several meters) and a hydrostatic-type pressure is present everywhere in the liquid steel: this is the ferrostatic pressure. This pressure is applied by the pool onto the solidified shell, which tends to inflate, just like a pressurized tube.

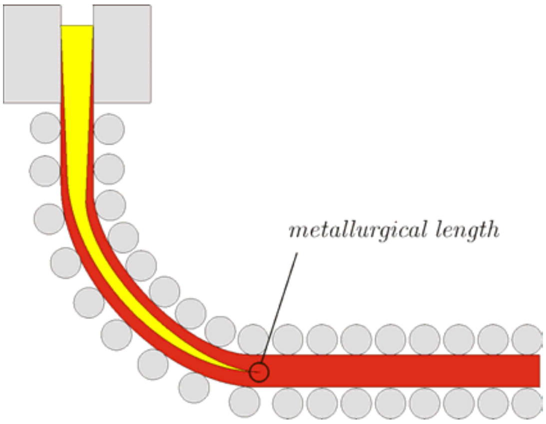

Figure 4: Closing of liquid pool: the metallurgical length

Secondary cooling being slower than primary one, the liquid pool is closing rather far from the bottom of the mould. Usually, when the section is completely solidified, a typical length of the strand is between 15 and 25 meters, depending on the product and the casting conditions. To avoid the development of too large ferrostatic pressure, it is necessary to limit the height of the fluid column. To do so, the steel strand is brought to a horizontal position: the strand should be bent and then straightened. They are two main ways to generate a bent strand: the first one is literally to bend a straight strand. This can be realised using rolls, the function of which being to guide and support the steel strand during its advance through the machine. In such a case the caster is qualified as vertical-curved machine, since the first part of the strand (and the mould particularly) is vertical. The second way to generate a bent strand is to use a curved mould so that the strand is directly solidifying with a constant curvature. Then only straightening operation is necessary. Such a caster is qualified as curved machine. Several types of caster exist: the Figure 5 illustrates the 5 main types of casters. Whatever the type of the caster is, the position of the rolls imposes the path followed by steel and it is possible this way to bend and straighten it.

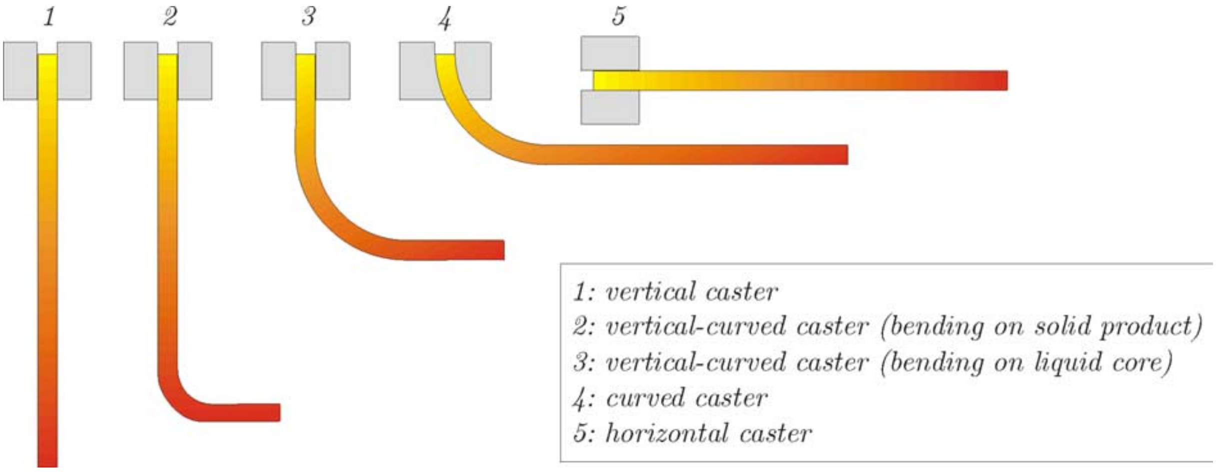

Figure 5: Geometry of different types of casters

Bending and straightening are rather delicate operations because of flexional stresses introduced in the material by this way:

- during bending: longitudinal tensile stress on extrados face and compression stress on intrados face of the strand (i.e. along casting axis)
- during straightening : longitudinal compression stress on extrados face and tensile stress on intrados face of the strand

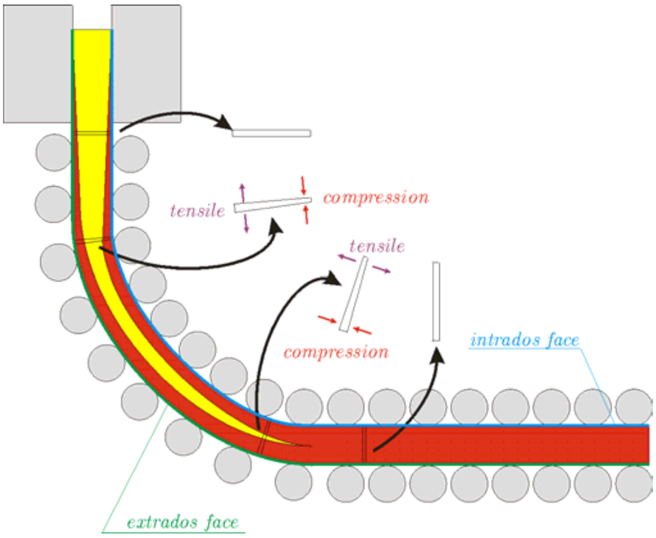

Figure 6: Longitudinal stresses during bending and straightening

These longitudinal tensile stresses, combined to transverse oscillation marks and low ductility of steel in a given range of temperature, maximize the risk of transverse cracks formation on surface of the cast product. The combination of all these conditions is particularly present on the intrados face during straightening.

Some rolls are motorised so that the strand can be extracted thanks to the transmission of an "extraction force" by friction between these extracting rolls and the surface of the product. The electrical motors are supplied in such a way that the speed of the strand in the machine ("casting speed") is regulated and generally constant (except in case of transition between successive heats cast).

Another effect of the rolls is to limit the bulging of the solid shell under ferrostatic pressure. In fact, the strand must pass through each pair of rolls and the gap d left between the rolls imposes the maximum thickness of the product at a given position in the caster. The shape of the strand (and its bulging) is thus similar to Figure 7.

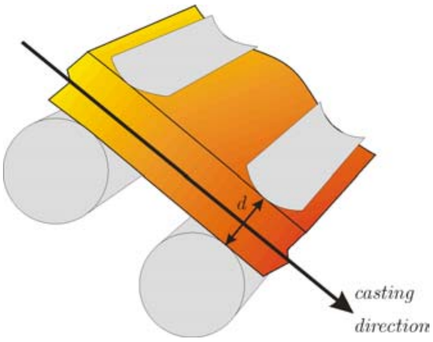

Figure 7: Bulging of the strand due to ferrostatic pressure

Without extracting rolls, the strand would not exit from the caster because the weight of the product is insufficient to overcome resisting forces, that is to say bending and straightening efforts as well as frictional effort of rolls spinning around their axis, even with ball bearing (low friction – theoretically).

One benefit of continuous casting is to provide to the product a shape close to the final section of the product. It is in fact very interesting to cast and to model the hot product which remains much malleable. For example, to produce flat products such as steel sheets, the cast product presents a rather wide rectangular section and it is called "slab". On the other hand, for long products such as beams or wires, the shape of the cast product is generally rectangular but closer to (or even) a square, the section of which can be large ("blooms") or smaller ("billets"). For "I-beams", it even exist a cast product called "beam blank" the cross section of which already being a I-shape allowing to reduce the number of passes during rolling.

2. Industrial objectives of the model

2.1. Thermo-mechanical model of continuous casting in the mould region

In a larger framework of a European Coal and Steel Community Steel Research Program, a steel producer ProfilARBED asked to M&S Department (MSM sector) of University of Liège to develop a continuous casting model. The purpose was to provide a coupled thermo-mechanical 2D analysis for a slice perpendicular to the strand axis. This slice moves downwards in the mould and the thickening of the shell is studied during its progression. From a mechanical point of view, this slice is in a generalized plane strain state, considering double symmetry and a rigid mould at constant temperature. The geometry of the mould is adapted as the slice is moving through the mould to take into account the mould taper. The thermal exchange conditions are also modified, depending on the contact between the strand and the mould.

The following numerical tools have been developed:

- A thermo-mechanical constitutive law for solidified steel, valid for a range of temperature going from the melting point to around 800°C (to completely cover the range of temperature observed during primary cooling). Because of strain rate sensitivity of steel at this very high range of temperature, an elasto-viscoplastic Norton-Hoff law has been chosen, developed and implemented in the finite element code LAGAMINE. This law also allows the degeneration of the law to represent, in a simple manner, the behaviour of the mushy and the liquid zones.
- The integration in a 2D thermo-mechanical finite element of
    - heat conduction;
    - solidification;
    - thermal expansion;
    - ferrostatic pressure;
    - mechanical law with thermal effect on the behaviour;

  - energy dissipated by plastic deformation.
- A unilateral contact element which manages the contact and loss of contact and the resulting variations in thermal exchange rates, as well as friction in the vertical movement of the strand and the resulting resistance to withdrawal.
- A mobile boundary element which models the mould taper.
- An efficient numerical strategy for the global resolution of the coupled thermo-mechanical problem: a staggered approach which allows different thermal and mechanical time steps.

Many parameters were available from data collection of the industrial partner and supplied for thermal and mechanical constitutive laws. However, parameters of the Norton-Hoff type law have been fit on experimental curves performed on a Gleeble device. The specific developments for this application are detailed in chapter V.

2.2. Prediction of the risk level in transverse cracks formation during bending and straightening of steel slabs. Study of the influence of some local defects.

After having developed the above first application, another steel producer contacted M&S Department for an extension of the model to the secondary cooling of the continuous casting process. In fact, under some conditions, transverse off-corner cracks were observed on continuously cast slabs. The mechanism of transverse cracking was already well known. Among others parameters, some local defects in caster can lead to the formation of this kind of transverse cracks: cooling rate defect, roll locking or roll misalignment are examples of such defects.

The purpose of the study was not to determine if these defects can generate such transverse cracks, but to attempt to classify them from the most critical to the less one in terms of risk of cracks formation. To do so, it has been necessary to define indexes which allow comparing each defect with the others.

Since the most critical zone of the caster is the straightening, almost the complete caster has been modelled, the temperature, stress and strain histories being essential for the study. The model is still based on the slice in generalized plane strain state. All details are available in chapter VI.

3. Main features of the model

3.1. General approach: 2D½ slice model

The model is based on a coupled thermal and mechanical analysis using finite element method. From initial settings, a complete three-dimensional analysis has seemed unworkable, because of numerical stability and convergence reasons, but also CPU cost. A so-called “2D½” approach has been preferred, taking advantage of the “generalized plane strain state” (see section III.1).

This approach consists in modelling a thin slice of the steel strand, perpendicular to the casting direction. Assuming a constant casting speed, time scale is equivalent to the position of the slice in the caster along the casting axis, the scale factor precisely being the casting speed.

The model allows studying thermal and mechanical evolution of the slice during its advance through the caster, including heat transfer, solidification, thermal shrinkage, stress development, ferrostatic pressure, control of bulging and application to the slab of extracting force.

Placing one after the other the successive results of the studied slice, a three-dimensional view of the process in steady-state conditions can be reproduced.

3.2. Thermo-mechanical finite element method

Nowadays, the finite element method has become a usual way to solve many physical problems. Many publications introduce and develop this method [ZIE00,RAP98], so that its general principles are assumed to be known and not reminded here.

The present model is implemented in the LAGAMINE non-linear finite element code, which has been developed at M&S Department of University of Liège since early eighties [GRO85,CES89,HAB01]. Since it is dedicated to solid mechanics modelling, LAGAMINE has been written in updated material (lagrangian) formalism. No fluid flow is thus modelled: molten steel is only present in the model to provide matter to solidify and to apply ferrostatic pressure).

Many applications and theses contributed to the development of the code up to its current state: among others, modelling of forging, rolling, deep drawing processes. The large displacements and large strains formalism has been detailed by Charlier [CHA87]. Cescotto, Charlier and Habraken developed the thermo-mechanical contact element [CHA90,HAB98b]. The thermo-mechanical coupling has been studied by Habraken in her Ph.D. thesis as well as phase transformations [HAB89,HAB92]. The generalized plane strain state has been introduced by Bourdouxhe [BOU86] and also used with shell elements in the Ph.D. thesis of Grisard [GRI93].

4. Outline of this thesis

This thesis is introducing first the theoretical developments necessary to model thermal and mechanical behaviour of the steel during continuous casting. After this introductive chapter, two chapters are dedicated to these topics.

In Chapter II, thermal behaviour and equations are presented. It includes a first section describing the solidification of steel and phase transformations, since this topic is fundamental in the description of the material behaviour. This metallurgical description has been introduced in the thermal model chapter because the primary parameter guiding solidification is the temperature. After that, thermal expansion is introduced, followed by internal conduction and thermal boundary conditions.

In Chapter III, dedicated to mechanical part of model, the generalized plane strain state is introduced and the way to use it in continuous casting modelling is developed: modelling of bending/straightening, application of an extraction force, determination of neutral axis. After that, the mechanical constitutive law is described. A unified elastic-viscoplastic constitutive law for steel at high temperature (solid as well as liquid) is proposed. The elastic domain is first introduced and then the viscoplastic domain. After that, the problem of determination of yield limit is presented as well as the loading/unloading criterion. Finally, some examples are presented. The analytical developments in the time integration of the viscoplastic law and in the stiffness matrix determination are reported in an appendix at the end of the thesis. After the constitutive law, the ferrostatic pressure element and the main assumptions involved in this pressure application are introduced. Finally, this chapter ends with the description of the thermo-mechanical contact element.

The Chapter IV is dedicated to the coupling between thermal and mechanical behaviour and the numerical problems linked to the spatiotemporal discretization. The staggered time-stepping scheme used in the present model is described.

After having developed all these theoretical topics, the two industrial applications introduced above (see section I.2) are detailed in two separated chapter.

In the Chapter V, the application of the model to a 125mm square billet is illustrated by some results. The study of an idealized mould is first presented and then a comparison of the billet behaviour with five different single tapered moulds is presented to underline the importance of the mould taper on the thermal and mechanical states of the billet.

In the Chapter VI, the model is applied to the second industrial application. In that context, some additional features have been adopted to take into account:

- the large amount of data concerning the heat transfer coefficients;
- the control of the bulging in a 2D½ slice model such the present one;
- the problem of the extracting force.

Two indexes of risk of transverse cracking are also introduced, before thermal and mechanical results are illustrated for a first reference case and then for three cases including some local defects in the caster.

To conclude, the Chapter VII summarizes what can be said at the present time about the work done up till now and it gives some perspectives for future developments.

5. Original contribution of this thesis

Many continuous casting models have been developed over the last twenty-five years. One must mentioned the team of J.K. Brimacombe of University of British Columbia who settled with his collaborators the bases of finite element modelling of continuous casting. Numerous publications of his team still remain of relevant interest today, on process decription, experimental measurements and modelling as well [BRI73, MAH91a,BAK93,DIP86,BRE93,CHA93,BRI93].

The work done by B.G. Thomas, first in the above team, then with his own team in the recent years at University of Illinois at Urbana-Champain, also represents a precious contribution to the subject with many publications and thesis [STO90, MOI93a, ZHU96, YU00]. This team has developed different models, from quite simple spreadsheet model [THO91] to more complex finite element ones, which take into account thermal, mechanical, fluid flow and phase changes aspects. These models place them in a good position among the continuous casting modellers, the current “CON2D” model being the fruit of one decade in thermal-mechanical modelling [LI03].

Many others teams have been working on the subject and related subject. Note that beside finite element and finite difference models, some analytical models have also been developed by mathematicians, especially at University of Jyväskylä (Finland) [LAI89,MAN90]

Before numerical modelling, the empirical knowledge of the process combined to experiments allowed improving the casting parameters and they remain important ways of investigation to better understand which are the parameters governing the process. One can not neglect the work done by the research and development teams in the industry and by the caster manufacturers (among others: IRSID for Arcelor Group, CRM in Belgium, Voest-Alpine Industrieanlagenbau). Without their impulsion towards characterization of the materials thermophysical properties, numerical models would remain without correct input data and thus useless.

The amount of publications dedicated to continuous casting modelling is so large that an exhaustive bibliography would be a delicate venture. It seems more reasonable to mention directly in the text the references when judged useful to the understanding.

The present model is implemented in the LAGAMINE code, in continuous development for more than twenty years now. A first model of continuous casting has been attempted in early nineties by Habraken (Research contract on continuous casting in M&S Department in partnership with ARBED industry, 1989-1991). However, this attempt, which was based on different constitutive laws for liquid and solid states, had strong convergence problems and accurate experimental data on steel behaviour at high temperature were lacking. In the framework of the two partnerships with industry mentioned above, the idea of continuous casting model has been revived with more success this time. I have personally taken part for almost six years now in the development and the improvements which led to the current model.

My personal contribution to the model consisted in:

- The determination of the parameters of the Norton-Hoff law based on experiments performed on Gleeble device.
- The implementation in the LAGAMINE finite element code and the validation of:
    - the mechanical constitutive law of Norton-Hoff with thermal effect, available in plane strain, axisymmetric and generalized plane strain states;
    - a 1D thermo-mechanical contact element coupled to the already existing 3D Coulomb friction law, with the transmission of the frictional effort perpendicular to the slice to the generalized plane strain state degrees of freedom, in order to take into account extraction force;
    - the ferrostatic pressure element;
    - the management of the large data collection on heat transfer coefficients in the water sprayed zones.
- The definition of heat transfer coefficients depending on the surface temperature of the strand and on the gap size in the mould (leading to a more stable convergence).

- The determination of a simple way to degenerate parameters of the mechanical law and the coefficient of thermal linear expansion, so that the lack of compressibility of the liquid phase does not causes unwanted effects in this lagrangian slice approach.
- The application on the generalized plane strain state of an external force corresponding to the extraction force. This force can be either defined "externally" according to a curve supplied by the steel producer for the concerned caster and casting conditions, or it can be computed in a coupled way, according to the in-plane behaviour of the slice and the assumptions about friction of the rolls spinning around their axis or friction in the mould.
- The introduction of springs used to control slab bulging in secondary cooling, the determination of an analytical expression of the stiffness of these springs to obtain a more realistic bulging shape than the one obtained with classical 2D slice models and the calibration of this stiffness to fit maximum bulging obtained with a bulging model.
- The modification in the sequence of computation in the staggered time-stepping analysis: first thermal, then mechanical analysis (instead of the contrary as used in some applications in the team up till this model).
- Some post-processing developments to generate 3D views of the results obtained in the 2D½ slice mode, allowing better analysis of the temperatures, stresses and strains in the modelling of the slab bending/straightening.
- The adaptation of parts of the LAGAMINE code and numerical tools (as staggered analysis management and post-processing software) for PC and UNIX stations.

Finally, beside these numerical developments, an important part of the work concerned many meetings and discussions with industrial partners as well as with IRSID. The aims of these meetings were to present partial results and to examine some assumptions concerning the caster working (in the mould, distribution of extraction force…) and the slab bulging.

II. Thermal Model

II. Thermal model

1. *Solidification of alloys and steel*

1.1. Crystalline structure

Most engineering materials are crystalline, that is to say that the atoms are arranged in a regular, structured and repeated manner. Each grain or crystallite is a kind of framework, characterized by the repetition of a unit cell. The length of the unit cell edges and the angles between crystallographic axes are referred as lattice parameters, which describe completely the geometry of the crystallite.

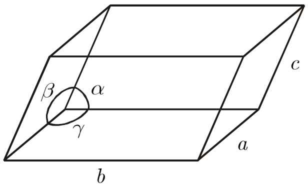

Figure 8: Geometry of a unit cell – the lattice parameters

Only seven different unit cells exist, they are represented in Table 1. They are also known as the seven crystal systems.

system	edges	angles	unit cell
cubic	$a = b = c$	$\alpha = \beta = \gamma = 90°$	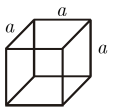
tetragonal	$a = b \neq c$	$\alpha = \beta = \gamma = 90°$	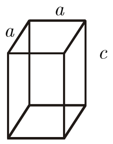
orthorhombic	$a \neq b \neq c$	$\alpha = \beta = \gamma = 90°$	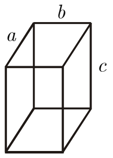

rhombohedral	$a = b = c$	$\alpha = \beta = \gamma \neq 90°$	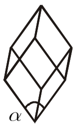
hexagonal	$a = b \neq c$	$\alpha = \beta = 90° \ / \ \gamma = 120°$	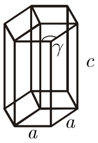
monoclinic	$a \neq b \neq c$	$\alpha = \gamma = 90° \neq \beta$	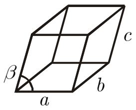
triclinic	$a \neq b \neq c$	$\alpha \neq \beta \neq \gamma \neq 90°$	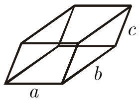

Table 1: Seven existing crystal systems

For a given crystal system, several dispositions of the atoms can be found to fill the 3D microstructure of the system. For example, with the cubic system, one can differentiate the simple cubic, the body-centred cubic (bcc) and the face-centred cubic (fcc) dispositions. Bravais classified 14 different ways to fill the 7 systems, also called the 14 crystal Bravais lattices:

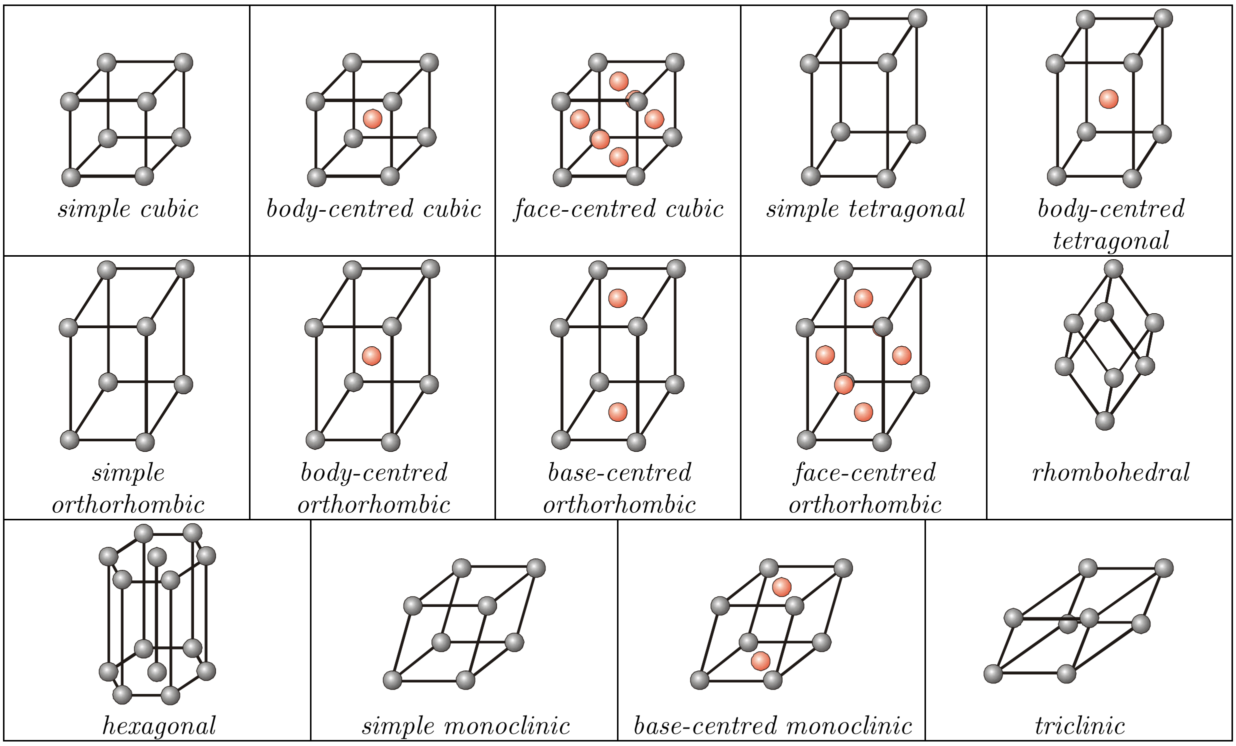

simple cubic
body-centred cubic
face-centred cubic
simple tetragonal
body-centred tetragonal
simple orthorhombic
body-centred orthorhombic
base-centred orthorhombic
face-centred orthorhombic
rhombohedral
hexagonal
simple monoclinic
base-centred monoclinic
triclinic

Figure 9: The 14 crystal Bravais lattices

Majority of metals crystallize in one of the three high-symmetry lattices: body-centred cubic, face-centred cubic and hexagonal close packet, the latter being more complicated than the Bravais lattice with 3 additional atoms between parallel “horizontal” planes:

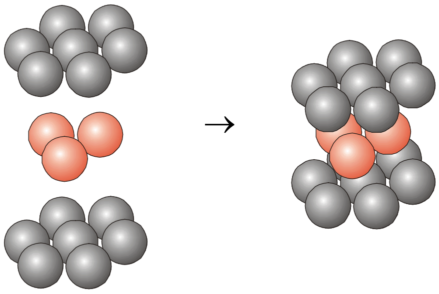

Figure 10: Hexagonal close packet lattice

Solid iron crystallises in two possible lattices: the body-centred cubic ferrite and face-centred cubic austenite.

Since the mass of the atoms constituting the crystal is known, it is possible to determine the mass density of the crystal. To do so, X-ray diffraction is used to determine spacing between adjacent planes (Bragg rule), then the ratio of mass to volume of one unit cell gives the mass density of the crystal.

1.2. Solid solutions

Up till now, only the perfectly repetitive structure of crystals has been considered, but it is not possible to avoid some contamination in practical materials. However, this contamination by impurities can be intentional, such as for metal alloys. As a result, many materials can be considered as solid solutions, which are homogeneous structures made of two or more components (distinct chemical substances).

There are two types of solid solutions:

- substitutional solid solutions: one component A (solute) dissolves in another one B (solvent), keeping the crystalline structure of the solvent B – for instance Ni dissolves in Cu crystalline structure;
- interstitial solid solutions: a smaller component A fit into free spaces of the crystalline structure of the larger component B – for instance C in ferrite crystal.

1.3. Phase diagrams

1.3.1. Pure materials

A phase is a chemically and structurally homogeneous portion of a microstructure. A single-phase microstructure can be polycrystalline, but each crystal grain only differs by its crystal orientation.

Any chemical substance can exist in different phases: gas, liquid and solid phases. Some components can present several solid phases, like pure iron, which presents two solid phases: ferrite (bcc) and austenite (fcc).

According to thermodynamics principles, the stable phase under some surroundings conditions (such as temperature and pressure) is the one presenting the lowest Gibbs free energy (at the equilibrium) in these conditions. The Figure 11 represents the evolution of Gibbs free energy for iron with respect to temperature (p = 1 atm) [COH94].

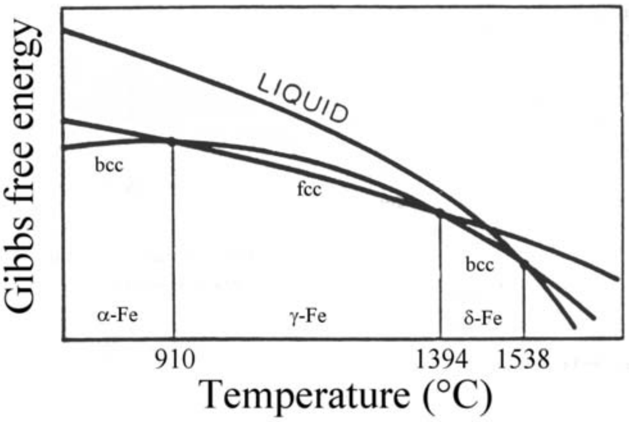

Figure 11: Gibbs free energy for iron with respect to temperature (p = 1 atm)

According to this figure:

- iron crystallise in bcc from room temperature up to 910°C - α-Fe (α-ferrite)
- iron crystallise in fcc structure from 910°C up to 1394°C - γ-Fe (austenite)
- iron crystallise in bcc structure from 1394°C up to 1538°C - δ-Fe (δ-ferrite)
- iron is liquid above 1538 °C

When two curves intersect, for instance at 1538 °C, two phases are in equilibrium, so they can coexist. If the temperature is decreasing, only δ-ferrite phase is stable, so that the liquid phase solidifies into δ-ferrite phase. This is exactly the same at 1394°C when the crystalline structure of iron changes from δ-ferrite (bcc) to austenite (fcc) and at 910°C (back to bcc) when α-ferrite appears.

This can be illustrated by the Gibbs phase rule:

$$F = N - \phi + v \tag{1}$$

where F is the number of degrees of freedom or variance, N the number of independent components, ϕ the number of phases in equilibrium and v the number of state variables, in general 2 – temperature T and pressure p. The variance F represents the number of state variables that can be changed without modification of the system phase.

For a pure metal ($N = 1$), the melting point corresponds to two simultaneous phases (liquid and solid – $\phi = 2$) and $F = 1 - 2 + 2 = 1$. That means that if one of the two state variables is fixed (temperature or pressure), it exists only one value of the other one to maintain simultaneously the two phases. For example, if the pressure is fixed (atmospheric pressure), it remains only one state variable (temperature – $v = 1$) and $F = 1 - 2 + 1 = 0$, so that the temperature cannot be changed without changing the system configuration (liquid+solid phases). In other words, it exists only one temperature at which liquid and solid phases coexist. This is illustrated on Figure 12, which is the phase diagram of pure iron.

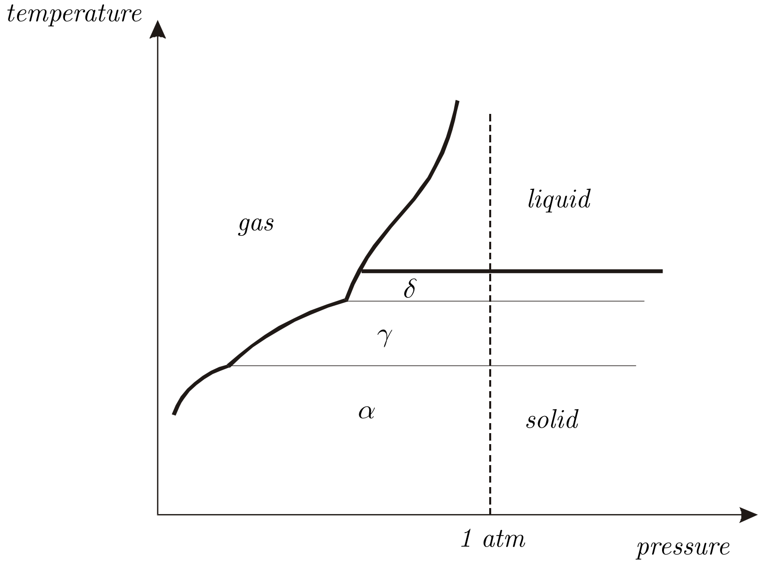

Figure 12: Phase diagram of pure iron [**SHA96**]

A phase diagram is a graphical representation of the state variables associated with microstructure. It divides the v-dimensions space (v being the number of state variables) into different zones where only one phase exists. At the boundary (lines) between two zones, both phases are in equilibrium. The coordinates of the points representing the boundaries correspond to the values of the states variables (T and p) at which the equilibrium is possible.

When two lines get in touch, three phases can be in equilibrium: such a point is called triple point. In such a case, $\phi = 3$ and the Gibbs phase rule gives $F = 1 - 3 + 2 = 0$. That means that no state variable can be changed without modifying the system configuration, the triple point is unique. This is evident on the phase diagram (Figure 12): any modification of temperature or pressure implies the disappearing of at least one of the three phases.

1.3.2. Complete solid solutions

As already mentioned above, pure materials are exceptional and the presence of impurities increases the number of components in the system. For example, considering a solid solution of two components (binary system), the number of components becomes equal to 2. Another state variable appear in this case: the composition of the system.

Considering that pressure is fixed (generally in industrial applications, $p = 1$ atm), two state variables are remaining: the Gibbs phase rule is thus $F = 2 - \phi + 1 = 3 - \phi$. So that two phases (for example, solid and liquid phases) can be maintained simultaneously in a range of temperature for a given composition as shown on Figure 13.

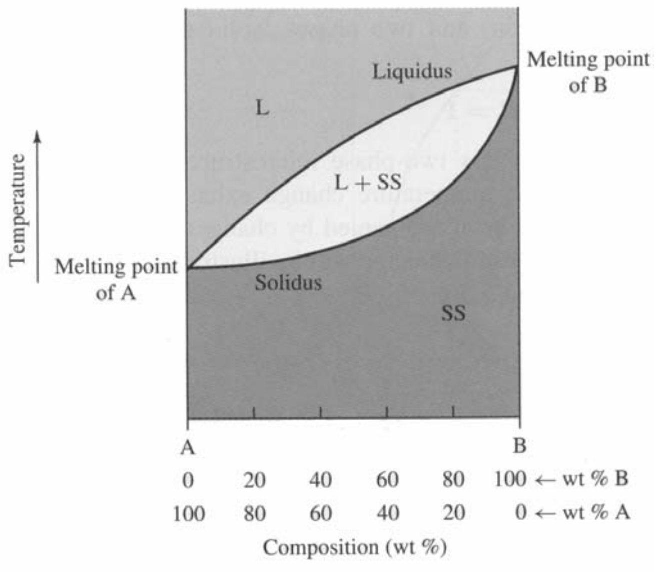

Figure 13: Phase diagram for binary system (complete solid solution) [**SHA96**]

The upper boundary of the two-phase region is called liquidus, that is the line above which single liquid phase is present. The lower boundary is the solidus. Between solidus and liquidus, one can speak of semisolid state. Because of its consistency, semisolid state is also often called mushy state.

These two boundaries also represent the composition of both phases at a given temperature. For instance, if the temperature is T_1, the composition of liquid and solid solution can be read on liquidus and solidus as shown on this figure:

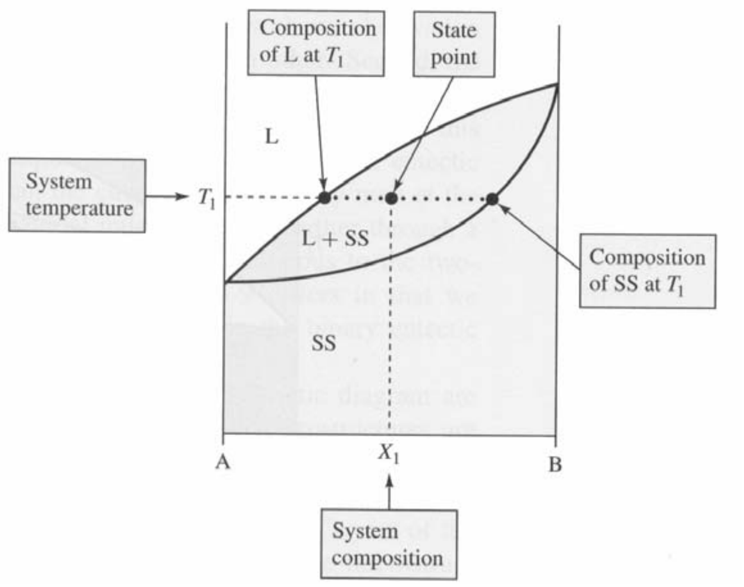

Figure 14: Composition of the two phases during phase transformation [**SHA96**]

Such a system is a complete solid solution, which is characterized by the possibility to replace any amount of one component (up to 100%) by atoms of the other. To do so, the two components must be quite similar, as defined by Hume-Rothery rules:

- less than 15% difference in atomic radii
- same crystal structure

- similar electronegativities
- same valence

If any rule is violated, only partial solubility (<100%) is possible.

1.3.3. Eutectic diagram without solid solution

Some components are so dissimilar that their solubility in each other is almost inexistent. That means that two different phases exist simultaneously at solid state: grains of pure A component beside grains of pure B can be observed.

At liquid state, both components are mixed, but when freezing, grains of either pure A, either pure B appear and grow, the other component remaining liquid.

However, for a given composition, both A and B components solidify at the same temperature, forming the so-called eutectic microstructure, characterized by fine alternative layers of A and B components.

The solidus is a horizontal line: the solidification always ends at the same temperature whatever is the composition, in particular for the eutectic composition, so that the solidus is also called eutectic temperature.

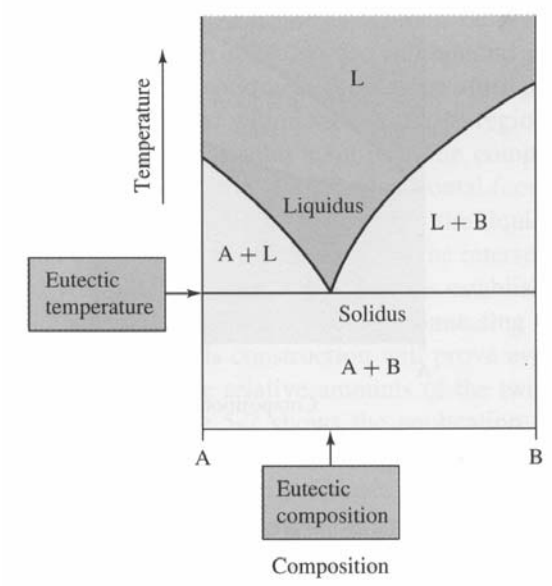

Figure 15: Binary eutectic phase showing no solid solution [**SHA96**]

1.3.4. Eutectic diagram with limited solid solution

For many binary systems, the two components present at least a partial solubility in each other. The phase diagram is thus quite similar to the previous one, except that B component can be solved in A component up to a limited concentration depending on the temperature: this forms a phase α. In the same way, A can be solved in B matrix, forming another phase β. The phase diagram becomes:

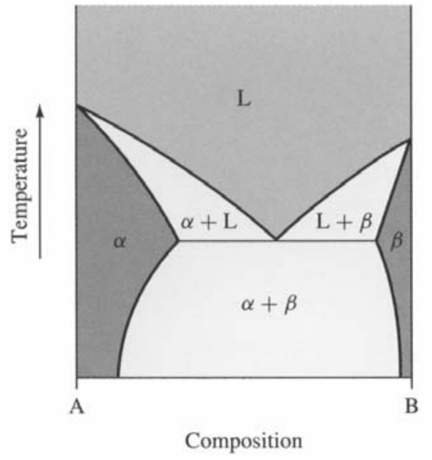

Figure 16: Binary eutectic phase with limited solid solution **[SHA96]**

1.3.5. Eutectoid diagram

The eutectic transformation can be written:

$$L_{eutectic} \xrightarrow{\text{cooling}} \alpha + \beta \tag{2}$$

Some binary systems presents the same kind of transformation, but a solid phase γ is transformed into two other solid phases:

$$\gamma \xrightarrow{\text{cooling}} \alpha + \beta \tag{3}$$

This eutectic-like transformation is called eutectoid. The corresponding temperature is the eutectoid temperature and the phase diagram is:

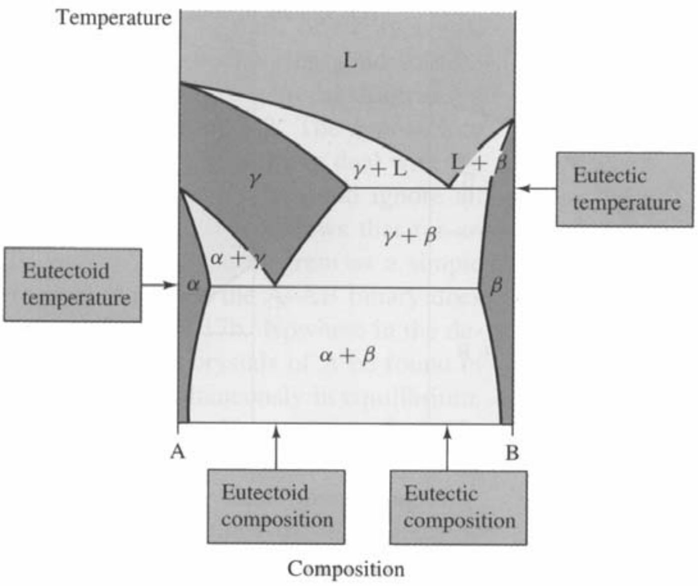

Figure 17: Eutectoid phase diagram **[SHA96]**

1.3.6. Peritectic diagram

In the previous diagrams, pure components (A and B) have a distinct melting temperature. In some binary systems, the two components A and B can form a stable compound AB.

To simplify, consider that the solubility of AB intermediate compound is almost inexistent in both A and B. The peritectic transformation consists in a mixture of solid solution and liquid (for instance $L + B$) transforming at constant temperature into another solid solution for example (AB):

$$L + B \underset{heating}{\overset{cooling}{\rightleftarrows}} AB \tag{4}$$

This situation is illustrated by Figure 18.

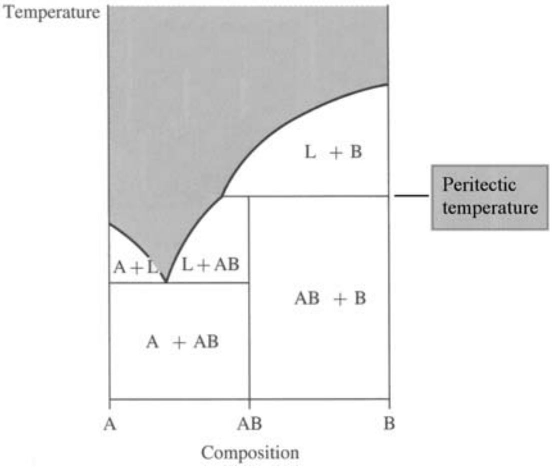

Figure 18: Peritectic phase diagram **[SHA96]**

The components A and B are said to undergo congruent melting, since the liquid formed upon melting has the same composition as the solid from which it was formed. At the opposite, the compound AB is said to undergo incongruent melting, i.e. the liquid formed upon melting has not the same composition than AB. The peritectic term is used to describe the incongruent melting phenomenon.

1.3.7. Fe-Fe_3C phase diagram

Steel is an alloy made of iron and carbon: Fe-C phase diagram should consequently be representative of equilibrium between both components of steel. However, although graphite C is more stable than the compound Fe_3C (cementite), the rate of graphite precipitation is much slower than that of cementite. The result is that in common steels, the Fe_3C phase is metastable, i.e. for all practical purposes it is stable with time and conforms to the Gibbs phase rule.

The Fe-Fe_3C phase diagram is represented on Figure 19. Three of the phase diagrams introduced above are present in Fe-Fe_3C phase diagram:

- eutectic transformation (1148°C, 4.30wt%), eutectic composition being known as ledeburite;
- eutectoid transformation (727°C, 0.77wt%), eutectoid composition being known as pearlite;

- peritectic transformation (1495°C, 0.18wt%), peritectic composition not having a specific name (simply austenite).

Note that ledeburite and pearlite are not phases. Only 4 phases exist in steel at any composition and temperature: these are bcc α-phase (ferrite), fcc γ-phase (austenite), bcc δ-phase (δ-ferrite) and Fe_3C compound (cementite). As already mentioned above, eutectic and eutectoid compositions are made of fine alternative layers of two components: austenite and cementite for ledeburite, and ferrite and cementite for pearlite.

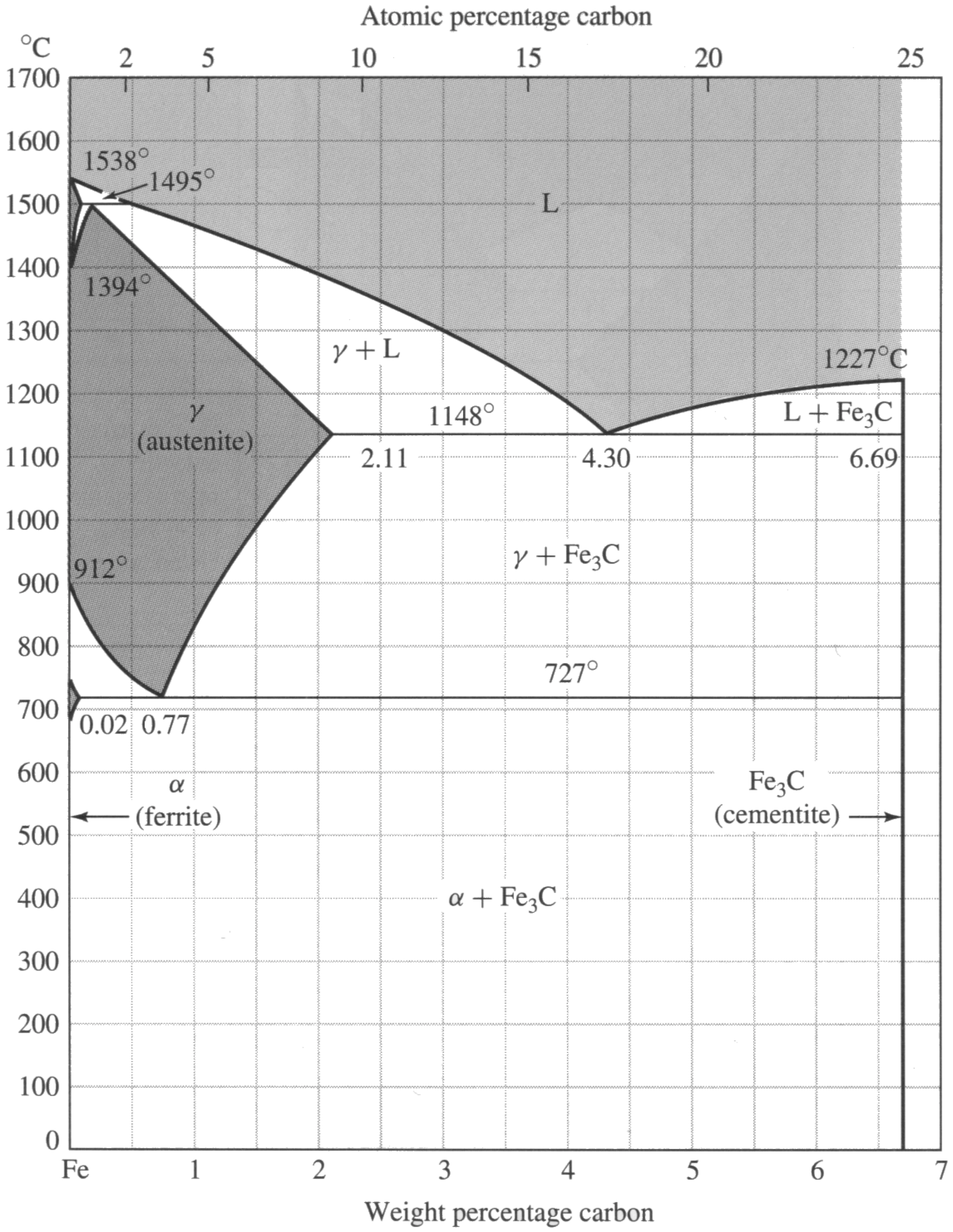

Figure 19: Fe-Fe_3C phase diagram **[SHA96]**

The boundary between irons and steels is identified as a carbon content of 2.11wt%, which corresponds to the carbon solubility limit in the austenite γ-phase. Amongst the steels, a common distinction between hyper- and hypo-eutectoid corresponds precisely to carbon content higher or lower than 0.77wt%.

Another distinction is made between low carbon steel (carbon content < 0.18wt%) and carbon steel (> 0.18wt%), i.e. below or over the carbon content in the peritectic composition (see detail of Fe-Fe$_3$C phase diagram in peritectic region on Figure 20). The difference between low carbon and carbon steels is the presence of δ-ferrite phase after the complete solidification and the δ→γ phase transformation at solid state, which affects some material properties such as mass density and thermal expansion.

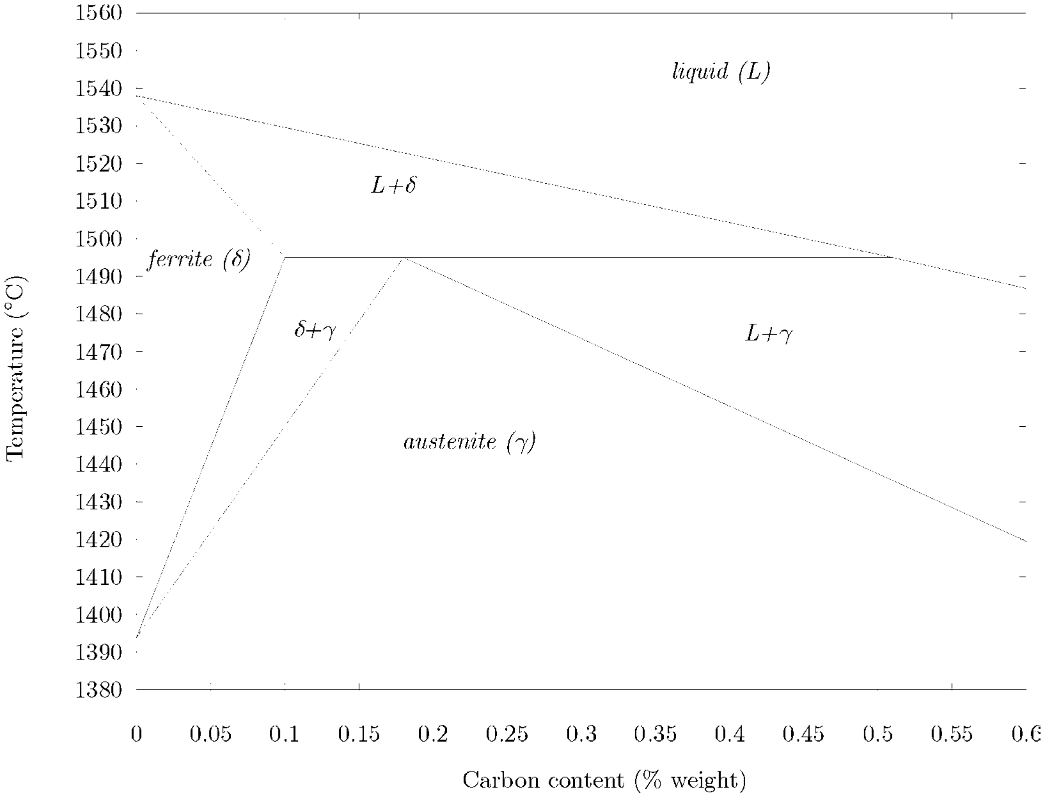

Figure 20: Fe-Fe$_3$C phase diagram in the peritectic region

1.4. The lever rule

This rule is used to determine in a two-phase region the amount of each phase. The relative amounts of the two phases can be easily determined from a mass balance.

Consider the simple case of the phase diagram of a complete solid solution. Initially, the composition is assumed to be liquid. It contains x_0% of B, thus 100%-x_0% of A component. While the temperature is decreasing down to liquidus, the composition remains the same. From the liquidus, solid solution appears and when the temperature reaches the solidus, only solid solution remains.

In the two-phase region, the sum of mass percentage of both phases (solid solution $\%SS$ and liquid $\%L$) is equal to 100%:

$$\%SS + \%L = 100\% \tag{5}$$

In other respects, the total amount of B component is constant and equal to x_0. Since the amounts of B in the solid solution (x_{SS}) and the liquid (x_L) are given by the solidus and liquidus curves, their sum must be equal to:

$$x_L.\%L + x_{SS}.\%SS = x_0 \tag{6}$$

Introducing (5) in relation (6):

$$x_L.\left(100\% - \%SS\right) + x_{SS}.\%SS = x_0 \tag{7}$$

or

$$\%SS = \frac{x_L - x_0}{x_L - x_{SS}} 100\% = \frac{b}{a+b} 100\% \tag{8}$$

and

$$\%L = 100\% - \%SS = \frac{x_0 - x_{SS}}{x_L - x_{SS}} 100\% = \frac{a}{a+b} 100\% \tag{9}$$

where a and b are the length of the segment represented on the following figure:

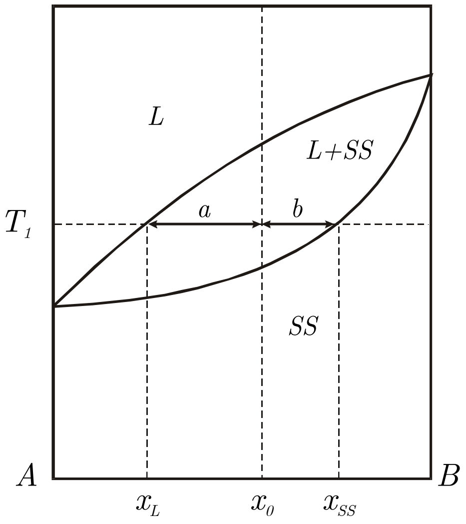

Figure 21: Lever rule

This rule is known as the lever rule (because of a mechanical analogy with a lever balanced on fulcrum).

Relations (8) and (9) are defining the fraction of each component. Instead of percentage, fractions are generally expressed in term of natural value (no unit):

$$\begin{cases} \text{liquid fraction} = f_L = \dfrac{\%L}{100\%} = \dfrac{a}{a+b} \\ \text{solid fraction} = f_s = \dfrac{\%SS}{100\%} = \dfrac{b}{a+b} \end{cases} \tag{10}$$

They are complementary, their sum being equal to unity so that:

$$f_L = 1 - f_s \tag{11}$$

1.5. Steel compostion during solidification: examples

The composition of two phases during phase transformation – Figure 14 – and the lever rule introduced above – relations (10) – allow studying the complete evolution of any alloy during solidification.

Consider for example steel at 3 different compositions in the peritectic region:

- a 0.05wt% low carbon steel
- a 0.15wt% low carbon steel
- a 0.42wt% carbon steel

The solidification of each one is be characterized by the apparition of different phases at different temperatures:

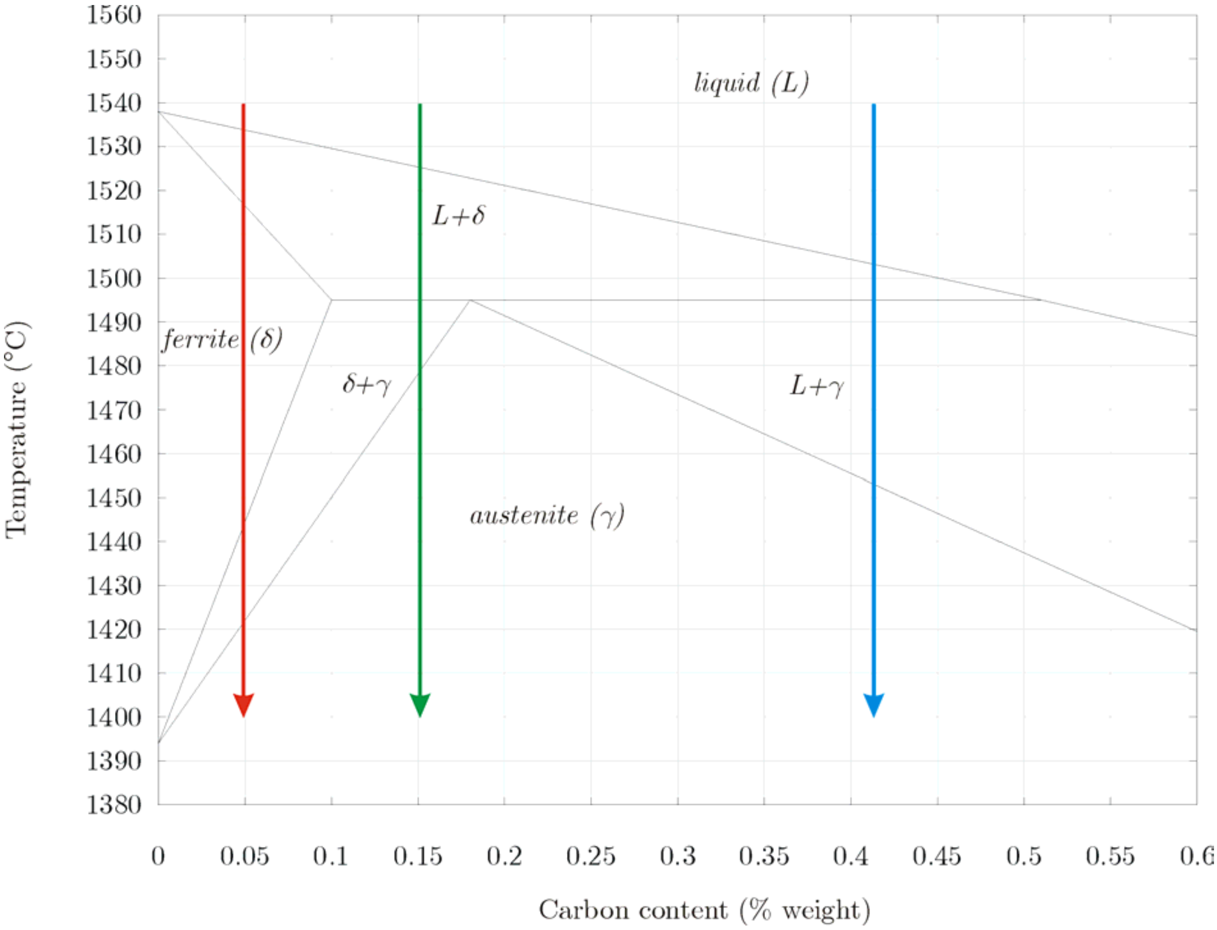

Figure 22: Solidification of 3 different compositions of steel

a. 0.05wt% low carbon steel

Characteristic temperatures are:

- liquidus: $T_L = 1538 + (1495 - 1538)\dfrac{0.05}{0.51} = 1534°\text{C}$
- solidus: $T_S = 1538 + (1495 - 1538)\dfrac{0.05}{0.10} = 1516.5°\text{C}$
- δ→γ beginning: $T_\delta = 1394 + (1495 - 1394)\dfrac{0.05}{0.10} = 1444.5°\text{C}$

- δ→γ ending: $T_\gamma = 1394 + (1495 - 1394)\dfrac{0.05}{0.18} = 1422°\mathrm{C}$

The following table summarize for each temperature range the carbon content in each phase (C_L, C_δ and C_γ) and the fraction of each phase (f_L, f_δ and f_γ).

		$T_L < T$	$T_S < T < T_L$	$T_\delta < T < T_S$	$T_\gamma < T < T_\delta$	$T < T_\gamma$
L-phase	C_L	0.05 %	$\dfrac{1538 - T}{1538 - 1495}0.51\%$	-	-	-
	f_L	1	$\dfrac{0.05\% - C_\delta(T)}{C_L(T) - C_\delta(T)}$	0	0	0
δ-phase	C_δ	-	$\dfrac{1538 - T}{1538 - 1495}0.10\%$	0.05 %	$\dfrac{T - 1394}{1495 - 1394}0.10\%$	-
	f_δ	0	$\dfrac{C_L(T) - 0.05\%}{C_L(T) - C_\delta(T)}$	1	$\dfrac{0.05\% - C_\gamma(T)}{C_\delta(T) - C_\gamma(T)}$	0
γ-phase	C_γ	-	-	-	$\dfrac{T - 1394}{1493 - 1394}0.18\%$	0.05 %
	f_γ	0	0	0	$\dfrac{C_\delta(T) - 0.05\%}{C_\delta(T) - C_\gamma(T)}$	1

For instance, at 1520°C, the material is made of liquid and δ-phase:

- carbon content in liquid is equal to $C_L = \dfrac{1538 - 1520}{1538 - 1495}0.51\% = 0.213\%$
- carbon content in δ-phase is equal to $C_\delta = \dfrac{1538 - 1520}{1538 - 1495}0.10\% = 0.042\%$
- liquid fraction is $f_L = \dfrac{0.05\% - 0.042\%}{0.213\% - 0.042\%} = 0.047$
- δ-phase fraction is $f_\delta = \dfrac{0.213\% - 0.05\%}{0.213\% - 0.042\%} = 0.953$

One can easily verify that the total carbon content at 1520°C is still:

$$0.213\mathrm{wt}\%\ 0.047 + 0.042\mathrm{wt}\%\ 0.953 = 0.05\mathrm{wt}\%$$

The Figure 23 shows the evolution with respect to temperature of liquid, δ-ferrite and γ-austenite phases and their carbon content in this 0.05wt%C low carbon steel.

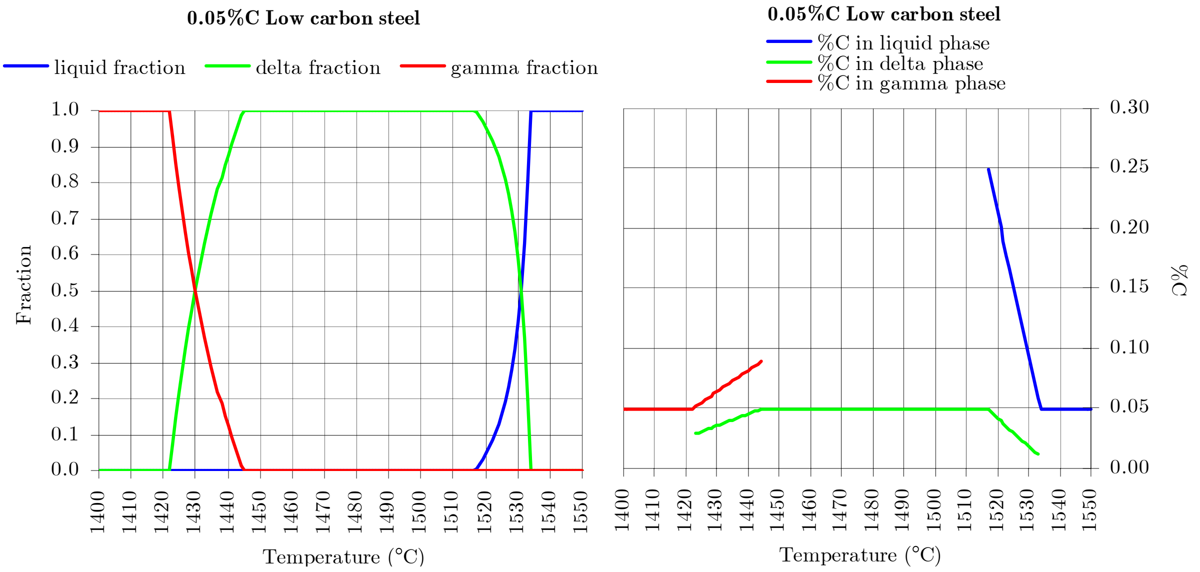

Figure 23: Fraction of liquid, δ-ferrite and γ-austenite phases and their carbon content in a 0.05wt%C low carbon steel with respect to temperature

b. 0.15wt% low carbon steel

Characteristic temperatures are:

- liquidus: $T_L = 1538 + (1495 - 1538)\dfrac{0.15}{0.51} = 1525°\text{C}$
- solidus: $T_S = 1495°\text{C}$ and δ→γ beginning: $T_\delta = 1495°\text{C}$
- δ→γ ending: $T_\gamma = 1394 + (1495 - 1394)\dfrac{0.15}{0.18} = 1478°\text{C}$

Note that the solidus corresponds to the apparition of both δ- and γ-phases (peritectic temperature). Hence the following table:

		$T_L < T$	$T_S < T < T_L$	$T = T_\delta = T_S$	$T_\gamma < T < T_\delta$	$T < T_\gamma$
L-phase	C_L	0.15 %	$\dfrac{1538 - T}{1538 - 1495}0.51\%$	-	-	-
	f_L	1	$\dfrac{0.15\% - C_\delta(T)}{C_L(T) - C_\delta(T)}$	0.122 → 0	0	0
δ-phase	C_δ	-	$\dfrac{1538 - T}{1538 - 1495}0.10\%$	0.10%	$\dfrac{T - 1394}{1495 - 1394}0.10\%$	-
	f_δ	0	$\dfrac{C_L(T) - 0.15\%}{C_L(T) - C_\delta(T)}$	0.878 → 0.375	$\dfrac{0.15\% - C_\gamma(T)}{C_\delta(T) - C_\gamma(T)}$	0
γ-phase	C_γ	-	-	0.18%	$\dfrac{T - 1394}{1493 - 1394}0.18\%$	0.15 %
	f_γ	0	0	0 → 0.625	$\dfrac{C_\delta(T) - 0.15\%}{C_\delta(T) - C_\gamma(T)}$	1

The Figure 24 shows the evolution with respect to temperature of liquid, δ-ferrite and γ-austenite phases and their carbon content in this 0.15wt%C low carbon steel.

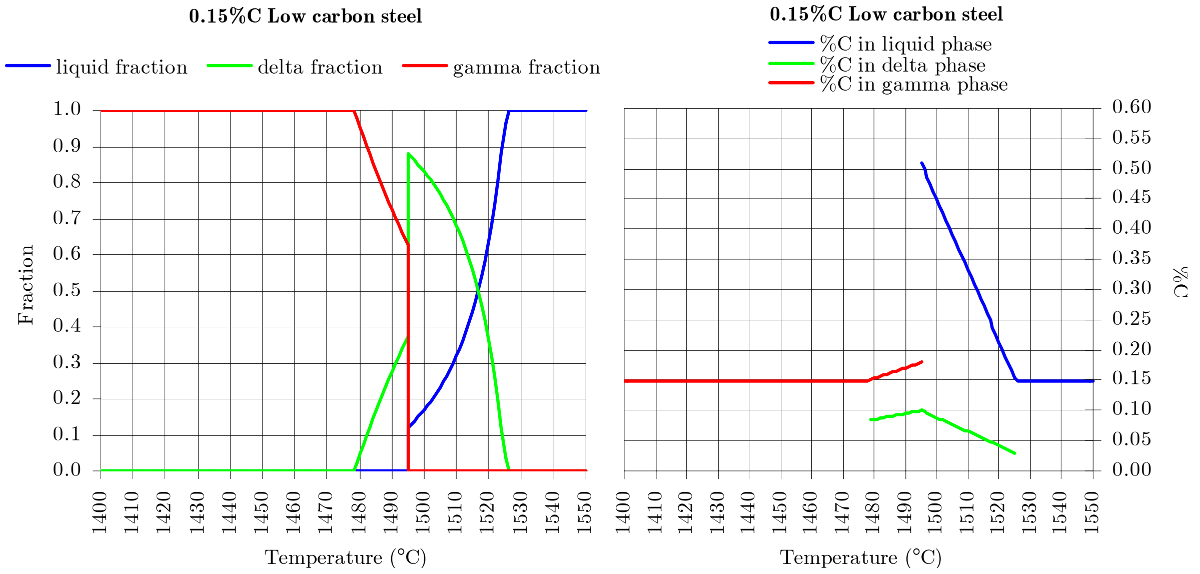

Figure 24: Fraction of liquid, δ-ferrite and γ-austenite phases and their carbon content in a 0.15wt%C low carbon steel with respect to temperature

c. 0.42wt% carbon steel

Characteristic temperatures are:

- liquidus: $T_L = 1538 + (1495 - 1538)\dfrac{0.42}{0.51} = 1502.5°\text{C}$
- L+δ→ L+γ transformation: $T_{\delta\to\gamma} = 1495°\text{C}$
- solidus: $T_S = 1495 + (1148 - 1495)\dfrac{0.42 - 0.18}{2.11 - 0.18} = 1452°\text{C}$

		$T_L < T$	$T_{\delta\to\gamma} < T < T_L$	$T = T_{\delta\to\gamma}$	$T_S < T < T_{\delta\to\gamma}$	$T < T_S$
L-phase	C_L	0.42 %	$\frac{1538-T}{1538-1495}0.51\%$	0.51%	$0.51\% + \frac{1495-T}{1495-1148}3.79\%$	-
	f_L	1	$\frac{0.42\% - C_\delta(T)}{C_L(T) - C_\delta(T)}$	$0.780 \to 0.723$	$\frac{0.42\% - C_\gamma(T)}{C_L(T) - C_\gamma(T)}$	0
δ-phase	C_δ	-	$\frac{1538-T}{1538-1495}0.10\%$	0.10%	-	-
	f_δ	0	$\frac{C_L(T) - 0.42\%}{C_L(T) - C_\delta(T)}$	$0.220 \to 0$	0	0
γ-phase	C_γ	-	-	0.18%	$0.18\% + \frac{1495-T}{1495-1148}1.93\%$	0.42 %
	f_γ	0	0	$0 \to 0.273$	$\frac{C_L(T) - 0.42\%}{C_L(T) - C_\gamma(T)}$	1

Note that at the peritectic temperature (1495°C) the δ-phase present in the liquid is transforming into γ-phase.

The Figure 25 shows the evolution with respect to temperature of liquid, δ-ferrite and γ-austenite phases and their carbon content in this 0.42wt%C low carbon steel.

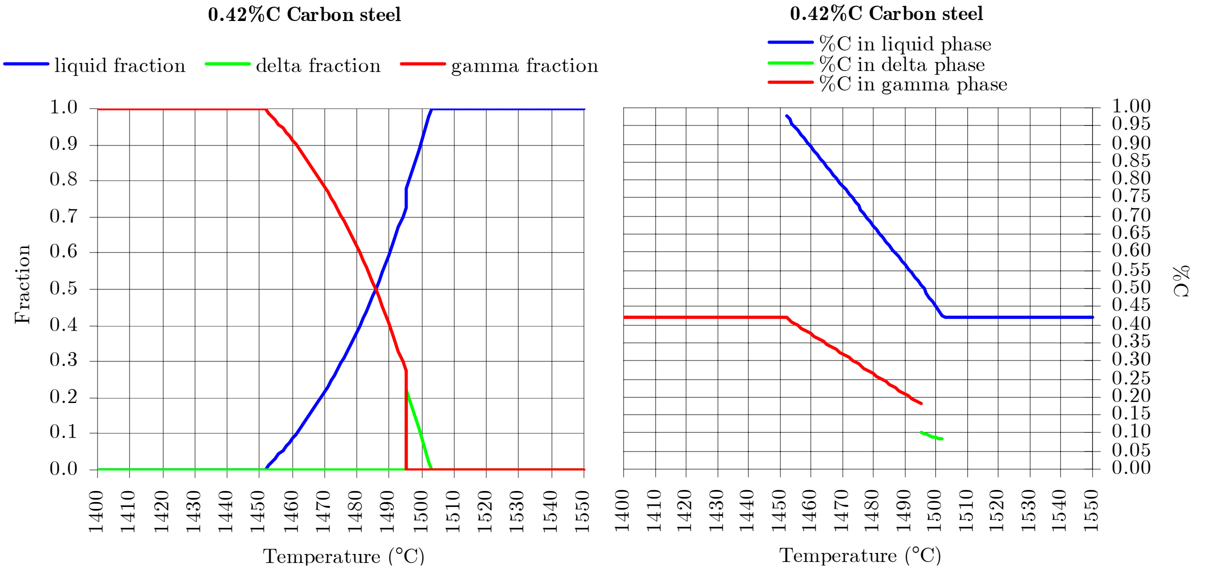

Figure 25: Fraction of liquid, δ-ferrite and γ-austenite phases and their carbon content in a 0.42wt%C low carbon steel with respect to temperature

1.6. TTT diagrams

All previous phase diagrams correspond to equilibrium. Actually, a third dimension should be added: time. In fact, time is necessary for the completion of solidification reaction and the duration depends on temperature. During slow cooling from the melt, phase diagrams at equilibrium can be considered as available. However, for higher cooling rates, time becomes an important factor and kinetics of phase transformation cannot be neglected. For most of melting and casting processes, equilibrium conditions are not followed.

TTT diagrams (for Temperature, Time and Transformation) are maps which summarize, for a given composition, the percentage completion of a given phase transformation on temperature and time axes. The Figure 26 shows a theoretical example of TTT diagram.

The curves present a horizontal asymptote meaning that the transformation never occurs above a given temperature (T_{mp} for melting point in this example). At a temperature relatively close to this temperature, the transformation is very slow and the duration for complete transformation decreases with temperature. The minimum duration is obtained at a temperature considerably below T_{mp}.

Note that the TTT diagram plotted on Figure 26 assumes that the transformation is completed at constant temperature. That means that while the material is cooling, temperature rate can be such that even TTT diagrams are not followed.

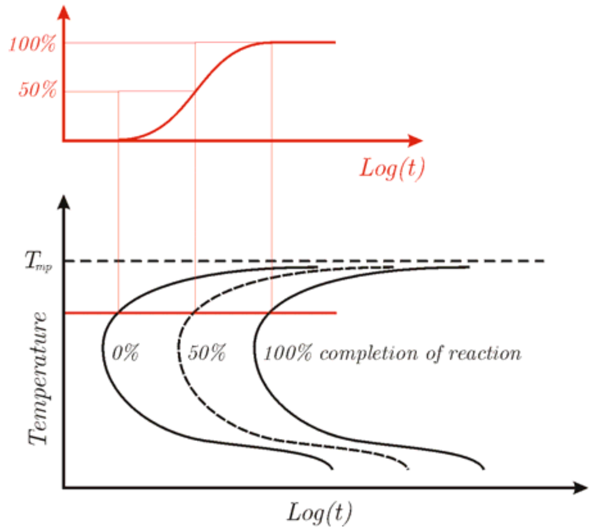

Figure 26: Theoretical example of TTT diagram

1.7. Assumptions in the model

Since the goal of the model is essentially a thermo-mechanical description of the material behaviour, it must not necessarily include also metallurgical modelling. Otherwise, the CPU time could increase dramatically. Moreover, a model a phase transformation requires TTT diagrams, one different mechanical constitutive law for each phase, more details about kinetics of transformation… all characteristic parameters that have to be collect and introduced in a model becoming more and more complex.

Phase transformations are not modelled, however their effect on some parameters are taken into account via thermal dependence of these parameters: thermal linear expansion (see II.2) and latent heat of solidification (see II.3) are illustrations of this thermo-metallurgical dependence.

The solid fraction, which is necessary to compute the ferrostatic pressure (see III.3), is assumed to vary linearly with respect to temperature:

$$\forall T \in \left[T_{sol}, T_{liq}\right] : 0 \le f_s(T) = \frac{T_{liq} - T}{T_{liq} - T_{sol}} \le 1 \tag{12}$$

In fact, this assumption is not too far from the observed evolution in equilibrium conditions, but it is quite different of a transient situation:

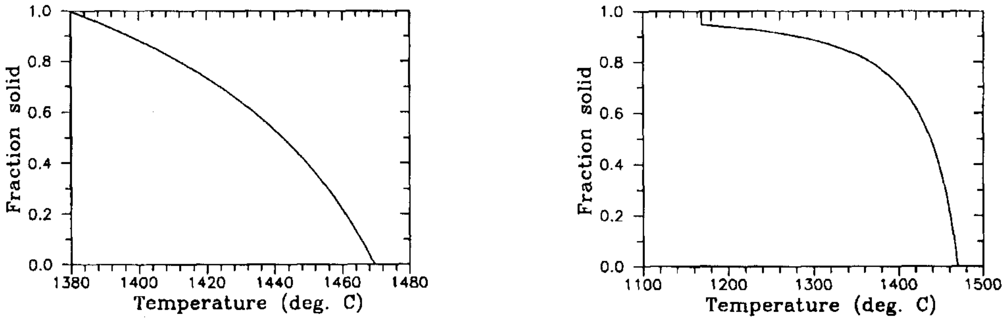

Figure 27: Examples of solid fraction vs. temperature for a commercial alloy steel at equilibrium condition (on the left) and non-equilibrium condition (on the right) [LEW00]

If such curves are available for the modelled material, their integration gives a more accurate solution.

2. Coefficient of thermal linear expansion

Temperature variation in any material induces volume changes: the volume occupied by the matter depends on the vibration energy of the atoms that constitute it. The measure of the relative volume variation is given by the coefficient of thermal expansion β:

$$\beta = \frac{1}{V}\left(\frac{\partial V}{\partial T}\right)_p \tag{13}$$

where V is the volume at temperature T (and constant pressure p).

In the same way, the coefficient of thermal linear expansion (TLE) α is defined as:

$$\alpha = \frac{1}{L}\left(\frac{\partial L}{\partial T}\right)_p \tag{14}$$

where L is the length in a given direction.

Assuming an isotropic thermal expansion, which is the case for most metallic materials, one can write:

$$1+\beta = \frac{V+\left(\frac{\partial V}{\partial T}\right)_p}{V} = \frac{\left[L+\left(\frac{\partial L}{\partial T}\right)_p\right]^3}{L^3} = (1+\alpha)^3 \tag{15}$$

$$\leftrightarrow \beta = 3\alpha + 3\alpha^2 + \alpha^3 \tag{16}$$

Since the magnitude of α for many metals and steel particularly is several orders below the unity (about 1.2 10^{-5} K^{-1} for steel), one can approximate β by:

$$\beta = 3\alpha \tag{17}$$

The thermal strain rate over a time step is given by:

$$\dot{\varepsilon}^{th} = \alpha\dot{T} \tag{18}$$

where $\dot{T}$ is the temperature rate during time step.

Unfortunately, there is no thermal expansion data available in the open literature materials in the semisolid and liquid state. However, many metals generally exhibit $\beta = 10^{-4}$ K^{-1} in the liquid phase just above their melting point or liquidus temperature [VAL02].

For solid phase, the temperature dependence is very complex: one can consider the effect of temperature, which is linked to the energy of vibration and/or motion of the atoms around their equilibrium position, but also the effect of phase changes on material contraction. Ideally, experiments should be performed to determine the variation of density $\rho(T)$ with respect to temperature. In such a case, a (mean) coefficient of TLE can be deducted from:

$$\alpha_m(T) = \sqrt[3]{\frac{\rho(T)}{\rho(T_0)}} - 1 \tag{19}$$

This coefficient is a "mean" value – and not differential as α defined in relation (14) – since it is representative of dilatation of the material with respect to a reference temperature (T_0).

If such measurements are not performed on the studied material, Chandra et al. proposed a procedure for prediction of TLE coefficient, including in the two-phase region of steel in the peritectic zone [CHA93]. This method has also been adopted by Moitra et al. [MOI93b]. This simple method is based on weighted average of the TLE of each phase in presence. In fact, according to steel composition and temperature, the amount of each phase and their carbon content can always be determined, at least if the equilibrium phase diagrams are assumed valid. This has been illustrated by the three examples shown in section II.1.5. Then, Chandra based his calculation on the specific volume of pure δ-iron and pure γ-iron, taking into account their temperature dependence defined by Wray [WRA80]:

$$\begin{cases} V_\delta(T) = 0.1234 + 9.38\ 10^{-6}\ \ (T - 20) \\ V_\gamma(T) = 0.1225 + 9.45\ 10^{-6}\ \ (T - 20) \end{cases} \tag{20}$$

where V_δ and V_γ are specific volume of pure δ-iron and pure γ-iron (in cm^3/g) and T the temperature (in °C). The carbon content is then taken into account thanks to regression analysis made by Fasiska et al. [FAS67] for δ-iron and Ridley et al. [RID70] for γ-iron. These works allowed writing the relation between the lattice parameter a as a function of carbon content (and temperature for γ-iron):

$$\begin{cases} a_{\delta,C} = a_{\delta,C=0} + 8.4\ 10^{-3} X_C \\ a_{\gamma,C} = a_{\gamma,C=0} + \left(0.0317 - 11.65\ 10^{-7} T - 0.05\ 10^{-7} T^2\right) W_C \end{cases} \tag{21}$$

where X_C is the atomic percentage of carbon and where W_C is the weight percentage of carbon.

According to this method, the Figure 28 illustrates the TLE coefficient for the 3 steel grades presented in II.1.5. These mean coefficients are defined with solidus temperature as reference and they are only considered in solid phase.

As this figure shows, the TLE coefficients are strongly different and the δ→γ transformation causes an important volume variation. However, these curves remain theoretical in the sense that they do not take into account the effect of other chemical substances present in steel. This is why the TLE coefficient used in the model are quite different from the values above (see industrial applications in chapters V and VI).

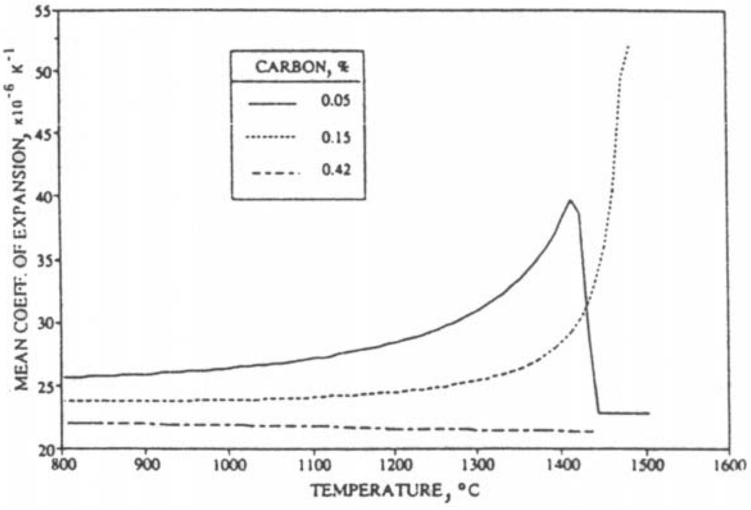

Figure 28: Variation of mean thermal linear expansion coefficient of 0.05wt%C, 0.15wt%C and 0.42wt%C steels **[CHA93]**

3. Internal heat conduction

The local expression of heat conservation gives the temperature field T as follows:

$$\rho c \frac{\partial T}{\partial t} = \nabla \cdot (k \nabla T) \tag{22}$$

where ρ is mass density, c specific heat and k thermal conductivity of the material. Specific heat represents the amount of heat necessary to raise the temperature of a unit mass sample by 1K. This expression is available inside the domain Ω including neither phase transformation nor heat source.

However, solidification is an exothermic process, i.e. some energy is given off by the system during this phase transformation. This energy is the latent heat of solidification and it must be taken into account in the energy balance. Under equilibrium conditions, the latent heat of fusion L_f and that of solidification L_s are essentially the same.

From the numerical point of view, various methods exist to model latent heat release during solidification. They can be classified in two families [LEW00]:

- front tracking methods [FIC00], where the interface between solid and liquid phases is tracked at each time step of the simulation;
- fixed grid methods, where both liquid and solid phases are treated as one continuous material, with different properties, but without any explicit boundary.

The most important advantage of the first family is to predict the location of the solid-liquid interface with accuracy, but it has the great drawback that it is not suitable for alloys, which present a finite freezing range.

Compared to the front tracking methods, fixed grid methods are much more suitable to the present model. The main advantages are the ability to apply these methods to alloys and to problems with multiple interfaces. In addition, they are easier to implement in an existing finite element code. The main disadvantage is a lower accuracy in interface. Among fixed grid methods, enthalpy methods and effective specific heat methods are quite usual.

Enthalpy methods consist in using the variation of enthalpy in the energy balance, so that:

$$\frac{\partial \mathcal{H}}{\partial t} = \nabla \cdot (k \nabla T) \tag{23}$$

where $\mathcal{H}$ is the enthalpy density, which is defined by:

$$\mathcal{H}(T) = \int_0^T \rho c \mathrm{d}\theta + \left(1 - f_s\right) L_F \tag{24}$$

where f_s is the solid fraction and L_F the latent heat of fusion.

Defining enthalpy density $\mathcal{H}$ at several temperatures, the energy balance (23) becomes:

$$\frac{\Delta \mathcal{H}}{\Delta T} \dot{T} = \nabla \cdot (k \nabla T) \tag{25}$$

In effective specific heat methods, the energy balance equation is written using the effective specific heat $\tilde{c}$:

$$\rho \tilde{c} \frac{\partial T}{\partial t} = \nabla \cdot (k \nabla T) \tag{26}$$

where $\tilde{c}$ is equal to the specific heat c in both solid and liquid zone, but it is defined in the mushy zone as a function of solid fraction f_s and specific latent heat l_F:

$$\tilde{c} = c - \frac{\mathrm{d}f_s}{\mathrm{d}T} l_f \tag{27}$$

Assuming the linear variation of f_s, cf. relation (12), the effective specific heat becomes:

$$\tilde{c} = c + \frac{l_f}{T_{liq} - T_{sol}} \tag{28}$$

so that a step variation appear in the $\tilde{c}$ vs. T curve is shown in a typical example on Figure 29. As this figure suggests, the use of effective specific heat method can be dangerous insofar as the size of the time step must be controlled: if the time step is too long, the temperature variation can be relatively large, for example decreases from 1530 °C to 1460 °C. In such a case, the effective latent heat $\tilde{c}$ seems not to vary during the time step (same value at the beginning and the end of the step) and the phase transformation is missed. At the opposite, enthalpy method allows to use any time step size.

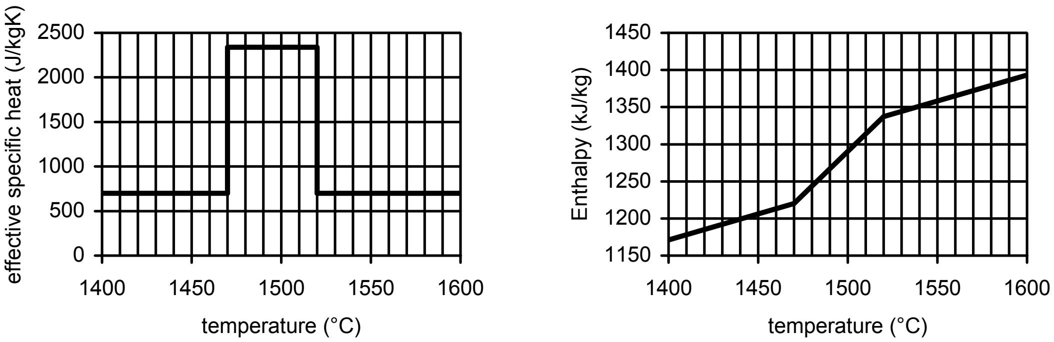

Figure 29: Example of typical variation of effective specific heat (on the left) and corresponding enthalpy (on the right).

With enthalpy methods, it is not necessary to know a priori the position of the interface to get a solution that verifies the conservation of heat. Because of its easy use and its accuracy, this method has been adopted in the model.

Note that among fixed grid methods, one can also mention the heat-flow methods, which introduce the latent heat as a heat generation term in the heat conduction equation:

$$\rho c \frac{\partial T}{\partial t} = \nabla \cdot (k \nabla T) + \frac{\partial f_s}{\partial t} l_f \tag{29}$$

This term has a non-zero value only for the nodes which undergo a change of phase during time step, the latent heat effects being added to the vector of the nodal heat flux in the system of equation. For this reason, the temperature of such nodes is maintained at the melting point till the latent heat associated to the node is completely released. Heat-flow methods are less accurate than other schemes and they are not suitable for alloys, since those solidify over a range of temperature.

4. Thermal boundary conditions

The studied domain is obviously not infinite and the temperature field on the boundary δΩ of the domain is expressed by one or more of the following conditions:

- essential condition (or Dirichlet condition): temperature is imposed $T(\underline{x},t) = \overline{T}$;
- natural condition (or Neumann condition): heat flux q is imposed $k\frac{\partial T}{\partial n} = q$;
- mixed condition (or Cauchy condition): heat flux is a linear function of the temperature field $k\frac{\partial T}{\partial n} = f(T)$.

The three types of thermal boundary conditions are applied in the model. The first one is used for initial conditions: the initial temperature field is imposed at the beginning of the simulation: $T(\underline{x},0) = \overline{T}_{ini}$. Along axes of symmetry, adiabatic walls are assumed: the corresponding boundary condition is a heat flux equal to zero, which is a particular case of natural condition so-called homogeneous Neumann condition.

Everywhere else on the boundary of the domain, mixed conditions are applied: the heat flux is proportional to the difference of temperature between the strand surface and the surroundings. The proportionality factor is the heat flux coefficient h, which depends on the nature of the heat flux:

$$k\frac{\partial T}{\partial n} = h\left(T - \overline{T}_a\right) \tag{30}$$

where $\overline{T}_a$ is the ambient temperature.

Three main ways of thermal exchange can be itemized: direct contact, convection and radiation.

In the first two cases, heat flux is typically govern by a relation similar to (30). Note that the heat transfer coefficient can be dependent on several parameters: nature of the bodies in contact (material of the strand and the mould or the rolls) or of the surroundings (air, water …), roughness of the surface of the bodies in contact, temperature of the bodies and surroundings … It is thus not excluded that the heat transfer coefficient h is dependent on the temperature of the studied body itself (the modelled slice of the strand).

At the opposite, in case of radiation, heat flux is rather governed by the Stefan-Boltzmann rule. Thermal radiation is the energy transferred by electromagnetic waves from the surface of the studied body (strand) to surroundings (anything: mould, rolls, atmosphere …). The total emissive power of a body is given by the Stefan-Boltzmann equation:

$$e = \varepsilon\sigma T^4 \tag{31}$$

where ε is the emissivity of the body (intrinsic characteristic), σ the radiation constant and T the surface temperature of the body. Both bodies – the strand and ambient (mould, rolls, air…) at temperature $\overline{T}_A$ – are emitting, so that the balance of radiations and the absorption of energy by the gap gives the effective heat transfer by radiation:

$$q_{rad} = \gamma\left(T^4 - \overline{T}_a^4\right) \tag{32}$$

with

$$\gamma = \frac{m^2\sigma}{0.75ad_{gap} + \dfrac{1}{\varepsilon_{strand}} + \dfrac{1}{\varepsilon_{mould}} - 1} \tag{33}$$

where m is the flux refractive index, a the flux absorption coefficient and d the thickness of the gap [STO99].

As the relation (32) clearly shows, the heat flux by radiation is not a linear function of the temperature and it does not fit to the definition of mixed boundary condition. However, one can consider that the heat transfer coefficient h is dependent on temperature. It is true for heat fluxes by direct contact and by convection. It is also possible to write relation (32) as follows:

$$\begin{aligned} q_{rad} &= \gamma\left(T^2+\overline{T}_a^2\right)\left(T+\overline{T}_a\right)\left(T-\overline{T}_a\right) \\ &= h\left(T\right)\left(T-\overline{T}_a\right) \end{aligned} \tag{34}$$

Thermal boundary conditions are so summarized:

- no heat flux along symmetry axes (adiabatic wall)
- where the steel strand is in contact (with the mould or rolls), heat flux is given by:

$$q_{cont} = h_{cont}\left(T\right)\left(T-\overline{T}_a\right) \tag{35}$$

- anywhere else, heat flux is the sum of the convective and radiative contributions:

$$\begin{aligned} q_{conv+rad} &= h_{conv}\left(T\right)\left(T-\overline{T}_a\right)+h_{rad}\left(T\right)\left(T-\overline{T}_a\right) \\ &= h_{conv+rad}\left(T\right)\left(T-\overline{T}_a\right) \end{aligned} \tag{36}$$

In other respect, since the heat flux is dependent on contact occurrence, it is coupled to mechanical behaviour.

III. Mechanical Model

III. Mechanical model

1. *Generalized plane strain state*

1.1. Principle

As already mentioned in section I.3.1, the model is based on generalized plane strain state. A thin slice, perpendicular to the casting axis is modelled. The middle plane of the slice is meshed (see Figure 30) and its thickness e at any point of coordinates (x,y) in the domain is governed by 3 degrees of freedom α_0, α_1 and α_2 according to the following expression:

$$e(x,y) = \alpha_0 + \alpha_1 x + \alpha_2 y \tag{37}$$

So a virtual (i.e. immaterial) node is defined in the finite element mesh by coordinates (α_0, α_1, α_2). These three “coordinates” are dedicated to the management of the generalized plane strain state. Each “coordinate” is associated in fact to one degree of freedom of equation (37). As it clearly appears:

- α_0 corresponds to the thickness of the slice at the origin of the axes x and y;
- α_1 and α_2 are representative of the variation of thickness respectively along x and y axes, in other words, they are gradients of thickness.

Since α_1 and α_2 are constant (with respect to coordinates x and y), the thickness of the slice can vary linearly in both directions of the plane. The thickness is constant along x (or y) direction if α_1 (respectively α_2) is equal to zero. That means that the slice is always confined between two planes, which are symmetric with respect to the middle plane of the slice:

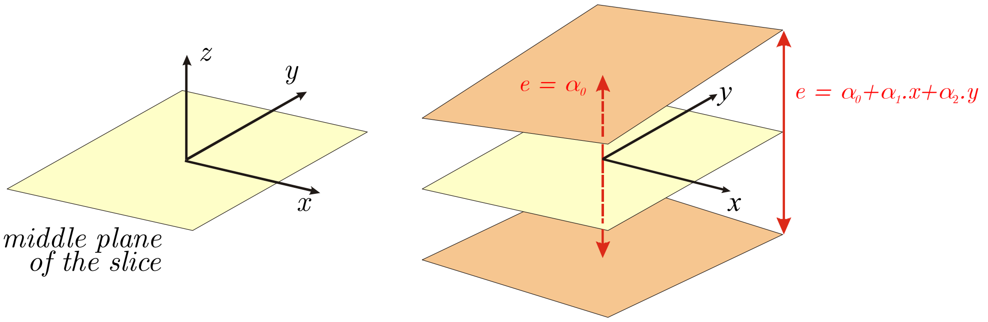

Figure 30: Thickness of the slice in generalized plane strain state

The three degrees of freedom α_0, α_1 and α_2 can be used like any other degree of freedom in the model, that is to say that they can be fixed, externally imposed or left free to vary:

- in the first case, the value is imposed and constant during the whole computation – this is equivalent to the fixation of a classical geometrical node;
- in the second case, it varies, but according to an externally imposed value – this is equivalent to an imposed displacement of a classical geometrical node;
- in the third case, the value is free to vary, but computed according to balance equation along z direction.

In the latter case, the balance equations are respectively for the three degrees of freedom:

$$\begin{cases} \int_\Omega \sigma_{zz}.da + \int_\Gamma \tau_z.ds = F_z^{external} & \text{for } \alpha_0 \text{ d.o.f.} \\ \int_\Omega \sigma_{zz}.x.da + \int_\Gamma \tau_z.x.ds = M_y^{external} & \text{for } \alpha_1 \text{ d.o.f.} \\ \int_\Omega \sigma_{zz}.y.da + \int_\Gamma \tau_z.y.ds = M_x^{external} & \text{for } \alpha_2 \text{ d.o.f.} \end{cases} \tag{38}$$

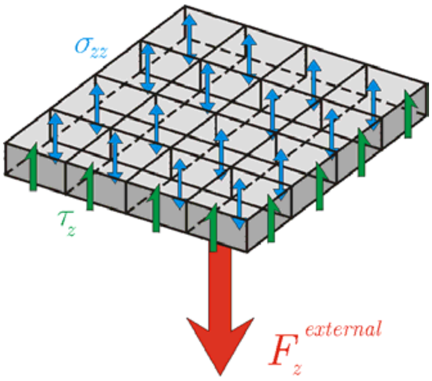

Figure 31: Equilibrium of the slice in generalized plane strain state

Whatever the management of the degrees of freedom is (free, fixed, imposed), the generalized plane strain state allows including in the model both stresses and strains along z direction $(\sigma_{zz} \neq 0 \text{ and } \varepsilon_{zz} \neq 0)$. Compared to other classical two-dimensional approaches, i.e. plane stress state and plane strain state, generalized plane strain state is thus richer: plane strain state only permits to model out-of-plane stresses $(\sigma_{zz} \neq 0$ but $\varepsilon_{zz} = 0)$, and plane stress state only the out-of-plane strains $(\varepsilon_{zz} \neq 0$ but $\sigma_{zz} = 0)$.

Since generalized plane strain state can be positioned between two-dimensional and three-dimensional analyses, it is qualified of “2D½” approach.

1.2. Bending and straightening using generalized plane strain state

Besides the advantage of including both out-of-plane stresses and out-of-plane strains, generalized plane strain state also permit to model slices of a bent and straightened strand, what is of prime importance for modelling the complete process.

In fact, one can consider a slice in the bent zone as being between two planes converging to the centre of curvature of the steel strand. The succession in time (thus along casting axis) of several slices gives a bent strand, as shown on Figure 32.

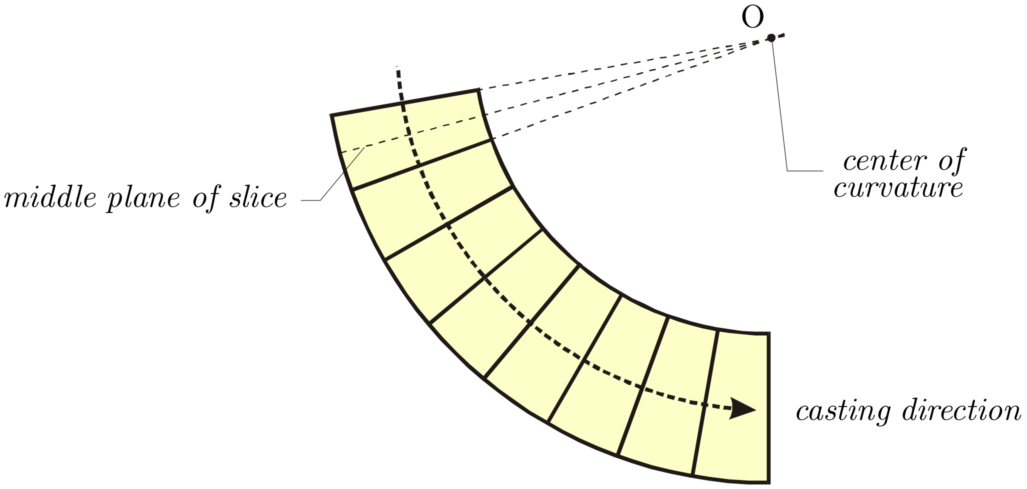

Figure 32: Succession of slices in bent zone

The way to determine α_0, α_1 and α_2 degrees of freedom according to caster geometry is described hereafter. The Figure 33 represents a slice in the "bent" zone of a slab: x and y are axes in the plane of the slice, respectively along width and height of the slab. The thickness of the slice is independent of x coordinate, but varies linearly along y direction. Henceforth we can consider that α_1 degree of freedom (corresponding to gradient of thickness of the slice along x direction) is equal to zero.

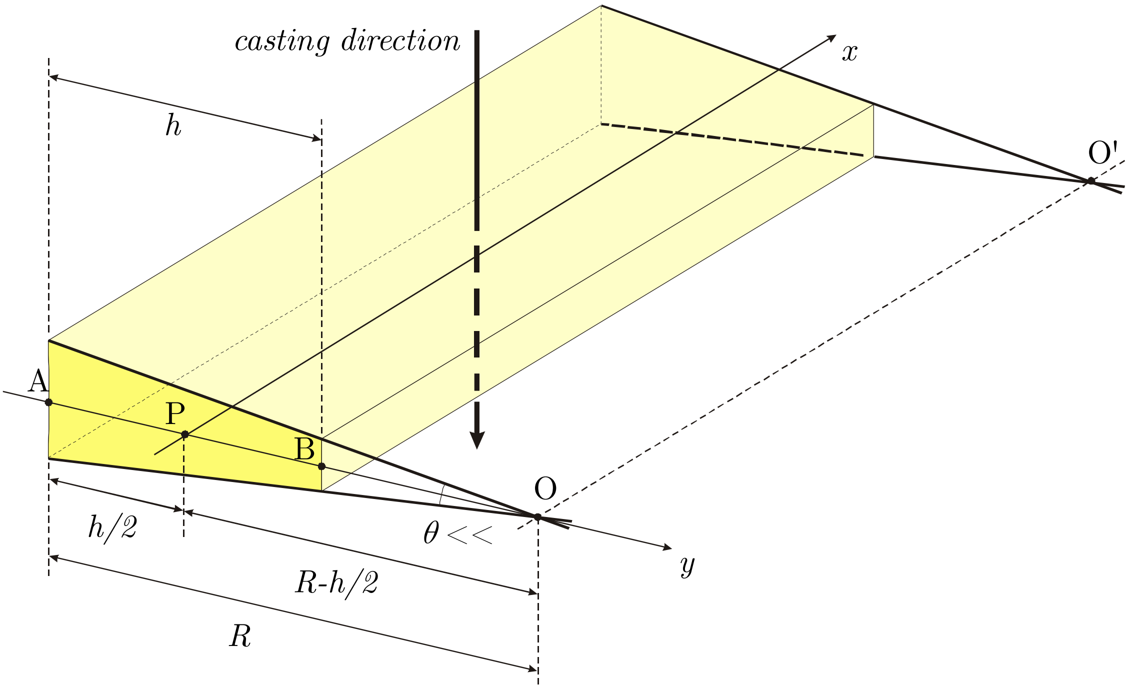

Figure 33: Geometry of a slice of a "bent"slab (not to scale)

The upper and lower planes delimiting the slice are converging to OO' straight line, which corresponds to the centre of curvature of the strand.

Considering a vertical plane, the abscise of which being $x = 0$, let's define 4 particular points on the middle plane of the slice (see Figure 33):

- A is the point on the extrados face
- P is the point at the origin of y axis ($y = 0$)
- B is the point on the intrados face
- O is the centre of curvature

Generally, the distance $|\mathrm{AO}|$ is known as radius of curvature R of the caster, indicated on the plans. In other respects, $|\mathrm{AB}|$ is the height h of the slab.

The thickness of the slice is governed by equation (37). Since $\alpha_1 = 0$, it can be simplified:

$$e(y) = \alpha_0 + \alpha_2 y \tag{39}$$

It corresponds to the distance between the upper and the lower planes, which vanishes in O:

$$e(y_{\mathrm{O}}) = \alpha_0 + \alpha_2 y_{\mathrm{O}} = \alpha_0 + \alpha_2 \left(R - \frac{h}{2} \right) = 0 \tag{40}$$

So there is a relation between α_0 and α_2 degrees of freedom expressing the curvature of the steel strand at a given time t:

$$\alpha_2(t) = -\frac{\alpha_0(t)}{R(t) - \dfrac{f(t)}{2}} \tag{41}$$

The radius of curvature R varies with respect to the position of the slice in the caster. For a vertical-curve machine, the strand is first straight, so R is infinite. Then, during bending, R is decreasing down to the characteristic radius of curvature R_0 of the caster. After the zone of constant curvature ($R = R_0$), the strand is straightened and R grows to infinity, when the strand is completely straightened and in horizontal position.

The value of the radius of curvature is given on the plans of the caster. It is measured at the level of each pair of rolls. So R is known for singular times, corresponding to the passage of the slice at the level each pair. When the slice is moving from one pair to the next one, the curvature $\chi = {}^{1}\!/_{R}$ is assumed to vary linearly. That way, there is no problem to start bending and to finish straightening, since the curvature tends to zero and is thus easy to use in computations, contrary to the infinite value of R.

In other respects, if the thickness of the slice is fixed at a given coordinate y_1, an additional relation is available and both degrees of freedom α_0 and α_2 are fixed:

$$\begin{cases} e(y_1) = \alpha_0 + \alpha_2 y_1 = \bar{e} \\ \alpha_2(t) = -\dfrac{\alpha_0(t)}{R(t) - \dfrac{f(t)}{2}} \end{cases} \tag{42}$$

hence

$$\alpha_0 = \frac{R - \dfrac{f}{2}}{R - \dfrac{f}{2} - y_1} \overline{e} \tag{43}$$

and

$$\alpha_2 = -\frac{\overline{e}}{R - \dfrac{f}{2} - y_1} \tag{44}$$

A typical case of the example above occurs when the neutral axis is imposed at a given position. In such a case all degrees of freedom of the generalized plane strain state are fixed and thus thickness, out-of-plane strain and strain rate also (see section III.1.4).

1.3. Application of extracting force

1.3.1. Origin of extracting force

Under ferrostatic pressure, the strand inflates between successive pairs of rolls. This leads to an effort δF_1 applied by the strand on the rolls:

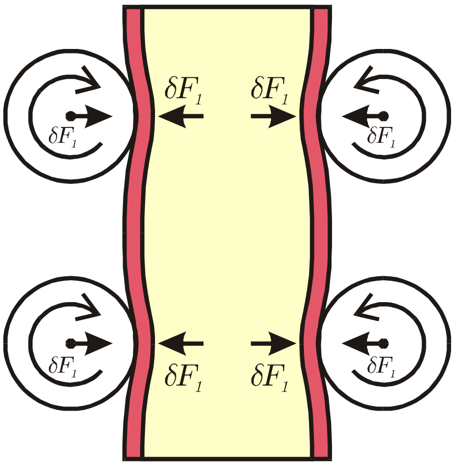

Figure 34: Force δF_1 applied by the strand on the rolls

While the strand is moving through the caster, all rolls are spinning around their axis. This is possible since the friction coefficient at contact between strand and rolls $\mu_{strand\text{-}roll}$ is higher than friction coefficient at the roll axis μ_{axis}:

- $\mu_{strand-roll} = 0.30$ (usual value in hot forging)
- $\mu_{axis} = 0.015$ (ball bearing)

At the opposite, if μ_{axis} becomes higher than $\mu_{strand\text{-}roll}$ then the roll does not spin anymore and the strand slides on the roll. This happens when a roll is locked (μ_{axis} tends to infinite value because of a local defect, clogging up with dirt, bad maintenance, etc).

To insure a constant velocity of the strand in the caster (casting speed), it is necessary to apply an extracting force to overcome the frictional resistance.

In case of locked roll, the resisting force δR_1 is obviously equal to:

$$\delta R_1 = \mu_{strand-roll}.\delta F_1 \tag{45}$$

In case of (almost-) free roll, the resistance is much lower and equal to:

$$\delta R_1 = \mu_{axis}.\delta F_1 \tag{46}$$

This value corresponds to the resisting couple δC_1 taking place at the roll axis when a constant angular velocity ω is imposed to the roll while a small friction tends to oppose.

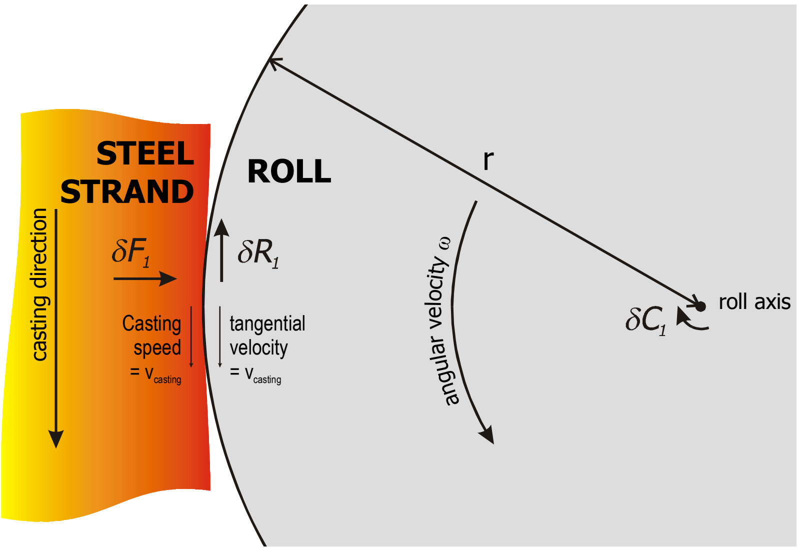

Figure 35: Resistance δR_1 due to friction at roll axis

Besides the bulging of the strand, bending of the strand (but also straightening) requires to rest on the rolls, so that a second type of effort δF_2 takes place on the rolls, as schematically shown on Figure 36.

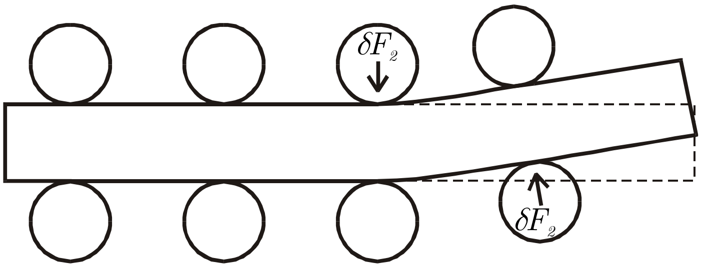

Figure 36: Effort δF_2 on the rolls due to bending (straightening)

Actually, the distribution of efforts on the rolls is much more complex: the strand is a kind of “highly hyperstatic beam” on a large amount of “fixations” (rolls), the latter figure giving some idea of the origin of δF_2. Just like for δF_1 and δR_1, δF_2 contributes by δR_2 to increase the resisting force, so that the increment of resistance δR for one roll is:

$$\delta R = \delta R_1 + \delta R_2 = \mu.(\delta F_1 + \delta F_2) \tag{47}$$

where μ is the minimum value between μ_{axis} and $\mu_{strand\text{-}roll}$. The sum of the contribution of all rolls gives the cumulated resistance R:

$$R = \sum_{rolls} \delta R_i = \sum_{rolls} (\delta R_1 + \delta R_2)_i \tag{48}$$

1.3.2. Extracting force, extracting rolls and distribution of work

Each roll withstands the advance of the strand in the caster. The global resistance R is thus increasing, considering the successive rolls and their contribution δR to the global resistance.

To insure a constant velocity of the strand, it is necessary to transmit to the strand an external force that is equal to the resisting force: this is the extracting force F.

To do so, some rolls are motorised (extracting rolls), which are symbolised by ⊗ on plans. They are numerous in the caster and the work of extraction is shared amongst them. The distribution of this work is not obvious.

To better understand this problem, let's make an analogy with a train (Figure 37): in a train, driving force comes from the locomotive and resistance from friction at the axis of each wheel of the wagons (and of the locomotive itself) – neglecting resistance due to air penetration.

If there was only one pair of extracting rolls at the end of the caster, the resisting force would increase from pair to pair and all the extracting force should be provided by the only motorised pair. This would correspond to a locomotive pulling all the wagons:

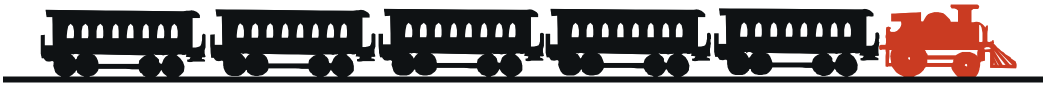

Figure 37: One locomotive pulling all the wagons

From the mechanical point of view, this situation would lead to an increasing tensile state (axial loading) of the strand:

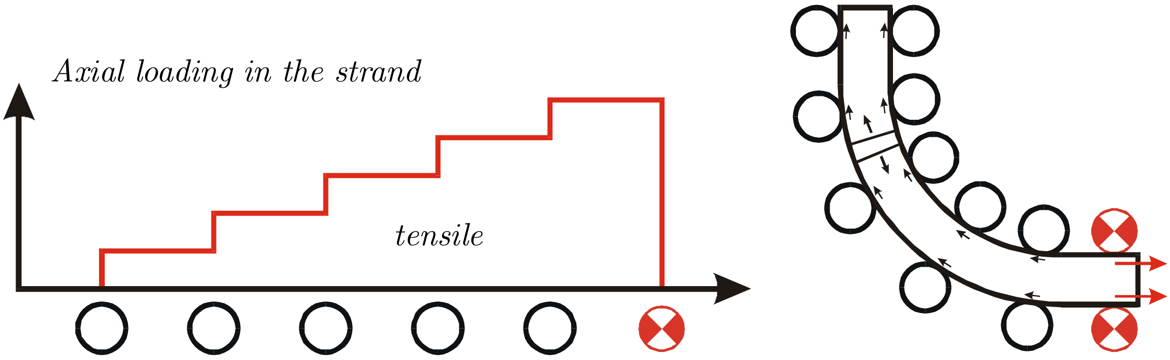

Figure 38: Evolution of the axial loading in the strand (one extracting pair of rolls at the end of the caster)

Obviously, the locomotive can be moved to another place in the train, for instance behind all the wagons, pushing all of them:

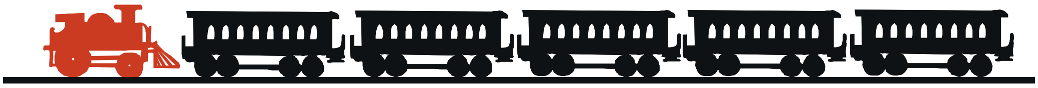

Figure 39: One locomotive pushing all the wagons

This is equivalent to one extracting pair of rolls at the top (beginning) of the caster. In this case, the axial loading of the strand is of compressive state:

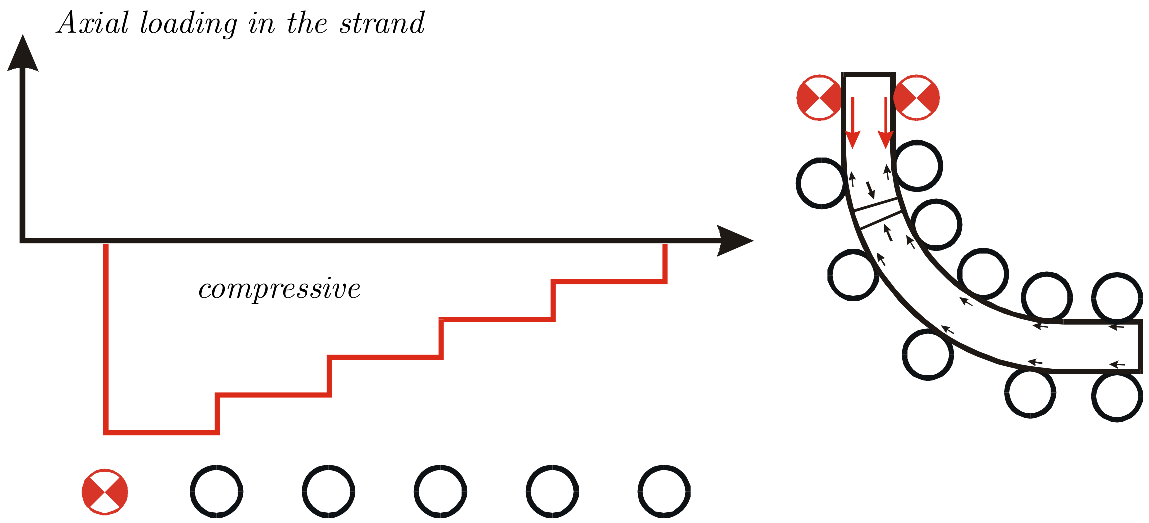

Figure 40: Evolution of the axial loading in the strand (one extracting pair of rolls at the beginning of the caster)

Actually, a caster with only one extracting pair is of course out of question for many reasons, but numerous pairs are distributed in the machine. Consider a train with several locomotives in one train, the problem of work sharing starts taking place. For instance, there are two locomotives as shown on Figure 41.

Figure 41: Train with two locomotives

A priori, it is impossible to know how they work. For example, one solution, which is the more efficient, would be equal work, each one pulling two wagons. But it is possible that the first one is pulling three wagons and the second one only one. Or the second one is the only one to work, pulling the two wagons in the back and pushing the two in the front and the first locomotive as well.

Any assumption is available if admissible. The same argument is possible for the continuous caster. Since rotation of extracting rolls is regulated to control the speed of the strand (and not the work made by the rolls), each extracting pair can either pull and/or push the steel strand trough the machine. The only certitude is that the cast product (i.e. the strand) is extracted from the caster so the global resisting force is overcome by the global extracting force.

Which assumption can be accepted? In absence of information, the less favourable to the problem should be used. For instance, if the aim of the study is to evaluate the risk of transverse cracking, axial tensile state is much more critical than axial compressive state. In that case, one reasonable solution is to consider that *each extracting pair of rolls provides exactly the work needed to overcome the resistance due to the preceding "free" rolls in the caster.* To continue analogy with the train of

Figure 41, this would correspond with two separated trains at the same velocity, the locomotive of each one pulling the wagons in the back, as shown on Figure 39.

Figure 42: Two separate trains with one locomotive

In that case, axial loading is increasing, from "free" pair to "free" pair, until one extracting pair is reached. At that moment, the (tensile) axial loading vanishes. Then it increases again with successive "free" pairs, and so on up to the exit of the caster.

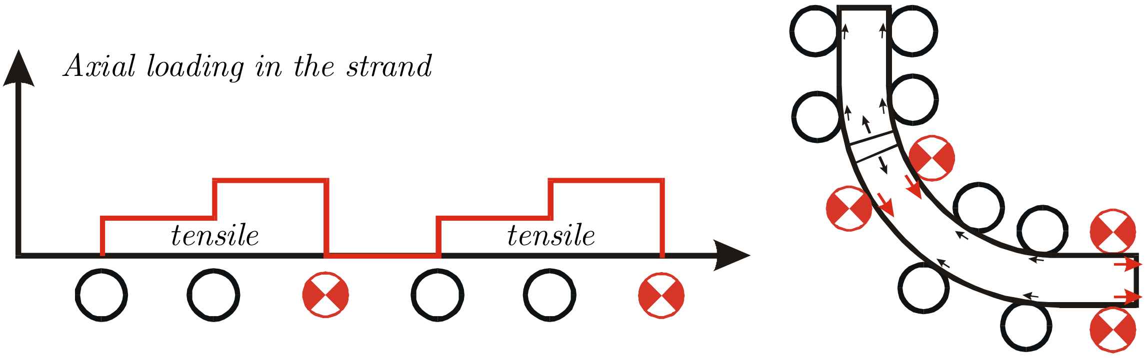

Figure 43: Evolution of the axial loading in the strand (several extracting pairs of rolls)

1.4. Neutral axis

During bending and straightening, the strand is subject to two types of loading: bending (from bending/straightening itself) and axial loading (from extracting force). The result is a combination of both, which implies that the position of the neutral axis is unknown a priori, since it depends on the value of both loadings.

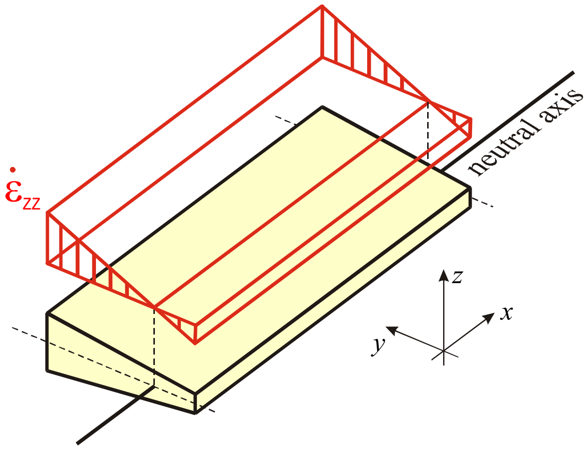

Figure 44: Position of neutral axis

If the position of neutral axis was known, the evolution of thickness would be determined and would give one relation more. For instance, assuming that neutral axis corresponds to axis x ($y = 0$) and that the thickness $\overline{e}$ is equal to unity, the relations (43) and (44) become:

$$\alpha_0 = \overline{e} = 1 \tag{49}$$

and

$$\alpha_2 = -\frac{1}{R - \dfrac{f}{2}} \tag{50}$$

At the opposite, since neutral axis is mobile and depending on loading conditions, both α_0 and α_2 are unknown and their value is evaluated according to relation (41) and equilibrium equation between out-of-plane stresses in the material (the slice of steel) and external forces (extracting force).

2. Elastic-viscoplastic constitutive law

2.1. Decomposition of total strain

During solidification processes, the total distortion of the material is due to several sources. Generally, total strain ε is assumed to be the sum of the following contributions:

- thermal strain ε^{th};
- phase transformation strain ε^{tr};
- elastic strain ε^{el};
- non-elastic (viscoplastic) strain ε^{vp};

2.1.1. Thermal and phase transformation strains

Thermal and phase transformation strains are linked to volume changes with temperature. The phenomenon has already been explained in details in chapter II.

The corresponding strain rate is given by:

$$\dot{\varepsilon}^{th} = \alpha \dot{T} \begin{pmatrix} 1 & 0 & 0 \\ 0 & 1 & 0 \\ 0 & 0 & 1 \end{pmatrix} \tag{51}$$

which is hydrostatic type strain rate.

As its name indicates, phase transformation strain appears when phase changes occur in the material. Since phase transformation is linked to temperature variation, it is commonly used to include this effect in the value of a "modified" coefficient of thermal linear expansion α^*, so that:

$$\dot{\varepsilon}^{th} + \dot{\varepsilon}^{tr} = \alpha^* \dot{T} \begin{pmatrix} 1 & 0 & 0 \\ 0 & 1 & 0 \\ 0 & 0 & 1 \end{pmatrix} \tag{52}$$

For simplification, α^* is simply (and abusively) noted α.

2.1.2. Mechanical strains

When subtracting the thermal and phase transformation strains from the total strain, the remaining term is the mechanical strain. The mechanical strain can be split into elastic strain and viscoplastic strain:

$$\varepsilon^{mec} = \varepsilon - \varepsilon^{th} - \varepsilon^{tr} = \varepsilon^{el} + \varepsilon^{vp} \tag{53}$$

The mechanical model is based on a unified elastic-viscoplastic constitutive law for steel at high temperature (solid as well as liquid). The following section introduces first the elastic domain and then the viscoplastic domain. After that, the problem of determination of yield limit is presented as well as the loading/unloading criterion. Finally, some examples are presented.

2.2. Elastic domain

2.2.1. Hooke's law for isotropic materials

Hooke's law gives the relation between stresses and strains for an elastic material, that is:

$$\sigma_{ij} = D_{ijkl}\varepsilon_{kl} \tag{54}$$

In the case of isotropic materials, some components of the matrix of elasticity $\underline{D}_{iso}$ are equal to zero, so that:

$$\underline{D}_{iso} = \frac{E}{(1+\nu)}\begin{pmatrix} \frac{1-\nu}{1-2\nu} & \frac{\nu}{1-2\nu} & \frac{\nu}{1-2\nu} & 0 & 0 & 0 \\ \frac{\nu}{1-2\nu} & \frac{1-\nu}{1-2\nu} & \frac{\nu}{1-2\nu} & 0 & 0 & 0 \\ \frac{\nu}{1-2\nu} & \frac{\nu}{1-2\nu} & \frac{1-\nu}{1-2\nu} & 0 & 0 & 0 \\ 0 & 0 & 0 & 1 & 0 & 0 \\ 0 & 0 & 0 & 0 & 1 & 0 \\ 0 & 0 & 0 & 0 & 0 & 1 \end{pmatrix} \tag{55}$$

Dealing only with isotropic materials, the "$_{iso}$" subscript will not be indicated in the text anymore. So Hooke's law for isotropic linear elastic material is:

$$\sigma_{ij} = \frac{E}{(1+\nu)(1-2\nu)}\left[(1-2\nu)\,\varepsilon_{ij} + \nu\varepsilon_{ll}\delta_{ij}\right] \tag{56}$$

The stress and strain tensors are generally decomposed into their mean and deviatoric values:

$$\begin{cases} \sigma_{ij} = \hat{\sigma}_{ij} + \sigma_m\delta_{ij} \\ \varepsilon_{ij} = \hat{\varepsilon}_{ij} + \varepsilon_m\delta_{ij} \end{cases} \quad \text{with} \quad \begin{cases} \sigma_m = \dfrac{\sigma_{11}+\sigma_{22}+\sigma_{33}}{3} \\ \varepsilon_m = \dfrac{\varepsilon_{11}+\varepsilon_{22}+\varepsilon_{33}}{3} \end{cases} \tag{57}$$

According to Hooke's law, the mean value of stresses is:

$$\begin{aligned}\sigma_m &= \frac{1}{3}\left(\sigma_{11}+\sigma_{22}+\sigma_{33}\right)\\ &= \frac{1}{3}\frac{E}{(1+\nu)(1-2\nu)}\left[(1-2\nu)\left(\varepsilon_{11}+\varepsilon_{22}+\varepsilon_{33}\right)+3\nu\left(\varepsilon_{11}+\varepsilon_{22}+\varepsilon_{33}\right)\right]\\ &= \frac{1}{3}\frac{E}{(1+\nu)(1-2\nu)}(1+\nu)\left(\varepsilon_{11}+\varepsilon_{22}+\varepsilon_{33}\right)=\frac{E}{(1-2\nu)}\varepsilon_m\end{aligned} \tag{58}$$

That is, using the bulk modulus $\chi=\dfrac{E}{3(1-2\nu)}$:

$$\sigma_m = 3\chi\varepsilon_m \tag{59}$$

Then, computing the deviatoric stresses and separating the diagonal terms ($i=j$) from the out-of-diagonal ones:

$$\begin{aligned}\hat{\sigma}_{11}=\sigma_{11}-\sigma_m &= \frac{E}{(1+\nu)(1-2\nu)}\left[(1-2\nu)\varepsilon_{11}+\nu\varepsilon_{ll}\right]-\frac{E}{1-2\nu}\varepsilon_m\\ &= \frac{E}{(1+\nu)(1-2\nu)}(1-2\nu)\varepsilon_{11}+\frac{E}{(1+\nu)(1-2\nu)}\nu 3\varepsilon_m-\frac{E}{1-2\nu}\varepsilon_m\\ &= \frac{E}{(1+\nu)}\varepsilon_{11}+\frac{E}{(1+\nu)(1-2\nu)}(3\nu-1-\nu)\varepsilon_m\\ &= \frac{E}{(1+\nu)}\left(\varepsilon_{11}-\varepsilon_m\right)=2G\left(\varepsilon_{11}-\varepsilon_m\right)=2G\hat{\varepsilon}_{11}\end{aligned} \tag{60}$$

where G is shear modulus.

In the same way:

$$\hat{\sigma}_{22}=2G\hat{\varepsilon}_{22} \tag{61}$$

$$\hat{\sigma}_{33}=2G\hat{\varepsilon}_{33} \tag{62}$$

For the out-of-diagonal terms:

$$\hat{\sigma}_{ij}=\sigma_{ij}=\frac{E}{1+\nu}\varepsilon_{ij}=2G\varepsilon_{ij}=2G\hat{\varepsilon}_{ij} \qquad \forall i\neq j \tag{63}$$

So that generalising equations (60) to (63):

$$\hat{\sigma}_{ij}=2G\hat{\varepsilon}_{ij} \qquad \forall i,j \tag{64}$$

And Hooke's law takes the convenient following expression:

$$\sigma_{ij}=2G\hat{\varepsilon}_{ij}+3\chi\varepsilon_m\delta_{ij} \tag{65}$$

2.2.2. Time integration of Hooke's law with temperature dependence

The relation (65) allows computing the stress rate easily by decomposition into deviatoric and mean values. The deviatoric part of stress rate is obtained deriving (64):

$$\begin{aligned}\hat{\dot{\sigma}}_{ij} &= 2G\hat{\dot{\varepsilon}}^{ela}_{ij} + 2\dot{G}\hat{\varepsilon}_{ij} \\ &= 2G\hat{\dot{\varepsilon}}^{ela}_{ij} + 2\frac{\partial G}{\partial T}\dot{T}\frac{1}{2G}\hat{\sigma}_{ij}\end{aligned} \tag{66}$$

$$\leftrightarrow \hat{\dot{\sigma}}_{ij} - \frac{1}{G}\frac{\partial G}{\partial T}\dot{T}\hat{\sigma}_{ij} = 2G\hat{\dot{\varepsilon}}^{ela}_{ij} \tag{67}$$

That is a first order linear differential equation, the type of which being:

$$y'(x) + p(x)\, y(x) = f(x) \tag{68}$$

and the solution of which being:

$$y(x) = \left[Cst + \int e^{A(x)} f(x)dx\right] e^{-A(x)} \tag{69}$$

where

$$A(x) = \int p(x)dx \tag{70}$$

Solving equation (67):

$$\rightarrow \text{“}A(x)\text{”} : \int\left(-\frac{1}{G}\right)\frac{\partial G}{\partial T}\dot{T}.dt = -\frac{G_B - G_A}{\Delta T}\int\frac{1}{G}dT \tag{71}$$

since the elastic shear modulus G is assumed varying linearly with respect to temperature during one step increment (its derivative is a constant). Hence the following expression for $G(T)$:

$$G = C_1.T + C_2 \tag{72}$$

The integration constants are defined by the value of G at the beginning (subscript $_A$) and at the end of the step (subscript $_B$):

$$\begin{cases} G_A = C_1.T_A + C_2 \\ G_B = C_1.T_B + C_2 \end{cases} \tag{73}$$

$$\rightarrow G_B - G_A = C_1.(T_B - T_A) \tag{74}$$

$$\rightarrow C_1 = \frac{G_B - G_A}{\Delta T} = \frac{\partial G}{\partial T} \quad \text{and} \quad C_2 = G_A - C_1.T_A \tag{75}$$

Relation (71) becomes:

$$\text{"}A(x)\text{"} = -C_1\int\frac{1}{C_1T + C_2}dT = -\frac{C_1}{C_1}\ln(C_1T + C_2) = -\ln G \tag{76}$$

$$\rightarrow \text{“ } e^{A(x)} \text{ ”} : e^{-\ln G} = \frac{1}{G} \quad \text{and} \quad \text{“ } e^{-A(x)} \text{ ”} : e^{\ln G} = G \tag{77}$$

And the solution of the differential equation (67) is:

$$\rightarrow \text{“ } y(x) \text{ ” : } \hat{\sigma}_{ij} = \left[Cst + \int \frac{1}{G} 2G \hat{\dot{\varepsilon}}_{ij} dt \right] G = GCst + 2G \hat{\dot{\varepsilon}}_{ij} t \tag{78}$$

Once again, expressing the relation at the beginning of the step, and the constant *Cst* can be determined:

$$\hat{\sigma}_{ij,A} = G_A Cst + 2G_A \hat{\dot{\varepsilon}}_{ij} t_A \tag{79}$$

$$\rightarrow Cst = \frac{\hat{\sigma}_{ij,A}}{G_A} - 2\hat{\dot{\varepsilon}}_{ij} t_A \tag{80}$$

The deviatoric part of the stress is so given at any time:

$$\hat{\sigma}_{ij} = \frac{G}{G_A} \hat{\sigma}_{ij,A} + 2G \hat{\dot{\varepsilon}}_{ij} \left(t - t_A \right) \tag{81}$$

More particularly, the integration of the deviatoric part of the stress at the end of the time step:

$$\hat{\sigma}_{ij,B} = \frac{G_B}{G_A} \hat{\sigma}_{ij,A} + 2.G_B.\hat{\dot{\varepsilon}}_{ij}.\Delta t \tag{82}$$

Concerning the mean value of stresses (cf. relation (59)):

$$\dot{\sigma}_m = 3\chi \dot{\varepsilon}_m + \frac{1}{\chi} \frac{\partial \chi}{\partial T} \dot{T} \sigma_m \tag{83}$$

$$\leftrightarrow \dot{\sigma}_m - \frac{1}{\chi} \frac{\partial \chi}{\partial T} \dot{T} \sigma_m = 3\chi \dot{\varepsilon}_m \tag{84}$$

which is the same type of differential equation. Using the same way for solving and assuming a linear variation of χ with respect to the temperature:

$$\text{“}A(x)\text{” : } \int \left(-\frac{1}{\chi} \right) \frac{\partial \chi}{\partial T} \dot{T} dt = -\frac{\chi_B - \chi_A}{\Delta T} \int \frac{1}{\chi} dT \quad \text{with} \quad \chi = C_1 T + C_2 \tag{85}$$

$$C_1 = \frac{\chi_B - \chi_A}{\Delta T} = \frac{\partial \chi}{\partial T} \text{ and } \quad C_2 = \chi_A - C_1 T_A \tag{86}$$

So that:

$$\text{“}A(x)\text{” : } -C_1 \int \frac{1}{C_1 T + C_2} dT = -\frac{C_1}{C_1} \ln\left(C_1 T + C_2 \right) = -\ln \chi \tag{87}$$

$$\rightarrow \quad \text{“ } e^{A(x)} \text{ ” : } e^{-\ln \chi} = \frac{1}{\chi} \quad \text{and} \quad \text{“ } e^{-A(x)} \text{ ” : } e^{\ln \chi} = \chi \tag{88}$$

And the solution of the differential equation (84) is:

$$\rightarrow \text{“ } y(x) \text{ ” : } \sigma_m = \left[Cst + \int \frac{1}{\chi} 3\chi \dot{\varepsilon}_m dt \right] \chi = \chi Cst + 3\chi \dot{\varepsilon}_m t \tag{89}$$

where *Cst* is a constant, which can be evaluated at the beginning of the step:

$$\sigma_{m,A} = \chi_A Cst + 3\chi_A \dot{\varepsilon}_m t_A \tag{90}$$

$$\leftrightarrow Cst = \frac{\sigma_{m,A}}{\chi_A} - 3\dot{\varepsilon}_m t_A \tag{91}$$

$$\rightarrow \sigma_m = \frac{\chi}{\chi_A}\sigma_{m,A} + 3\chi\dot{\varepsilon}_m \left(t - t_A\right) \tag{92}$$

And more particularly, at the end of the step:

$$\sigma_{m,B} = \frac{\chi_B}{\chi_A}\sigma_{m,A} + 3\chi_B \dot{\varepsilon}_m \Delta t \tag{93}$$

Finally, the complete expression of the elastic stress tensor at the end of the step is:

$$\sigma_{ij,B} = \left(\frac{G_B}{G_A}\hat{\sigma}_{ij,A} + 2G_B \dot{\hat{\varepsilon}}_{ij}\Delta t\right) + \left(\frac{\chi_B}{\chi_A}\sigma_{m,A} + 3\chi_B \dot{\varepsilon}_m \Delta t\right)\delta_{ij} \tag{94}$$

2.3. Viscoplastic domain

2.3.1. Basics of theory of plasticity

The purpose of this section is obviously not to develop theory of plasticity, but before studying viscoplastic behaviour of steel at high temperature, some basics and equations of theory of plasticity are reminded.

During a uniaxial tensile test on a mild steel sample (at ambient temperature), the following true stress-strain curve is obtained:

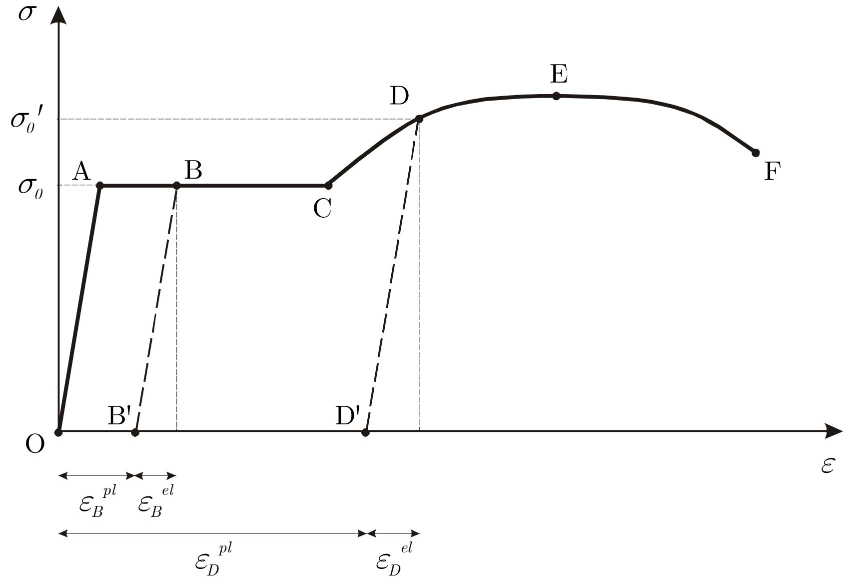

Figure 45: Schematic stress-strain curve for a tensile test on a mild steel sample.

The first part of the curve represents the elastic domain (from O to A) where the strain is reversible and the relationship between stress and strain is assumed linear (and is generally so observed). The elastic behaviour is given by Hook's law, which has been reminded in the previous paragraph.

When no more reversible strain can be applied to the material (A), the only way to deform the sample is to produce irreversible strain. The level of the stress has reached σ_0 described as yield limit. Starting from this point, the sample can be deformed with a constant stress: we are in the perfectly plastic domain, which is physically linked to the migration of dislocations in the material.

If the sample is unloaded from B, the stress-strain curve follows the BB' straight line, which is parallel to the elastic path OA.

Splitting the total strain in reversible elastic strain and irreversible plastic strain:

$$\varepsilon_B^{total} = \varepsilon_B^{el} + \varepsilon_B^{pl} \tag{95}$$

When reloading the sample, the curve follows B'B and then the plastic strain restarts to grow until point C. Then the activation force to move dislocations has to increase so that the stress grows in the same way: this is hardening (from C to E). In this domain loading and unloading can also be driven, but when reloading, the actual yield stress σ_0' is higher than the initial one σ_0. The material has been hardened.

This hardening is not unlimited, but stress reaches a maximum value in E. Then, continuing to elongate the sample, the stress decreases until the sample breaking in F. This zone of decreasing stress is the softening behaviour.

Remark: The previous stress-strain curve represents the idealised behaviour of mild steel. Many steel products are hardened so their stress-strain curve is drawn on Figure 46:

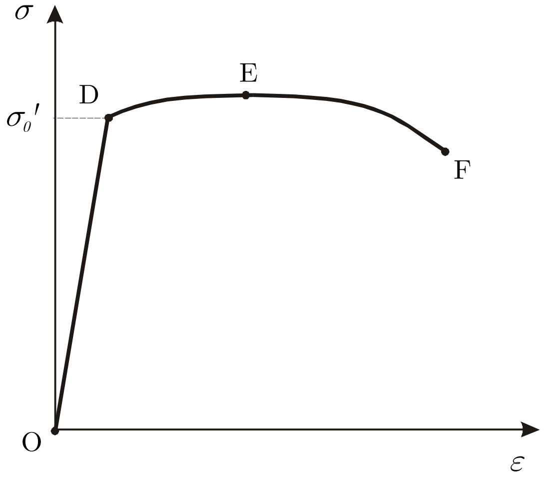

Figure 46: Stress-strain curve for hardened steel.

2.3.2. Yield locus: elasticity/plasticity criterion

As described in the previous paragraph in a tensile test, the accessible zone of the $\sigma{-}\varepsilon$ plane is the area between the strain axis ε and the $\sigma{-}\varepsilon$ curve, including this curve. Considering the only plastic strain, Figure 46 becomes Figure 47:

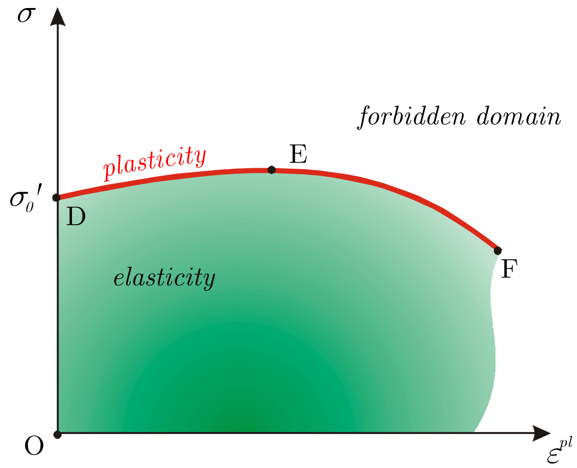

Figure 47: Stress-plastic strain curve for hardened steel.

Any situation represented by a (σ,ε) couple values under the curve is representative of pure elastic state (loading or unloading), while a couple of values on the curve represents a plastic state.

The yield locus is a mathematical expression $f(\underline{\sigma})$ which separates the elastic domain from the plastic one. Such an expression is also called plasticity criterion and it should be (conventionally):

- negative in elastic domain;
- equal to zero in plastic domain;
- never positive (according to the forbidden domain).

Since the observation on a tensile test can be extended to more complex loading, this criterion should also be available for multidimensional stress state so that it is a scalar, but function of the stress tensor $\underline{\sigma}$. In the stress space, the yield locus is the surface defined by the equation:

$$f(\underline{\sigma}) = 0 \tag{96}$$

Some usual assumptions are required to choose the yield locus expression [RAP98].

- *Isotropy of the material*

  A consequence of this first assumption is that the plasticity criterion $f(\underline{\sigma})$ is independent of the reference axes system. In particular, it is possible to choose the principal stresses axes as reference. In this system, the stress tensor becomes diagonal so that the plasticity criterion depends only on the three principal stresses:

$$f(\sigma_I,\sigma_{II},\sigma_{III}) \leq 0 \tag{97}$$

  Moreover, isotropy induces that switching any principal values in the criterion does not change the criterion:

$$f(\sigma_I,\sigma_{II},\sigma_{III}) = f(\sigma_{II},\sigma_I,\sigma_{III}) = \ldots \tag{98}$$

  Instead of principal stresses, stress invariants can also be used:

$$\begin{aligned} I_{\underline{\sigma}} &= tr(\underline{\sigma}) = \sigma_{ii} = \sigma_I + \sigma_{II} + \sigma_{III} \\ II_{\underline{\sigma}} &= \frac{1}{2}\left(\sigma_{ii}\sigma_{jj} - \sigma_{ij}\sigma_{ji}\right) = \sigma_I\sigma_{II} + \sigma_{II}\sigma_{III} + \sigma_I\sigma_{III} \\ III_{\underline{\sigma}} &= \det(\underline{\sigma}) = \sigma_I\sigma_{II}\sigma_{III} \end{aligned} \tag{99}$$

and the criterion becomes:

$$f(I_{\underline{\sigma}}, II_{\underline{\sigma}}, III_{\underline{\sigma}}) \leq 0 \tag{100}$$

- *Isotropic hardening*

  This assumption leads to the equivalence of tensile and compression hardening. In fact, for most of materials, once the hardening happens in one direction (i.e. in tensile state), the yield stress in the other direction (i.e. in compression) does not increases in the same way, but remains the same or is lower than the initial value (Bauschinger effect).

  At the opposite, not considering this effect, isotropic hardening is assumed:

  $$f(\sigma_I, \sigma_{II}, \sigma_{III}) = f(-\sigma_I, -\sigma_{II}, -\sigma_{III}) \tag{101}$$

  So, the yield locus is and always remains symmetric with respect to the origin of axes.

- *Deviatoric character of plasticity in metals*

  For steel (as well as for metals in general and high density polymers), it is observed (testing a sample of material in an oedometer) that plastic strains are not dependent on hydrostatic stress level, so the plasticity criterion cannot vary when any additional hydrostatic pressure is applied:

  $$f(\sigma_I, \sigma_{II}, \sigma_{III}) = f(p+\sigma_I, p+\sigma_{II}, p+\sigma_{III}) \tag{102}$$

  Geometrically, this property means that the yield locus is a cylinder, the axis of which being parallel to the direction (1,1,1) in principal stresses axes.

  Moreover, the mean stress σ_m can be considered as a hydrostatic pressure (“p”$= \sigma_m$), so:

  $$f(\hat{\sigma}_I, \hat{\sigma}_{II}, \hat{\sigma}_{III}) = f(\sigma_I, \sigma_{II}, \sigma_{III}) \tag{103}$$

  since

  $$\hat{\underline{\sigma}} = \underline{\sigma} - \sigma_m \underline{I} \tag{104}$$

- *Convex shape of yield locus*

  This is a consequence of maximal work principle, which will be introduced in a further section (see section 2.3.3). Such yield locus can be represented by Figure 48:

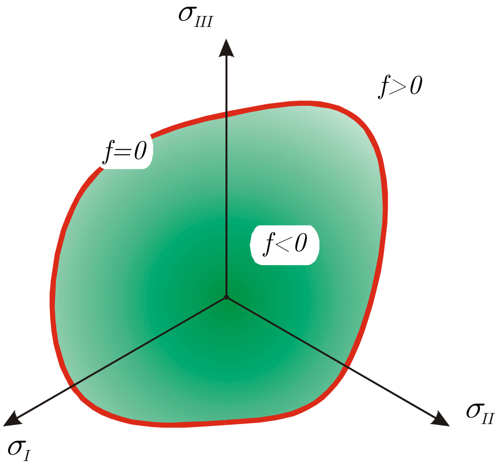

Figure 48: Yield locus.

According to all these assumptions, it is possible to define the $f(\underline{\sigma})$ function. Von Mises proposed the equation of a right circular cylinder [MIS13], the equation of which is:

$$f = (\sigma_I - \sigma_{II})^2 + (\sigma_{II} - \sigma_{III})^2 + (\sigma_{III} - \sigma_I)^2 - 2\sigma_0^2 \leq 0 \tag{105}$$

where σ_0 is the yield limit in simple tension or compression. In such a case, $\sigma_{II} = \sigma_{III} = 0$, and the criterion becomes:

$$f = 2\sigma_I^2 - 2\sigma_0^2 \leq 0 \tag{106}$$

$$\leftrightarrow \sigma_I \leq \sigma_0 \tag{107}$$

Writing the Von Mises criterion as a function of principal deviatoric stresses:

$$\begin{aligned} f &= (\sigma_I - \sigma_{II})^2 + (\sigma_{II} - \sigma_{III})^2 + (\sigma_{III} - \sigma_I)^2 - 2\sigma_0^2 \\ &= (\hat{\sigma}_I - \hat{\sigma}_{II})^2 + (\hat{\sigma}_{II} - \hat{\sigma}_{III})^2 + (\hat{\sigma}_{III} - \hat{\sigma}_I)^2 - 2\sigma_0^2 \\ &= 2\left(\hat{\sigma}_I^2 + \hat{\sigma}_{II}^2 + \hat{\sigma}_{III}^2 - \hat{\sigma}_I.\hat{\sigma}_{II} - \hat{\sigma}_{II}.\hat{\sigma}_{III} - \hat{\sigma}_{III}.\hat{\sigma}_I\right) - 2\sigma_0^2 \end{aligned} \tag{108}$$

thanks to assumption of hydrostatic pressure independence – relation (103).

Since the trace of a deviatoric tensor is equal to zero:

$$\begin{aligned} \hat{\sigma}_I + \hat{\sigma}_{II} + \hat{\sigma}_{III} &= \sigma_I - \sigma_m + \sigma_{II} - \sigma_m + \sigma_{III} - \sigma_m \\ &= \sigma_I + \sigma_{II} + \sigma_{III} - 3\sigma_m \\ &= 0 \end{aligned} \tag{109}$$

so that:

$$\begin{cases} \hat{\sigma}_I = -\hat{\sigma}_{II} - \hat{\sigma}_{III} \\ \hat{\sigma}_{II} = -\hat{\sigma}_I - \hat{\sigma}_{III} \\ \hat{\sigma}_{III} = -\hat{\sigma}_I - \hat{\sigma}_{II} \end{cases} \tag{110}$$

and :

$$\begin{aligned}\hat{\sigma}_I\hat{\sigma}_{II} + \hat{\sigma}_{II}\hat{\sigma}_{III} + \hat{\sigma}_{III}\hat{\sigma}_I &= \hat{\sigma}_I(-\hat{\sigma}_I - \hat{\sigma}_{III}) + \hat{\sigma}_{II}(-\hat{\sigma}_I - \hat{\sigma}_{II}) + \hat{\sigma}_{III}(-\hat{\sigma}_{II} - \hat{\sigma}_{III}) \\ &= -\hat{\sigma}_I^2 - \hat{\sigma}_{II}^2 - \hat{\sigma}_{III}^2 - (\hat{\sigma}_I\hat{\sigma}_{II} + \hat{\sigma}_{II}\hat{\sigma}_{III} + \hat{\sigma}_{III}\hat{\sigma}_I)\end{aligned} \tag{111}$$

hence:

$$\hat{\sigma}_I\hat{\sigma}_{II} + \hat{\sigma}_{II}\hat{\sigma}_{III} + \hat{\sigma}_{III}\hat{\sigma}_I = -\frac{1}{2}\left(\hat{\sigma}_I^2 + \hat{\sigma}_{II}^2 + \hat{\sigma}_{III}^2\right) \tag{112}$$

Introducing (112) in (108):

$$f = 2\left(\hat{\sigma}_I^2 + \hat{\sigma}_{II}^2 + \hat{\sigma}_{III}^2 + \frac{1}{2}\hat{\sigma}_I^2 + \frac{1}{2}\hat{\sigma}_{II}^2 + \frac{1}{2}\hat{\sigma}_{III}^2\right) - 2\sigma_0^2 \le 0 \tag{113}$$

$$\rightarrow f = 2\frac{3}{2}\left(\hat{\sigma}_I^2 + \hat{\sigma}_{II}^2 + \hat{\sigma}_{III}^2\right) - 2\sigma_0^2 \le 0 \tag{114}$$

or

$$f' = \frac{1}{3}f = \hat{\sigma}_I^2 + \hat{\sigma}_{II}^2 + \hat{\sigma}_{III}^2 - \frac{2}{3}.\sigma_0^2 \le 0 \tag{115}$$

that is the equation of a cylinder, the axis of which being along the trisectrix of the principal axes, and the radius of which being equal to $\sqrt{\frac{2}{3}}\sigma_0$ (see Figure 49).

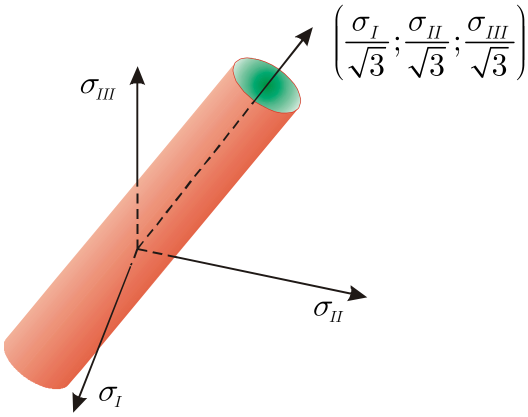

Figure 49: Von Mises yield locus.

Introducing the second invariant of deviatoric stress tensor $\underline{\hat{\sigma}}$:

$$\begin{aligned}II_{\underline{\hat{\sigma}}} &= \hat{\sigma}_I\hat{\sigma}_{II} + \hat{\sigma}_{II}\hat{\sigma}_{III} + \hat{\sigma}_{III}\hat{\sigma}_I \\ &= -\frac{1}{2}\left(\hat{\sigma}_I^2 + \hat{\sigma}_{II}^2 + \hat{\sigma}_{III}^2\right)\end{aligned} \tag{116}$$

Von Mises criterion simply becoming equivalent to:

$$f' = -2II_{\underline{\hat{\sigma}}} - \frac{2}{3}\sigma_0^2 \le 0 \tag{117}$$

or

$$f'' = \frac{3}{2} f' = -3II_{\underline{\hat{\sigma}}} - \sigma_0^2 \leq 0 \tag{118}$$

It is convenient to define a “reference” stress that could be directly compared to the yield stress σ_0 in order to determine if the loading state is in elastic or plastic domain. This stress $\overline{\sigma}_{VM}$, which is called equivalent stress of Von Mises, is given by:

$$f'' = \overline{\sigma}_{VM} - \sigma_0 \leq 0 \tag{119}$$

so that

$$\overline{\sigma}_{VM} = \sqrt{-3.II_{\underline{\hat{\sigma}}}} = \sqrt{\frac{3}{2} \hat{\sigma}_{ij}.\hat{\sigma}_{ij}} \tag{120}$$

Von Mises criterion is particularly suitable to many ductile metals behaviour, hence its use in many models. Numerous other criterions also exist to overcome the limitations of Von Mises criterion (due to the previous assumptions). In the present model of continuous casting, Von Mises criterion has been insufficient since viscosity of the material is neglected in this criterion. So an elasto-viscoplastic law has been developed as an extension of the plastic theory.

2.3.3. Plastic flow rule (large strains)

Knowing the yield surface expression, it is necessary to study how the plastic strain tensor evolves during plastic loading, i.e. to define a plastic flow rule.

The jacobian tensor $\underline{F}$ describes the relation between actual coordinate $\underline{x}$ and initial coordinate $\underline{X}$ as follows:

$$\underline{F} = \frac{\partial \underline{x}}{\partial \underline{X}} \tag{121}$$

The velocity $\underline{v}$ being temporal derivative of actual coordinate:

$$\underline{v} = \frac{\partial \underline{x}}{\partial t} \tag{122}$$

The velocity gradient tensor is so:

$$\underline{L} = \frac{\partial \underline{v}}{\partial \underline{x}} = \frac{\partial \underline{v}}{\partial \underline{X}} \frac{\partial \underline{X}}{\partial \underline{x}} = \underline{\dot{F}} \underline{F}^{-1} \tag{123}$$

This tensor is generally split into its symmetric and anti-symmetric parts. The symmetric part is the strain rate tensor $\underline{D}$ or $\underline{\dot{\varepsilon}}$:

$$\underline{D} = \frac{1}{2} \left(\underline{L} + \underline{L}^T \right) \equiv \underline{\dot{\varepsilon}} \tag{124}$$

The anti-symmetric part is the spin tensor $\underline{\omega}$:

$$\underline{\omega} = \frac{1}{2} \left(\underline{L} - \underline{L}^T \right) \tag{125}$$

The evolution of stress tensor in plastic domain is driven by the plastic strain evolution or, more precisely, by the plastic strain rate $\underline{\dot{\varepsilon}}^{pl}$. A simple rule of additive elastic and plastic strain rates is applied:

$$\underline{\dot{\varepsilon}} = \underline{\dot{\varepsilon}}^{pl} + \underline{\dot{\varepsilon}}^{el} \tag{126}$$

For large strains, this additive decomposition of total strain is available assuming small elastic strains, what is generally true for metals [HOF01].

The problem of the evolution of stress tensor is commonly divided into two parts: determination of the direction of plastic strain rate and computation of its amplitude.

It is generally assumed that the plastic strain rate is normal to the yield surface. This assumption follows from the maximal work principle, or Hill's principle [HIL50]: *The work done by the actual surface forces* $\underline{\sigma}$ *in the prescribed displacements is greater than that done by the surface forces corresponding to any other equilibrium state of plastic stress* $\underline{\sigma}^*$ *:*

$$\forall \underline{\sigma}^* \mid f(\underline{\sigma}^*) \le 0 \ , \ \underline{\sigma}^* : \underline{\dot{\varepsilon}}^{pl} \le \underline{\sigma} : \underline{\dot{\varepsilon}}^{pl} \tag{127}$$

or

$$(\underline{\sigma}^* - \underline{\sigma}) : \underline{\dot{\varepsilon}}^{pl} \le 0 \tag{128}$$

In the deviatoric plane, the relation (128) can be illustrated as on Figure 50:

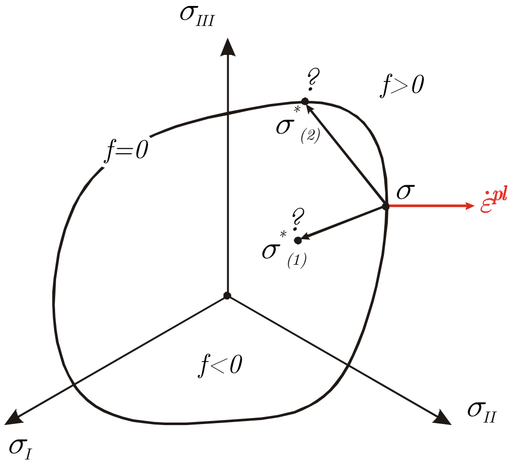

Figure 50: Normality rule.

The only way to ensure the maximum work principle for any stress tensor $\underline{\sigma}^*$ is that the strain rate is pointing like the outward normal to the surface. Moreover, it is now clear that this principle implies that the yield surface must be convex, otherwise, the principle could be transgressed (hence the convex shape assumption).

So the plastic strain rate is proportional to the normal tensor:

$$\exists \dot{\lambda}^{pl} > 0 : \underline{\dot{\varepsilon}}^{pl} = \dot{\lambda}^{pl} \frac{\partial f}{\partial \underline{\sigma}} \tag{129}$$

This expression is the Prandtl-Reuss plastic flow rule. It is qualified associated (to the yield surface) because the plastic strain rate derives from the yield surface. Sometimes, for instance in soils mechanics, an associated flow rule can be not associated because it induces the wrong modelling of phenomena such as dilatancy [SCH88]. In this case, another potential g is chosen instead of f so that the relation gives the right answer. $\dot{\lambda}^{pl}$ is called plastic multiplier.

2.3.4. Plastic flow rule associated to Von Mises criterion

A first remark is that the yield surface *f(σ̲)* must be derivable with respect to the stress. It is checked for the Von Mises criterion, but not for all criterions, such as Tresca criterion where sharp angles present lack of derivability and $\dot{\underline{\varepsilon}}^{pl}$ cannot be defined.

Associating Von Mises criterion (119) to plastic flow rule (129):

$$\begin{aligned} \dot{\varepsilon}_{ij}^{pl} &= \dot{\lambda}^{pl} \frac{\partial f"}{\partial \sigma_{ij}} = \dot{\lambda}^{pl} \frac{\partial}{\partial \sigma_{ij}} \left(\bar{\sigma}_{VM} - \sigma_0 \right) = \dot{\lambda}^{pl} \frac{\partial}{\partial \sigma_{ij}} \left(\sqrt{\frac{3}{2} \hat{\sigma}_{kl} \hat{\sigma}_{kl}} \right) \\ &= \dot{\lambda}^{pl} \frac{1}{2} \frac{1}{\sqrt{\frac{3}{2} \hat{\sigma}_{kl} \hat{\sigma}_{kl}}} \frac{\partial \left(\frac{3}{2} \hat{\sigma}_{kl} \hat{\sigma}_{kl} \right)}{\partial \sigma_{ij}} = \dot{\lambda}^{pl} \frac{1}{2} \frac{1}{\bar{\sigma}_{VM}} \frac{3}{2} 2 \hat{\sigma}_{kl} \frac{\partial \hat{\sigma}_{kl}}{\partial \sigma_{ij}} \end{aligned} \tag{130}$$

with

$$\begin{aligned} \frac{\partial \hat{\sigma}_{kl}}{\partial \sigma_{ij}} &= \frac{\partial \left(\sigma_{kl} - \frac{1}{3} \sigma_{pp} \delta_{kl} \right)}{\partial \sigma_{ij}} = \frac{\partial \sigma_{kl}}{\partial \sigma_{ij}} - \frac{1}{3} \frac{\partial \sigma_{pp}}{\partial \sigma_{ij}} \delta_{kl} \\ &= \delta_{ik} \delta_{jl} - \frac{1}{3} \delta_{ip} \delta_{jp} \delta_{kl} = \delta_{ik} \delta_{jl} - \frac{1}{3} \delta_{ij} \delta_{kl} \end{aligned} \tag{131}$$

hence

$$\dot{\varepsilon}_{ij}^{pl} = \dot{\lambda}^{pl} \frac{1}{\bar{\sigma}_{VM}} \frac{3}{2} \hat{\sigma}_{kl} \left(\delta_{ki} . \delta_{lj} - \frac{1}{3} \delta_{ij} . \delta_{kl} \right) = \frac{3 \dot{\lambda}^{pl}}{2 \bar{\sigma}_{VM}} \hat{\sigma}_{ij} \tag{132}$$

or

$$\hat{\sigma}_{ij} = \frac{2 \bar{\sigma}_{VM}}{3 \dot{\lambda}^{pl}} \dot{\varepsilon}_{ij}^{pl} \tag{133}$$

Since the relation (119) is applied here during plastic flow:

$$\bar{\sigma}_{VM} = \sigma_0 \tag{134}$$

so that

$$\sigma_0^2 = \bar{\sigma}_{VM}^2 = \frac{3}{2} \hat{\sigma}_{ij} \hat{\sigma}_{ij} = \frac{3}{2} \left(\frac{2 \bar{\sigma}_{VM}}{3 \dot{\lambda}^{pl}} \right)^2 \dot{\varepsilon}_{ij}^{pl} \dot{\varepsilon}_{ij}^{pl} = \left(\frac{\bar{\sigma}_{VM}}{\dot{\lambda}^{pl}} \right)^2 \frac{2}{3} \dot{\varepsilon}_{ij}^{pl} \dot{\varepsilon}_{ij}^{pl} \tag{135}$$

Defining the equivalent plastic strain rate:

$$\bar{\dot{\varepsilon}}_{VM}^{pl} = \sqrt{\frac{2}{3} \dot{\varepsilon}_{ij}^{pl} \dot{\varepsilon}_{ij}^{pl}} \tag{136}$$

(135) becomes:

$$\sigma_0^2 = \left(\frac{\sigma_0}{\dot{\lambda}^{pl}}\right)^2 \left(\dot{\bar{\varepsilon}}_{VM}^{pl}\right)^2 \qquad \leftrightarrow \qquad \dot{\lambda}^{pl} = \dot{\bar{\varepsilon}}_{VM}^{pl} \tag{137}$$

and the plastic flow rule associated to Von Mises criterion is:

$$\dot{\varepsilon}_{ij}^{pl} = \frac{3\dot{\bar{\varepsilon}}_{VM}^{pl}}{2\sigma_0}\hat{\sigma}_{ij} \tag{138}$$

Remarks:

- Since only Von Mises equivalent stress is considered, the $_{VM}$ subscript will not be mentioned anymore. From now on, using the symbols $\bar{\sigma}$, $\bar{\varepsilon}$ and $\dot{\bar{\varepsilon}}$ will assume those are Von Mises equivalent stress, strain and strain rate.
- Since $\frac{3\dot{\bar{\varepsilon}}_{VM}^{pl}}{2\sigma_0}$ is a scalar and $\hat{\sigma}_{ij}$ is deviatoric, the plastic strain rate (and plastic strain) must be deviatoric too and:

$$\dot{\hat{\varepsilon}}_{ij}^{pl} = \dot{\varepsilon}_{ij}^{pl} = \frac{3\dot{\bar{\varepsilon}}_{VM}^{pl}}{2\sigma_0}\hat{\sigma}_{ij} \quad \text{and} \quad \dot{\bar{\hat{\varepsilon}}}_{VM}^{pl} = \dot{\bar{\varepsilon}}_{VM}^{pl} = \sqrt{\frac{2}{3}\dot{\varepsilon}_{ij}^{pl}\dot{\varepsilon}_{ij}^{pl}} = \sqrt{\frac{2}{3}\dot{\hat{\varepsilon}}_{ij}^{pl}\dot{\hat{\varepsilon}}_{ij}^{pl}} \tag{139}$$

2.3.5. Viscoplastic behaviour of steel at high temperature: Norton-Hoff law

It is well known that metals at high temperature present a viscous behaviour, that is to say that the strain rate influences the stress level. To summarize, three ranges of temperature can be defined:

3. $T < \frac{1}{3}T_{melting}$: no viscosity
4. $\frac{1}{3}T_{melting} < T < \frac{2}{3}T_{melting}$: viscosity – yield limit
5. $\frac{2}{3}T_{melting} < T$: viscosity – no yield limit

where T is the absolute temperature (in K).

Norton described this behaviour (for a 1D problem) thanks to a power law:

$$\sigma = k\dot{\varepsilon}^m \tag{140}$$

where the exponent m is sensitivity coefficient to strain rate ($0<m<1$). For a given value of m (characteristic of the material and the temperature), the lower the strain rate is, the lower the stress is, as shown on Figure 51.

When m is equal to 1.0, the law describes the behaviour of a Newtonian fluid. The stress level increases linearly with respect to strain rate. On the other hand, when m is equal to zero, there is no viscous effect anymore: stress level is constant and equal to k, whatever is the value of the strain rate.

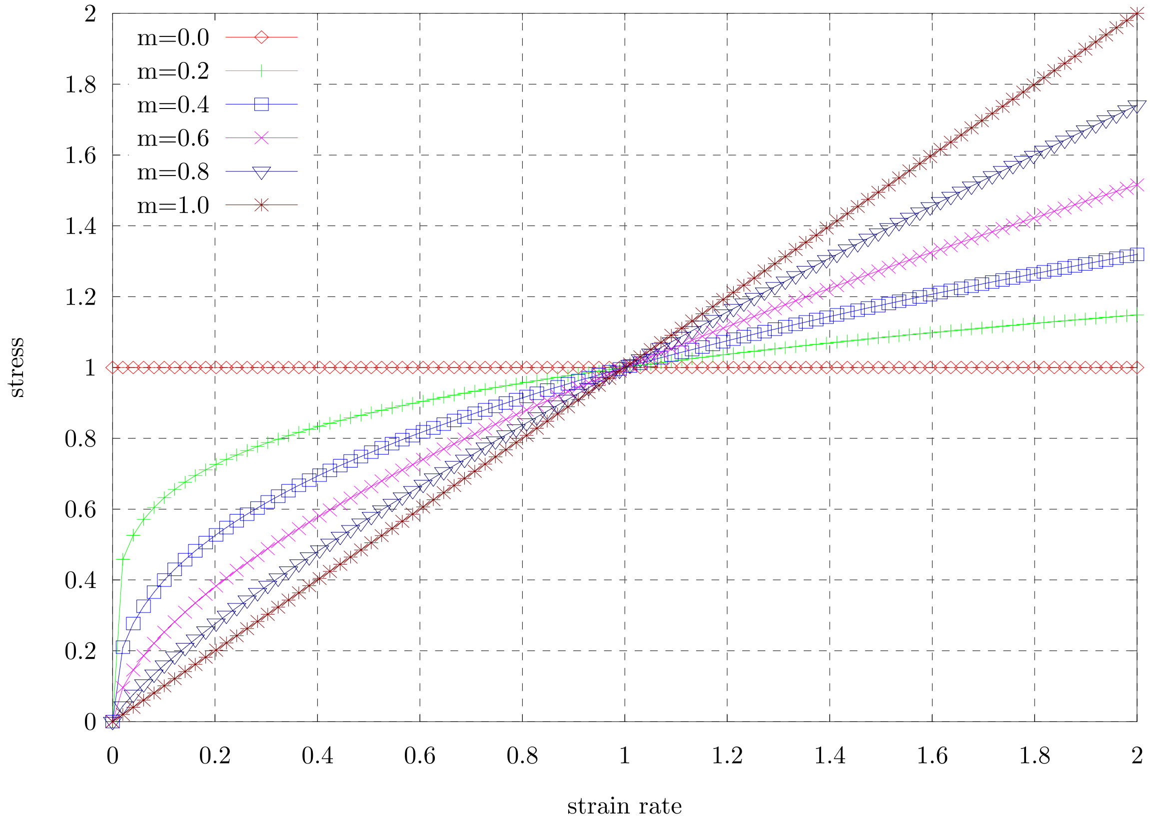

Figure 51: Evolution of stress level with respect to strain rate (Illustration of the Norton law (140) with k=1 and m=0.0 to 1.0)

In the medium range of temperature ($\frac{1}{3}T_{melting} < T < \frac{2}{3}T_{melting}$), it is necessary to introduce a yield limit σ_0 under which the behaviour of the material is in elastic domain. To take it into account, it is easy to modify the relation (140) this way:

$$\sigma = \sigma_0 + k\left(\dot{\varepsilon}^{vp}\right)^m \tag{141}$$

In multidimensional context, this law can be expressed in terms of (Von Mises) equivalent values:

$$\bar{\sigma} = \sigma_0 + k\left(\bar{\dot{\varepsilon}}^{vp}\right)^m \tag{142}$$

with

$$\bar{\dot{\varepsilon}}^{vp} = \sqrt{\frac{2}{3}\dot{\varepsilon}_{ij}^{vp}\dot{\varepsilon}_{ij}^{vp}} \tag{143}$$

The tensorial relations describing the elasto-viscoplasticity have been formulated by Perzyna:

$$\begin{cases} \underline{\dot{\varepsilon}} = \underline{\dot{\varepsilon}}^{el} + \underline{\dot{\varepsilon}}^{vp} & (144) \\ \underline{\dot{\varepsilon}}^{el} = \underline{\underline{D}}^{-1} \cdot \underline{\dot{\sigma}} & (145) \\ \underline{\dot{\varepsilon}}^{vp} = \dfrac{\sqrt{3}}{2\bar{\sigma}} \left\langle \dfrac{\bar{\sigma} - \sigma_0}{\sqrt{3}K} \right\rangle^{\frac{1}{m}} \underline{\hat{\sigma}} & (146) \end{cases}$$

The second relation expresses the increase of elastic strain during hardening, as shown on Figure 52:

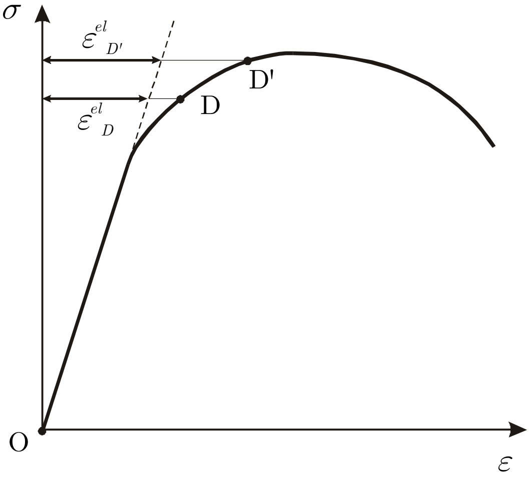

Figure 52: Increase of elastic strain during hardening

In the relation (146), the notation $\langle x \rangle$ is equivalent to:

$$\langle x \rangle = \left| \begin{array}{l} x \text{ if } x > 0 \\ 0 \text{ if } x \leq 0 \end{array} \right. \tag{147}$$

So, in the relation (146), $\underline{\dot{\varepsilon}}^{vp}$ is equal to zero under the yield limit.

In absence of an evident yield limit (third and highest range of temperature: $\frac{2}{3} T_{melting} < T$), Perzyna's equations become:

$$\left\{ \begin{array}{lr} \underline{\dot{\varepsilon}} = \underline{\dot{\varepsilon}}^{el} + \underline{\dot{\varepsilon}}^{vp} & (148) \\ \underline{\dot{\varepsilon}}^{el} = \underline{\underline{C}}^{-1} \cdot \underline{\dot{\sigma}} & (149) \\ \underline{\dot{\varepsilon}}^{vp} = \dfrac{\sqrt{3}}{2\bar{\sigma}} \left(\dfrac{\bar{\sigma}}{\sqrt{3}K} \right)^{\frac{1}{m}} \underline{\hat{\sigma}} & (150) \end{array} \right.$$

From equation (150), it is possible to compute the equivalent stress:

$$\sqrt{\frac{2}{3} \underline{\dot{\varepsilon}}^{vp} : \underline{\dot{\varepsilon}}^{vp}} = \sqrt{\frac{2}{3} \frac{3}{4\bar{\sigma}^2} \left(\frac{\bar{\sigma}}{\sqrt{3}K} \right)^{\frac{2}{m}} \underline{\hat{\sigma}} : \underline{\hat{\sigma}}} \tag{151}$$

$$\begin{aligned} \bar{\dot{\varepsilon}}^{vp} &= \sqrt{\frac{2}{3} \frac{3}{4\bar{\sigma}^2} \left(\frac{\bar{\sigma}}{\sqrt{3}K} \right)^{\frac{2}{m}} \underline{\hat{\sigma}} : \underline{\hat{\sigma}}} \\ \leftrightarrow \quad &= \sqrt{\frac{1}{3\bar{\sigma}^2} \left(\frac{\bar{\sigma}}{\sqrt{3}K} \right)^{\frac{2}{m}}} \sqrt{\frac{3}{2} \underline{\hat{\sigma}} : \underline{\hat{\sigma}}} \\ &= \frac{1}{\sqrt{3}} \left(\frac{1}{\sqrt{3}K} \right)^{\frac{1}{m}} \bar{\sigma}^{\frac{1}{m}} \end{aligned} \tag{152}$$

$$\leftrightarrow \bar{\sigma} = K\left(\sqrt{3}\right)^{m+1}\left(\dot{\bar{\varepsilon}}^{vp}\right)^{m} \tag{153}$$

Introducing (153) in (150):

$$\underline{\dot{\varepsilon}}^{vp} = \frac{\sqrt{3}}{2\bar{\sigma}}\left(\frac{K\left(\sqrt{3}\right)^{m+1}\left(\dot{\bar{\varepsilon}}^{vp}\right)^{m}}{\sqrt{3}K}\right)^{\frac{1}{m}}\underline{\hat{\sigma}} = \frac{\sqrt{3}}{2\bar{\sigma}}\sqrt{3}.\dot{\bar{\varepsilon}}^{vp}.\underline{\hat{\sigma}} = \frac{3\dot{\bar{\varepsilon}}^{vp}}{2\bar{\sigma}}\underline{\hat{\sigma}} \tag{154}$$

which is viscoplastic flow rule associated to Von Mises criterion, similar to relation (138) found for plasticity.

It is possible to simplify these relations, neglecting the elastic strain rate (pure viscoplasticity). In that case:

$$\begin{cases} \underline{\dot{\varepsilon}}^{el} = \underline{0} \\ \underline{\dot{\varepsilon}} = \underline{\dot{\varepsilon}}^{vp} \end{cases} \tag{155}$$

The relation (150) and (154) become:

$$\begin{cases} \underline{\dot{\varepsilon}} = \dfrac{\sqrt{3}}{2\bar{\sigma}}\left(\dfrac{\bar{\sigma}}{\sqrt{3}K}\right)^{\frac{1}{m}}\underline{\hat{\sigma}} \\ \underline{\dot{\varepsilon}} = \dfrac{3\dot{\bar{\varepsilon}}}{2\bar{\sigma}}\underline{\hat{\sigma}} \end{cases} \tag{156}$$

$$\leftrightarrow \frac{\sqrt{3}}{2\bar{\sigma}}\left(\frac{\bar{\sigma}}{\sqrt{3}K}\right)^{\frac{1}{m}}\underline{\hat{\sigma}} = \frac{3\dot{\bar{\varepsilon}}}{2\bar{\sigma}}\underline{\hat{\sigma}} \tag{157}$$

$$\leftrightarrow \left(\frac{\bar{\sigma}}{\sqrt{3}K}\right)^{\frac{1}{m}} = \sqrt{3}\dot{\bar{\varepsilon}} \tag{158}$$

$$\leftrightarrow \bar{\sigma} = \sqrt{3}K\left(\sqrt{3}.\dot{\bar{\varepsilon}}\right)^{m} \tag{159}$$

And introducing relation (159) in the viscoplastic flow rule (156):

$$\underline{\dot{\varepsilon}} = \frac{3\dot{\bar{\varepsilon}}}{2\sqrt{3}K\left(\sqrt{3}.\dot{\bar{\varepsilon}}\right)^{m}}\underline{\hat{\sigma}} = \frac{1}{2K\left(\sqrt{3}.\dot{\bar{\varepsilon}}\right)^{m-1}}\underline{\hat{\sigma}} \tag{160}$$

or

$$\underline{\hat{\sigma}} = 2K\left(\sqrt{3}.\dot{\bar{\varepsilon}}\right)^{m-1}\underline{\dot{\varepsilon}} \tag{161}$$

which is the tensorial relation governing pure viscoplasticity, known as Norton-Hoff law. In terms of equivalent, Norton-Hoff law is written:

$$\bar{\sigma} = \sqrt{\frac{3}{2}\underline{\hat{\sigma}}:\underline{\hat{\sigma}}} = \sqrt{\frac{3}{2}}2K\left(\sqrt{3}.\dot{\bar{\varepsilon}}\right)^{m-1}\sqrt{\frac{3}{2}}\sqrt{\frac{2}{3}\underline{\dot{\varepsilon}}:\underline{\dot{\varepsilon}}} = 3K\left(\sqrt{3}.\dot{\bar{\varepsilon}}\right)^{m-1}\dot{\bar{\varepsilon}} = \sqrt{3}K\left(\sqrt{3}.\dot{\bar{\varepsilon}}\right)^{m} \tag{162}$$

Norton-Hoff law is quite suitable to model steel behaviour at very high temperature, such as in continuous casting. In fact, the relation (161) describes the behaviour of a generalized Newtonian fluid, incompressible with a nonlinear viscosity equals to $K\left(\sqrt{3}.\dot{\bar{\varepsilon}}\right)^{m-1}$.

2.3.6. Modification of Norton-Hoff law

From the relation (162) – the Norton-Hoff law – it appears that for a constant equivalent strain rate, the equivalent stress is constant. In order to introduce softening and hardening effect in the model, it is thus necessary to modify the Norton-Hoff law. The relation in terms of equivalent values can take the following form:

$$\overline{\sigma} = K_o e^{-p_1\bar{\varepsilon}}\sqrt{3}p_2(\sqrt{3}.\dot{\bar{\varepsilon}})^{p_3}\,\bar{\varepsilon}^{p_4} \tag{163}$$

where p_1, p_2, p_3, p_4 have each their own effect on the shape of $\sigma{-}\varepsilon$ curves:

- p_1 has an effect in the large strains domain so that softening can be fitted thanks to this parameter; Figure 53 shows the effect of an increasing and a decreasing of p_1 by 20% for one temperature and one strain rate. It clearly appears that increasing the value of p_1 it is possible to model the softening in the material.

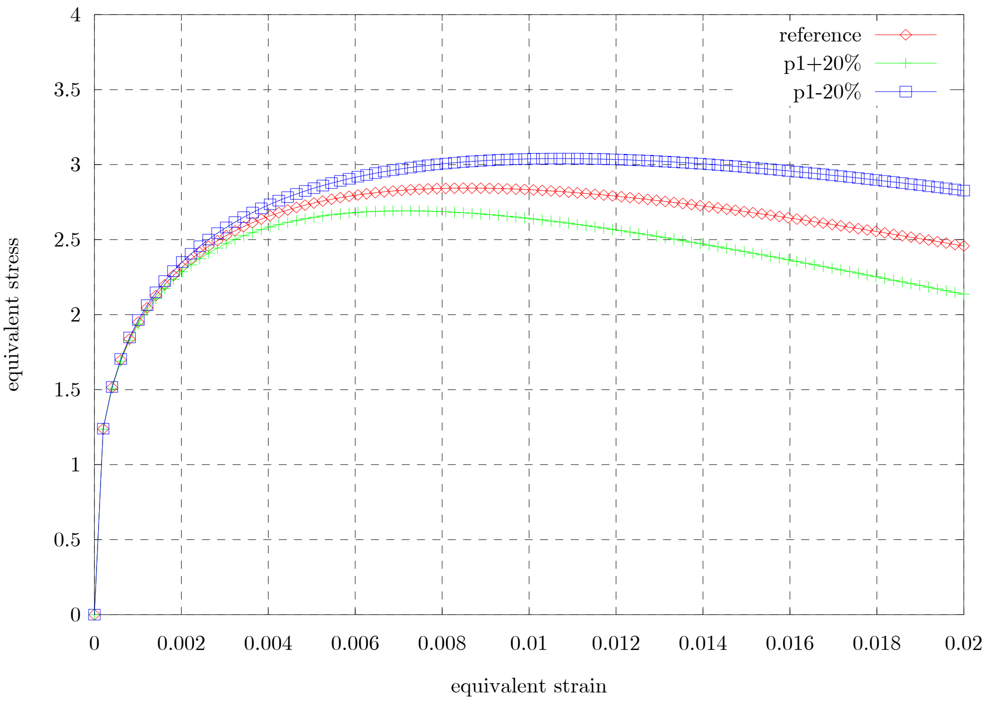

Figure 53: Effect of the increasing/decreasing of p_1 by 20% (for one temperature and one strain rate)

- p_2, just like K_0, has an effect on the level of the curve;
  Remark: K_0 and p_2 have the same effect on the curve, but they are treated differently by the code: while p_2 is only used to fit the level of the curve on tensile tests results, K_0 can be used as a yield limit by the user (see section III.2.2 hereafter).

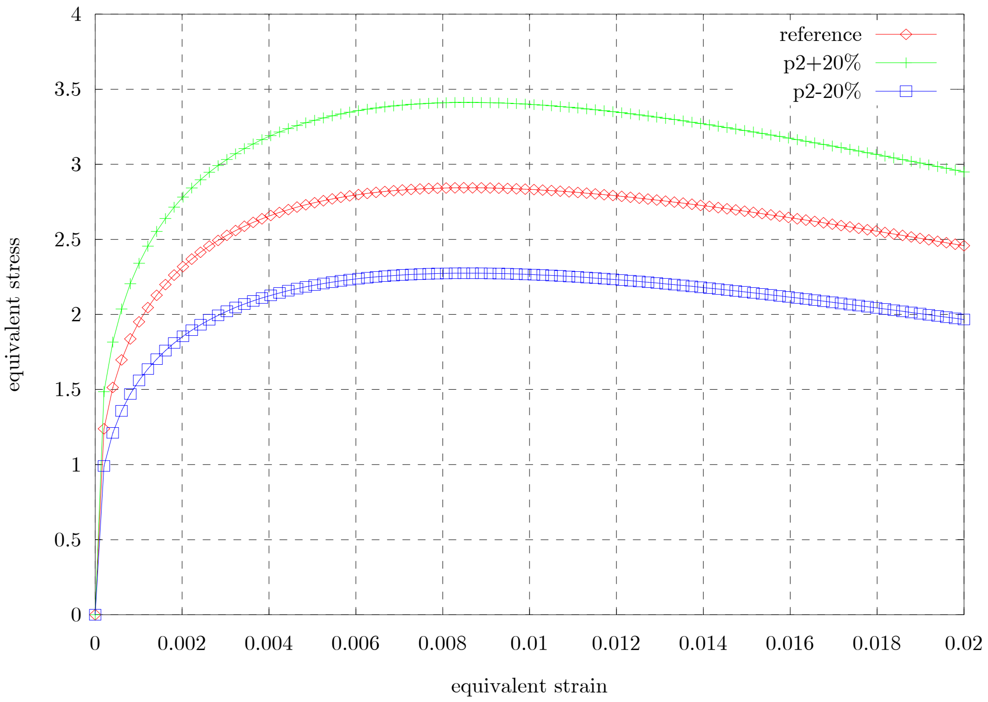

Figure 54: Effect of the increasing/decreasing of p_2 by 20%
(for one temperature and one strain rate)

- p_3, which is the exponent of the strain rate, is used to model viscosity, regulating the distance between curves for different strain rates. Figure 55 shows the effect of the increasing/decreasing of p_3 by 20%. Assuming that all parameters have been fit on the reference curve at a strain rate of 0.001 s^{-1}, 3 curves at a double strain rate (0.002 s^{-1}) are shown respectively for a given p_3 parameter and p_3 ± 20%.

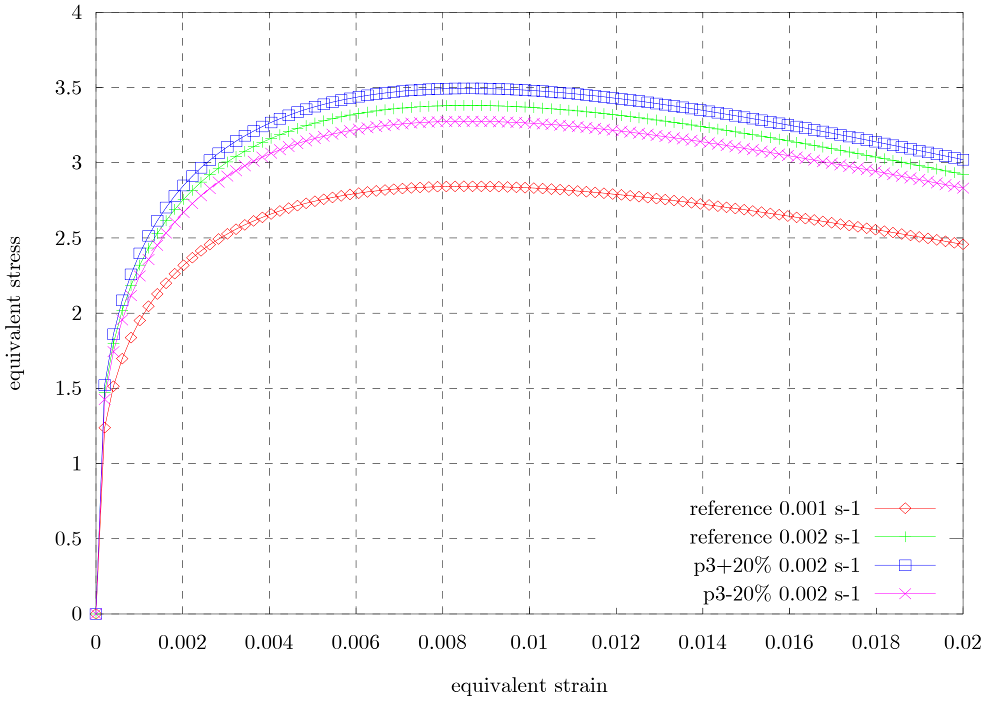

Figure 55: Effect of the increasing/decreasing of p_3 by 20%
(for one temperature and two strain rates)

- p_4 has an effect in the small strains domain (used to fit hardening). Changing the value of p_4, it is possible to significantly modify the slope of the curve in its initial part.

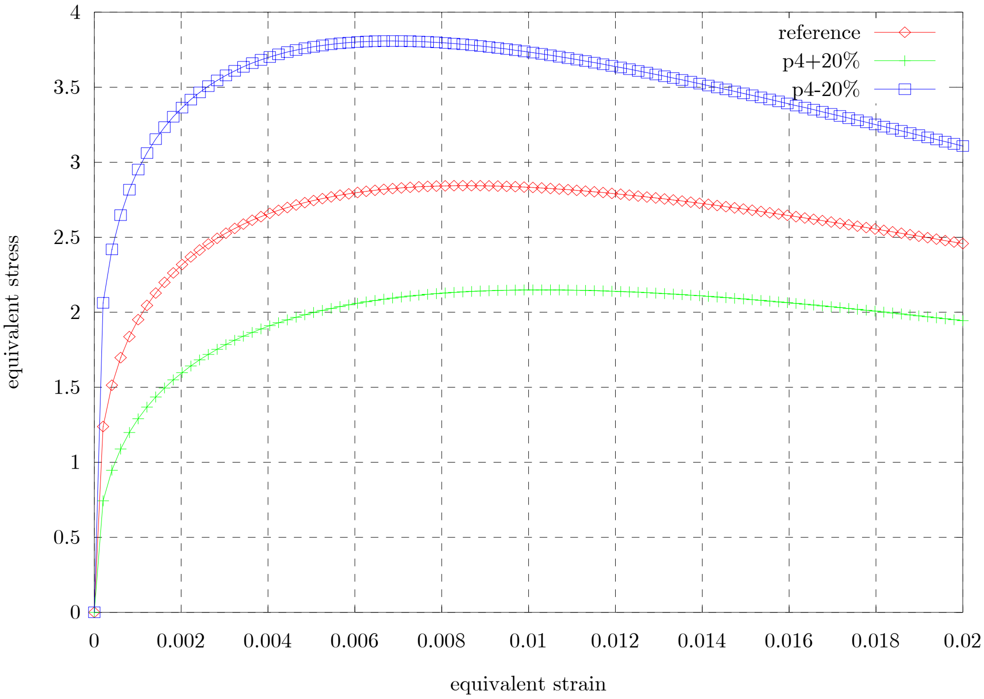

Figure 56: Effect of the increasing/decreasing of p_4 by 20% (for one temperature and one strain rate)

The tensorial expression of this modified Norton-Hoff law can be expressed. Inverting relation (163):

$$\bar{\dot{\varepsilon}} = \frac{1}{\sqrt{3}}\left(\frac{\bar{\sigma}}{K_0 e^{-p_1\bar{\varepsilon}} p_2 \sqrt{3}.\bar{\varepsilon}^{p_4}}\right)^{\frac{1}{p_3}} \tag{164}$$

and introducing this in the viscoplastic flow rule associated with Von Mises criterion (cf. relation (154)), one obtain:

$$\begin{aligned} \hat{\dot{\varepsilon}}_{ij} &= \frac{3\bar{\dot{\varepsilon}}}{2\bar{\sigma}}\hat{\sigma}_{ij} = \frac{3}{2}\frac{1}{\bar{\sigma}}\frac{1}{\sqrt{3}}\left(\frac{\bar{\sigma}}{K_0 e^{-p_1.\bar{\varepsilon}} p_2 \sqrt{3}.\bar{\varepsilon}^{p_4}}\right)^{\frac{1}{p_3}} \hat{\sigma}_{ij} \\ &= \frac{\sqrt{3}}{2}\left(\bar{\sigma}^2\right)^{\frac{1-p_3}{2p_3}}\left(\frac{1}{K_0 e^{-p_1.\bar{\varepsilon}} p_2 \sqrt{3}.\bar{\varepsilon}^{p_4}}\right)^{\frac{1}{p_3}} \hat{\sigma}_{ij} \end{aligned} \tag{165}$$

or

$$\hat{\dot{\varepsilon}}_{ij} = \frac{1}{2}\left(\sqrt{3}\right)^{1+2\frac{1-p_3}{2.p_3}-\frac{1}{p_3}}\left(-J_2\right)^{p_5}\left(\frac{1}{K_0 e^{-p_1.\bar{\varepsilon}} p_2 \sqrt{3}.\bar{\varepsilon}^{p_4}}\right)^{\frac{1}{p_3}} \hat{\sigma}_{ij} \tag{166}$$

$$\Rightarrow \quad \dot{\hat{\varepsilon}}_{ij} = \frac{\left(-J_2\right)^{p_5} e^{\frac{p_1}{p_3}\overline{\varepsilon}} \, \overline{\varepsilon}^{-\frac{p_4}{p_3}}}{2\left(K_0 p_2\right)^{\frac{1}{p_3}}} \hat{\sigma}_{ij} \tag{167}$$

where $J_2 = II_{\underline{\hat{\sigma}}} = -\frac{1}{2}\hat{\sigma}_{ij}\hat{\sigma}_{ij} = -\frac{1}{3}\overline{\sigma}^2$ and $p_5 = \frac{1-p_3}{2p_3}$

2.3.7. Implicit time integration of modified Norton-Hoff law

Time integration of the constitutive law consists in determination of stress tensor at the end of the time step as a function of its value at the beginning of the time step and some other values such as temperature T, strain and strain rate tensors $\underline{\varepsilon}$ and $\underline{\dot{\varepsilon}}$.

Two integration schemes have been tested: the implicit scheme and the Euler's semi-implicit scheme. However, the first one was more stable and accurate [HAB98a], thus only the implicit scheme has been maintained and developed hereafter.

Still using subscripts $_A$ and $_B$ for beginning and end of time step (cf. section III.2.2.2), the first order development of the deviatoric stress tensor $\underline{\hat{\sigma}}(t)$ with respect to time t is:

$$\underline{\hat{\sigma}}_B = \underline{\hat{\sigma}}_A + \left.\dot{\underline{\hat{\sigma}}}\right|_{t_A+\theta.\Delta t_{AB}} \Delta t_{AB} \qquad 0 \le \theta \le 1 \tag{168}$$

where Δt_{AB} is the time step.

Considering viscoplastic flow rule associated to Von Mises criterion:

$$\underline{\dot{\varepsilon}}^{vp} = \frac{3\overline{\dot{\varepsilon}}^{vp}}{2\overline{\sigma}} \underline{\hat{\sigma}} \tag{169}$$

and the modified Norton-Hoff constitutive law:

$$\overline{\sigma} = K_o e^{-p_1 \overline{\varepsilon}^{vp}} \sqrt{3} p_2 (\sqrt{3}.\overline{\dot{\varepsilon}}^{vp})^{p_3} \left(\overline{\varepsilon}^{vp}\right)^{p_4} \tag{170}$$

or

$$\overline{\dot{\varepsilon}}^{vp} = \frac{\overline{\sigma}^{\frac{1}{p_3}} e^{\frac{p_1}{p_3}\overline{\varepsilon}^{vp}}}{\sqrt{3}\left(\sqrt{3}K_0 p_2\right)^{\frac{1}{p_3}} \left(\overline{\varepsilon}^{vp}\right)^{\frac{p_4}{p_3}}} \tag{171}$$

then, introducing (170) in (169) and isolating the deviatoric stress tensor $\underline{\hat{\sigma}}$:

$$\underline{\hat{\sigma}} = 2K_0 e^{-p_1 \overline{\varepsilon}^{vp}} p_2 \left(\sqrt{3}.\overline{\dot{\varepsilon}}^{vp}\right)^{p_3-1} \left(\overline{\varepsilon}^{vp}\right)^{p_4} \underline{\dot{\varepsilon}}^{vp} \tag{172}$$

or

$$\begin{aligned}\underline{\dot{\varepsilon}}^{vp} &= \frac{3}{2\overline{\sigma}}\frac{\overline{\sigma}^{\frac{1}{p_3}}e^{\frac{p_1}{p_3}\overline{\varepsilon}^{vp}}}{\sqrt{3}\left(\sqrt{3}K_0p_2\right)^{\frac{1}{p_3}}\left(\overline{\varepsilon}^{vp}\right)^{\frac{p_4}{p_3}}}\underline{\hat{\sigma}} = \left(\frac{\overline{\sigma}}{\sqrt{3}}\right)^{\frac{1-p_3}{p_3}}\frac{e^{\frac{p_1}{p_3}\overline{\varepsilon}^{vp}}}{2\left(K_0p_2\right)^{\frac{1}{p_3}}\left(\overline{\varepsilon}^{vp}\right)^{\frac{p_4}{p_3}}}\underline{\hat{\sigma}} \\ &= \left(\frac{\overline{\sigma}^2}{3}\right)^{\frac{1-p_3}{2.p_3}}\frac{e^{\frac{p_1}{p_3}\overline{\varepsilon}^{vp}}}{2\left(K_0p_2\right)^{\frac{1}{p_3}}\left(\overline{\varepsilon}^{vp}\right)^{\frac{p_4}{p_3}}}\underline{\hat{\sigma}} = \frac{\left(-J_2\right)^{p_5}e^{\frac{p_1}{p_3}\overline{\varepsilon}^{vp}}}{2\left(K_0p_2\right)^{\frac{1}{p_3}}\left(\overline{\varepsilon}^{vp}\right)^{\frac{p_4}{p_3}}}\underline{\hat{\sigma}}\end{aligned} \tag{173}$$

The elastic stress tensor – cf. relation (65)– can be split into:

$$\begin{cases}\underline{\hat{\sigma}} = 2G\underline{\hat{\varepsilon}}^{el} \\ \sigma_m = 3\chi\varepsilon_m^{mec}\end{cases} \tag{174}$$

$$\leftrightarrow \qquad \begin{cases}\underline{\hat{\sigma}} = 2G\left(\underline{\hat{\varepsilon}}^{tot} - \underline{\hat{\varepsilon}}^{vp}\right) \\ \sigma_m = 3\chi\left(\varepsilon_m - \varepsilon_m^{th}\right)\end{cases} \tag{175}$$

since thermal (and phase transformation) strain being taken into account in the present thermomechanical approach.

Deriving (175) with respect to time *t*:

$$\begin{cases}\underline{\dot{\hat{\sigma}}} = 2\frac{\partial G}{\partial T}\dot{T}\left(\underline{\hat{\varepsilon}}^{tot} - \underline{\hat{\varepsilon}}^{vp}\right) + 2G\left(\underline{\dot{\hat{\varepsilon}}}^{tot} - \underline{\dot{\hat{\varepsilon}}}^{vp}\right) = \frac{1}{G}\frac{\partial G}{\partial T}\underline{\hat{\sigma}}\dot{T} + 2G\left(\underline{\dot{\hat{\varepsilon}}}^{tot} - \underline{\dot{\hat{\varepsilon}}}^{vp}\right) \\ \dot{\sigma}_m = 3\frac{\partial \chi}{\partial T}\dot{T}\left(\varepsilon_m - \varepsilon_m^{th}\right) + 3\chi\left(\dot{\varepsilon}_m - \dot{\varepsilon}_m^{th}\right) = \frac{1}{\chi}\frac{\partial \chi}{\partial T}\sigma_m\dot{T} + 3\chi\left(\dot{\varepsilon}_m - \dot{\varepsilon}_m^{th}\right)\end{cases} \tag{176}$$

Focussing on the deviatoric stress rate:

$$\begin{aligned}\underline{\dot{\hat{\sigma}}} &= \left(2.G.\underline{\dot{\hat{\varepsilon}}}^{tot}\right) + \left(\frac{1}{G}\frac{\partial G}{\partial T}.\underline{\hat{\sigma}}.\dot{T} - 2.G.\underline{\dot{\hat{\varepsilon}}}^{vp}\right) \\ &= \left(2.G.\underline{\dot{\hat{\varepsilon}}}^{tot}\right) + \left(\frac{1}{G}\frac{\partial G}{\partial T}.\underline{\hat{\sigma}}.\dot{T} - G.\frac{J_2^{\,p_5}.e^{\frac{p_1}{p_3}\overline{\varepsilon}^{vp}}}{\left(K_0.p_2\right)^{\frac{1}{p_3}}.\left(\overline{\varepsilon}^{vp}\right)^{\frac{p_4}{p_3}}}.\underline{\hat{\sigma}}\right) \\ &= \underline{f}\left(T(t)\right) + \underline{g}\left(\underline{\hat{\sigma}}(t), \overline{\varepsilon}^{vp}(t), T(t)\right)\end{aligned} \tag{177}$$

where

$$\begin{cases}\underline{f}\left(T(t)\right) = 2G\underline{\dot{\hat{\varepsilon}}}^{tot} \\ \underline{g}\left(\underline{\hat{\sigma}}(t), \overline{\varepsilon}^{vp}(t), T(t)\right) = \frac{1}{G}\frac{\partial G}{\partial T}\underline{\hat{\sigma}}\dot{T} - G\frac{\left(-J_2\right)^{p_5}e^{\frac{p_1}{p_3}\overline{\varepsilon}^{vp}}}{\left(K_0p_2\right)^{\frac{1}{p_3}}\left(\overline{\varepsilon}^{vp}\right)^{\frac{p_4}{p_3}}}\underline{\hat{\sigma}}\end{cases} \tag{178}$$

Introducing (177) in (168):

$$\begin{aligned}
\underline{\hat{\sigma}}_B &= \underline{\hat{\sigma}}_A + \left(\underline{f}(T) + \underline{g}(\underline{\hat{\sigma}},\bar{\varepsilon}^{vp},T)\right)_{t_A+\theta.\Delta t_{AB}} \Delta t_{AB} \\
&= \underline{\hat{\sigma}}_A + \left(\underline{f}(T)\Big|_A + \underline{g}(\underline{\hat{\sigma}},\bar{\varepsilon}^{vp},T)\Big|_A\right)\Delta t_{AB} \\
&\quad + \left(\frac{\partial \underline{f}}{\partial T}\bigg|_A \theta \Delta T_{AB}\right)\Delta t_{AB} + \left(\frac{\partial \underline{g}}{\partial \underline{\hat{\sigma}}}\bigg|_A \theta \Delta \underline{\hat{\sigma}}_{AB}\right)\Delta t_{AB} \\
&\quad + \left(\frac{\partial \underline{g}}{\partial \bar{\varepsilon}^{vp}}\bigg|_A \theta \Delta \bar{\varepsilon}^{vp}_{AB}\right)\Delta t_{AB} + \left(\frac{\partial \underline{g}}{\partial T}\bigg|_A \theta \Delta T_{AB}\right)\Delta t_{AB}
\end{aligned} \tag{179}$$

And isolating $\Delta\underline{\hat{\sigma}}_{AB}$:

$$\begin{aligned}
\left(\underline{I} - \frac{\partial \underline{g}}{\partial \underline{\hat{\sigma}}}\bigg|_A \theta \Delta t_{AB}\right)\Delta\underline{\hat{\sigma}}_{AB} &= \left(\underline{f}(T)\Big|_A + \underline{g}(\underline{\hat{\sigma}},\bar{\varepsilon}^{vp},T)\Big|_A\right)\Delta t_{AB} \\
&\quad + \left(\frac{\partial \underline{f}}{\partial T}\bigg|_A + \frac{\partial \underline{g}}{\partial T}\bigg|_A\right)\Delta T_{AB}\theta\Delta t_{AB} \\
&\quad + \frac{\partial \underline{g}}{\partial \bar{\varepsilon}^{vp}}\bigg|_A (\Delta\bar{\varepsilon}^{vp})_{AB}\,\theta\Delta t_{AB}
\end{aligned} \tag{180}$$

which can be written:

$$\underline{A}\cdot\Delta\underline{\hat{\sigma}} = \underline{F} \tag{181}$$

For the 2D½ general plane strain state and after some analytical developments, which are detailed in Appendix (section 1), the system (181) can be written using the following expression:

$$\begin{bmatrix}
\beta+\alpha\hat{\sigma}_{11}\hat{\sigma}_{11} & \alpha\hat{\sigma}_{22}\hat{\sigma}_{11} & \alpha 2\hat{\sigma}_{12}\hat{\sigma}_{11} & \alpha\hat{\sigma}_{33}\hat{\sigma}_{11} \\
\alpha\hat{\sigma}_{11}\hat{\sigma}_{22} & \beta+\alpha\hat{\sigma}_{22}\hat{\sigma}_{22} & \alpha 2\hat{\sigma}_{12}\hat{\sigma}_{22} & \alpha\hat{\sigma}_{33}\hat{\sigma}_{22} \\
\alpha\hat{\sigma}_{11}\hat{\sigma}_{12} & \alpha\hat{\sigma}_{22}\hat{\sigma}_{12} & \beta+\alpha 2\hat{\sigma}_{12}\hat{\sigma}_{12} & \alpha\hat{\sigma}_{33}\hat{\sigma}_{12} \\
\alpha\hat{\sigma}_{11}\hat{\sigma}_{33} & \alpha\hat{\sigma}_{22}\hat{\sigma}_{33} & \alpha 2\hat{\sigma}_{12}\hat{\sigma}_{33} & \beta+\alpha\hat{\sigma}_{33}\hat{\sigma}_{33}
\end{bmatrix}
\begin{Bmatrix} \Delta\hat{\sigma}_{11} \\ \Delta\hat{\sigma}_{22} \\ \Delta\hat{\sigma}_{12} \\ \Delta\hat{\sigma}_{33} \end{Bmatrix}
= \mu \begin{Bmatrix} \hat{\dot{\varepsilon}}^{tot}_{11} \\ \hat{\dot{\varepsilon}}^{tot}_{22} \\ \hat{\dot{\varepsilon}}^{tot}_{12} \\ \hat{\dot{\varepsilon}}^{tot}_{33} \end{Bmatrix}
+ \eta \begin{Bmatrix} \hat{\sigma}_{11} \\ \hat{\sigma}_{22} \\ \hat{\sigma}_{12} \\ \hat{\sigma}_{33} \end{Bmatrix} \tag{182}$$

which is equivalent to:

$$\underline{A}\cdot\Delta\underline{\hat{\sigma}} = (\beta\underline{I} + \alpha\underline{\hat{\sigma}}\otimes\underline{a})\cdot\Delta\underline{\hat{\sigma}} = \mu\underline{\hat{\dot{\varepsilon}}}^{tot} + \eta\underline{\hat{\sigma}} \tag{183}$$

where:

$$\underline{a} = \begin{Bmatrix} \hat{\sigma}_{11} \\ \hat{\sigma}_{22} \\ 2\hat{\sigma}_{12} \\ \hat{\sigma}_{33} \end{Bmatrix} \tag{184}$$

with all $\hat{\sigma}_{ij}$ defined at the beginning of the step and α and β defined in Appendix (section 1).

The solution of the system is thus:

$$\Delta\underline{\hat{\sigma}} = \mu\underline{A}^{-1}\cdot\underline{\dot{\hat{\varepsilon}}}^{tot} + \eta\underline{A}^{-1}\cdot\underline{\hat{\sigma}} \tag{185}$$

Assuming that $\underline{A}^{-1}$ can be written:

$$\underline{A}^{-1} = \gamma\underline{I} - \delta\underline{\hat{\sigma}}\otimes\underline{a} = \left(\beta\underline{I} + \alpha\underline{\hat{\sigma}}\otimes\underline{a}\right)^{-1} \tag{186}$$

$$\begin{aligned} & \underline{A}\cdot\underline{A}^{-1} &&= \left(\beta\underline{I} + \alpha\underline{\hat{\sigma}}\otimes\underline{a}\right)\cdot\left(\gamma\underline{I} - \delta\underline{\hat{\sigma}}\otimes\underline{a}\right) \\ \rightarrow & &&= \beta\gamma\underline{I} - \beta\delta\underline{\hat{\sigma}}\otimes\underline{a} + \alpha\gamma\underline{\hat{\sigma}}\otimes\underline{a} - \alpha\delta\underline{\hat{\sigma}}\otimes\underline{a}\cdot\underline{\hat{\sigma}}\otimes\underline{a} \\ & &&= \underline{I} \end{aligned} \tag{187}$$

Assuming that

$$\beta\gamma = 1 \Leftrightarrow \gamma = \frac{1}{\beta} \tag{188}$$

then:

$$\begin{aligned} & \underline{I} - \beta\delta\underline{\hat{\sigma}}\otimes\underline{a} + \frac{\alpha}{\beta}\underline{\hat{\sigma}}\otimes\underline{a} - \alpha\delta\underline{\hat{\sigma}}\otimes\underline{a}\cdot\underline{\hat{\sigma}}\otimes\underline{a} = \underline{I} \\ & \Leftrightarrow -\beta\delta\underline{\hat{\sigma}}\otimes\underline{a} + \frac{\alpha}{\beta}\underline{\hat{\sigma}}\otimes\underline{a} - \alpha\delta\underline{\hat{\sigma}}\otimes\left(\underline{a}\cdot\underline{\hat{\sigma}}\right)\otimes\underline{a} = \underline{0} \\ & \Leftrightarrow \left(-\beta\delta + \frac{\alpha}{\beta} - \alpha\delta\underline{a}\cdot\underline{\hat{\sigma}}\right)\underline{\hat{\sigma}}\otimes\underline{a} = \underline{0} \\ & \Leftrightarrow -\delta\left(\beta + \alpha\underline{a}\cdot\underline{\hat{\sigma}}\right) + \frac{\alpha}{\beta} = 0 \\ & \Leftrightarrow \delta = \frac{\alpha}{\beta}\frac{1}{\beta + \alpha\underline{a}\cdot\underline{\hat{\sigma}}} \end{aligned} \tag{189}$$

Hence

$$\underline{A}^{-1} = \frac{1}{\beta}\underline{I} - \frac{\alpha}{\beta}\frac{1}{\beta + \alpha\underline{a}\cdot\underline{\hat{\sigma}}}\underline{\hat{\sigma}}\otimes\underline{a} \tag{190}$$

And the solution of the system (185) becomes:

$$\begin{aligned} \Delta\underline{\hat{\sigma}} &= \mu\left(\gamma\underline{I} - \delta\underline{\hat{\sigma}}\otimes\underline{a}\right)\cdot\underline{\dot{\hat{\varepsilon}}}^{tot} + \eta\left(\gamma\underline{I} - \delta\underline{\hat{\sigma}}\otimes\underline{a}\right)\cdot\underline{\hat{\sigma}} \\ &= \mu\gamma\underline{\dot{\hat{\varepsilon}}}^{tot} - \mu\delta\underline{\hat{\sigma}}\otimes\underline{a}\cdot\underline{\dot{\hat{\varepsilon}}}^{tot} + \eta\gamma\underline{\hat{\sigma}} - \eta\delta\underline{\hat{\sigma}}\otimes\underline{a}\cdot\underline{\hat{\sigma}} \\ &= \left(\mu\gamma\right)\underline{\dot{\hat{\varepsilon}}}^{tot} + \underline{\hat{\sigma}}\left(-\mu\delta\underline{a}\cdot\underline{\dot{\hat{\varepsilon}}}^{tot} + \eta\gamma - \eta\delta\underline{a}\cdot\underline{\hat{\sigma}}\right) \\ &= CC_1\underline{\dot{\hat{\varepsilon}}}^{tot} + CC_2\underline{\hat{\sigma}} \end{aligned} \tag{191}$$

with:

$$\begin{cases} CC_1 = \mu\gamma = \dfrac{\mu}{\beta} \\ CC_2 = -\mu\delta\underline{a}\cdot\underline{\dot{\hat{\varepsilon}}}^{tot} + \dfrac{\eta}{\beta} - \eta\delta\underline{a}\cdot\underline{\hat{\sigma}} \end{cases} \tag{192}$$

What concerns the hydrostatic stress appearing in (176):

$$\begin{aligned}\sigma_{m,B} &= \sigma_{m,A} + \Delta\sigma_m \\ &= \sigma_{m,A} + \left(\frac{1}{\chi}\frac{\partial\chi}{\partial T}\sigma_{m,A}\dot{T} + 3\chi\left(\dot{\varepsilon}_m - \dot{\varepsilon}_m^{th}\right)\right)\Delta t \\ &= \left(1 + \frac{1}{\chi}\frac{\partial\chi}{\partial T}\Delta T\right)\sigma_{m,A} + 3\chi\left(\dot{\varepsilon}_m - \dot{\varepsilon}_m^{th}\right)\Delta t\end{aligned} \tag{193}$$

The stress tensor at the end of the time step is thus:

$$\begin{aligned}\underline{\sigma}_B &= \underline{\hat{\sigma}}_B + \sigma_{m,B}\,"\delta_{ij}" \\ &= \underline{\hat{\sigma}}_A + \Delta\underline{\hat{\sigma}} + \left(\sigma_{m,A} + \Delta\sigma_m\right)"\delta_{ij}" \\ &= \left\{\begin{matrix}\left(1+CC_2\right)\hat{\sigma}_{11,A} + CC_1\hat{\dot{\varepsilon}}_{11}^{tot} + \left(1 + \frac{1}{\chi}\frac{\partial\chi}{\partial T}\Delta T\right)\sigma_{m,A} + 3\chi\left(\dot{\varepsilon}_m - \dot{\varepsilon}_m^{th}\right)\Delta t \\ \left(1+CC_2\right)\hat{\sigma}_{22,A} + CC_1\hat{\dot{\varepsilon}}_{22}^{tot} + \left(1 + \frac{1}{\chi}\frac{\partial\chi}{\partial T}\Delta T\right)\sigma_{m,A} + 3\chi\left(\dot{\varepsilon}_m - \dot{\varepsilon}_m^{th}\right)\Delta t \\ \left(1+CC_2\right)\hat{\sigma}_{12,A} + CC_1\hat{\dot{\varepsilon}}_{12}^{tot} \\ \left(1+CC_2\right)\hat{\sigma}_{33,A} + CC_1\hat{\dot{\varepsilon}}_{33}^{tot} + \left(1 + \frac{1}{\chi}\frac{\partial\chi}{\partial T}\Delta T\right)\sigma_{m,A} + 3\chi\left(\dot{\varepsilon}_m - \dot{\varepsilon}_m^{th}\right)\Delta t\end{matrix}\right\}\end{aligned} \tag{194}$$

In large strains/displacements field, one has to add the correction of objective derivatives (Jaumann in the present model). Thus instead of $\underline{\sigma}_B$, the stress tensor computed by relation (194) is noted $\underline{s}_B$:

$$\underline{s}_B = \left\{\begin{matrix}\left(1+CC_2\right)\hat{\sigma}_{11,A} + CC_1\hat{\dot{\varepsilon}}_{11}^{tot} + \left(1 + \frac{1}{\chi}\frac{\partial\chi}{\partial T}\Delta T\right)\sigma_{m,A} + 3\chi\left(\dot{\varepsilon}_m - \dot{\varepsilon}_m^{th}\right)\Delta t \\ \left(1+CC_2\right)\hat{\sigma}_{22,A} + CC_1\hat{\dot{\varepsilon}}_{22}^{tot} + \left(1 + \frac{1}{\chi}\frac{\partial\chi}{\partial T}\Delta T\right)\sigma_{m,A} + 3\chi\left(\dot{\varepsilon}_m - \dot{\varepsilon}_m^{th}\right)\Delta t \\ \left(1+CC_2\right)\hat{\sigma}_{12,A} + CC_1\hat{\dot{\varepsilon}}_{12}^{tot} \\ \left(1+CC_2\right)\hat{\sigma}_{33,A} + CC_1\hat{\dot{\varepsilon}}_{33}^{tot} + \left(1 + \frac{1}{\chi}\frac{\partial\chi}{\partial T}\Delta T\right)\sigma_{m,A} + 3\chi\left(\dot{\varepsilon}_m - \dot{\varepsilon}_m^{th}\right)\Delta t\end{matrix}\right\} \tag{195}$$

The stress tensor at the end of the step and considering the Jaumann correction becomes thus:

$$\underline{\sigma}_B = \left\{\begin{matrix}s_{11} + 2\left(\omega_E\Delta t\right)s_{12} \\ s_{22} - 2\left(\omega_E\Delta t\right)s_{12} \\ s_{12} + \left(\omega_E\Delta t\right)\left(s_{22} - s_{11}\right) \\ s_{33}\end{matrix}\right\} \tag{196}$$

with $\omega_E = \frac{1}{2}\left(L_{12} - L_{21}\right)$.

2.3.8. Analytical compliance matrix

Compliance matrix can be computed by perturbations method. However, to reduce CPU time, an analytical compliance matrix has been introduced in the model. It is computed according to an iterative method: the time step is divided into time sub-intervals and the compliance matrix of the *i*th sub-interval is computed from the one of the previous *i-1*th sub-interval.

From relations (191) and (194):

$$\hat{\underline{s}}_B = CC_1 \hat{\dot{\underline{\varepsilon}}}^{tot} + \left(1 + CC_2\right) \hat{\underline{\sigma}}_A \tag{197}$$

Assuming a perturbation of the velocity gradient tensor $d\underline{L}$, the corresponding perturbation of the deviatoric stress tensor is:

$$d\hat{\underline{s}}_B = dCC_1 \hat{\dot{\underline{\varepsilon}}}^{tot} + CC_1 d\hat{\dot{\underline{\varepsilon}}}^{tot} + dCC_2 \hat{\underline{\sigma}}_A + \left(1 + CC_2\right) d\hat{\underline{\sigma}}_A \tag{198}$$

where

$$d\hat{\dot{\underline{\varepsilon}}}^{tot} = \begin{Bmatrix} d\hat{\dot{\varepsilon}}_{11}^{tot} \\ d\hat{\dot{\varepsilon}}_{22}^{tot} \\ d\hat{\dot{\varepsilon}}_{12}^{tot} \\ d\hat{\dot{\varepsilon}}_{33}^{tot} \end{Bmatrix} = \begin{bmatrix} \frac{2}{3} & -\frac{1}{3} & 0 & 0 & -\frac{1}{3} \\ -\frac{1}{3} & \frac{2}{3} & 0 & 0 & -\frac{1}{3} \\ 0 & 0 & \frac{1}{2} & \frac{1}{2} & 0 \\ -\frac{1}{3} & -\frac{1}{3} & 0 & 0 & \frac{2}{3} \end{bmatrix} \begin{Bmatrix} dL_{11} \\ dL_{22} \\ dL_{12} \\ dL_{21} \\ dL_{33} \end{Bmatrix} = \underline{MDL} \cdot d\underline{L} \tag{199}$$

Analytical developments are reported in section 2 of the Appendix. They lead to the following expression:

$$\begin{aligned} d\hat{\underline{\sigma}}_B &= \underline{M}_{\sigma S} \cdot \left(\underline{M}_{SL} \cdot d\underline{L} + \underline{M}_{SS} \cdot d\hat{\underline{\sigma}}_A\right) + \underline{M}_{\sigma L} \cdot d\underline{L} \\ &= \underline{M}_{\sigma S} \cdot \underline{M}_{SS} \cdot d\hat{\underline{\sigma}}_A + \left(\underline{M}_{\sigma S} \cdot \underline{M}_{SL} + \underline{M}_{\sigma L}\right) \cdot d\underline{L} \\ &= \underline{A}_{\sigma\sigma} \cdot d\hat{\underline{\sigma}}_A + \underline{A}_{\sigma L} \cdot d\underline{L} \end{aligned} \tag{200}$$

If the time step Δt is divided into *NINTV* time sub-steps :

$$dt = \frac{\Delta t}{NINTV} \tag{201}$$

Noting that:

$$d\hat{\underline{\sigma}}_A = \hat{\underline{C}}_{i-1} \cdot d\underline{L} dt \tag{202}$$

where $\hat{\underline{C}}_{i-1}$ is the deviatoric part of compliance matrix of the $(i-1)^{th}$ sub-step, so that for the actual i^{th} sub-step:

$$\begin{aligned} d\hat{\underline{\sigma}}_B &= \left(\underline{A}_{\sigma\sigma}\right)_i \cdot \hat{\underline{C}}_{i-1} \cdot d\underline{L} dt + \left(\underline{A}_{\sigma L}\right)_i \cdot d\underline{L} \\ &= \left(\left(\underline{A}_{\sigma\sigma}\right)_i \cdot \hat{\underline{C}}_{i-1} + \frac{1}{dt}\left(\underline{A}_{\sigma L}\right)_i\right) d\underline{L} dt = \hat{\underline{C}}_i \cdot d\underline{L} dt \end{aligned} \tag{203}$$

Hence :

$$\underline{\hat{C}}_i = \left(\underline{A}_{\sigma\sigma}\right)_i \cdot \underline{\hat{C}}_{i-1} + \frac{1}{dt}\left(\underline{A}_{\sigma L}\right)_i \tag{204}$$

The hydrostatic part of the compliance matrix is:

$$\left(\underline{C}_{\chi}\right)_i = \frac{\chi}{3dt}\underline{I} \tag{205}$$

and the total compliance matrix at i^{th} sub-step is computed recursively:

$$\underline{C}_i = \underline{\hat{C}}_i + \left(\underline{C}_{\chi}\right)_i = \left(\underline{A}_{\sigma\sigma}\right)_i \cdot \underline{\hat{C}}_{i-1} + \frac{1}{dt}\left(\underline{A}_{\sigma L}\right)_i + \frac{\chi}{3dt}\underline{I} \tag{206}$$

2.4. From elasticity to viscoplasticy: yield limit

The elastic-viscous-plastic constitutive law has been programmed in such a way that the user can either input the yield limit as the law parameter K_0 or let the program compute it automatically.

In the first case, the parameter K_0 can be defined by at several temperatures so that the yield limit becomes temperature dependent, but it does not depend on the strain rate. This first choice allows neglecting of the elastic part when K_0 is defined very small. For higher values, it can induce some discontinuities, as shown on Figure 57. Once the yield limit K_0 is achieved, a "jump" can be necessary to go from the elastic domain to the viscous-plastic curve. In fact, the value of K_0 has been fitted for only one equivalent strain rate (for example $\dot{\overline{\varepsilon}}_2$ on Figure 57), but when the strain rate is different the problem takes place. This solution is thus not recommended.

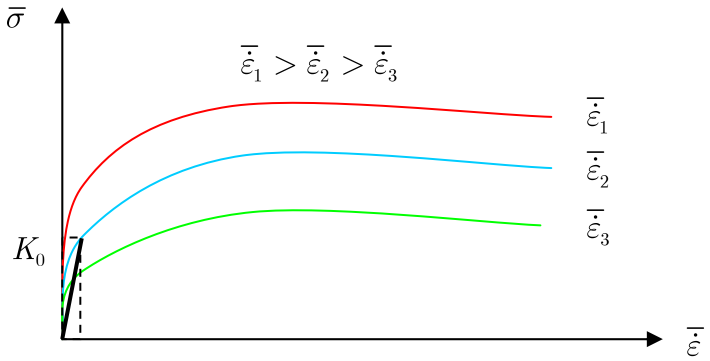

Figure 57: Problem of yield limit determination

In the second choice, the yield limit σ_y is automatically computed. It is simply the equivalent stress at the intersection point between elastic straight line:

$$\overline{\sigma} = E\overline{\varepsilon} \tag{207}$$

and the Norton-Hoff curve

$$\overline{\sigma} = K_o.e^{-p_1\overline{\varepsilon}}.\sqrt{3}.p_2(\sqrt{3}.\dot{\overline{\varepsilon}})^{p3}.\overline{\varepsilon}^{p4} \tag{208}$$

This intersection corresponds to the solution of the following equation:

$$f(\overline{\varepsilon}) = K_o.e^{-p_1\overline{\varepsilon}}.\sqrt{3}.p_2(\sqrt{3}.\dot{\overline{\varepsilon}})^{p3}.\overline{\varepsilon}^{p4} - E\overline{\varepsilon} = 0 \tag{209}$$

Newton-Raphson's algorithm was first adopted to solve this problem:

$$\overline{\varepsilon}_{k+1} = \overline{\varepsilon}_k - \frac{f(\overline{\varepsilon}_k)}{f\,'(\overline{\varepsilon}_k)} \tag{210}$$

where

$$f\,'(\overline{\varepsilon}_k) = \overline{\sigma} \cdot (\frac{p_4}{\overline{\varepsilon}_k} - p_1) - E \tag{211}$$

The convergence occurs when $\left|\overline{\varepsilon}_{k+1} - \overline{\varepsilon}_k\right| < \delta$ where δ is the required precision and if the solution is $\overline{\varepsilon} = \overline{\varepsilon}^*$, the yield limit is given by:

$$\sigma_y = E\overline{\varepsilon}^* \tag{212}$$

However, some convergence problems appeared in this algorithm of yield limit determination. Hence, a middle point algorithm has been preferred: it is longer to converge, but the solution is always found.

2.5. Loading/unloading criterion

Since the law must be available both for loading and unloading case, it needs a criterion to determine when one or the other case occurs. This criterion is assumed not dependent on the thermal part of the strain rate. Consider the mechanical strain rate, which is defined as follows:

$$\underline{\dot{\varepsilon}}^{mech} = \underline{\dot{\varepsilon}}^{tot} - \underline{\dot{\varepsilon}}^{th} = \underline{\dot{\varepsilon}}^{tot} - \underline{Diag}(\alpha\dot{T}, \alpha\dot{T}, \alpha\dot{T}) = \underline{\dot{\varepsilon}}^{tot} - \alpha\dot{T}\underline{I} \tag{213}$$

The loading/unloading criterion is then determined this way:

$$\begin{cases} \underline{\sigma} \cdot \underline{\dot{\varepsilon}}^{mech} \geq 0 & \text{loading or neutral} \\ \underline{\sigma} \cdot \underline{\dot{\varepsilon}}^{mech} < 0 & \text{unloading} \end{cases} \tag{214}$$

Hereafter, two simple illustrations of the criterion are given.

2.5.1. First example*: without thermal effect*

Initial situation:

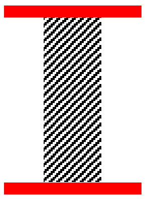

$\sigma = 0$

$$\dot{\varepsilon}^{mech} = \dot{\varepsilon}^{tot} - \dot{\varepsilon}^{th} = 0$$

$$\sigma \cdot \dot{\varepsilon}^{mech} = 0$$

→ no effect

First step: compression

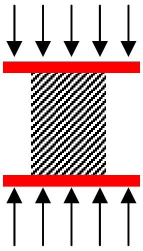

$\sigma < 0$

$$\dot{\varepsilon}^{mech} = \dot{\varepsilon}^{tot} - \dot{\varepsilon}^{th} = \dot{\varepsilon}^{tot} < 0$$

$$\sigma \cdot \dot{\varepsilon}^{mech} > 0$$

→ loading ✓

Second step: unloading

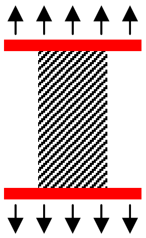

$\sigma < 0$

$$\dot{\varepsilon}^{mech} = \dot{\varepsilon}^{tot} - \dot{\varepsilon}^{th} = \dot{\varepsilon}^{tot} > 0$$

$$\sigma \cdot \dot{\varepsilon}^{mech} < 0$$

→ unloading ✓

2.5.2. Second example: *including thermal effect*

Initial situation:

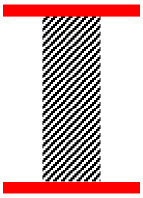

$\sigma = 0$

$$\dot{\varepsilon}^{mech} = \dot{\varepsilon}^{tot} - \dot{\varepsilon}^{th} = 0$$

$$\sigma \cdot \dot{\varepsilon}^{mech} = 0$$

→ no effect

First step: compression

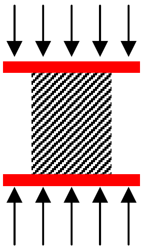

$\sigma < 0$

$$\dot{\varepsilon}^{mech} = \dot{\varepsilon}^{tot} - \dot{\varepsilon}^{th} = \dot{\varepsilon}^{tot} < 0$$

$$\sigma \cdot \dot{\varepsilon}^{mech} > 0$$

→ loading ✓

Second step: ΔT < 0

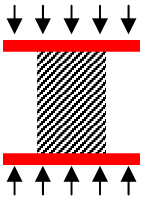

$\sigma < 0$

$$\dot{\varepsilon}^{mech} = \dot{\varepsilon}^{tot} - \dot{\varepsilon}^{th} = -\dot{\varepsilon}^{th} > 0$$

$$\sigma \cdot \dot{\varepsilon}^{mech} < 0$$

→ unloading ✓

2.6. Analytical vs. numerical verification : study of a small cylinder

Many numerical simulations of tensile test on a small cylinder have been performed to check the accuracy of the constitutive law. Some illustrations are shown hereafter for the following cases:

- simple tensile test at constant strain rate (Figure 58)
- simple tensile test with sudden variation of strain rate (Figure 59)
- simple tensile test with softening (Figure 60)
- simple tensile test with unloading (Figure 61)
- simple tensile test with unloading in softening domain (Figure 62)

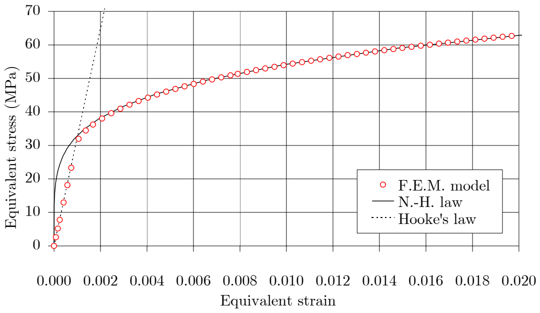

Figure 58: Simple tensile test at constant strain rate

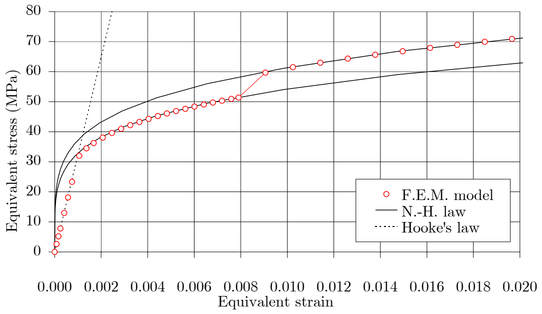

Figure 59: Simple tensile test with sudden variation of strain rate

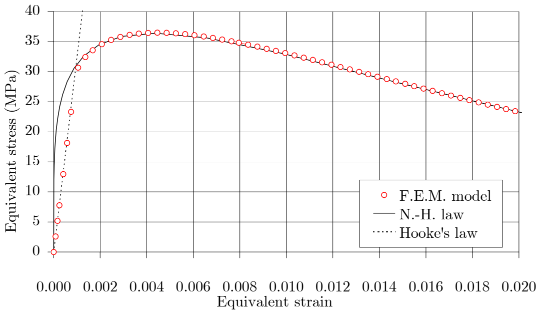

Figure 60: Simple tensile test with softening

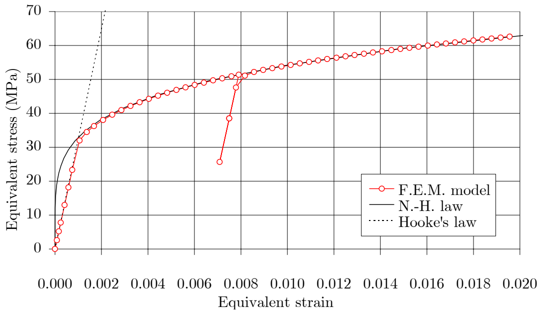

Figure 61: Simple tensile test with unloading

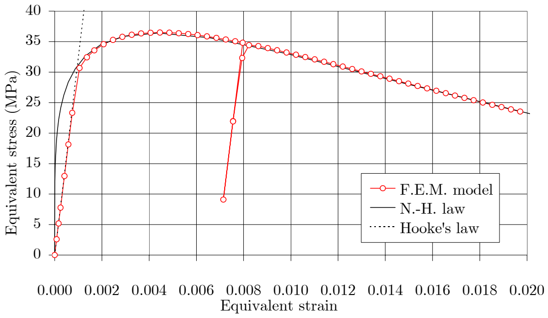

Figure 62: Simple tensile test with unloading in softening domain

The slight difference between numerical and analytical stress-strain plotting can be explained by the evolution of strain rate during the simulation: tensile test is performed moving the nodes of the finite element. The displacement of these nodes is evolving linearly during time. In large strains, this linear displacement is not exactly equivalent to constant strain rate. At the opposite, only one analytical curve has been plotted (corresponding to a unique equivalent strain rate).

3. Ferrostatic pressure

As long as liquid steel remains in the core of the slab, the ferrostatic pressure is applied by the column of fluid on the solidified shell. The thickness of this shell – or penetration depth of the solidification d – can be approximated by the following empirical formulation (well known in casting industry):

$$d = K\sqrt{t} \tag{215}$$

where t is the time and K is a characteristic parameter of the caster, the product and the casting conditions. For example, assuming that $K = 25\text{mm}/\sqrt{\text{min}}$ (convenient units in continuous casting), the duration to solidify a 200mm thick product is about:

$$t = \left(\frac{200/2}{25}\right)^2 = 16\,\text{min} \tag{216}$$

Considering a constant casting speed of 1.2 m/min, the metallurgical length would be:

$$L = vt = 1.2\frac{\text{m}}{\text{min}}16\,\text{min} = 19.2\text{m} \tag{217}$$

The ferrostatic pressure in the liquid phase p_f is similar to hydrostatic pressure in water. It is equal to the specific weight γ multiplied by the depth under free surface D:

$$p_f = \gamma D \tag{218}$$

In the solid phase, the ferrostatic pressure is obviously equal to zero. In the mushy zone, several assumptions could be discussed, two extreme limits being defined. The first one is to consider that the ferrostatic pressure exists until the whole solidification of the domain. The second extreme assumption is to consider that ferrostatic pressure vanishes since solid fraction appears. The diagram of ferrostatic pressure vs. temperature corresponding to both extreme assumptions would be:

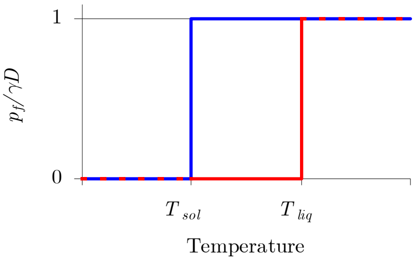

Figure 63: Extreme solutions for ferrostatic pressure in mushy state

Actually, as far as liquid steel is free to move in the mushy zone, i.e. to move between dendrites, the ferrostatic pressure can be transmitted to the solid fraction. At the opposite, when solidification is almost finished, the remaining “bubbles” of liquid steel are surrounded with solid phase and they are not in contact with the liquid pool anymore. The ferrostatic pressure in the liquid bubble becomes much more complex to determine since liquid shrinks during solidification and thus the pressure should decrease.

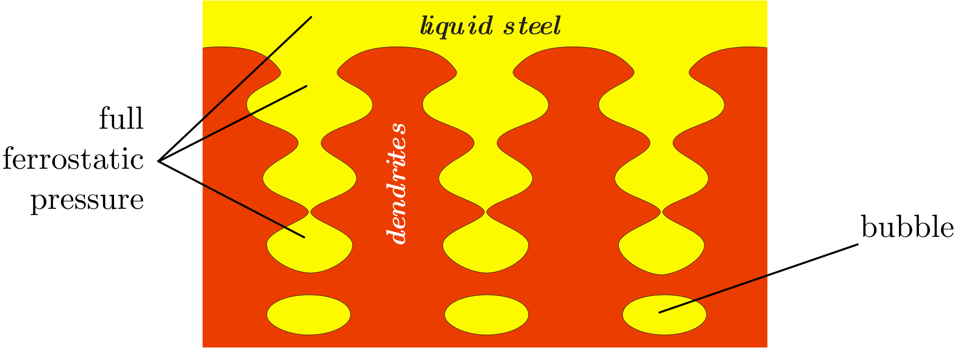

Figure 64: Schematic representation of mushy zone

At the size level of finite elements, such an acute description of the phenomenology is not taken into account and thus a macroscopic formulation must be considered. The following assumption has been adopted:

$$p_f = \gamma D\left(1 - f_s\right) \tag{219}$$

which means that the ferrostatic pressure p_f decrease linearly with the apparition of the solid fraction f_s. In the liquid phase, the pressure is fully developed and it vanishes when the solidification is completed.

Since solid fraction f_s has been assumed to vary linearly with temperature (cf. relation **(12)** in section II.2), it is the same for ferrostatic pressure:

$$p_f = \begin{cases} \gamma D & \text{if } T_{liq} < T \\ \gamma D \dfrac{T - T_{sol}}{T_{liq} - T_{sol}} & \text{if } T_{sol} < T < T_{liq} \\ 0 & \text{if } T < T_{sol} \end{cases} \tag{220}$$

which is an intermediate solution between the two extreme solutions above. This solution is shown on the Figure 65:

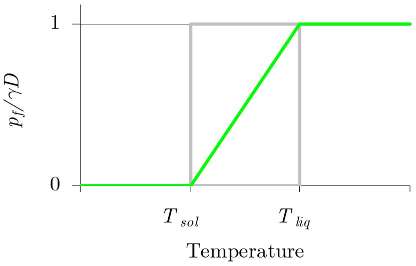

Figure 65: Ferrostatic pressure vs. temperature

A specific finite element has been developed for ferrostatic pressure. It is defined by the eight nodes of a plane element to which it is coupled (so the geometry of both elements is and remains identical).

In any element, the ferrostatic pressure is computed as follows: the average temperature of the element (mean value of the eight nodes and average value in time step) is determined for ferrostatic pressure computation according to relation (220). The nodal forces are then computed and applied: they are pointing outward the element.

Consider two adjacent finite elements: if the average temperature of both elements is above the liquidus, the ferrostatic pressure is identical and there is no resulting force. At the opposite, if one element is liquid and the adjacent is in mushy (or solid) state, the ferrostatic pressure is different and the resulting nodal forces at the interface are corresponding to the application of the pressure from the liquid to the solid (see Figure 66).

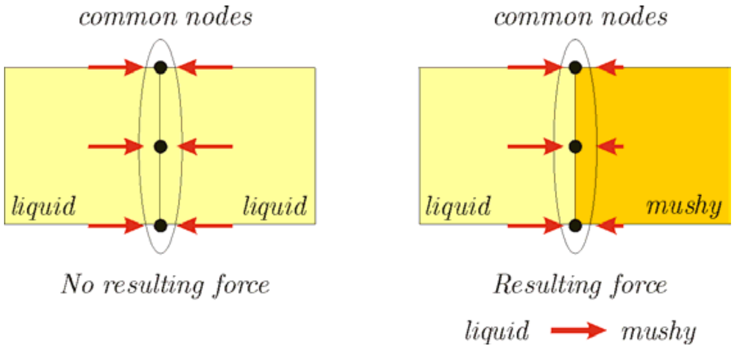

Figure 66: Two adjacent finite elements and force resulting from ferrostatic pressure

Note that the value of the ferrostatic pressure in the mushy state does not influence the force applied on the solid shell. Consider 3 successive elements, first in liquid state, second in mushy state and the third in solid state. The ferrostatic pressure in the liquid and the solid ones is known for sure. Whatever is the assumption for the ferrostatic pressure in the mushy one, the force balance is such that the pressure applied on the boundary of the solid element is always equal to the ferrostatic pressure in the liquid.

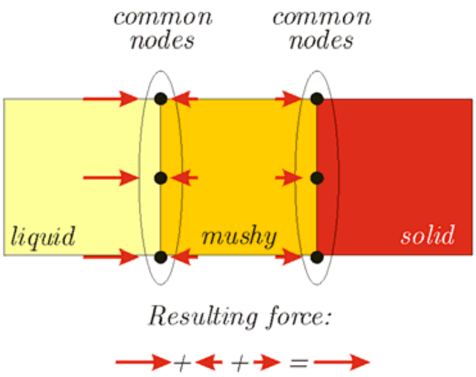

Figure 67: Transmission of full ferrostatic pressure form the liquid to the solid shell

Thus the assumption on the ferrostatic pressure in the mushy state has an influence:

- on the stress field in the mushy elements;
- on the solid shell when the liquid pool is almost closed (near the metallurgical length) – no more liquid remains in the slice, but only mushy in the core and a thick solidified shell.

4. Mechanical contact

4.1. Phenomenology and general aspects

4.1.1. Local and global approaches

There are many ways to describe – model – the contact between two bodies. Both analytical and numerical developments help to formulate of this particular aspect of material forming, which is non-linear in essence.

One classification separates the models in two main approaches: local and global approaches. In the local approach, irregularities at the surface are modelled in such a way that contact occurs at a very low scale as represented on the Figure 68:

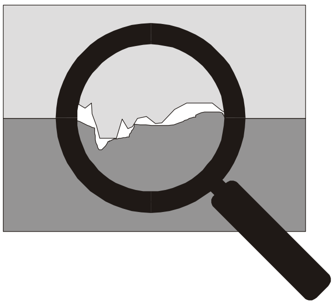

Figure 68: Local approach: contact at very low scale (dry contact)

Many parameters have to be taken into account, but roughness of the surfaces in contact and wear are of prime importance. In such a approach, another parameter is also essential: the presence of a third "body" (dust or lubricant), which can hardly modify the mechanical aspects of contact. In this case, theory of lubrication is applied.

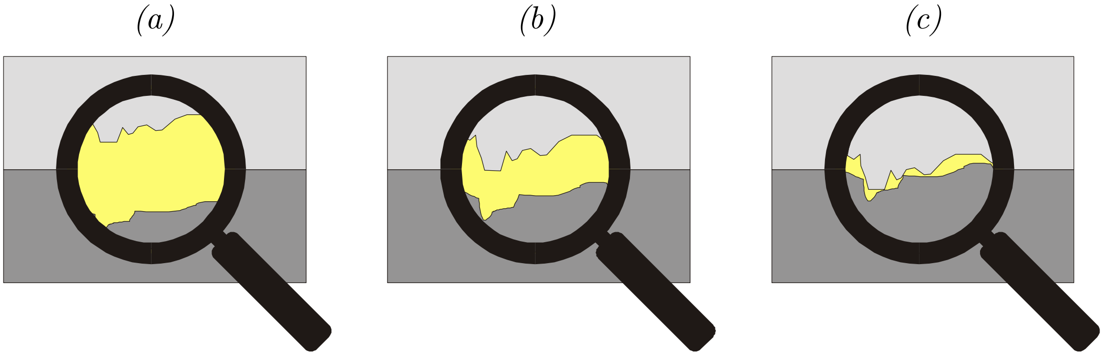

Figure 69: Lubricated contact:
Thick/thin film lubricated contacts (a/b) and boundary lubricated contact (c)

The Figure 69 shows different situations of lubricated contact. When the film is thick, roughness is not influential (but the viscosity of the lubricant is important). At the opposite, with a thin film, the roughness of the surface is important and the asperities can interact during sliding. The lubricant film can also be influenced by the presence of solid particles (solid lubricant as well as dust or disintegrated asperities due to wear) or gas (air,…).

In a global approach, a set of global parameters is introduced in the contact model in such a way that the global answer is quite correct. Constitutive laws are statistical representations of the behaviour at a lower scale (asperities scale). This approach is analogous to the macroscopic assumption of continuous material in theory of plasticity, instead of considering all grains and their boundaries.

Since the dimensions of finite elements are several orders of magnitude larger than asperities, a global approach has been adopted, considering dry contact.

4.1.2. Notations

The aim of a contact model is to determinate the reciprocal loading applied by each body in contact with another. This loading is composed of two forces per unit of surface:

- the first one is normal to the contact surface, the contact pressure $\underline{p}$
- the second one is tangential to the contact surface, the friction $\underline{\tau}$

Considering the following local axes at one point on the contact surface of one of the two bodies:

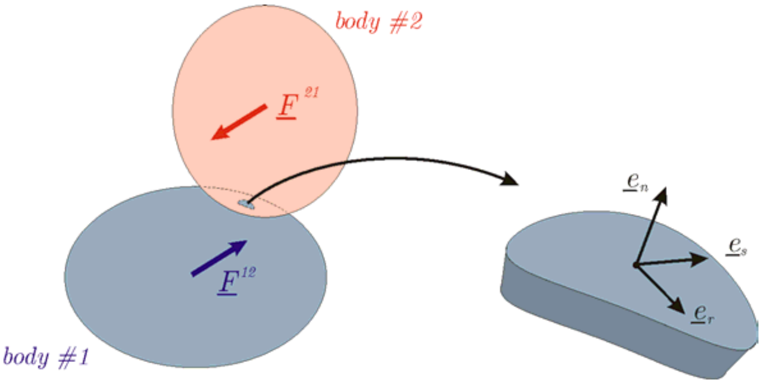

Figure 70: Local axes at one point of contact

If $\underline{F}^{ij}$ is the force applied by body i on body j, then:

$$\underline{F}^{ij} = -\underline{F}^{ji} \tag{221}$$

Assuming punctual contact, the force $\underline{F}^{21}$ applied by body #2 on body #1 can be decomposed along local axes:

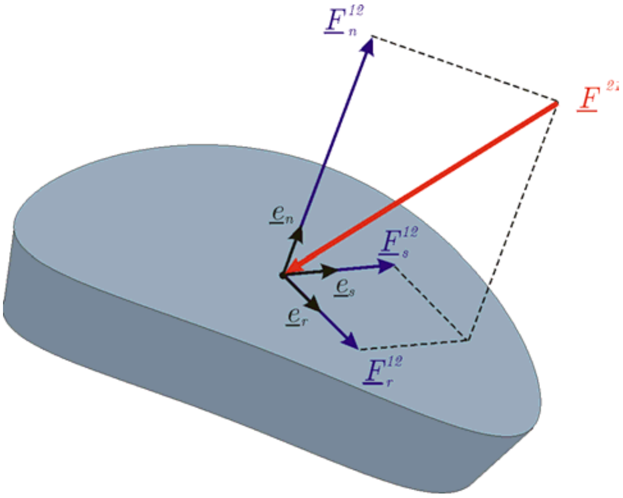

Figure 71: Decomposition of the reaction at contact point

$$\begin{cases} \underline{F}^{12}_n = -\left(\underline{F}^{21} \cdot \underline{e}_n\right)\underline{e}_n \\ \underline{F}^{12}_r = -\left(\underline{F}^{21} \cdot \underline{e}_r\right)\underline{e}_r \\ \underline{F}^{12}_s = -\left(\underline{F}^{21} \cdot \underline{e}_s\right)\underline{e}_s \end{cases} \tag{222}$$

If the contact broadens to a contact surface, applied forces per unit surface (contact stresses) can be defined and their integration must be equal to the total applied force $\underline{F}^{12}$:

$$\int_{\text{contact surface}} \left(\underline{\sigma}_n + \underline{\tau}_r + \underline{\tau}_s\right) ds = \underline{F}^{21} \tag{223}$$

Locally (on contact surface $ds \to 0$), relation (222) becomes:

$$\begin{cases} \underline{\sigma}_n = \left(\underline{T} \cdot \underline{e}_n\right)\underline{e}_n = \left(\underline{e}_n \otimes \underline{e}_n\right) \cdot \underline{T} \\ \underline{\tau}_r = \left(\underline{T} \cdot \underline{e}_r\right)\underline{e}_r = \left(\underline{e}_r \otimes \underline{e}_r\right) \cdot \underline{T} \\ \underline{\tau}_s = \left(\underline{T} \cdot \underline{e}_s\right)\underline{e}_s = \left(\underline{e}_s \otimes \underline{e}_s\right) \cdot \underline{T} \end{cases} \tag{224}$$

where $\underline{T}$ is the force per unit surface applied on the studied body.

A contact stress tensor $\underline{\sigma}_c$ can be defined in the local axes:

$$\underline{\sigma}_c = \begin{Bmatrix} \sigma_n \\ \tau_r \\ \tau_s \end{Bmatrix} = \begin{Bmatrix} p \\ \tau_r \\ \tau_s \end{Bmatrix} \tag{225}$$

$\underline{\sigma}_n$ being the normal component of the applied force per unit surface $\underline{T}$. It is thus equal to contact pressure p. $\underline{\tau}_r$ and $\underline{\tau}_s$ are tangent to the contact surface and their sum is equal to the friction $\underline{\tau}$, which is the normal projection of $\underline{T}$ on the contact surface:

$$\underline{\tau} = \underline{\tau}_r + \underline{\tau}_s = \left(\underline{e}_r \otimes \underline{e}_r + \underline{e}_s \otimes \underline{e}_s\right) \cdot \underline{T} \tag{226}$$

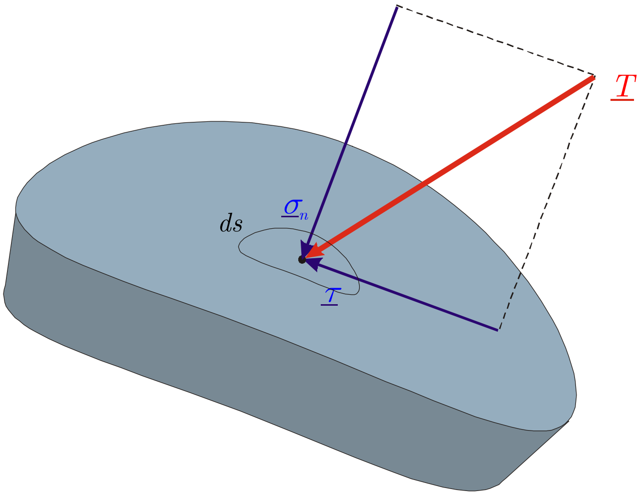

Figure 72: Decomposition of applied force $\underline{T}$ (per unit surface) into normal stress $\underline{\sigma}_n$ and tangential stress $\underline{\tau}$ (friction)

The aim of constitutive contact laws is the evaluation of the relationship between friction $\underline{\tau}$ and contact pressure p, taking into account different contact parameters, such as relative velocity, temperature, rheology of both solids in contact, roughness and wear of surfaces, time and many others. Some usual laws are introduced in section 4.2.

4.1.3. *Unilateral contact*

Considering two bodies in contact and $\underline{v}_1$ and $\underline{v}_2$ the velocities at the contact points, respectively on the surface of body #1 and body #2:

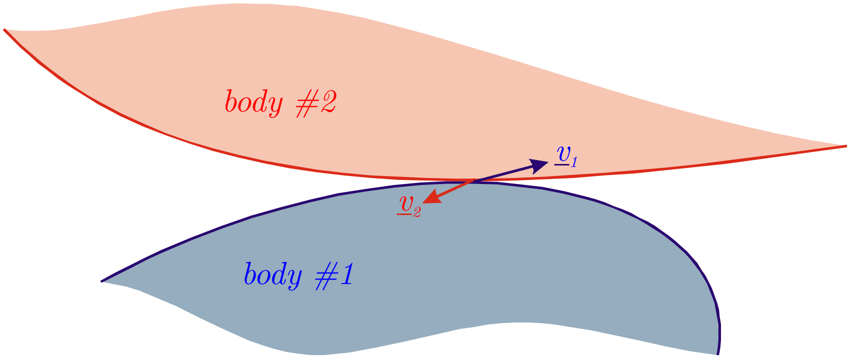

Figure 73: Bodies in contact and velocities at contact points

Assuming $\Delta\underline{v}$ is the relative velocity of contact point on body #1 with respect to velocity of contact point on body #2:

$$\Delta\underline{v} = \underline{v}_1 - \underline{v}_2 \tag{227}$$

The condition of no penetration during contact is given by:

$$\Delta\underline{v}\cdot\underline{e}_n \leq 0 \tag{228}$$

where $\underline{e}_n$ is the unit outward vector normal to the contact surface of the body #1. The Figure 74 illustrates this condition: two bodies in contact having different velocities.

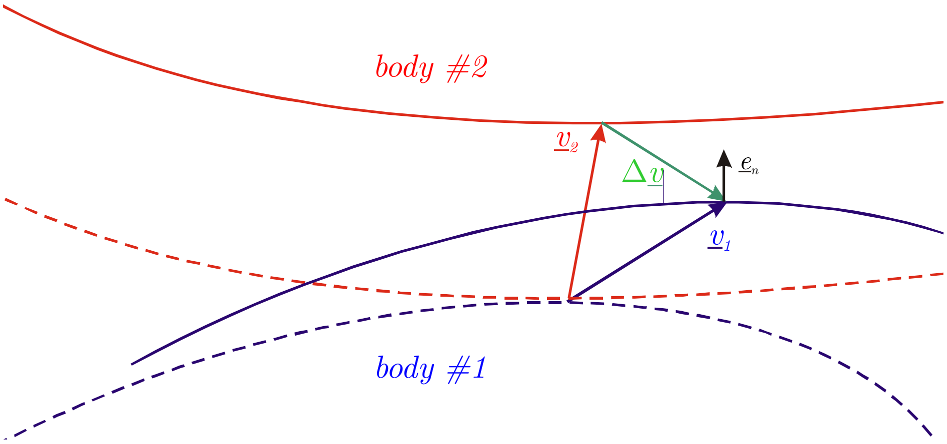

Figure 74: Illustration of no penetration condition

According to the latter figure and relation (228), if the dot product $\Delta\underline{v}\cdot\underline{e}_n$ is equal to zero, there are two possibilities:

- either the relative velocity is perpendicular to the normal vector, i.e. the relative movement is tangential and the bodies are sliding on each other
- or the relative velocity is the nil vector, i.e. the velocity of both bodies is the same, the bodies are sticking

The loss of contact occurs when the dot product $\Delta\underline{v}\cdot\underline{e}_n$ is negative. If it was positive, it would means that the first body is penetrating the second one.

Now considering the value of σ_n, the contact is characterized by:

$$\sigma_n \geq 0 \tag{229}$$

It can be equal to zero when the contact is unloaded, the two bodies touching each other, but without loading. Otherwise, if there is a mechanical interaction between both bodies, the normal stress is positive and equal to the contact pressure – excluding cohesion, which can introduce a negative normal stress until debonding of the bodies. In lack of contact, the normal stress σ_n is equal to zero since the bodies do not interact.

Both kinetic and mechanical conditions presented above are summarized in the following set of equations, known as Signorini's conditions of unilateral contact:

$$\begin{cases} \sigma_n \geq 0 \\ \Delta\underline{v}\cdot\underline{e}_n = 0 \\ \left(\Delta\underline{v}\cdot\underline{e}_n\right)\cdot\underline{\sigma}_n = 0 \end{cases} \tag{230}$$

The third relation above implies that the contact stress is equal to zero when the contact is lost (i.e. when $\Delta\underline{v}\cdot\underline{e}_n < 0$), and that the contact remains ($\Delta\underline{v}\cdot\underline{e}_n = 0$) when the pressure is maintained ($\sigma_n > 0$).

Signorini's conditions are illustrated on the following figure:

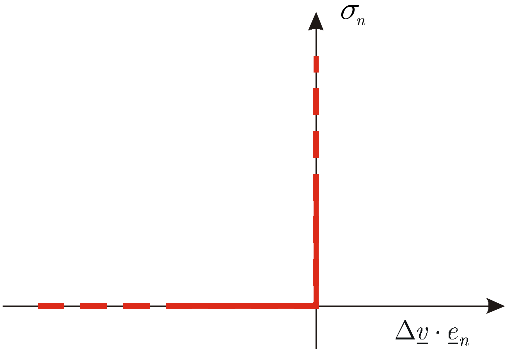

Figure 75: Accessible values (in red) according to Signorini's unilateral contact conditions

4.2. Some usual constitutive contact laws

4.2.1. Coulomb's model

The first contact law, maybe the most common one, is the Coulomb's law. The absolute value of friction $|\tau|$ is limited to a maximum value τ_c equal to:

$$\tau_c = \mu p + b \tag{231}$$

where μ is the friction coefficient, p the contact pressure and b the cohesion [CHA87].

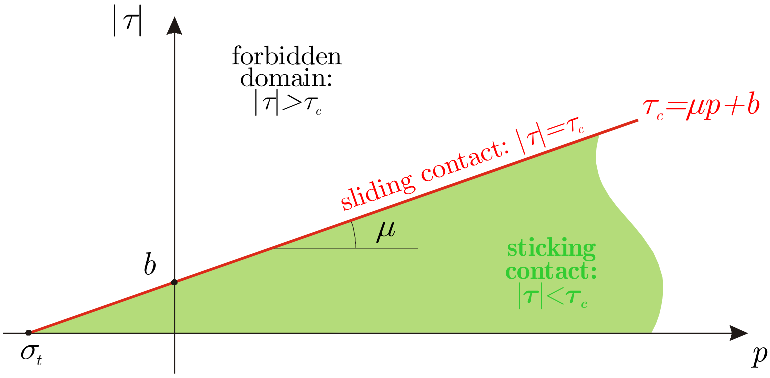

Figure 76: Coulomb's friction model

As long as the tangential loading is lower than the critical value τ_c, the contact is sticking: no relative displacement between the bodies in contact can be observed. When the critical value τ_c is reached, the bodies are sliding on each other and the friction τ_c is equal to τ_c. These observations are analogous to the elastoplasticity formalism with a surface of plasticity (sliding contact) containing the elastic domain (sticking contact). For this reason, the critical τ_c can be qualified of "threshold" tangential stress.

In lack of contact pressure, sliding occurs when the tangential stress $|\tau|$ reaches the value of b. To loose contact, the contact pressure p must be negative and equal to:

$$\sigma_t = -\frac{b}{\mu} \tag{232}$$

Assuming isotropic friction, the critical value τ_c does not depend on the direction of sliding.

In other respects, in continuous casting, the contact between the strand and the mould or the rolls is not characterized by any cohesion. For this reason, b will be neglected and the contact pressure is always positive (contact occurs) or equal to zero.

4.2.2. Limitation of the frictional threshold value

A local study of contact can lead to consider that the Coulomb's model should be limited in such a way that the stress state cannot transgress a yield criterion. This is especially true when then contact pressure reaches high values. Orowan studied that particular behaviour in the case of rolling [ORO45].

In fact, according to Coulomb's model (231), while the contact pressure becomes very high, friction can reach so high values that rough spots yield in the weakest material in contact. This phenomenon is like yielding of the contact surface. In such a case, the value of p and τ can be limited according to the following relation:

$$\sqrt{p^2 + 3\tau^2} \leq p_0 \tag{233}$$

which is the equation of an ellipse in the p-$|\tau|$ plane, as shown on Figure 77.

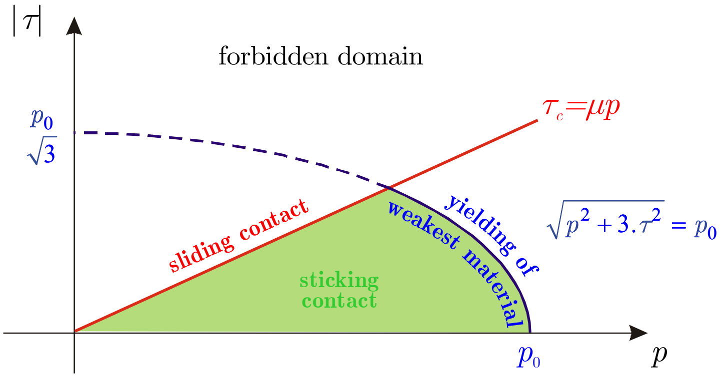

Figure 77: Limitation of Coulomb friction law

4.2.3. Tresca's model

In the Tresca's contact model, the threshold tangential stress τ_c is assumed to be a fraction of the maximal shear stress in the weakest material in contact [RAP98]:

$$\tau_c = m\frac{p_0}{\sqrt{3}} \quad \text{with} \quad 0 < m < 1 \tag{234}$$

If the contact is not frictional (perfectly lubricated surfaces), the coefficient m tends to zero. On the other hand, if m is equal to 1, the contact is sticking.

Tresca's contact model is thus:

$$\begin{cases} \tau < m\dfrac{p_0}{\sqrt{3}} & \text{sticking contact} \\ \tau = m\dfrac{p_0}{\sqrt{3}} & \text{sliding contact} \\ \tau > m\dfrac{p_0}{\sqrt{3}} & \text{impossible} \end{cases} \tag{235}$$

This model correspond to the presence of an interfacial material (layer in-between the bodies), the yield limit of which being mp_0.

4.2.4. Viscoplastic models: Norton-Hoff model

Coulomb and Tresca friction laws are based on threshold and flow notions: once a critical value τ_c is reached, the tangential stress τ remains equal to this value. This is analogous to plastic flow rule, the outside part of the "flow" surface remaining always not accessible.

In viscoplastic models [RAP98], the tangential stress τ can reach higher values than the threshold stress:

$$\begin{cases} \tau \leq \tau_c & \rightarrow \text{sticking contact} \\ \tau > \tau_c & \rightarrow \tau - \tau_c = \min\left(\alpha\dfrac{p_0}{\sqrt{3}}\left(\dfrac{|\underline{v}|}{u}\right)^n ; \dfrac{p_0}{\sqrt{3}}\right) \end{cases} \tag{236}$$

where α and n characterize the contact surfaces and the rheology of the material.

For example, here is the application of Norton-Hoff law, which is suitable for a pure viscoplastic behaviour (lubricants such oil …), i.e. no threshold value (τ_c=0):

$$\underline{\tau} = -\alpha K\left|\underline{v}\right|^n \frac{\underline{v}}{|\underline{v}|} = -\beta\left|\underline{v}\right|^n \frac{\underline{v}}{|\underline{v}|} \tag{237}$$

The main difficulty using such models is the determination of both β and n parameters.

4.3. Penalty technique

Both aspects of contact, mechanical or geometrical, can be privileged following one or another method of resolution. Geometrical aspect covers the non-penetration condition, while mechanical one concerns pressure and friction.

A first approach consists in giving the exact geometry regardless to contact conditions. Stresses are then deduced from imposed strain. This method is generally performed thanks to lagrangian multipliers. Its advantage is that the exact geometry is respected, but it introduces new degrees of freedom that are multipliers and it requires adapted algorithms.

In another approach, the right forces are applied on the solids and the geometry follows. The parts of the solids that penetrate into one another are rejected in order to respect, as well as possible, the non-penetration condition. This is the basis of the penalty technique.

Considering two bodies coming into contact, the distance d between them decrease to zero, then the contact pressure (thus σ_n) increase suddenly. From the numerical point of view, this phenomena is expressed by in an infinite value in the stiffness matrix of the system:

$$\begin{cases} \dfrac{\partial \sigma_n}{\partial d} = 0 \text{ until contact occurs} \\ \dfrac{\partial \sigma_n}{\partial d} \to \infty \text{ during contact} \end{cases} \tag{238}$$

To avoid numerical problems, it is convenient to admit a progressive interpenetration of the bodies, but penalizing it so that it remains as slight as possible. In case of penetration, a repulsive stress σ_p takes place in order to reject the body entering. This stress is proportional to the distance of penetration d:

$$\sigma_p = K_p d \tag{239}$$

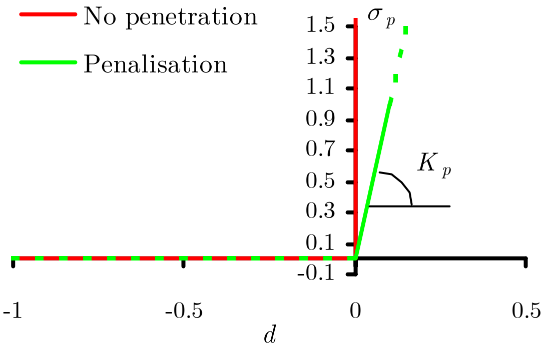

Figure 78: Penalisation of penetration

Another infinite term appears concerning sliding contact. Let e be the relative tangential displacement of two bodies in contact. If friction τ is lower than the critical value τ_c defined in section 4.2.1, no sliding e occurs. Friction can increase up to this critical value before any displacement can be measured. So, during sticking contact, the derivative of τ with respect to the displacement e is also infinite. At the opposite, once the friction reaches the critical value τ_c, sliding occurs and the displacement continues without any increase of friction. This is summarized on the figure hereafter:

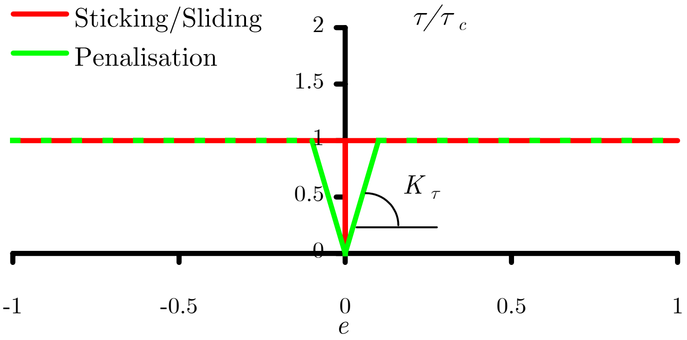

Figure 79: Penalisation of sticking contact

In a way, penalisation allows to consider penetration d as a reversible phenomenon (when contact pressure is removed, the penetration decreases and vanishes) and sliding e can be decomposed into a reversible part e^{rev} and an irreversible one e^{ir}:

$$\begin{cases} e = e^{rev} = \dfrac{\tau}{K_\tau} & \text{if } \tau < \tau_c \\ e = e^{rev} + e^{ir} = \dfrac{\tau_c}{K_\tau} + e^{ir} & \text{if } \tau = \tau_c \end{cases} \tag{240}$$

Now considering in local axes ($\underline{e}_n$, $\underline{e}_r$, $\underline{e}_s$) the relative displacement $\underline{u}$ of one body with respect to the second one, $\underline{u}$ can be decomposed in 3 components:

$$\underline{u} = \begin{Bmatrix} u \\ v \\ w \end{Bmatrix} = \begin{Bmatrix} u^{rev} \\ v^{rev} + v^{ir} \\ w^{rev} + w^{ir} \end{Bmatrix} \tag{241}$$

Dissipation of energy being linked to irreversible phenomena, it should be only dependent on sliding. The dissipation rate is thus:

$$\dot{D} = \tau_r \dot{v}^{ir} + \tau_s \dot{w}^{ir} \tag{242}$$

By analogy with plastic theory presented in section III.2.3, it is possible to define a "plastic" (i.e. contact) flow rule associated to (sliding) dissipation [CHA87,HRY91].

Using a associated flow rule linked to Coulomb's model (231), the pseudo-"strain rate" is normal to the "yield locus":

$$\dot{\varepsilon}_i^{ir} = \dot{\lambda} \frac{\partial f}{\partial \sigma_i} \tag{243}$$

where

$$f = \tau - \tau_c = \tau - \left(\mu \sigma_n + b\right) \tag{244}$$

When deriving (244) with respect to the normal stress (contact pressure):

$$\dot{\varepsilon}_n^{ir} = \dot{u}^{ir} = \dot{\lambda} \frac{\partial\left(\tau - \mu\sigma_n - b\right)}{\partial \sigma_n} \neq 0 \tag{245}$$

So, a flow rule associated to Coulomb's model leads to an irreversible penetration rate $\dot{u}^{ir}$, which is not coherent with physical basics of contact. It is thus necessary to use non-associated flow rule:

$$\dot{\varepsilon}_i^{ir} = \dot{\lambda} \frac{\partial g}{\partial \sigma_i} \tag{246}$$

where g is a function not depending on σ_n. For example, it can be:

$$g = |\tau| - b = \sqrt{\tau_r^2 + \tau_s^2} - b \tag{247}$$

With such a g function:

$$\underline{\dot{\varepsilon}}^{ir} = \dot{\lambda}\frac{\partial g}{\partial \underline{\sigma}} = \begin{Bmatrix} \dot{u}^{ir} \\ \dot{v}^{ir} \\ \dot{w}^{ir} \end{Bmatrix} = \begin{Bmatrix} 0 \\ \dot{\lambda}\dfrac{\tau_r}{|\tau|} \\ \dot{\lambda}\dfrac{\tau_s}{|\tau|} \end{Bmatrix} \tag{248}$$

The parameter λ provides the amplitude of the irreversible sliding. It can be used as an internal variable defining the contact state. During sliding, f hardens, but the consistency condition must be fulfilled:

$$\dot{f} = 0 \tag{249}$$

with f depending on "hardening":

$$f(\lambda) = |\tau| - \left[\mu(\lambda)\sigma_n + b(\lambda)\right] \tag{250}$$

Hence

$$\dot{f} = \frac{\partial f}{\partial \underline{\sigma}} \cdot \underline{\dot{\sigma}} + \frac{\partial f}{\partial \lambda}\dot{\lambda} = 0 \tag{251}$$

$$\leftrightarrow \dot{\lambda} = -\frac{\partial \lambda}{\partial f}\left(\frac{\partial f}{\partial \underline{\sigma}} \cdot \underline{\dot{\sigma}}\right) = -\frac{\partial \lambda}{\partial f}\left(\frac{\partial f}{\partial \sigma_n}\dot{\sigma}_n + \frac{\partial f}{\partial \tau_r}\dot{\tau}_r + \frac{\partial f}{\partial \tau_s}\dot{\tau}_s\right) \tag{252}$$

Introducing $\dot{\lambda}$ in relation (248):

$$\begin{aligned} \dot{v}^{ir} &= \dot{\lambda}\frac{\tau_r}{|\tau|} = -\frac{\partial \lambda}{\partial f}\left(\frac{\partial f}{\partial \sigma_n}\dot{\sigma}_n + \frac{\partial f}{\partial \tau_r}\dot{\tau}_r + \frac{\partial f}{\partial \tau_s}\dot{\tau}_s\right)\frac{\tau_r}{|\tau|} \\ &= -\frac{1}{-\left[\dfrac{\partial \mu}{\partial \lambda}\sigma_n + \dfrac{\partial b}{\partial \lambda}\right]}\left(-\mu\dot{\sigma}_n + \frac{\tau_r}{|\tau|}\dot{\tau}_r + \frac{\tau_s}{|\tau|}\dot{\tau}_s\right)\frac{\tau_r}{|\tau|} \\ &= \frac{1}{\mu'\sigma_n + b'}\left(\frac{\tau_r\dot{\tau}_r + \tau_s\dot{\tau}_s}{|\tau|} - \mu\dot{\sigma}_n\right)\frac{\tau_r}{|\tau|} \\ &= \frac{1}{f'(\lambda)}\left(\frac{\tau_r\dot{\tau}_r + \tau_s\dot{\tau}_s}{|\tau|} - \mu\dot{\sigma}_n\right)\frac{\tau_r}{|\tau|} \end{aligned} \tag{253}$$

where $f'(\lambda) = \dfrac{\partial f(\lambda)}{\partial \lambda}$

In the same way:

$$\dot{w}^{ir} = \frac{1}{f'}\left(\frac{\tau_r\dot{\tau}_r + \tau_s\dot{\tau}_s}{|\tau|} - \mu\dot{\sigma}_n\right)\frac{\tau_s}{|\tau|} \tag{254}$$

So that (248) becomes:

$$\underline{\dot{\varepsilon}}^{ir} = \begin{Bmatrix} \dot{u}^{ir} \\ \dot{v}^{ir} \\ \dot{w}^{ir} \end{Bmatrix} = \frac{1}{f'} \begin{pmatrix} 0 & 0 & 0 \\ -\mu \frac{\tau_r}{|\tau|} & \frac{\tau_r^2}{|\tau|^2} & \frac{\tau_r \tau_s}{|\tau|^2} \\ -\mu \frac{\tau_s}{|\tau|} & \frac{\tau_r \tau_s}{|\tau|^2} & \frac{\tau_s^2}{|\tau|^2} \end{pmatrix} \begin{Bmatrix} \dot{\sigma}_n \\ \dot{\tau}_r \\ \dot{\tau}_s \end{Bmatrix} \tag{255}$$

And

$$\begin{aligned} \underline{\dot{\varepsilon}} = \begin{Bmatrix} \dot{u}^{rev} + \dot{u}^{ir} \\ \dot{v}^{rev} + \dot{v}^{ir} \\ \dot{w}^{rev} + \dot{w}^{ir} \end{Bmatrix} &= \begin{Bmatrix} \frac{\dot{\sigma}_n}{K_p} \\ \frac{\dot{\tau}_r}{K_\tau} \\ \frac{\dot{\tau}_s}{K_\tau} \end{Bmatrix} + \frac{\alpha}{f'} \begin{pmatrix} 0 & 0 & 0 \\ -\mu \frac{\tau_r}{|\tau|} & \frac{\tau_r^2}{|\tau|^2} & \frac{\tau_r \tau_s}{|\tau|^2} \\ -\mu \frac{\tau_s}{|\tau|} & \frac{\tau_r \tau_s}{|\tau|^2} & \frac{\tau_s^2}{|\tau|^2} \end{pmatrix} \begin{Bmatrix} \dot{\sigma}_n \\ \dot{\tau}_r \\ \dot{\tau}_s \end{Bmatrix} \\ &= \begin{pmatrix} \frac{1}{K_p} & 0 & 0 \\ -\frac{\alpha\mu}{f'} \frac{\tau_r}{|\tau|} & \frac{1}{K_\tau} + \frac{\alpha}{f'} \frac{\tau_r^2}{|\tau|^2} & \frac{\alpha}{f'} \frac{\tau_r \tau_s}{|\tau|^2} \\ -\frac{\alpha\mu}{f'} \frac{\tau_s}{|\tau|} & \frac{\alpha}{f'} \frac{\tau_r \tau_s}{|\tau|^2} & \frac{1}{K_\tau} + \frac{\alpha}{f'} \frac{\tau_s^2}{|\tau|^2} \end{pmatrix} \begin{Bmatrix} \dot{\sigma}_n \\ \dot{\tau}_r \\ \dot{\tau}_s \end{Bmatrix} \\ &= \underline{D}\underline{\dot{\sigma}} \end{aligned} \tag{256}$$

where

$$\begin{cases} \alpha = 0 & \text{if } |\tau| < \tau_c \\ \alpha = 1 & \text{if } |\tau| = \tau_c \end{cases} \tag{257}$$

Time integration of contact stress tensor can be achieved inverting the matrix $\underline{D}$. Its determinant is equal to:

$$\begin{aligned} |\underline{D}| &= \frac{1}{K_p} \left[\left(\frac{1}{K_\tau} + \frac{\alpha}{f'} \frac{\tau_r^2}{|\tau|^2} \right) \left(\frac{1}{K_\tau} + \frac{\alpha}{f'} \frac{\tau_s^2}{|\tau|^2} \right) - \frac{\alpha}{f'} \frac{\tau_r \tau_s}{|\tau|^2} \frac{\alpha}{f'} \frac{\tau_r \tau_s}{|\tau|^2} \right] \\ &= \frac{1}{K_p} \left[\frac{1}{K_\tau^2} + \frac{1}{K_\tau} \frac{\alpha}{f'} \frac{\tau_r^2}{|\tau|^2} + \frac{1}{K_\tau} \frac{\alpha}{f'} \frac{\tau_s^2}{|\tau|^2} \right] \\ &= \frac{1}{K_p} \frac{1}{K_\tau^2} \left[1 + \frac{\alpha K_\tau}{f'} \frac{\tau_r^2 + \tau_s^2}{|\tau|^2} \right] \\ &= \frac{f' + \alpha K_\tau}{K_p K_\tau^2 f'} \end{aligned} \tag{258}$$

The inverse of matrix D can be computed and one arrives to:

$$\underline{D}^{-1} = \frac{K_p K_\tau^2 f'}{f' + \alpha K_\tau} \begin{pmatrix} \frac{f' + \alpha K_\tau}{K_\tau^2 f'} & 0 & 0 \\ \frac{1}{K_\tau} \frac{\alpha\mu}{f'} \frac{\tau_r}{|\tau|} & \frac{1}{K_p}\left(\frac{1}{K_\tau} + \frac{\alpha}{f'} \frac{\tau_s^2}{|\tau|^2} \right) & -\frac{1}{K_p} \frac{\alpha}{f'} \frac{\tau_r \tau_s}{|\tau|^2} \\ \frac{1}{K_\tau} \frac{\alpha\mu}{f'} \frac{\tau_s}{|\tau|} & -\frac{1}{K_p} \frac{\alpha}{f'} \frac{\tau_r \tau_s}{|\tau|^2} & \frac{1}{K_p}\left(\frac{1}{K_\tau} + \frac{\alpha}{f'} \frac{\tau_r^2}{|\tau|^2} \right) \end{pmatrix} \tag{259}$$

Let $X = \frac{f' + \alpha K_\tau}{K_\tau}$, so that

$$\underline{D}^{-1} = \frac{K_p K_\tau f'}{X} \begin{pmatrix} \frac{X}{K_\tau f'} & 0 & 0 \\ \frac{1}{K_\tau} \frac{\alpha\mu}{f'} \frac{\tau_r}{|\tau|} & \frac{1}{K_p}\left(\frac{1}{K_\tau} + \frac{\alpha}{f'} \frac{\tau_s^2}{|\tau|^2} \right) & -\frac{1}{K_p} \frac{\alpha}{f'} \frac{\tau_r \tau_s}{|\tau|^2} \\ \frac{1}{K_\tau} \frac{\alpha\mu}{f'} \frac{\tau_s}{|\tau|} & -\frac{1}{K_p} \frac{\alpha}{f'} \frac{\tau_r \tau_s}{|\tau|^2} & \frac{1}{K_p}\left(\frac{1}{K_\tau} + \frac{\alpha}{f'} \frac{\tau_r^2}{|\tau|^2} \right) \end{pmatrix} \tag{260}$$

$$= \begin{pmatrix} K_p & 0 & 0 \\ K_p \frac{\alpha\mu}{X} \frac{\tau_r}{|\tau|} & \frac{f'}{X} + K_\tau \frac{\alpha}{X} \frac{\tau_s^2}{|\tau|^2} & -K_\tau \frac{\alpha}{X} \frac{\tau_r \tau_s}{|\tau|^2} \\ K_p \frac{\alpha\mu}{X} \frac{\tau_s}{|\tau|} & -K_\tau \frac{\alpha}{X} \frac{\tau_r \tau_s}{|\tau|^2} & \frac{f'}{X} + K_\tau \frac{\alpha}{X} \frac{\tau_r^2}{|\tau|^2} \end{pmatrix}$$

And

$$\begin{Bmatrix} \sigma_n \\ \tau_r \\ \tau_s \end{Bmatrix} = \begin{pmatrix} K_p & 0 & 0 \\ K_p \frac{\alpha\mu}{X} \frac{\tau_r}{|\tau|} & \frac{f'}{X} + K_\tau \frac{\alpha}{X} \frac{\tau_s^2}{|\tau|^2} & -K_\tau \frac{\alpha}{X} \frac{\tau_r \tau_s}{|\tau|^2} \\ K_p \frac{\alpha\mu}{X} \frac{\tau_s}{|\tau|} & -K_\tau \frac{\alpha}{X} \frac{\tau_r \tau_s}{|\tau|^2} & \frac{f'}{X} + K_\tau \frac{\alpha}{X} \frac{\tau_r^2}{|\tau|^2} \end{pmatrix} \begin{Bmatrix} \dot{u} \\ \dot{v} \\ \dot{w} \end{Bmatrix} \tag{261}$$

The dependence of f with respect to λ expresses the dependence of the contact law (relation between friction τ and contact pressure σ_n) with respect to “plasticity”. If this dependence exists, it means that friction coefficient μ and/or cohesion b are evolving during plasticity (for Coulomb’s model). This phenomenon would be analogous to hardening (or softening) in classical theory of plasticity. Softening is observed when the contact surface is in evolution during sliding, because of wear for example. Hardening can happen in some materials (soil mechanics) or in case of modifications in the lubricant layer (thickness, viscosity, temperature, velocity …).

In the present model of continuous casting, neither hardening nor softening is taken into account ($f' = \frac{\partial f(\lambda)}{\partial \lambda} = 0$), so that $X = \alpha$ and:

$$\begin{Bmatrix} \sigma_n \\ \tau_r \\ \tau_s \end{Bmatrix} = \begin{pmatrix} K_p & 0 & 0 \\ K_p \mu \frac{\tau_r}{|\tau|} & K_\tau \frac{\tau_s^2}{|\tau|^2} & -K_\tau \frac{\tau_r \tau_s}{|\tau|^2} \\ K_p \mu \frac{\tau_s}{|\tau|} & -K_\tau \frac{\tau_r \tau_s}{|\tau|^2} & K_\tau \frac{\tau_r^2}{|\tau|^2} \end{pmatrix} \begin{Bmatrix} \dot{u} \\ \dot{v} \\ \dot{w} \end{Bmatrix} \tag{262}$$

4.4. Contact element

The element is defined by 2 or 3 nodes, which are conventionally numbered from the first to the last when the solid is on the left and its foundation (a tool or another solid) is on its right. As the model is in 2D½, a 2D friction law could appear to be sufficient. However, in order to introduce extraction force in the model, the integration of friction in the out-of-plane direction is necessary. Thus, the 3D Coulomb friction law is associated to the contact element: the in-plane stresses – called σ_n and τ_r in the above section – are integrated as explained hereafter, while the out-of-plane friction is integrated to determine the nodal forces applied on the degrees of freedom of the generalized plane strain state.

Local axes are defined as follows: $\underline{e}_u$ is the internal normal to the solid and $\underline{e}_v$ is tangential to the surface and oriented from the first to the third node:

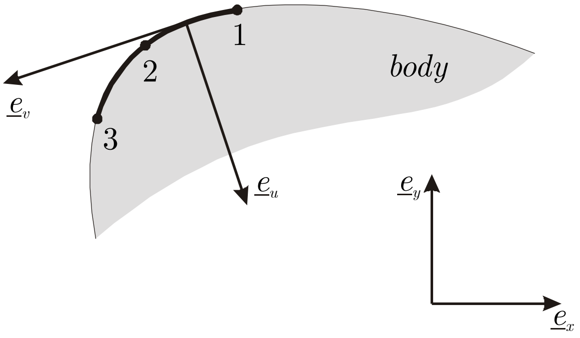

Figure 80: Local axes for contact element.

Let $N_{i = 1,2,3}$ be interpolation function of node *i*. For a three nodes element, we have:

$$\begin{cases} N_1 = \frac{1}{2}\xi(\xi - 1) & \text{for node 1 (x=-1)} \\ N_2 = 1 - \xi^2 & \text{for node 2 } (\xi = 0) \\ N_3 = \frac{1}{2}\xi(\xi + 1) & \text{for node 3 } (\xi = +1) \end{cases} \tag{263}$$

and

$$\begin{cases} x_\xi = N_{i,\xi} x_i \\ y_\xi = N_{i,\xi} y_i \end{cases} \tag{264}$$

The rotation matrix R is:

$$\begin{Bmatrix} e_u \\ e_v \end{Bmatrix} = \frac{1}{s_\xi} \begin{pmatrix} -y_\xi & x_\xi \\ x_\xi & y_\xi \end{pmatrix} \begin{Bmatrix} e_x \\ e_y \end{Bmatrix} = R \begin{Bmatrix} e_x \\ e_y \end{Bmatrix} \tag{265}$$

with

$$s_\xi = \sqrt{x_\xi^2 + y_\xi^2} \tag{266}$$

In corotational formalism, contact stresses (σ_n and τ_r) and velocities ($\dot{u}\,\text{and}\,\dot{v}$) are expressed in the local axes.

The coordinates of the nodes of the foundation (mould or roll according to the position of the slice) are noted with "*f*" superscript:

$$\begin{cases} x^f = N_i(\xi) x_i^f \\ y^f = N_i(\xi) y_i^f \end{cases} \quad i = 1 \rightarrow 3 \tag{267}$$

4.4.1. Distance between the solid and the foundation

The contact occurrence depends on the distance between the solid and the foundation. The distance from any point at the surface of the solid (x^s, y^s) to the foundation is measured normally to the surface of the solid. The first thing to determine is the coordinates of the intersection between this normal and the foundation surface:

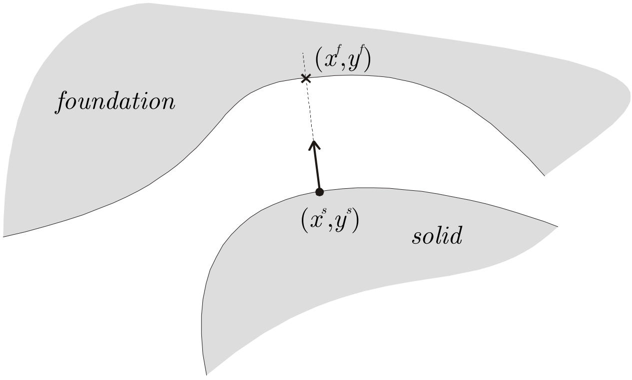

Figure 81: Research for the distance from a point at surface of the solid to the foundation.

The equation of the normal to the surface is given by:

$$\frac{x - x^s}{y_\xi} - \frac{y - y^s}{x_\xi} = 0 \tag{268}$$

The equation of a parabolic segment of the foundation is:

$$\begin{cases} x^f = \dfrac{x_1^f - 2x_2^f + x_3^f}{2}\xi^2 + \dfrac{x_3^f - x_1^f}{2}\xi + x_2^f \\ y^f = \dfrac{y_1^f - 2y_2^f + y_3^f}{2}\xi^2 + \dfrac{y_3^f - y_1^f}{2}\xi + y_2^f \end{cases} \tag{269}$$

The intersection (x^f,y^f) is located on both:

$$x_\xi\left(x^f - x^s\right) - y_\xi\left(y^f - y^s\right) = 0 \tag{270}$$

Let $DX = \dfrac{x_\xi}{s_\xi}$ and $DY = \dfrac{y_\xi}{s_\xi}$. The equation to solve becomes:

$$\begin{aligned}&\left(\frac{x_1^f - 2x_2^f + x_3^f}{2}DX - \frac{y_1^f - 2y_2^f + y_3^f}{2}DY\right)\xi^2\\&+\left(\frac{x_3^f - x_1^f}{2}DX - \frac{y_3^f - y_1^f}{2}DY\right)\xi + \left[\left(x_2^f - x^s\right)DX - \left(y_2^f - y^s\right)DY\right] = 0\end{aligned} \tag{271}$$

which is a second order polynomial equation, the type of which is $a.\xi^2 + b.\xi + c = 0$. The solution is thus given by:

$$\begin{cases}\xi = \dfrac{-b \pm \sqrt{b^2 - 4ac}}{2a} & \text{if } a \neq 0 \text{ and } b^2 - 4ac > 0\\ \xi = -\dfrac{\mathrm{c}}{\mathrm{b}} & \text{if } a = 0\\ \text{no solution} & \text{if } a \neq 0 \text{ and } b^2 - 4ac < 0\end{cases} \tag{272}$$

The third case corresponds to lack of intersection between the normal and the considered segment of foundation (see Figure 82).

Moreover, the intersection occurs only if it is between nodes 1 and 3, in other words if the solution is $-1 \leq \xi \leq +1$.

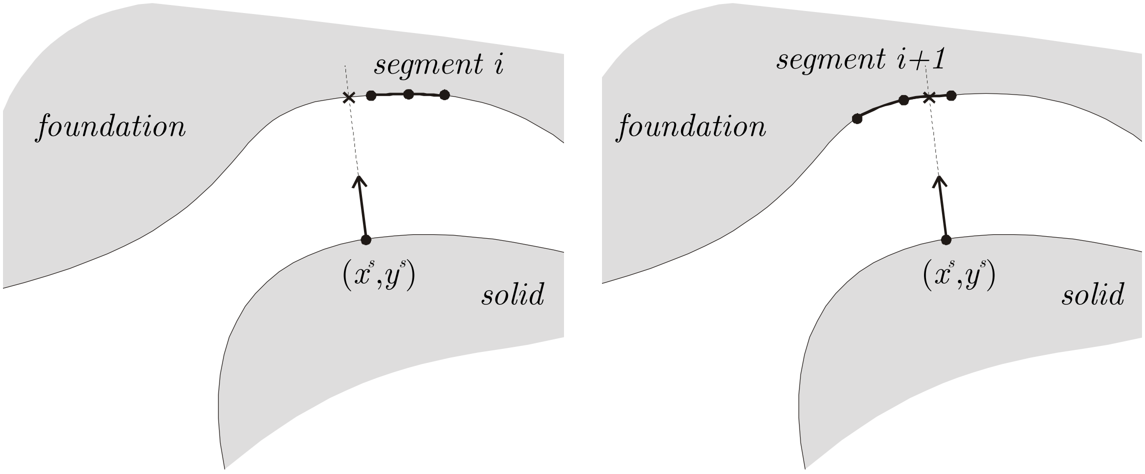

Figure 82: No intersection with segment i, but segment i+1

Once the intersection is determined, the distance can be computed:

$$d = -\left(x^f - x^s\right)DY + \left(y^f - y^s\right)DX \tag{273}$$

4.4.2. Virtual work

The virtual work during contact (including friction) is:

$$\delta w = \int \underline{\sigma} \cdot \delta \underline{\varepsilon} \; d\delta = \int \begin{bmatrix} \sigma_n & \tau_r \end{bmatrix} \begin{bmatrix} \delta d \\ \delta v \end{bmatrix} d\delta \tag{274}$$

with

$$\begin{cases} \delta d = -\left(\delta x^f - \delta x^s\right) DY + \left(\delta y^f - \delta y^s\right) DX \\ \delta v = \left(\delta x^f - \delta x^s\right) DX + \left(\delta y^f - \delta y^s\right) DY \end{cases} \tag{275}$$

Only $\dot{v}$ and δv are known and v cannot be determined for large strain problems. For the solid:

$$\begin{cases} \delta x^s = N_i\left(\xi^s\right) \delta x_i^s \\ \delta y^s = N_i\left(\xi^s\right) \delta y_i^s \end{cases} \tag{276}$$

and for the foundation:

$$\begin{cases} \delta x^f = N_i\left(\xi^f\right) \delta x_i^f \\ \delta y^f = N_i\left(\xi^f\right) \delta y_i^f \end{cases} \tag{277}$$

So that we can split virtual work into solid part and foundation part:

$$\begin{cases} \delta w^s = \left(\int\limits_S \left(\sigma_n DY - \tau_r DX\right) N_i\left(\xi^s\right) dS \right) \delta x_i^s + \left(\int\limits_S \left(-\sigma_n DX - \tau_r DY\right) N_i\left(\xi^s\right) dS \right) \delta y_i^s \\ \delta w^f = \left(\int\limits_f \left(-\sigma_n DY + \tau_r DX\right) N_i\left(\xi^f\right) dS \right) \delta x_i^f + \left(\int\limits_f \left(\sigma_n DX + \tau_r DY\right) N_i\left(\xi^f\right) dS \right) \delta y_i^f \end{cases} \tag{278}$$

4.4.3. Gauss integration

Integration of a function f in the 1D space (ξ) is given by:

$$\int\limits_S f \;\, dS = \int\limits_{-1}^{1} f \left|J\right| e \;\, d\xi \tag{279}$$

where e is the thickness of the studied 2D solid and $|J|$ the determinant of the jacobian matrix of the transformation $(x,y) \rightarrow \xi$, which is:

$$\left|J\right| = \sqrt{x_\xi^2 + y_\xi^2} = s_\xi \tag{280}$$

Classically, the integration is computed numerically, using a two or three integration points of Gauss scheme. So the integral is:

$$\int\limits_S f \;\, dS = \sum_{PI} f \left|J\right| e W_{GAUSS} = \sum_{PI} f s_\xi e W_{GAUSS} \tag{281}$$

4.5. Stiffness matrix

The easier way to determine stiffness matrix is to derive nodal forces:

$$\begin{cases} dF_x^i = \underbrace{\sum_{IP}\left(d\sigma_n y_\xi - d\tau_r x_\xi\right) N_i e W}_{\text{classical matrix}\, dF_{x,y}^{Hi}} + \underbrace{\sum_{IP}\left(\sigma_n dy_\xi - \tau_r dx_\xi\right) N_i e W}_{\text{stress matrix}\ dF_{x,y}^{ci}} \\ dF_y^i = \sum_{IP}\left(-d\sigma_n x_\xi - d\tau_r y_\xi\right) N_i e W + \sum_{IP}\left(-\sigma_n dx_\xi - \tau_r dy_\xi\right) N_i e W \end{cases} \tag{282}$$

where e is the thickness of the 2D studied problem and w the weight of Gauss integration.

To develop stress matrix $dF_{x,y}^{ci}$, we have:

$$\begin{cases} x_\xi = N_{j,\xi} x_j \\ dx_\xi = N_{j,\xi} dx_j \\ dy_\xi = N_{j,\xi} dy_j \end{cases} \tag{283}$$

So that:

$$\begin{cases} dF_x^{ci} = -\sum_{IP} \tau_r N_{j,\xi} N_i e W dx_j + \sum_{IP} \sigma_n N_{j,\xi} N_i e W dy_j \\ dF_y^{ci} = -\sum_{IP} \sigma_n N_{j,\xi} N_i e W dx_j - \sum_{IP} \tau_r N_{j,\xi} N_i e W dy_j \end{cases} \tag{284}$$

In tensorial formalism, we obtain:

$$\begin{Bmatrix} dF_x^{ci} \\ dF_y^{ci} \end{Bmatrix} = \sum_{IP} \begin{pmatrix} -\tau_r & \sigma_n \\ -\sigma_n & -\tau_r \end{pmatrix} N_i N_{j,\xi} e W \begin{Bmatrix} dx_j \\ dy_j \end{Bmatrix} \tag{285}$$

For the classical matrix $dF_{x,y}^{Hi}$, we can write that:

$$\underline{\dot{\sigma}} = \begin{Bmatrix} \dot{\sigma}_n \\ \dot{\tau} \end{Bmatrix} = \underline{D} \begin{Bmatrix} \dot{u} \\ \dot{v} \end{Bmatrix} = \underline{D}\underline{\dot{\varepsilon}} \tag{286}$$

The shape of the matrix $\underline{D}$ being (cf. relation (262)):

$$\underline{D} = \begin{pmatrix} D_{uu} & D_{uv} \\ D_{vu} & D_{vv} \end{pmatrix} = \begin{pmatrix} D_{uu} & 0 \\ D_{vu} & D_{vv} \end{pmatrix} \tag{287}$$

Considering that relation (286) between rates is also available between small variations:

$$\partial\underline{\sigma} = \begin{Bmatrix} \partial\sigma_n \\ \tau \end{Bmatrix} = \underline{D} \begin{Bmatrix} \partial d \\ \partial v \end{Bmatrix} = \underline{D}\partial\underline{\varepsilon} \tag{288}$$

Since

$$\begin{cases} \partial d = DY\partial x^s - DX\partial y^s \\ \partial v = -DX\partial x^s - DY\partial y^s \end{cases} \quad \text{or} \quad \partial\underline{\varepsilon} = \begin{Bmatrix} \partial d \\ \partial v \end{Bmatrix} = \frac{1}{s_\xi} \begin{pmatrix} -y_\xi & x_\xi \\ y_\xi & y_\xi \end{pmatrix} \begin{Bmatrix} \partial x^s \\ \partial y^s \end{Bmatrix} \tag{289}$$

(288) becomes

$$\begin{aligned}\begin{Bmatrix} d\sigma_n \\ d\tau \end{Bmatrix} &= \underline{D}\begin{Bmatrix} du \\ dv \end{Bmatrix} = \underline{DR}\begin{Bmatrix} dx \\ dy \end{Bmatrix} = \begin{pmatrix} D_{uu} & 0 \\ D_{vu} & D_{vv} \end{pmatrix}\frac{1}{s_\xi}\begin{pmatrix} -y_\xi & x_\xi \\ x_\xi & y_\xi \end{pmatrix}\begin{Bmatrix} dx \\ dy \end{Bmatrix} \\ &= \frac{1}{s_\xi}\begin{pmatrix} -D_{uu}y_\xi & D_{uu}x_\xi \\ -D_{vu}\cdot y_\xi + D_{vv}\cdot x_\xi & D_{vu}\cdot x_\xi + D_{vv}\cdot y_\xi \end{pmatrix}\begin{Bmatrix} dx \\ dy \end{Bmatrix}\end{aligned} \tag{290}$$

We know that:

$$\begin{Bmatrix} dF_x^{Hi} \\ dF_y^{Hi} \end{Bmatrix} = \sum_{PI}\begin{pmatrix} -y_\xi & x_\xi \\ x_\xi & y_\xi \end{pmatrix}\begin{Bmatrix} d\sigma_n \\ d\tau_r \end{Bmatrix} N_i eW = \sum_{PI} s_\xi \begin{pmatrix} -DY & DX \\ DX & DY \end{pmatrix}\begin{Bmatrix} d\sigma_n \\ d\tau_r \end{Bmatrix} N_i eW \tag{291}$$

and introducing (290):

$$\begin{aligned}\begin{Bmatrix} dF_x^{Hi} \\ dF_y^{Hi} \end{Bmatrix} &= \sum_{PI} s_\xi \begin{pmatrix} -DY & DX \\ DX & DY \end{pmatrix}\frac{1}{s_\xi}\begin{pmatrix} -D_{uu}y_\xi & D_{uu}x_\xi \\ -D_{vu}y_\xi + D_{vv}x_\xi & D_{vu}x_\xi + D_{vv}y_\xi \end{pmatrix}\begin{Bmatrix} dx \\ dy \end{Bmatrix} N_i eW \\ &= \sum_{PI}\frac{s_\xi N_i eW}{s_\xi^2}\begin{pmatrix} C_{xx} & C_{xy} \\ C_{yx} & C_{yy} \end{pmatrix}\begin{Bmatrix} dx \\ dy \end{Bmatrix}\end{aligned} \tag{292}$$

where

$$\begin{cases} C_{xx} = D_{uu}y_\xi^2 - D_{vu}y_\xi x_\xi + D_{vv}x_\xi^2 \\ C_{xy} = -D_{uu}x_\xi y_\xi + D_{vu}x_\xi^2 + D_{vv}x_\xi y_\xi \\ C_{yx} = -D_{uu}x_\xi y_\xi - D_{vu}y_\xi^2 + D_{vv}x_\xi y_\xi \\ C_{yy} = D_{uu}x_\xi^2 + D_{vu}x_\xi y_\xi + D_{vv}y_\xi^2 \end{cases} \tag{293}$$

Using isoparametric relation for nodes coordinates:

$$\begin{cases} dx = N_j dx_j \\ dy = N_j dy_j \end{cases} \tag{294}$$

Finally:

$$\begin{Bmatrix} dF_x^{Hi} \\ dF_y^{Hi} \end{Bmatrix} = \sum_{PI}\frac{N_i N_j eW}{s_\xi}\begin{pmatrix} C_{xx} & C_{xy} \\ C_{yx} & C_{yy} \end{pmatrix}\begin{Bmatrix} dx_j \\ dy_j \end{Bmatrix} \tag{295}$$

and

$$\begin{Bmatrix} dF_x \\ dF_y \end{Bmatrix} = \begin{Bmatrix} dF_x^{ci} \\ dF_y^{ci} \end{Bmatrix} + \begin{Bmatrix} dF_x^{Hi} \\ dF_y^{Hi} \end{Bmatrix} = \sum_{PI} N_i N_j eW \left[\begin{pmatrix} -\tau_r & \sigma_n \\ -\sigma_n & -\tau_r \end{pmatrix} + \frac{1}{s_\xi}\begin{pmatrix} C_{xx} & C_{xy} \\ C_{yx} & C_{yy} \end{pmatrix}\right]\begin{Bmatrix} dx_j \\ dy_j \end{Bmatrix} \tag{296}$$

IV. Thermal-mechanical coupling: Staggered analysis

IV. Thermal-mechanical coupling: Staggered analysis

Casting processes – continuous or not – involve many physical phenomena: heat transfer, phase transformation, stress development, fluid flow, electromagnetic force… that are not trivial to model. Even if each phenomenon can be approached by more or less complex models, one cannot ignore the numerous couplings between the involved disciplines: thermal analysis, metallurgy, solid and fluid mechanics, electromagnetism.

In the present model, only thermal and (solid) mechanical aspects are taken into account. The problem is expressed in terms of a Galerkin finite element discrete projection in space and a time marching scheme for the evolution of the primary nodal variables (displacements and temperatures). That means that an infinite-dimensional transient system – the steel strand and its surroundings – is modelled by a sequence of discrete nonlinear equations, the solution of which provides the evolution of internal variables (strains, stresses…). Two types of strategies can perform this spatiotemporal discretization:

- Simultaneous time-stepping algorithms solve both thermal and mechanical equilibrium equations together, thus advancing primary nodal variables simultaneously. These algorithms are characterized by large and unsymmetrical systems of equations. They also require the implementation of coupling terms in constitutive laws and the stiffness matrix. Moreover, it is not possible to take advantage of the time scales involved in the mechanical and the thermal parts (generally different).
- Staggered time-stepping algorithms split the system into smaller sub-problems. In the present model, a first one governs mechanical evolution and a second one the thermal aspects. The two sub-problems are thus evolving separately with different time steps if necessary and the system of equations is easier to solve, since coupling terms between displacements and temperature evolution are not taken into account.

Even if simultaneous time-stepping algorithm was already implemented in the LAGAMINE code [HAB89] (as well as coupled thermo-mechanical constitutive laws), a new staggered time-stepping algorithm has been used. The applied time-stepping scheme is described on the following figure:

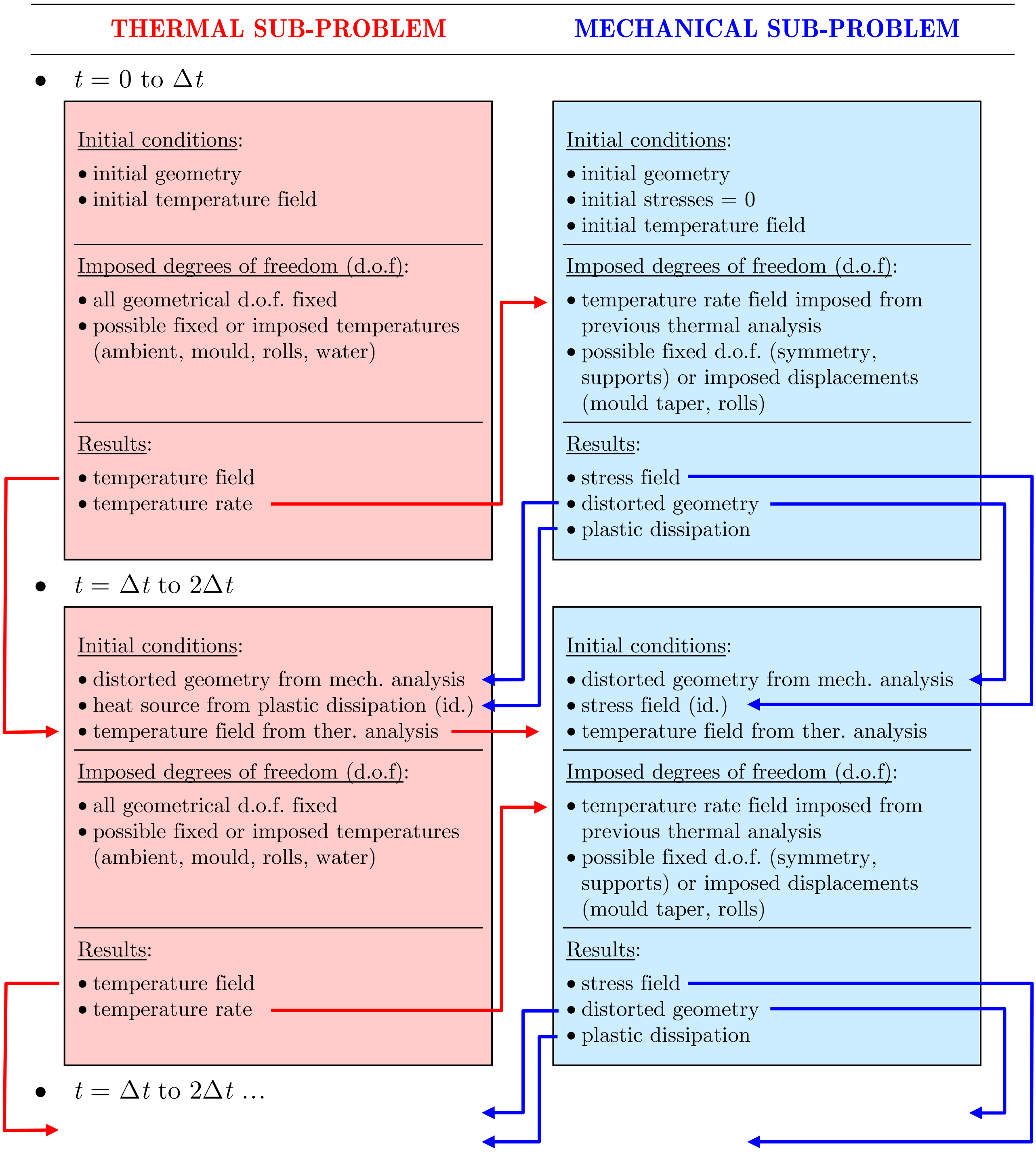

Figure 83: Staggered time-stepping algorithm

As it can be noticed, mechanical and thermal evolutions are not completely separated. The evolution of the temperature field is taken into account in the mechanical sub-problem and the distortion of the material in the thermal one as well as heat generation by plastic dissipation.

Time scale is divided into intervals Δt. At the end of each interval, information about thermal and mechanical evolutions is exchanged between sub-problems. At this stage in the development of the model, each time interval Δt is computed only one time for each thermal and mechanical sub-problems. Ideally, iterations for each interval should be performed in order to make the solution more accurate. In lack of such iterations, the geometry used in the thermal analysis at the i^{th} interval is fixed and equal to its configuration at the end of the previous mechanical interval (i–1), since its evolution is not yet known for the actual one (i).

Previously, this staggered scheme had been developed for rolling modelling with the LAGAMINE code, but the dominant thermomechanical coupling in that case was the heat due to plastic dissipation and the evolution of contact zones (thus geometry of the problem). It was therefore natural to consider first the mechanical aspect before to compute thermal evolution.

At the opposite, the dominant thermomechanical coupling in continuous casting is the thermal shrinkage. For this reason, the sequence of computation has been inverted with respect to what it was before (mechanical, then thermal), so that it begins now with thermal analysis followed by mechanical one (see Figure 83). This simple modification made the model much more stable, especially for the first steps of mechanical computation. Previously, the situation was in fact the following:

Consider a node on the surface of the strand in contact with the mould. If the staggered time-stepping scheme begins with mechanical analysis, heat flow equation for the i$^{\text{th}}$ interval has not yet been solved and thus the temperature evolution is unknown. For the very first step, no information about temperature rate being available, the most logical assumption is to consider that temperature remains constant. Calling $T^A_{1,mech}$ the temperature at the beginning (^{A}) of the first mechanical interval ($_{1,mech}$) and $T^B_{1,mech}$ the one at the end (^{B}), one have:

$$T^A_{1,mech} = T^B_{1,mech} = \bar{T}_{ini} \tag{297}$$

Since the temperature is constant during the first interval, no thermal shrinkage appears. Then, the thermal sub-problem is run providing the temperature at the end of the first thermal interval $T^B_{1,ther}$. The second mechanical interval is then computed, assuming that the temperature at the beginning is equal the one at the end of the previous thermal interval:

$$T^A_{2,mech} = T^B_{1,mech} \tag{298}$$

and that temperature rate is identical to the one of the previous thermal interval:

$$\dot{T}_{2,mech} = \frac{T^B_{1,mech} - T^A_{1,mech}}{\Delta t} \tag{299}$$

Then, the second thermal interval is computed and so on…

In the typical case of a hot body (steel strand) in contact with a cold surface (the mould), the temperature evolution is approximately as follows:

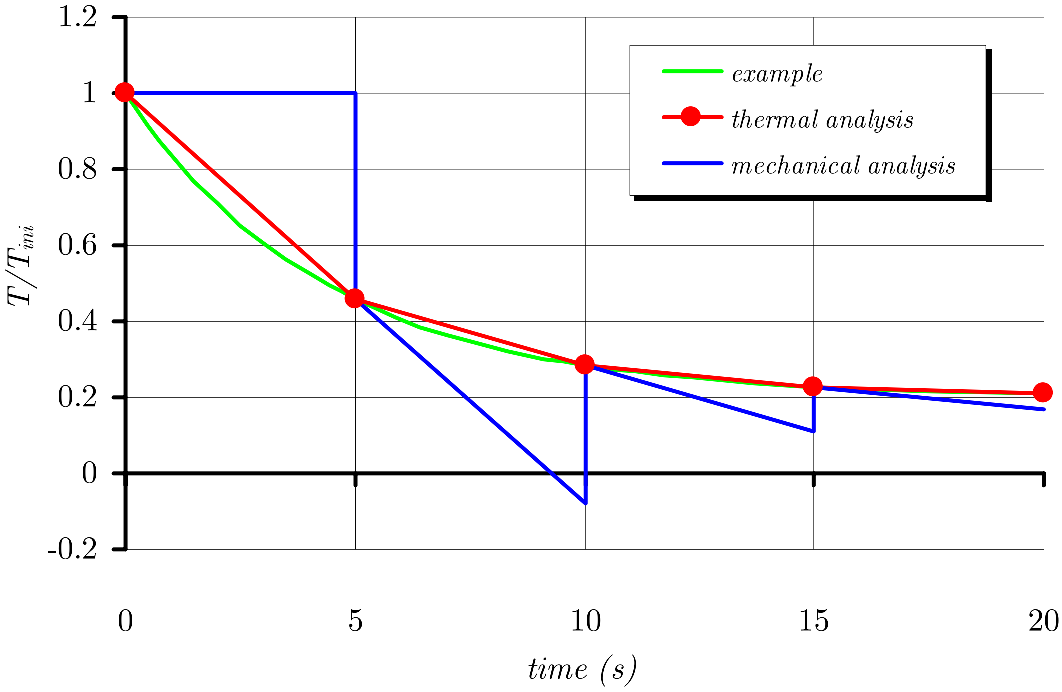

Figure 84: Temperature evolution at the surface of a hot body in contact with a cold surface (academic example)

Assuming an interval Δt equal to 5s in this example, the red dots represent the temperatures computed by the thermal analysis, then introduced in the mechanical analysis. According to the previous description of the old staggered time-stepping scheme, the evolution of (imposed) temperature in the mechanical analysis is given by the blue curve which is completely wrong in the first intervals of this example. In some circumstances, the temperature rate in the first interval can be so large that the prediction of temperature for the second mechanical interval becomes out of physical sense (negative temperature in the example of Figure 84).

For all these reasons, the thermal computation before the mechanical one allows introducing the right temperature and temperature rate in the mechanical sub-problem, since they already have been computed for the current interval in the thermal sub-problem. The modification of staggered time-stepping scheme was thus absolutely justified, leading to the one presented on Figure 83.

Note that the case of Figure 84 occurs many times in continuous casting: each time the strand loses contact or returns in contact (with the mould or the rolls), but also when the modelled slice enters or quit a water spray cooling zone. In all these cases, the heat transfer coefficient varies largely and rapidly, leading to the same kind of situation as the example illustrated above.

V. 1st Industrial application: Modelling of a 125mm square billet in the mould region. Effect of the mould taper.

V. 1st industrial application: Modelling of a 125mm square billet in the mould region. Effect of the mould taper.

1. Definition of the problem

1.1. Context of the study

The context in which the model has been developed has already been introduced at the beginning of this publication, in section I.2.1.

The present chapter presents the results obtained in this framework with a 125mm square billet, but also an extension to the initial goal with several simulations demonstrating the importance of the mould taper.

After having applied the model on the billet, it has been used with more complex sections (beam blanks). However, this further analysis has been made by the industrial partner, which uses the model to better understand the thermo-mechanical behaviour of the strand in the mould region. The results on beam blanks are not illustrated here.

1.2. Importance of the mould taper

In the mould of continuous casting, an air gap tends to form between the solidifying shell and the mould wall as the shell is cooling and shrinking. This is particularly true in the corners were initial thermal shrinkage is higher, since corners are in contact with two faces of the mould and thus subject to more heat removal. The typical shape of cross sections becomes something like those shown on Figure 85.

When such an air gap is forming, the thermal resistance between the strand and the mould increases dramatically and heat exchange decreases in proportion. In such a case, the solid shell can even be reheated by the liquid core instead of cooling. It is thus evident that if the mould could follow exactly the thermal shrinkage of the strand, it would insure a continuous contact and improve the heat removal.

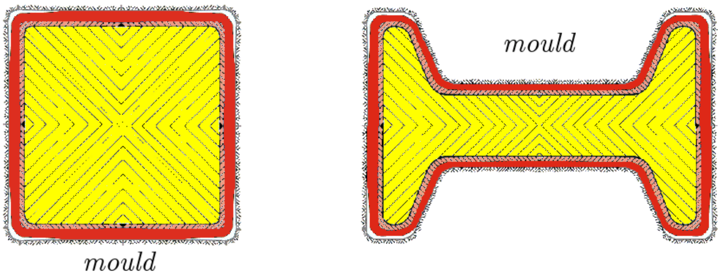

Figure 85: Typical shape of a billet and a beam blank in the mould and formation of gap in the corners (thermal shrinkage is amplified)

For this reason, moulds are tapered. Units of mould taper are %/m: they express the relative variation of a linear dimension of the mould section (the width of the billet for example) as a percentage per meter in the casting direction. The Figure 86 shows an example for a billet mould.

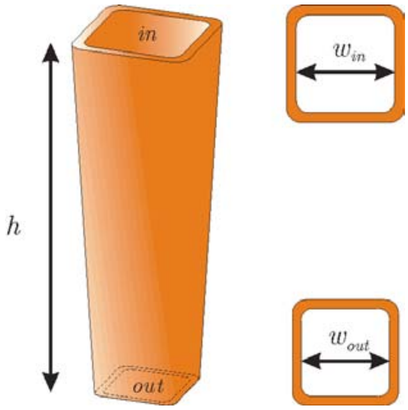

Figure 86: Mould taper for a billet mould

Generally, the reference section is that one at the exit of the mould (the bottom). In fact, if someone changes the mould taper for any reason (improvement of heat exchange), the dimensions of the section at the exit of the mould should ideally remain unchanged, otherwise the rest of the caster (rolls) does not fit to the product anymore. Thus, the mould taper t is evaluated as follows:

$$t = \frac{w_{in} - w_{out}}{w_{out} h} 100\% \tag{300}$$

where w_{in} and w_{out} are the internal dimensions (width) at the top and the bottom of the mould and h is the height of the mould expressed in m.

From relation (300), it is clear that:

- positive taper corresponds to $w_{in} > w_{out}$, i.e the mould is “closing” in the casting direction;
- negative taper corresponds to $w_{in} < w_{out}$, i.e the mould is “opening” in the casting direction.

Moulds can be qualified as single tapered, double tapered and even triple tapered, according to their vertical profile. Parabolic tapers also exist and they are recommended for high speed casting of billets [HOR98,LIN98]. Note that the taper is not always unique all along the perimeter of the section. For slab casting, it is usual to see positive taper for the narrow faces and no taper for the wide ones. For beam blanks casting, the taper is much more complex with positive and negative tapers depending on the part of the perimeter.

The determination of the optimal taper is very complex. Obviously, it is different for each cross section and each composition of steel. This optimization can be performed by empirical and iterative way. However, such trials are expensive and an initial idea of the ideal taper shape can be very helpful to quickly reach optimization.

Finite element method fits quite well for this task: any cross section can be modelled and after the model is built (and validated), many calculations can be performed without (almost) any additional cost, except CPU time.

1.3. Geometry of the cast product and the mould

Only the 125mm square billet casting is presented in this publication. In order to avoid stress concentration, corners of the section are rounded, using a 5mm curvature radius. The cross section is thus the one illustrated on Figure 87:

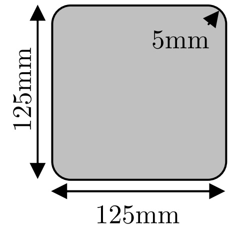

Figure 87: Cross section of the 125mm studied billet

The active height of the mould is 600mm: the mould is in fact 700mm high, but the metal level is 100mm below the top of the mould.

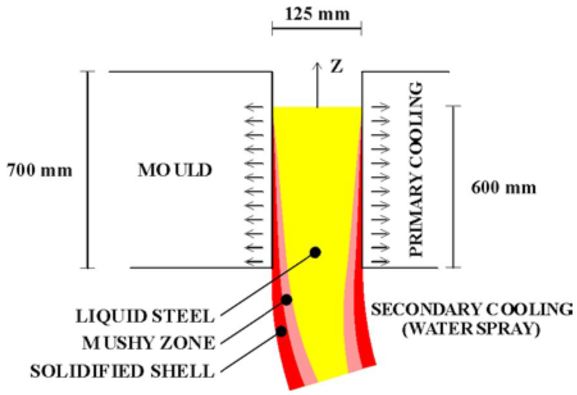

Figure 88: Mould geometry

Thanks to the double symmetry of the section and due to the verticality of the mould (no curvature), only one quarter of the slice is studied, applying the right boundary conditions along these symmetry axes. The casting speed is relatively high and is equal to 3.6m/min or 60mm/s.

The corresponding finite element mesh is composed of quadratic quadrangular plane elements (8 nodes). Those elements are of course larger in the centre of the slice, where almost no cooling occurs (i.e. no solidification). At the opposite, they are smaller in the surface and corner regions. Plane elements manage both thermal aspects (internal heat conduction and solidification latent heat) and mechanical behaviour (elastic-viscoplastic law). Specific elements are defined for ferrostatic pressure modelling. Thermo-mechanical contact elements are defined on the external boundary of the mesh.

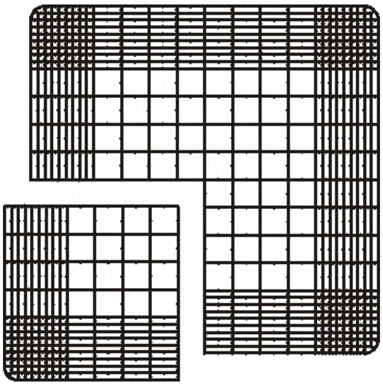

Figure 89: Studied quarter of slice and plane elements mesh.

The mould is modelled by a rigid body, the shape of which being defined by linear and parabolic segments. The displacement of the nodes defining these segments is imposed step by step to follow the taper as the slice is advancing through the mould. The temperature of the segments can also be modified to take into account the variation of the internal mould surface temperature with respect to the position of the slice in the mould. However, in the next results, a constant mould temperature has been assumed (160°C).

1.4. Thermal parameters

1.4.1. *Initial conditions*

Thermal initial conditions are very simplified: the temperature of the slice is assumed to be uniform and equal to the casting temperature, i.e. about 40°C above the liquidus temperature. This is in agreement with the lack of fluid flow modelling: the most logical assumption is to consider that the very first slice is at the casting temperature. However, this is not correct: it is well known that even just below the meniscus, the solid shell is already in formation. The introduction of a non uniform temperature field could certainly be a next step in the improvement of the present model.

1.4.2. *Heat transfer coefficient*

Mould heat transfer is very complex and it has been studied in numerous publications [SIN74,BLA87-88,CHA93,ABR96,STO00]. Heat extraction from the billet is achieved through the different layers involved in the process: from the solid shell, through the molten powder, the air gap and the mould to the water cooling system inside the mould. Moreover, one must take into account contact resistances. In the present model, two global heat transfer coefficients are applied: a first one when contact occur and a second one (depending on gap size) when contact is lost.

Heat transfer coefficient depends on the distance *d* between the strand and the mould. Electrical analogy of thermal resistance is represented on Figure 90:

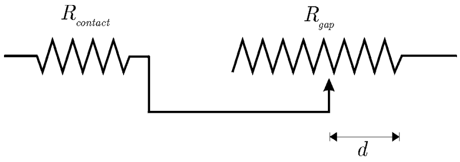

Figure 90: Electrical analogy of thermal resistance

In case of contact, the distance *d* is equal to zero. The heat transfer coefficient is assumed to be equal to 1.6kW/m^{2}K. In lack of contact, the thermal resistance of the gap is assumed to vary linearly with the distance *d*. The thermal conductivity of the gap k_{gap} is assumed to be equal to 0.15W/mK. The global heat transfer coefficient is thus equal to the inverse of the total thermal resistance:

$$h = \frac{1}{R_{tot}} = \frac{1}{R_{contact} + R_{gap}} = \frac{1}{\dfrac{1}{h_{contact}} + \dfrac{1}{k_{gap}} d} = \frac{h_{contact} k_{gap}}{k_{gap} + h_{contact} d} \tag{301}$$

Thus the heat transfer coefficient as a function of the distance between the strand and the mould is the following:

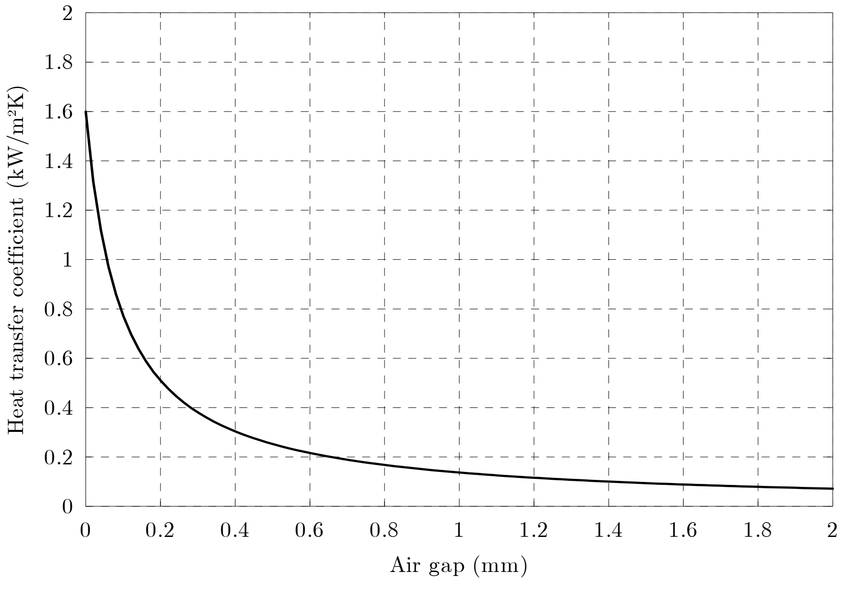

Figure 91: Evolution of heat transfer coefficient with respect to the distance between the strand and the mould

This continuous coefficient has been preferred to a previous assumption that consisted in considering a dual value for the heat transfer coefficient: one in case of contact, another one in lack of contact, but no dependence on the size of the gap. In that case, the convergence of the simulation was much more difficult, since every loss of contact (and every return to contact) was going with sudden and sharp variation of heat transfer coefficient, so that numerical thermal shocks were often occurring.

Note that the heat transfer coefficient is not dependent on the temperature in this application. However, this possibility has been implemented in the model and it has been used in the second industrial application of the model (see chapter VI).

1.4.3. Thermal linear expansion coefficient

As already mentioned in section II.2, thermal shrinkage is taken into account only in the solid phase. In the present application, carbon steel is cast (0.18<wt%C<0.51) so that there is no phase transformation $\delta \rightarrow \gamma$ in completely solidified state.

The coefficient of thermal linear expansion α has been fixed to 13.5 10^{-6} K^{-1} according to data provided by industrial partner. This is quite lower with respect to the value of 22 10^{-6} K^{-1} found in section II.2 for coefficient α of austenite. However, it is similar to the value adopted indicated by the second partner (15 10^{-6} K^{-1}), which is described in the very next chapter VI. As already mentioned in section II.2, the difference between these values can be imputed to alloying elements, which modify the thermal linear expansion coefficient. More precise analysis is necessary to determine the coefficient α, for instance by an experimental way. Otherwise, some publications supply such kind of information for many different steels (for example [RIC73]).

1.5. Mechanical parameters

An large part of the initial work consisted in the identification of the parameters for the constitutive (thermo-) elastic-viscoplastic law. These parameters were fit on experimental curves of tensile tests, which were performed on a Gleeble device with steel samples at high temperature (800°C to 1475°C) and for several strain rates (1 10^{-4} s^{-1} to 5 10^{-3} s^{-1}). The set of experimental curves has thus allowed fitting the parameters of Norton-Hoff law, each parameter being defined for a given temperature.

1.6. Modelling of the liquid behaviour

The slice is made of a liquid core, a solidifying external shell and an intermediate mushy zone. The amount of matter is fixed during all the computation (lagrangian approach). In other respects, the generalized plane strain state statutes that the slice is delimited by two planes.

Consider the only thermal shrinkage in the liquid: actually, when the liquid is cooling (and before solidification), it shrinks. If one considers two planes delimiting a slice, in reality, thermal shrinkage of the liquid is compensated by liquid flow: the metal level in the mould decreases. In the model however, since no matter exchange between the slice and surroundings is allowed, thermal shrinkage of the liquid implies automatically diminution of the volume that it occupies in the slice. This creates in the middle of the slice a kind of suction and the solidified shell follows the thermal shrinkage of the liquid, since no void can be created between the two phases (the material is and remains continuous). The Figure 92 shows in plane how it happens.

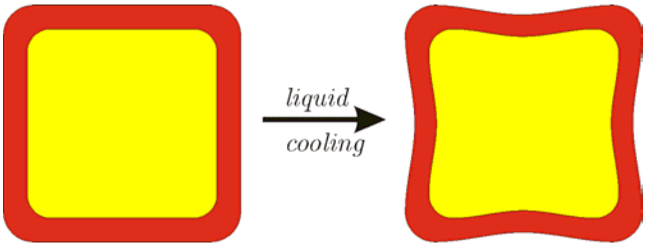

Figure 92: Distortion of the solidified shell when liquid shrinks in the slice model

This is physically not in accord with reality. To correct this default, thermal expansion coefficient is assumed to be equal to zero in the liquid zone. Such a way, any temperature variation in a liquid part does not affect the volume occupied by this part. That allows saying that the volume released by thermal shrinkage is automatically filled by continuous supplying of the slice with liquid in the pool.

In the mushy zone, the same zero-coefficient is assumed. This fits well with the behaviour of liquid which is free to move between dendrites (cf. Figure 64). At the interface liquid/solid face, any shrinkage due to phase transformation is also compensated by liquid supply. On the other hand, where liquid “bubbles” are solidifying, one can consider that thermal shrinkage really occurs. However, this one has not been taken into account.

So thermal shrinkage is only modelled in the solid phase (completely solidified). This assumption is similar to that made by other authors [DIP86,CHA93].

Beside the thermal expansion coefficient, another parameter has to be taken equal to zero in the liquid phase: Poisson coefficient ν. Liquid steel is almost incompressible, so that its Poisson coefficient should tend to 0.5. If the solid shell is distorted (for any reason: contact with the mould, thermal shrinkage), the liquid is moving in or out of the slice. For example, if the solid shell shrinks, the space inside decreases and the liquid it expulsed, as shown on Figure 93. In the present model, a constant amount of both liquid and solid phases is always confined between two planes (generalized plane strain state), the thickness of the entire slice being governed by relation (37). That means that if the liquid tends to move the planes apart, it is balance by the solid which withstand to this movement and an out-of-plane tensile state appears in the solid shell. To avoid such a phenomenon, which has no physical meaning in the process, the Poisson coefficient of liquid is equal to zero.

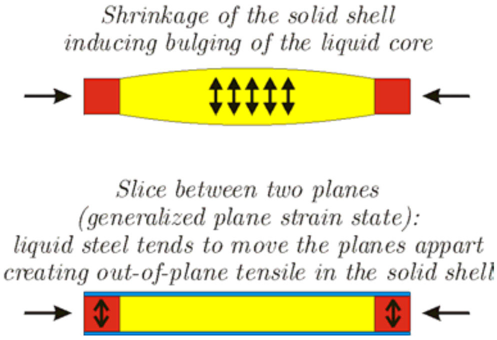

Figure 93: Effect of incompressibility of the liquid in the slice

2. Results

2.1. Idealised mould

In this first modelling, the behaviour of the strand is computed assuming that the mould follows exactly the strand during its thermal shrinkage. Contact is thus assumed to permanently occur, but without introducing any contact pressure. The distorted geometry of strand would give the ideal mould geometry.

2.1.1. Billet distortion

As first result, the Figure 94 shows the billet section 600mm below the meniscus, i.e. the ideal shape for the mould exit. As it clearly appears, the corner is going inward, while the billet is bulging at the mid-faces. Note that the displacements are amplified by a factor 10 to see better the distortion.

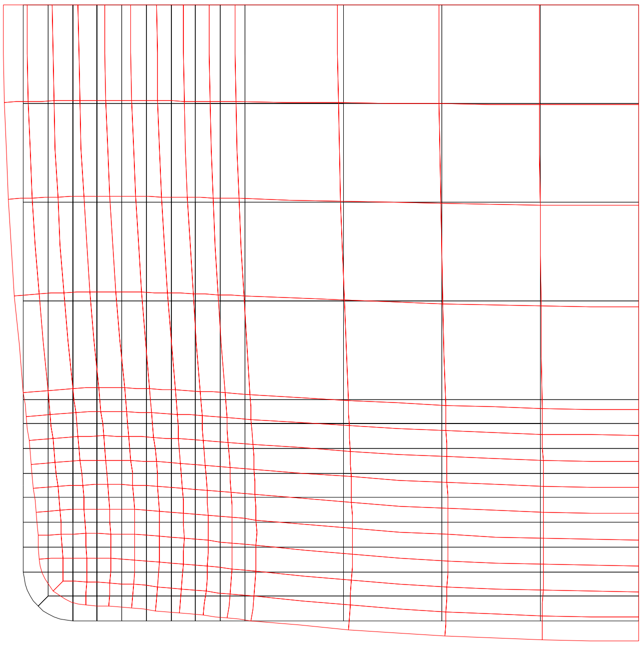

Figure 94: Distorted ¼ billet section (in red) at the exit of the mould with respect to initial section (in black), amplification of displacements by factor=10

The dimensions of the billet under these conditions are represented on Figure 95.

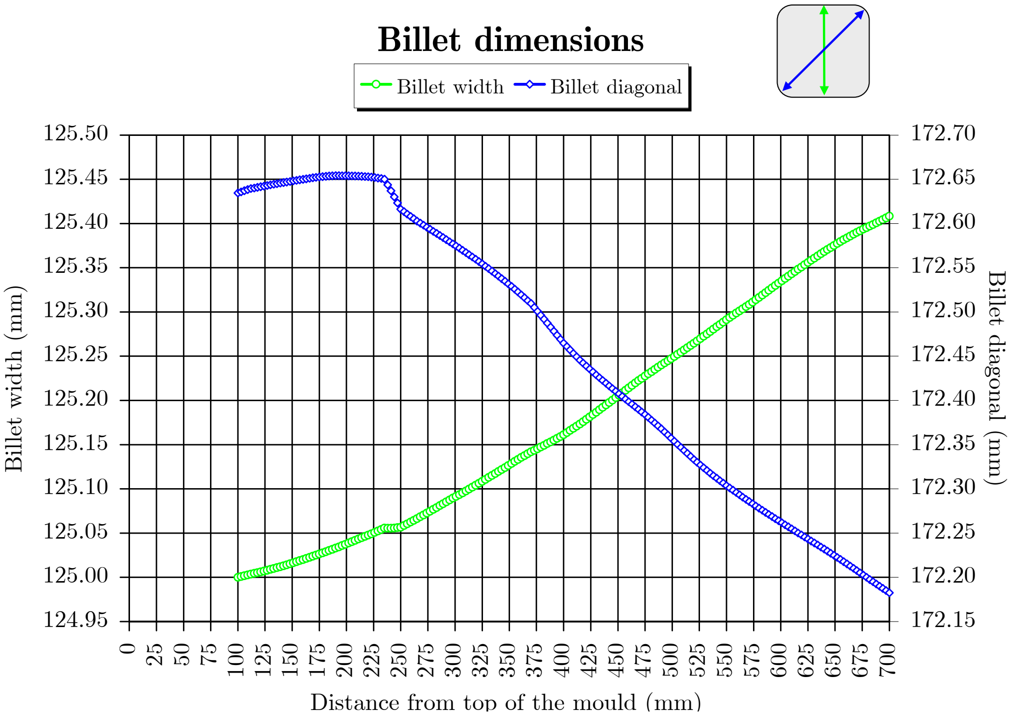

Figure 95: Dimensions of the billet (width and diagonal)

The bulging of the mid-faces is thus about 0.4mm and relatively linear with respect to distance from the top of the mould. The corresponding taper is thus:

$$t_{mid\text{-}face} = \frac{125 - 125.4}{125.4 \;\, 0.6} 100\% = -0.53\% \,/\, \mathrm{m} \tag{302}$$

In the corner, the first 125mm of casting is approximately vertical, the diagonal decreases from 172.65mm to 172.18mm. A double taper could be recommended:

$$\begin{cases} t = 0\% \,/\, \mathrm{m} & 0 \rightarrow 225\mathrm{mm} \\ t = \dfrac{172.65 - 172.18}{172.18 \;\, 0.475} = +0.57\% \,/\, \mathrm{m} & 225 \rightarrow 700\mathrm{mm} \end{cases} \tag{303}$$

2.1.2. Thickness of solidified shell and temperature at the exit of the mould

The thickness of the solid shell has reached about 4.75mm around the mid-face and 9.9mm in the corner (in diagonal). This is due to the higher heat removal in the corner (two faces in contact with the mould). The temperature goes in the same way, as shown on Figure 97: in mid-face the temperature is about 1515K (or 1242°C), while in the corner the temperature is 1328K (or 1055°C).

These results constitute a maximum cooling state in the sense that a real mould does not follow exactly the thermal shrinkage of the billet. The consequences are a thinner solidified shell and higher surface temperature. However, comparing these values in both cases (idealized and real mould), one can expect to have a qualitative appreciation of a given mould taper.

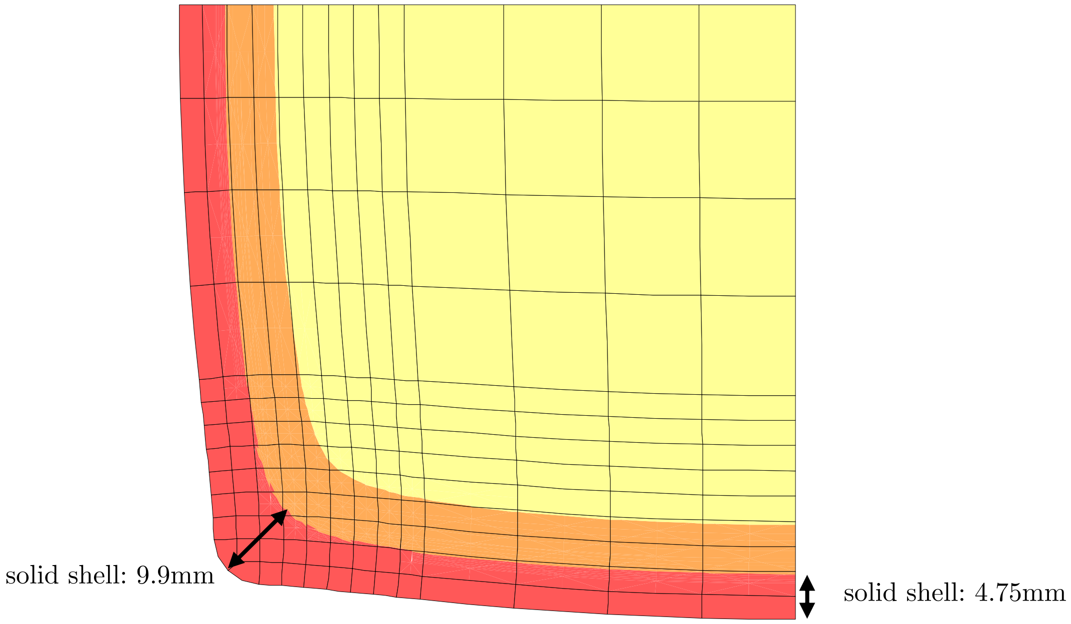

Figure 96: Solid, mushy and liquid states in the ¼ billet slice at the exit of the mould

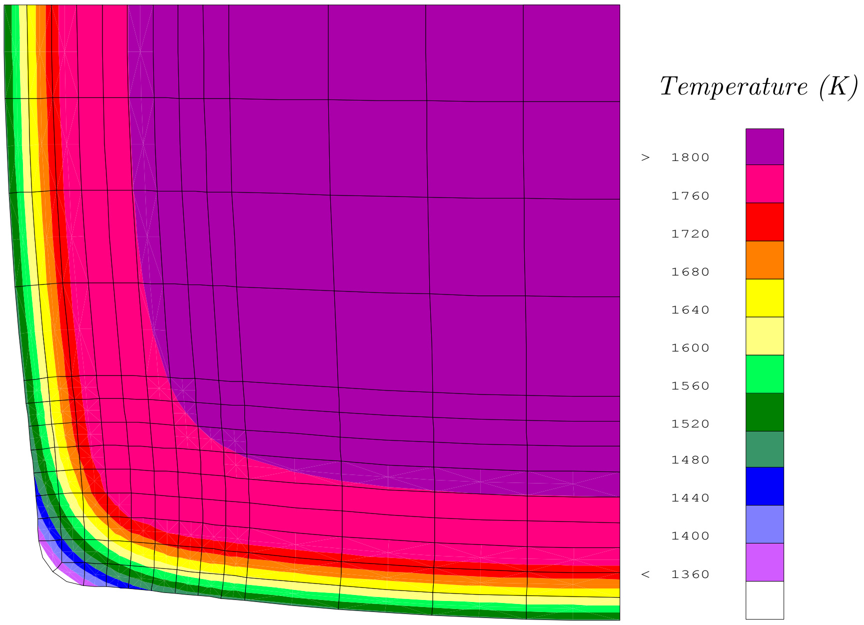

Figure 97: Temperature field (in K) in the ¼ billet slice at the exit of the mould

In the casting direction, the temperature profiles of mid-faces and corners are illustrated in the Figure 98. As already mentioned in section V.1.4.1, the initial temperature is uniform in the slice, while in reality it is not. Solid phase appears first in the corner about 60mm below the meniscus and a complete solid shell (all around the perimeter of the slice) starts to grow from 85mm under meniscus. This is a drawback of the model, which can be modified using another initial temperature field.

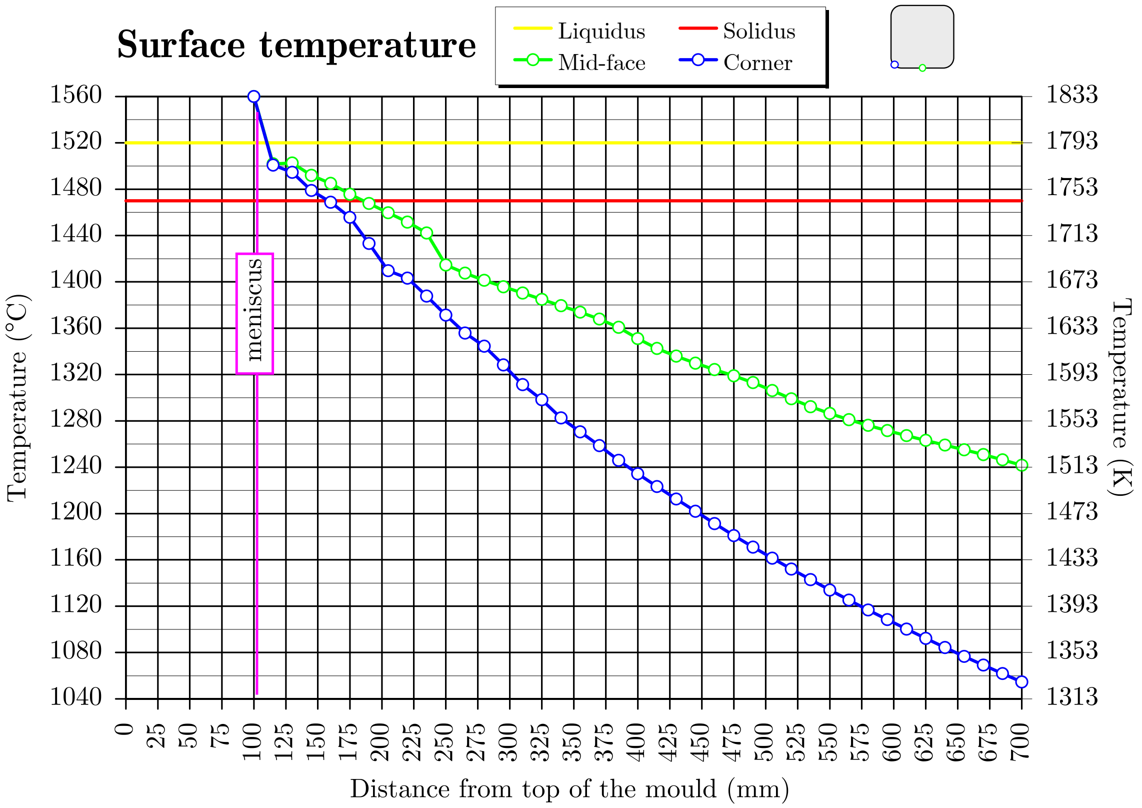

Figure 98: Profile temperature

2.1.3. Heat removal from the ¼ slice

To go further in the optimization, it is possible to define an objective function and to run successive simulations, modifying the mould taper in such a way that the objective function tends to an optimum. This objective function should be representative of the overall good adequacy between the mould shape and the billet shrinkage. For instance, this function could be the heat removal, which should be maximized, tending to heat removal with the idealized mould. The Figure 99 shows heat removal from the slice at each time step, thus as a function of distance to free surface. The total heat removed from the ¼ slice is equal to 142.7 kJ.

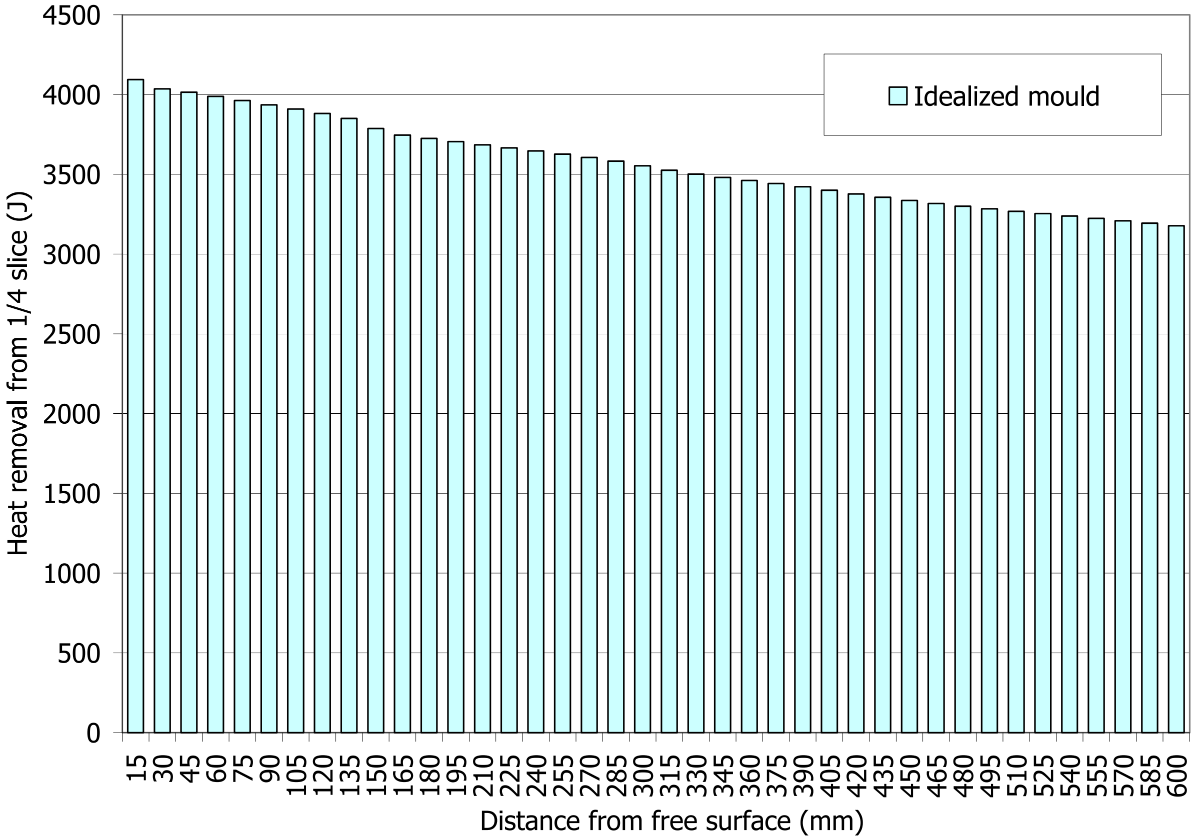

Figure 99: Heat removal form the ¼ slice as a function of distance to free surface

2.2. Real mould

In the present section, the results obtained with 5 different tapers are shown. These tapers are single tapers equal to: +3%/m, +1%/m, 0%/m, -1%/m and -3%/m. They are "academic" examples of the influence of the mould taper on heat removal. Note that these tapers are constant both in the casting direction (single taper) and along the perimeter of the billet (same taper for corner and mid-face).

2.2.1. Heat removal from the ¼ slice

First results to be shown are the heat removal from the ¼ slice – see Figure 100 to Figure 102. For each taper, the comparison is made with the heat removal obtained with the idealized mould (cf. Figure 99).

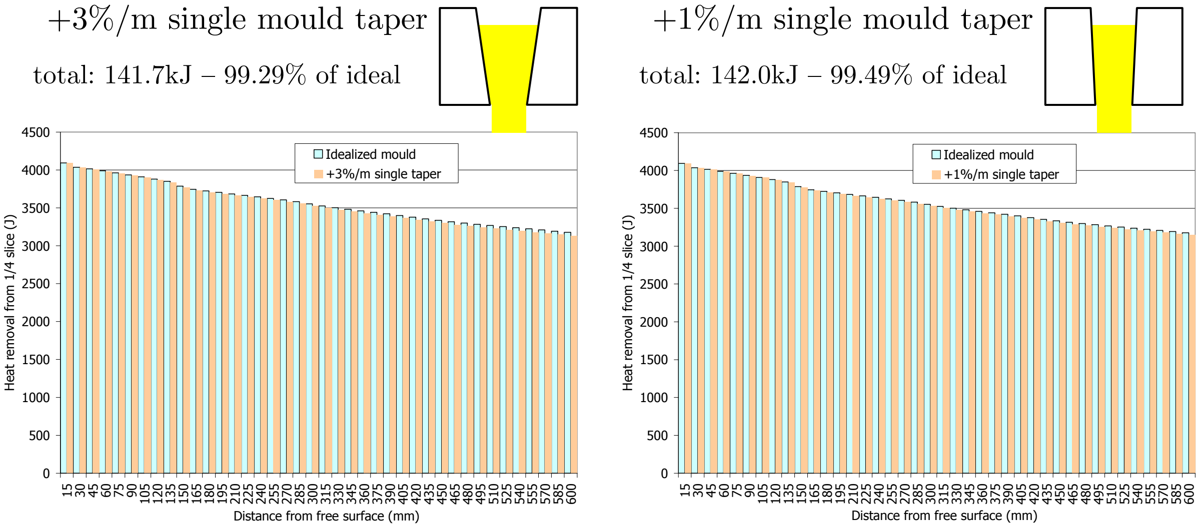
+3%/m single mould taper

total: 141.7kJ – 99.29% of ideal

+1%/m single mould taper

total: 142.0kJ – 99.49% of ideal

Figure 100: Heat removal from the ¼ slice for positive tapers (+3%/m and +1%/m)

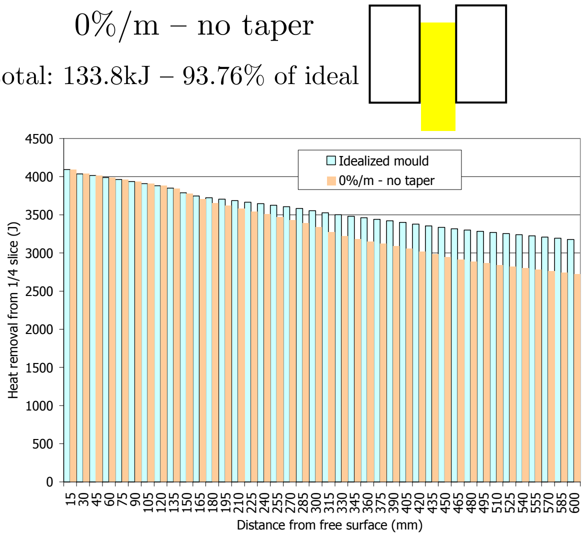
0%/m – no taper

total: 133.8kJ – 93.76% of ideal

Figure 101: Heat removal from the ¼ slice in lack of mould taper (0%/m)

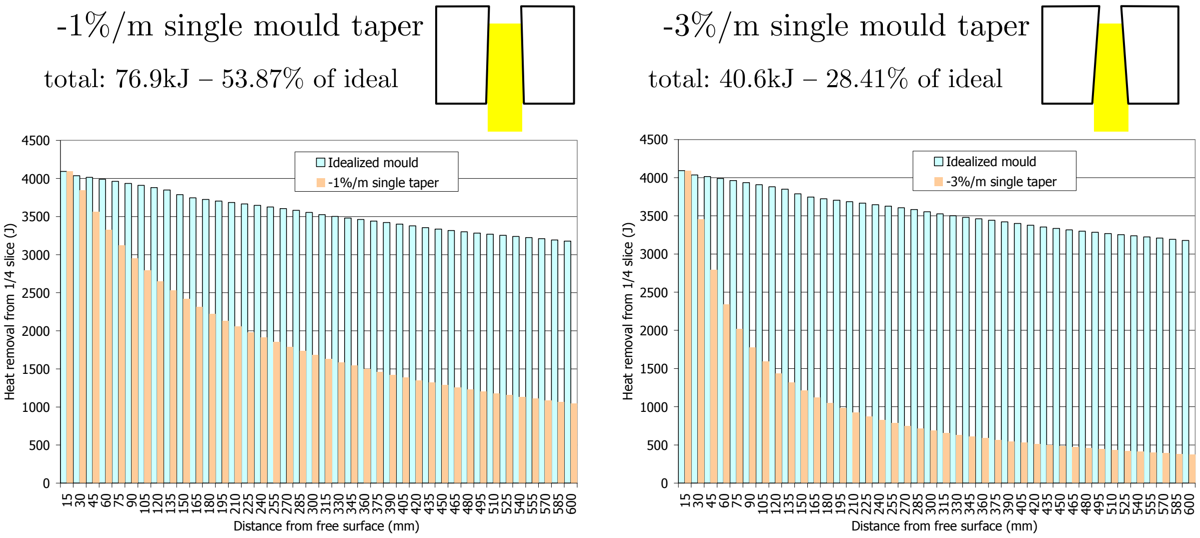
-1%/m single mould taper

total: 76.9kJ – 53.87% of ideal

-3%/m single mould taper

total: 40.6kJ – 28.41% of ideal

Figure 102: Heat removal from the ¼ slice for negative tapers (-1%/m and -3%/m)

The analysis of the above figures indicates that positive tapers (+1%/m and +3%/m) allow removing almost the same amount of heat from the slice as the idealized mould (more than 99%). If the mould is not tapered (0%/m), the total amount of heat removal decreases below 94%. In fact, during the first steps, the heat removal is quite identical, then it decreases. For negative tapers, heat extraction is much lower.

The Figure 103 summarizes the heat removal in all cases:

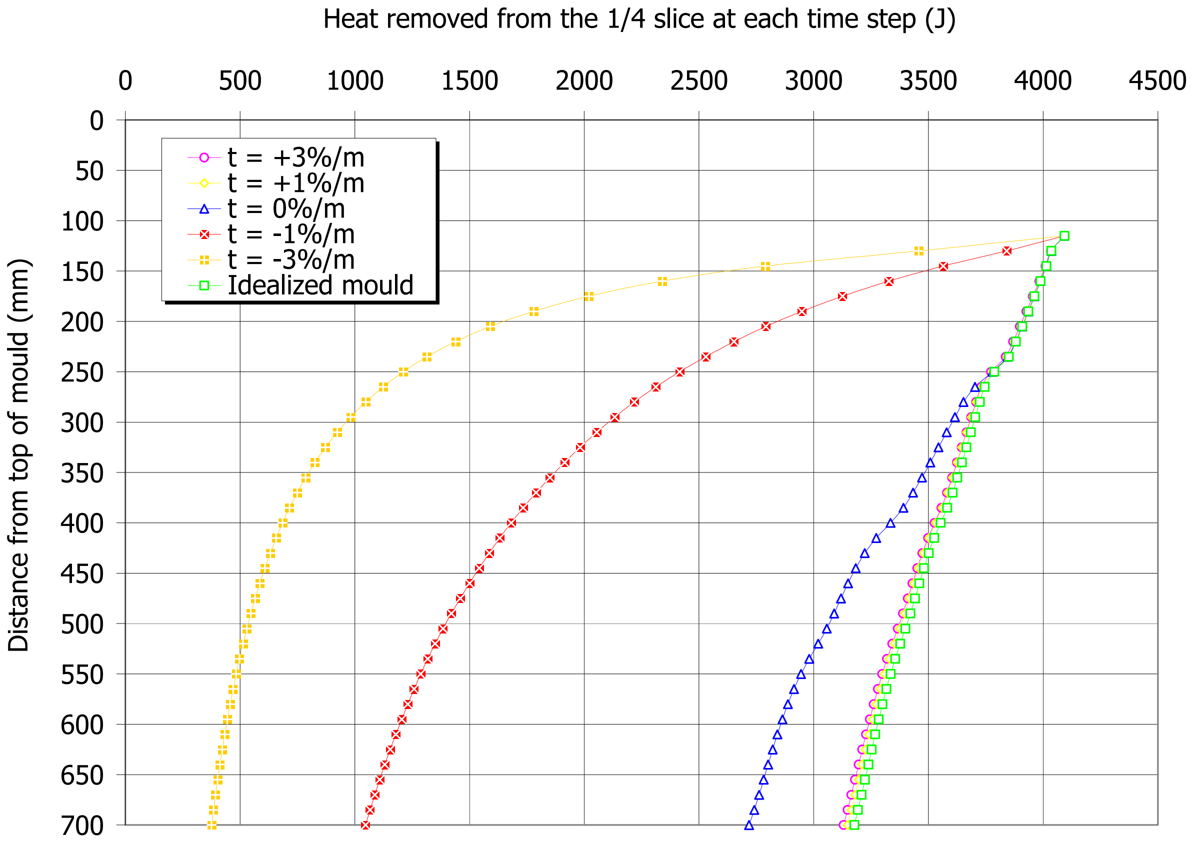

Figure 103: Heat removed from the ¼ slice

2.2.2. Thickness of solidified shell and temperature at the exit of the mould

The amount of heat removal can be translated in terms of solidification progression. The thickness of the solidified shell is in correlation with heat removal. The following figures show for each mould taper the solid, mushy and liquid states (Figure 104 to Figure 108) and temperature field (Figure 109 to Figure 113) in the slice at the exit of the mould. They clearly show that:

- in the case of positive taper, solidified shell is almost as thick as for idealized mould;
- in lack of taper (0%/m), the mid-face are in contact and heat removal is insured, while in the corner, the contact is lost and heat removal through air gap causes the temperature in the corner to be lower than in mid-face (see Figure 111);
- in case of negative taper, the contact is lost all along the perimeter because the mould is opening in the casting direction and heat removal is too low.

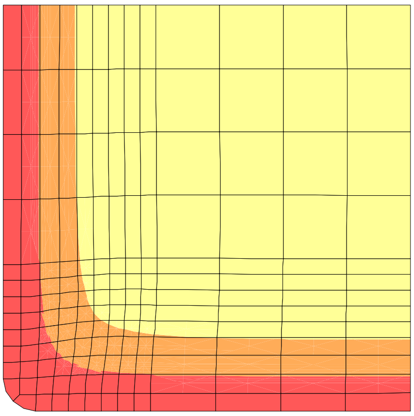

+3%/m mould taper

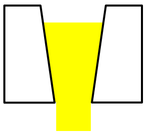

shell thickness:
mid-face 4.75mm
corner 9.8mm

Figure 104: Solid, mushy and liquid states in the ¼ billet slice at the exit of the mould

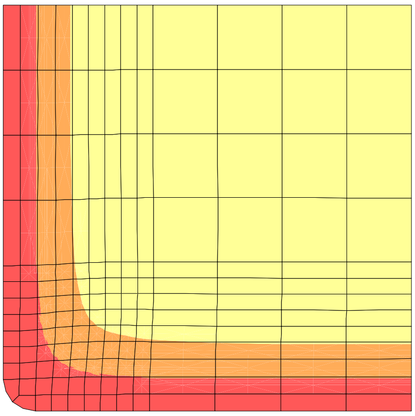

+1%/m mould taper

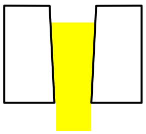

shell thickness:
mid-face 4.75mm
corner 8.9mm

Figure 105: Solid, mushy and liquid states in the ¼ billet slice at the exit of the mould

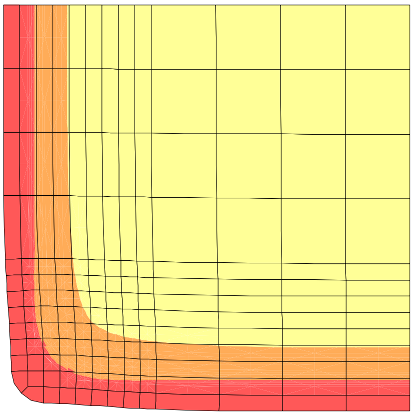

0%/m mould taper

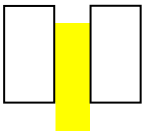

shell thickness:
mid-face 4.75mm
corner 7.2mm

Figure 106: Solid, mushy and liquid states in the ¼ billet slice at the exit of the mould

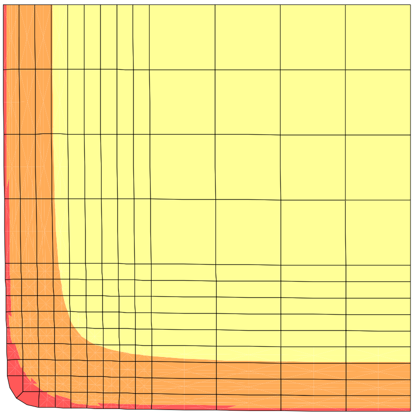

-1%/m mould taper

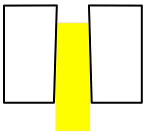

shell thickness:
mid-face 0.5mm
corner 3.5mm

Figure 107: Solid, mushy and liquid states in the ¼ billet slice at the exit of the mould

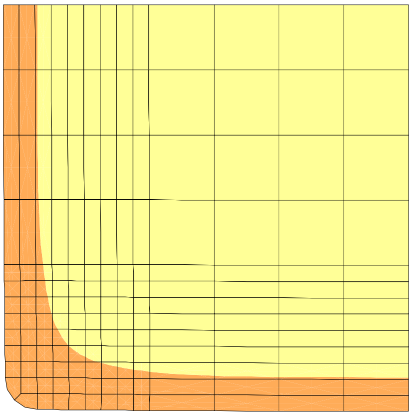

-3%/m mould taper

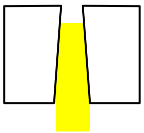

shell thickness:
mid-face 0mm
corner 0mm

Figure 108: Solid, mushy and liquid states in the ¼ billet slice at the exit of the mould

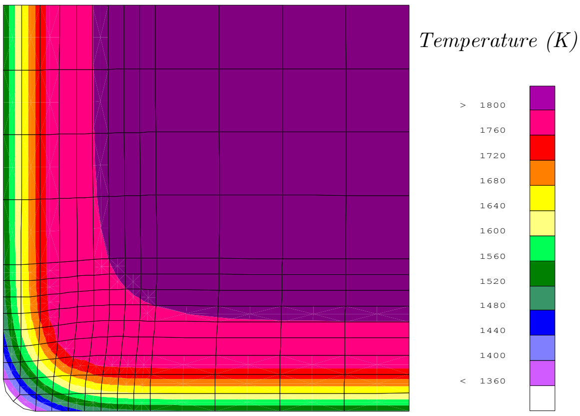

+3%/m mould taper

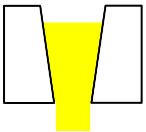

surface temperature:
mid-face 1515K (1242°C)
corner 1326K (1053°C)

Figure 109: Temperature field in the ¼ billet slice at the exit of the mould

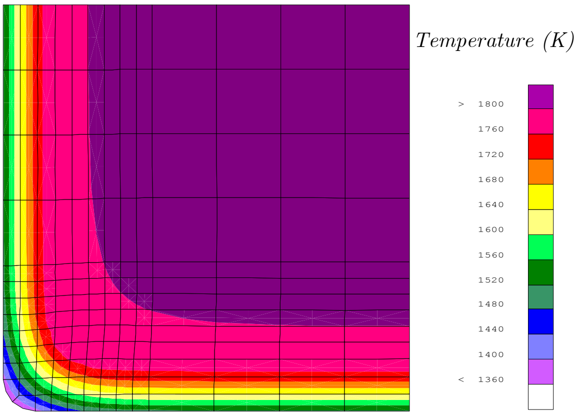

+1%/m mould taper

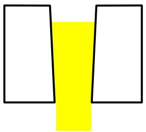

surface temperature:
mid-face 1515K (1242°C)
corner 1365K (1092°C)

Figure 110: Temperature field in the ¼ billet slice at the exit of the mould

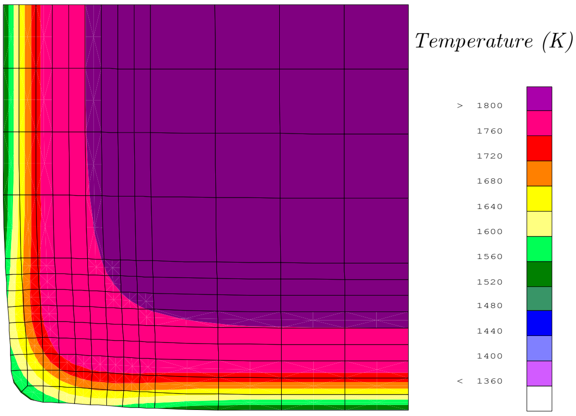

0%/m mould taper

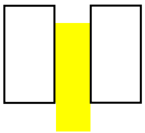

surface temperature:
mid-face 1515K (1242°C)
corner 1555K (1282°C)

Figure 111: Temperature field in the ¼ billet slice at the exit of the mould

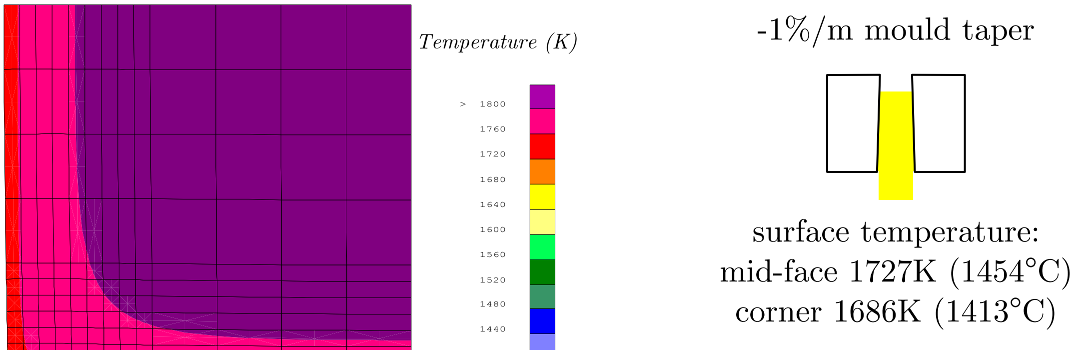

-1%/m mould taper

surface temperature:
mid-face 1727K (1454°C)
corner 1686K (1413°C)

Figure 112: Temperature field in the ¼ billet slice at the exit of the mould

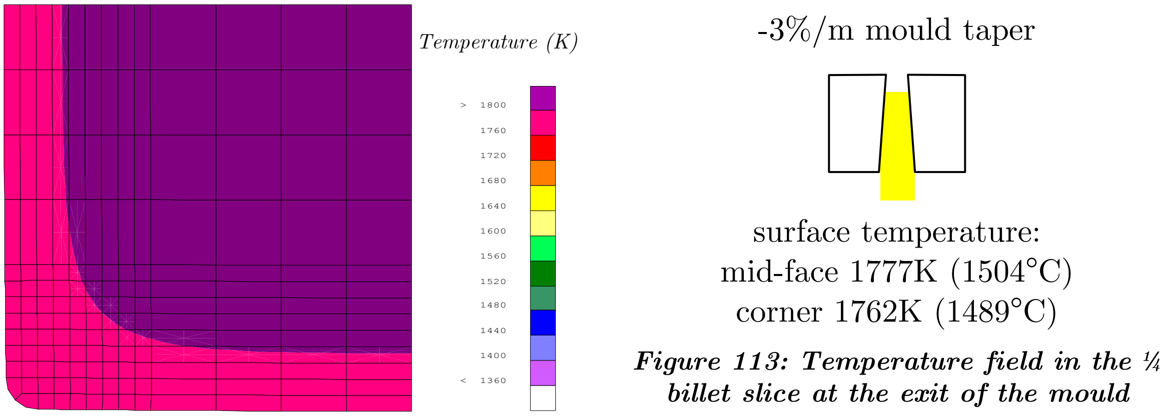

-3%/m mould taper

surface temperature:
mid-face 1777K (1504°C)
corner 1762K (1489°C)

Figure 113: Temperature field in the ¼ billet slice at the exit of the mould

2.2.3. Mechanical state of the billet

From the previous figures, one can think that the +3%/m single taper is the best one, since it reaches almost same results as idealized mould in terms of surface temperature as well as thickness of solid shell. In fact, the higher the taper is, the better the heat removal is, since contact is always ensured. However, one cannot ignore that higher taper induces higher contact pressure and thus high stresses in the thin weak solidifying shell. Moreover, excessive taper increases the resistance to withdraw and exacerbates mould wear [DIP86].

The following figures show the Von Mises equivalent stress in the ¼ slice at the exit of the mould for idealized mould and positive single taper moulds.

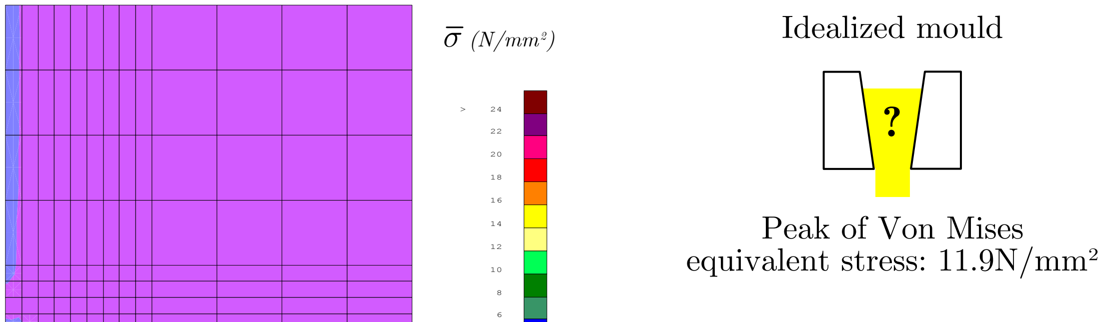

Idealized mould

Peak of Von Mises
equivalent stress: 11.9N/mm^2

Figure 114: Von Mises equivalent stress in the ¼ billet slice at the exit of the mould

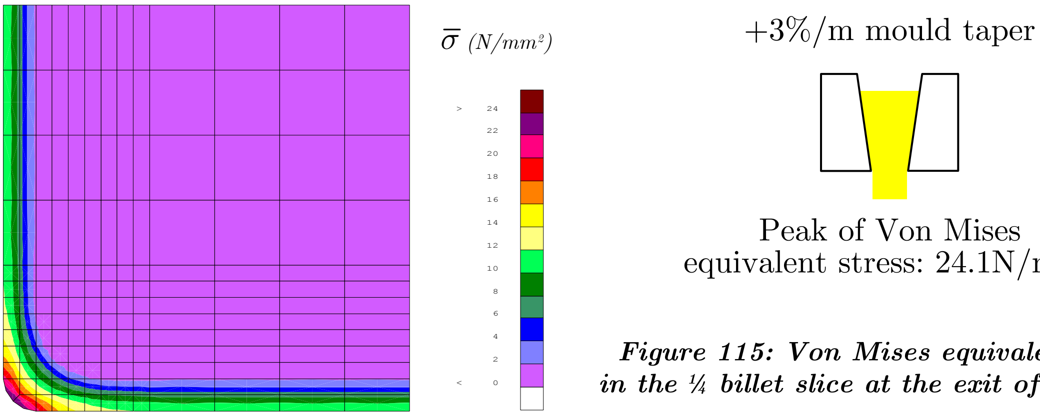

Figure 115: Von Mises equivalent stress in the ¼ billet slice at the exit of the mould

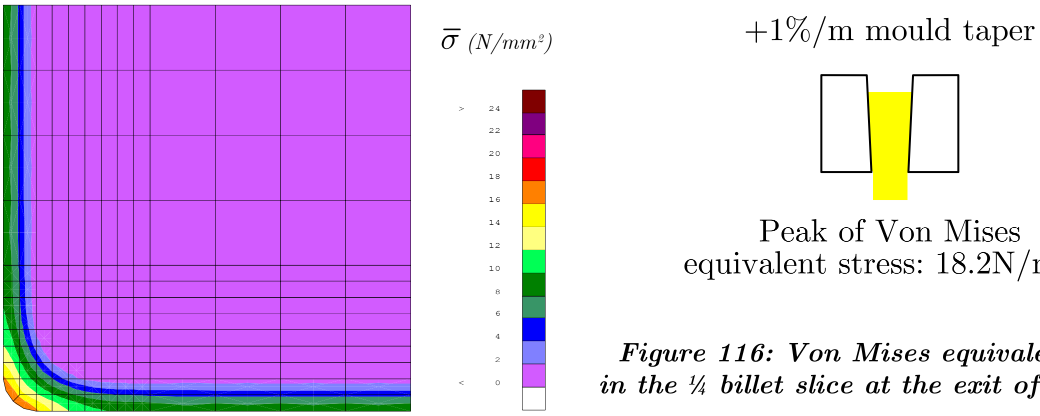

Figure 116: Von Mises equivalent stress in the ¼ billet slice at the exit of the mould

In the case of the idealized mould (Figure 114), higher stresses are present in the corner. The peak value is almost 12N/mm². This stress state corresponds to the sum of thermal stresses (more developed in the corner, which is colder) and bending due to bulging of the solid shell under ferrostatic pressure.

In the case of positive taper, the contact between the billet and the mould implies an additive contribution of pressure and the stress level increases in the corner as well as along the faces. According to Figure 115 and Figure 116, it is evident that the +1%/m taper is better than the +3%/m one, since the peak value is about 18N/mm² vs. 24N/mm² and the equivalent stress along the faces is also one range below in the scale: 8-10N/mm² vs. 10-12N/mm².

2.3. To an automatic optimization of mould taper

As this stage, the model already provides much information about thermal and mechanical behaviour of the billet. It is thus possible to optimize "manually" the mould taper, if some criteria are defined. These criteria can be:

- maximization of heat removal
- maximization of solid shell thickness
- minimization of surface temperature
- minimization of contact pressure
- minimization of average and/or peak equivalent stress
- …

Many criteria are possible, but a solution verifying all of them at the same time probably does not exist. The engineer's experience can help to choose the right combination of all this parameters. However, for automatic optimization (using a numerical algorithm), it is necessary to define an objective function, which combines two or more criteria in such a way that the solution can be evaluated and classified among others solution. Then the optimization algorithm should provide the best compromise between the criteria and thus the "best" mould taper.

This next stage in the model development goes further the objective of the thesis and it is not more detailed. Note that recently a graduate student has used the model and previous results to try an optimization using a Levenberg-Marquart algorithm. Unfortunately, some numerical problems and the difficulty to define the objective function did not allow defining the optimum taper [MIE03].

2.4. Mould distortion

Finally, one should take care that the mould also distorts due to temperature elevation. In fact, if an optimal taper can be found, this is in steady-state, thus when the mould is "hot" and not at room temperature.

This is not a real problem: steel producers command the mould with dimensions in working conditions. The role of the mould manufacturer is to ensure that the distorted mould exactly fits the taper that the producer asked for. To give an idea of the amplitude of the mould distortion, a relatively simple model is shown hereafter.

Just as an illustration, here is an example made on two billet moulds. The first one is not tapered and the second one is +1%/m tapered. They are modelled assuming a 3D thermo-elastic behaviour. Initially, the temperature of the moulds is uniform and equal to 25°C. Then the temperature of the external and internal surfaces is rising up to the temperature profiles shown on Figure 117. These profiles are typical mould temperature for this kind of product and dimensions [MAH91a,RID94]. The temperature is the highest a little below the meniscus level (were heat removal is highest). Internal and external surface temperatures are different: the internal surface is in contact with the strand and the external one is cooled by water flow. These profiles are assumed not to vary along the perimeter (same temperature profile for corners and mid-faces).

According to Figure 119, the dilatation of the moulds is such that the internal dimension (width) of the mould is about 0.20-0.25mm larger than at the room temperature, i.e. about one half of the billet bulging (cf. Figure 95). It is thus significant and must be integrated in the design of the mould.

Note that this model is strongly simplified in the material behaviour and boundary conditions. In other respect, it does not take into account the support of the Cu tube constituting the mould. More refined models are necessary to compute the exact mould distortion, including coupling between strand and mould thermo-mechanical behaviour.

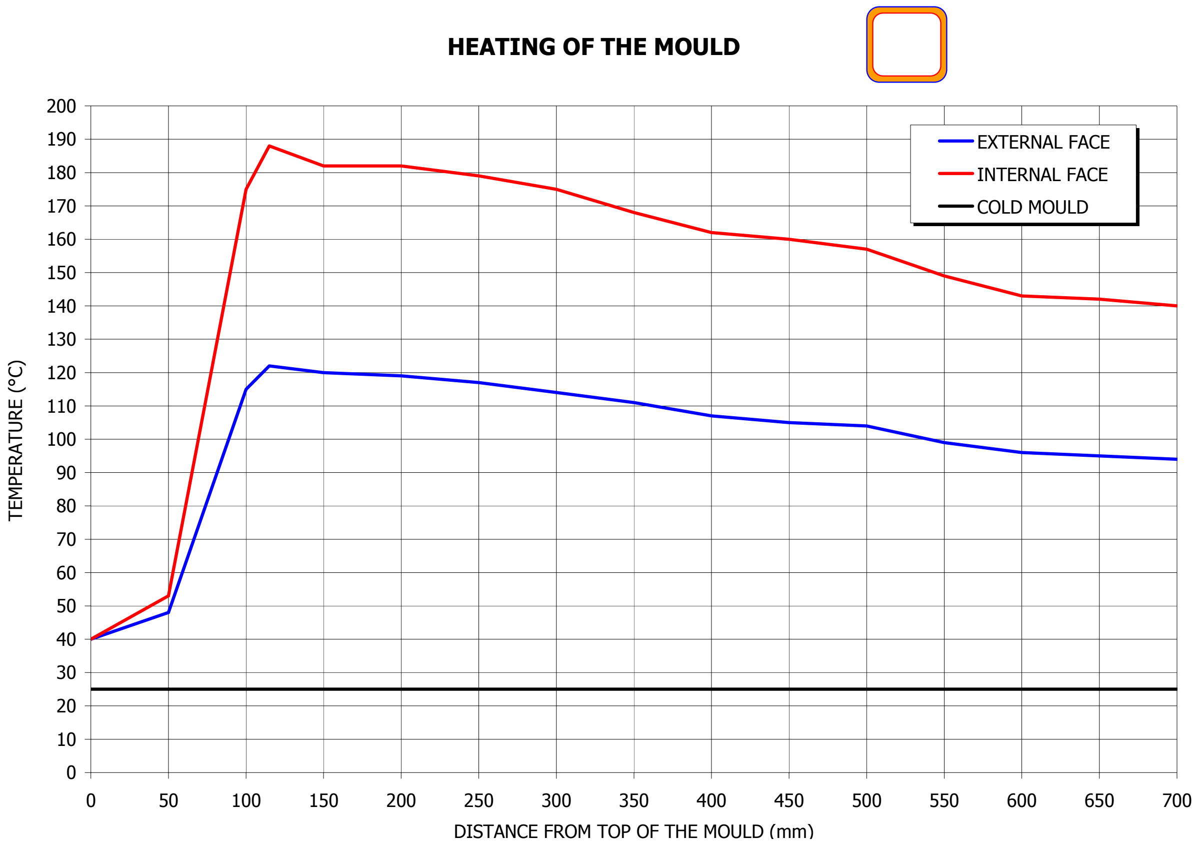

Figure 117: Temperature of the mould

The thermal distortion of both moulds is shown on Figure 118 to Figure 120.

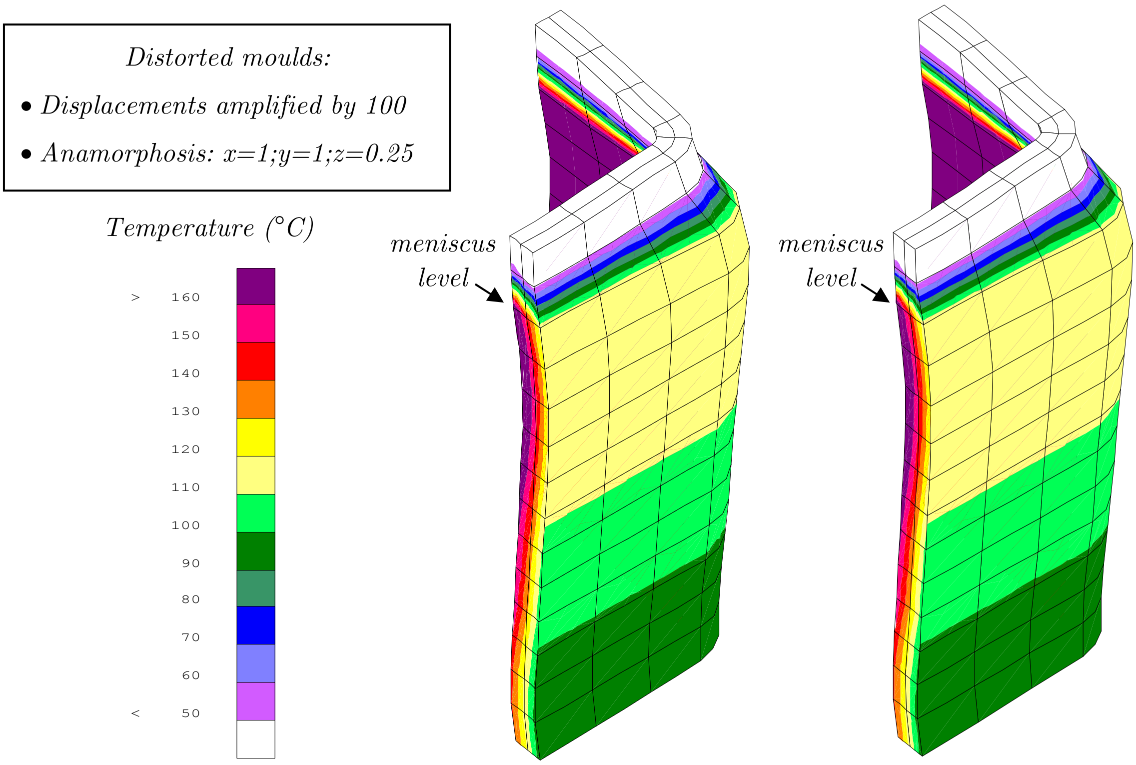

Figure 118: Temperature field distortion of not tapered (on the left) and +1%/m (on the right) tapered moulds

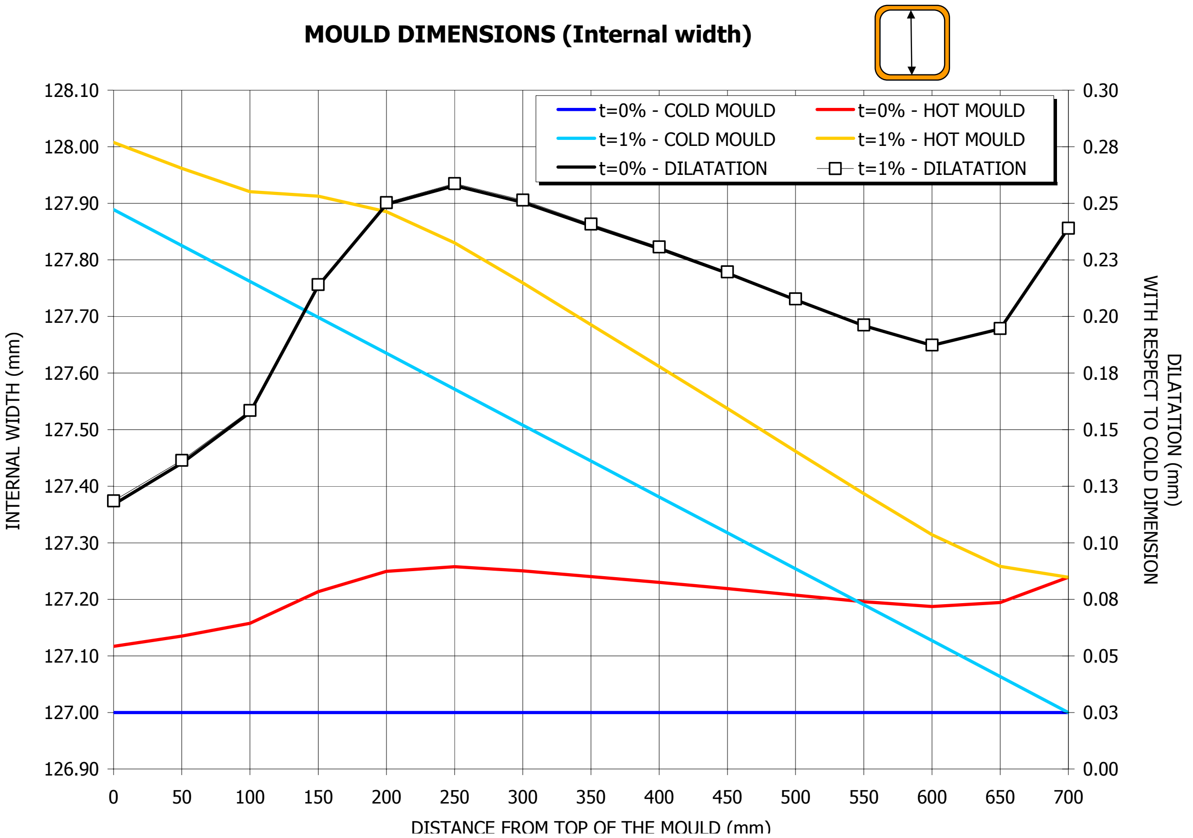

Figure 119: Internal width of the hot mould for 0%/m and 1%/m tapers

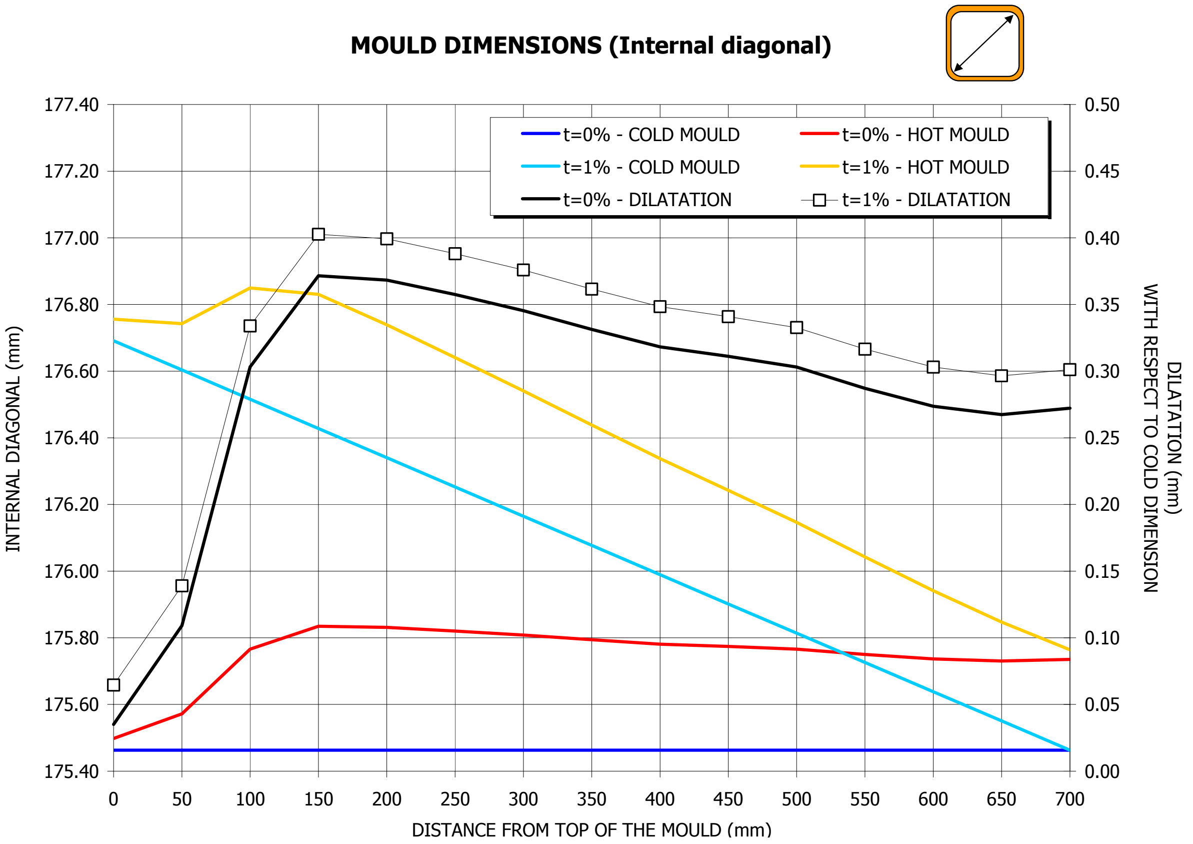

Figure 120: Internal diagonal of the hot mould for 0%/m and 1%/m tapers

3. Discussion

The model has been applied according to a first assumption of idealized mould, which provides the natural deformation of the billet, without any mechanical interaction with the mould. It has been found that the billet bulges on the faces and shrinks in the corners. This billet distortion represents the ideal mould taper for a continuous contact between the billet and the mould. However, this result strongly depends on simplifications and assumptions made in the formulation of the model (2D model, uniform initial temperature of the slice, no coupling between strand and mould behaviour, material behaviour, heat transfer coefficients…).

From the practical and technical points of view, such a mould could not be used, since the faces of the billet below the mould should be planar to ensure good contact with further rolls and to provide a geometry fulfilling the tolerance on the dimensions of the product. Thus, the model should be run again using a "negative shrinkage" shape for the initial geometry of slice, so that thermal shrinkage lead to a 125mm square billet at the exit of the mould (see Figure 121). Note that such an ideal taper is much more complex than a simple or double taper: it varies all along the vertical direction, as well as along the perimeter of the product.

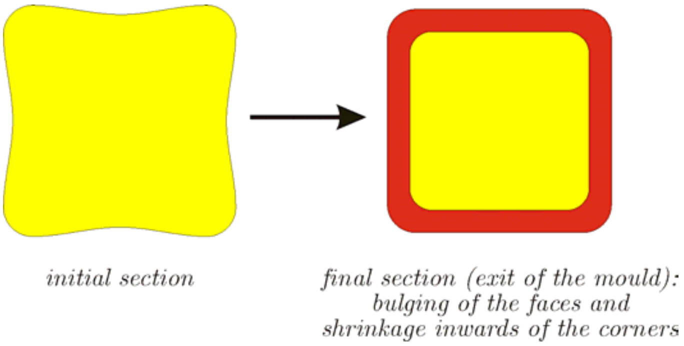

Figure 121: Ideal initial section (left) leading to 125mm square billet at the exit of the mould (right)

In a second step, real moulds with simple taper have been considered. Five different tapers have been modelled in order to show the importance of this parameter. As expected, the best heat extraction is obtained with a positive taper. However, the taper must be limited to avoid high stress development. To apply an automatic optimization of the mould taper, a criterion must be defined, taking into account mechanical and thermal aspects.

Concerning the validation of the results, some models from the literature are quite similar to the present model. Unhappily, they never exactly correspond to the same casting conditions and the comparison is thus quite difficult. However, one publication is worth noting: a new type of mould for billet casting is presented. To show the efficiency of this new mould, its manufacturer (Voest-Alpine Industrieanlagenbau – VAI) has used a 2D thermo-mechanical transient finite element model with 3 single taper moulds (0.2%/m, 0.8%/m and 1.3%/m) and its new mould, called DIAMOLD™. The Figure 122 shows the pressure distribution between the strand and the mould at middle height and at the exit of the mould.

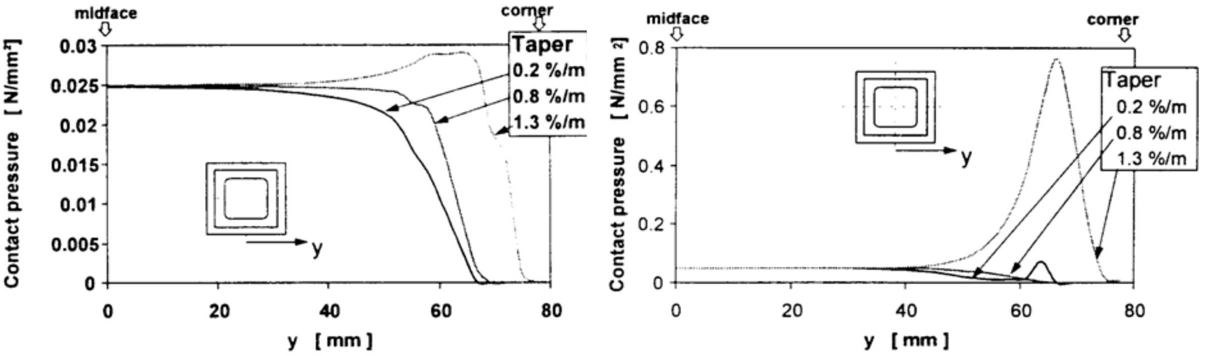

Figure 122: Pressure distribution vs. billet cross-section at middle height of the mould (left) and at the exit of the mould (right), model by [**MÖR98**]

In that case, highly tapered mould (1.3%/m) induces pressure peaks near the corner, resulting in drastically increased friction and stresses in the material.

Their conclusion is that there are two different requirements concerning the taper in the mid-face and in the corner region:

- an excessive taper in the mid-face provides homogeneous strand shell growth;
- a reduced taper in the corner area in the lower part of the mould ensures a limitation of the friction forces.

In other respects, it is well known from heat transfer measurements [BRI73,MAH91] that billet shrinkage is more intense in the upper part of the mould than in the lower part. For this reason it is recommended not to use a single taper, but rather a parabolic one for example. According to these remarks, a new mould has been designed as shown in Figure 123.

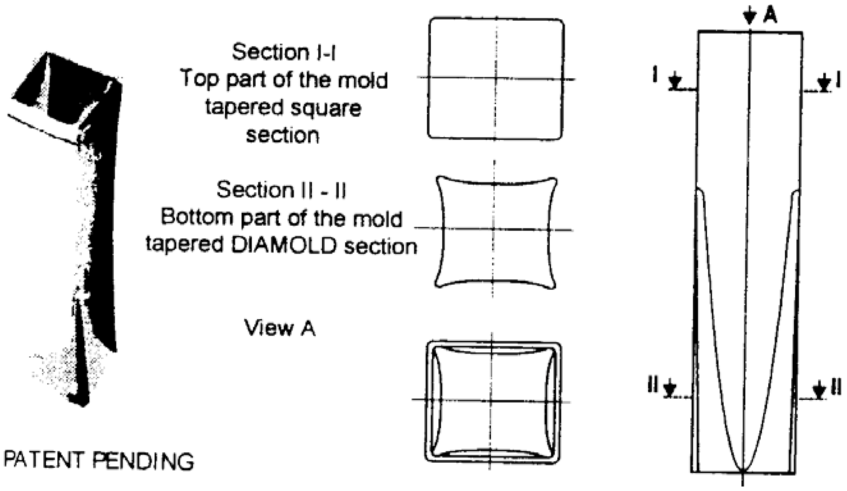

Figure 123: High speed billet casting, DIAMOLD™ [**MÖR98**]

The debate about the optimum taper remains open. However, it seems clear from the results of the LAGAMINE model that the taper of billet moulds must be different on the mid-face and the corner, what is confirmed by the position of VAI and its new mould. The excessive taper in the mid-face area admitted by this one can be linked to the stress field found in the LAGAMINE model (cf. Figure 115 and Figure 116). In fact, the stress in the mid-face area is mush lower than in the corner. That means that if no problem occurs in the corner (especially no interfacial cracks in the mushy zone), there is no reason that any problem occurs in the mid-face area. Thus a higher mould taper in this area cannot be dramatic.

Another advantage of the new mould proposed is linked to the bulging of the billet after the exit of the mould. In fact, one can expect that an incurved shape of the mould in the bottom zone provides to the billet a "negative" bulging, which is compensated by ferrostatic pressure when the billet is just coming out of the mould below the exit of this one. This could solve the problem mentioned at the beginning of this discussion (cf. Figure 121).

Globally, one can conclude that even if the model is able to represent the thermo-mechanical behaviour of the billet in the mould, the definition of the criteria to respect for an optimal taper still requires discussion and will be subject to modifications.

VI. 2nd Industrial application: Evaluation of risk of transverse cracking during bending and straightening of steel slabs & influence of some local defects

VI. 2nd Industrial application: Evaluation of risk of transverse cracking during bending and straightening of steel slabs & influence of some local defects

1. Geometry of the problem

1.1. Cast product

In this second application, the model is applied to a flat product (slab), the dimensions of which being 1200mm x 220mm at ambient temperature. The bending/straightening axis corresponds to the minimum principal moment of inertia. The cross section of the cast product presents a double symmetry with respect to its principal axes:

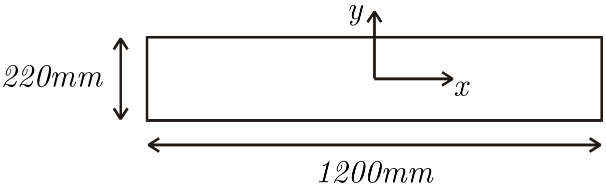

Figure 124: Cross section of the cast product at ambient temperature

Despite the double symmetry of the initial geometry, only the symmetry with respect to the y-axis is taken into account because bending introduces dissymmetry with respect to x-axis in terms of thickness, strains and stresses. So, one half of the strand is modelled, taking into account the only symmetry with respect to a vertical plane.

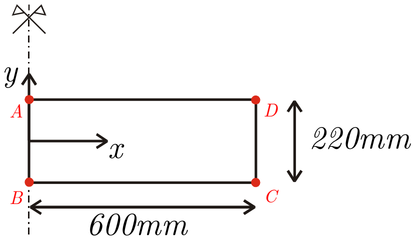

Figure 125: Half-slice of strand considering symmetry with respect to vertical plane

The following boundary limits can henceforth be applied along *AB* edge (see Figure 125):

- no displacement in *x* direction
- free displacement in *y* direction except for one node to avoid rigid body displacement (arbitrary, the node at the origin of the axes *x*, *y*)
- no heat flux in *x* direction (adiabatic wall)

Casting speed is 1.2m/min.

1.2. Caster geometry

1.2.1. *Radius of curvature*

The complete geometry of the caster will not be presented. However, some information about curvature can be useful. The caster is a vertical-curve machine, so that it can be characterized by:

- a vertical mould, the height of which being 900mm
- a 1st vertical zone below the mould and before bending zone, with 8 pairs of rolls the diameter of which being relatively small
- a 2nd zone corresponding to the bending of the strand up to a radius of curvature of about 8m, which is achieved progressively with 7 pairs of rolls
- a 3rd zone with constant curvature
- a 4th zone corresponding to straightening with 8 pairs of rolls
- a 5th horizontal zone

1.2.2. *Rolls geometry*

This caster is characterized by rather small cylinders, the diameter of which varying from 130mm below the mould up to 275mm at the end. The distance between two rolls of one pair – the aperture left for the slab passing – gives the maximum thickness of the slab.

Since the slab is globally cooling when moving towards the caster, thermal shrinkage could cause bad contact between rolls and slab. The aperture between the rolls is thus decreasing step by step.

In other respect, after straightening, the aperture is reduced by 0.1mm every roll step. This is tapering of the rolls is the “soft reduction” technique which is used in slab casting to counteract solidification shrinkage and reduce macrosegregation in the centre of the section [BAR98,BAR00]. In some casters, the position of the soft reduction can be modified in order to adapt it to transient casting conditions (dynamic soft reduction [LIN98]). But this is out of purpose, since soft reduction in the present caster is located after straightening.

Note that the model is used to determine the risk level of transverse cracks formation during bending and straightening, so the caster is modelled up to one segment (five pairs of rolls) after the end of straightening.

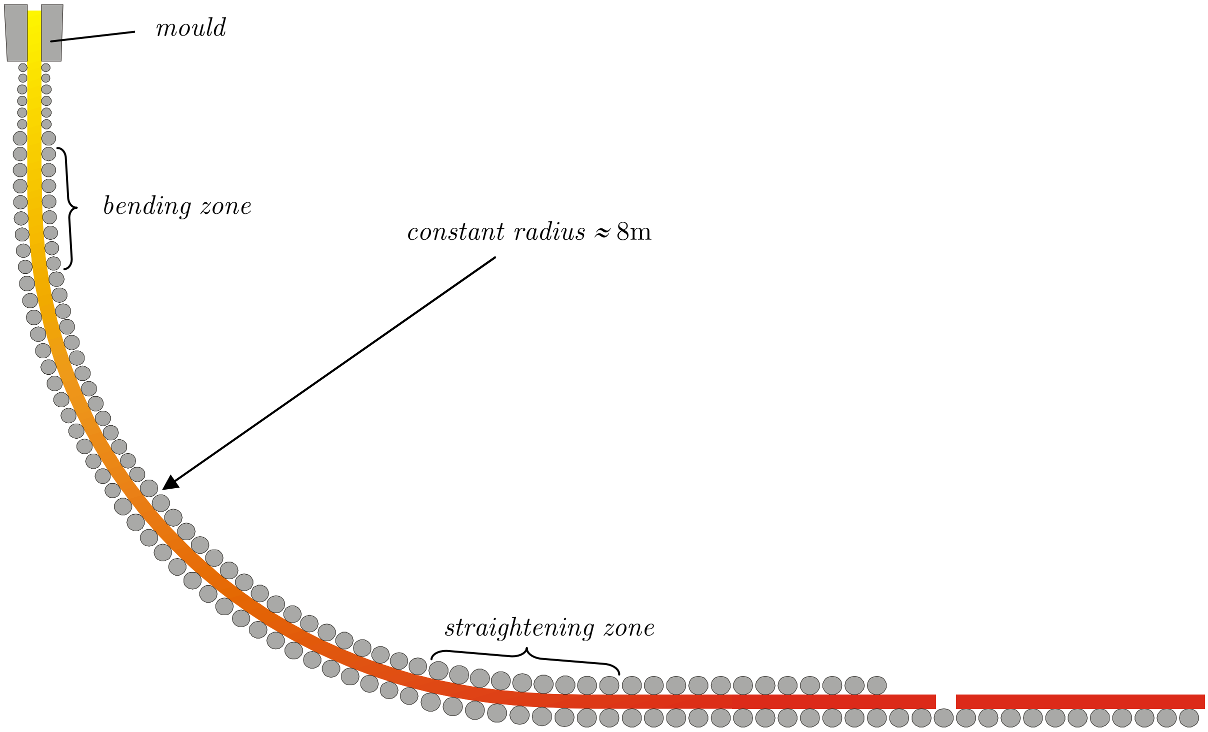

Figure 126: Sketch of the caster

1.2.3. Water spray cooling

Secondary cooling is performed using water spray systems, which can be schematically represented as follows:

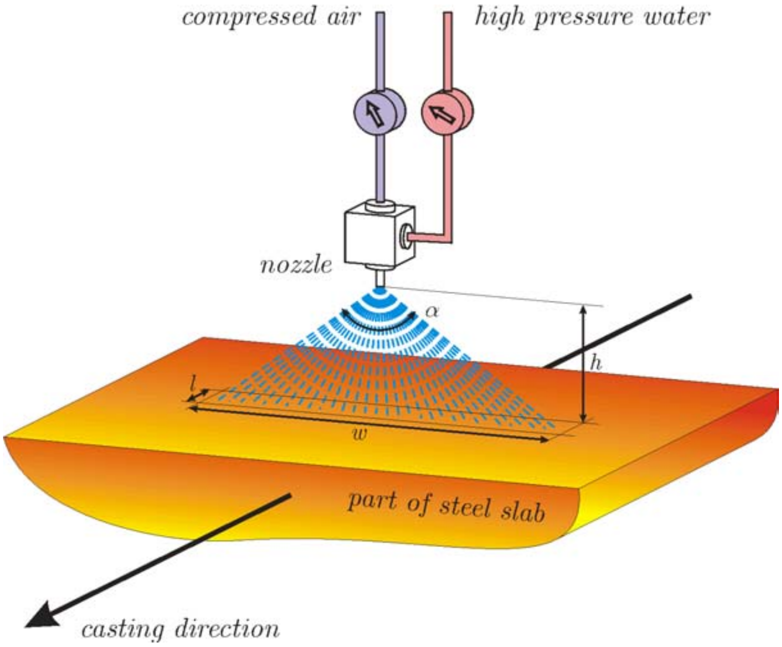

Figure 127: Water spray cooling (secondary cooling)

A nozzle is characterized (among others) by the angular aperture α and the distance h with respect to the strand surface (see Figure 127). The width of the sprayed area is thus given by:

$$w = 2h \tan\frac{\alpha}{2} \tag{304}$$

In the direction of casting, the length l of spraying is quite similar for each type of nozzle and rather narrow with respect to the other direction. Typically, $w \approx$ 400-1000mm, while $l \approx$ 40-70mm. The reason is the topology of the caster: in fact, successive rolls are relatively close and the gap is such small that the angular aperture θ of the spray in casting direction is limited, as pictured on Figure 128:

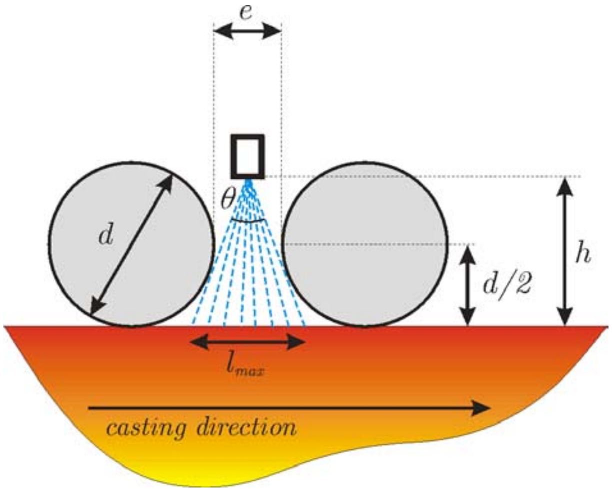

Figure 128: Limited aperture θ of the spray in casting direction

As it clearly appears, the maximum length $l_{\max}$ is given by:

$$\frac{l_{\max}}{h} = \frac{e}{h - \frac{d}{2}} \leftrightarrow l_{\max} = \frac{2eh}{2h - d} \tag{305}$$

For example, between rolls #7 and #8, we have the following values:

$$l_{\max} = \frac{2.35.210}{2.210 - 215} \simeq 72mm \tag{306}$$

Since the water sprays cannot cover the whole slab surface, it remains some zones in the shade of rolls. It is thus possible to define 4 types of heat loss zones (see Figure 129), which recur all along the caster.

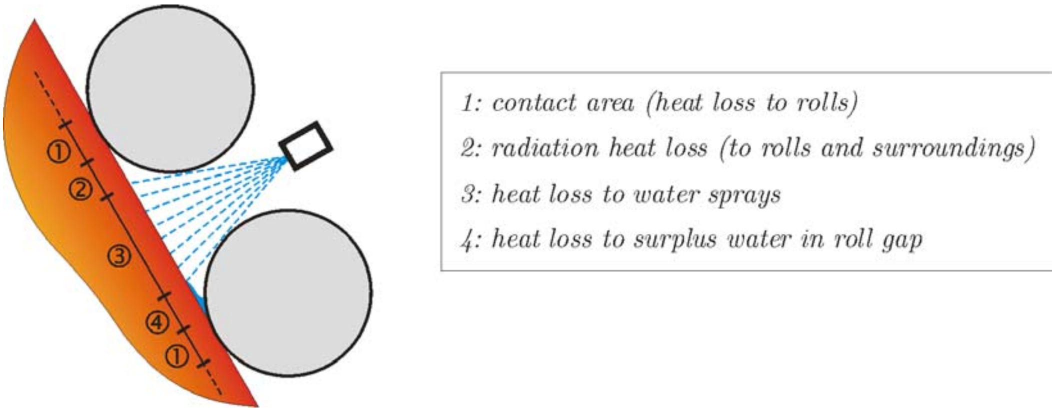

Figure 129: Different and repetitive heat losses

1. first type is the contact zones between the slab and the support rolls;
2. second one is characterized by radiation heat loss to rolls and surroundings – these zones are in the shade of the preceding roll;
3. third type in under the water sprays;
4. fourth and last type, where surplus water flows from the sprayed zone down to the next roll, accumulating in the roll gap.

2. Thermal and mechanical parameters

2.1. Steel grade and material properties

For evident reasons of confidentiality, steel grade and material properties are not published in details here. However, consider a low carbon steel. Most of material parameters have been provided by IRSID for such a grade, except for heat transfer coefficients under sprays. These coefficients have been determined experimentally for:

- 6 surface temperatures (700-800-900-1000-1100-1200°C)
- 4 models of nozzles present on the caster
- 4 water flow rates

For each test, heat transfer coefficient has been determined at 4 distances from the nozzle (first one plumb and three others further: see Figure 130).

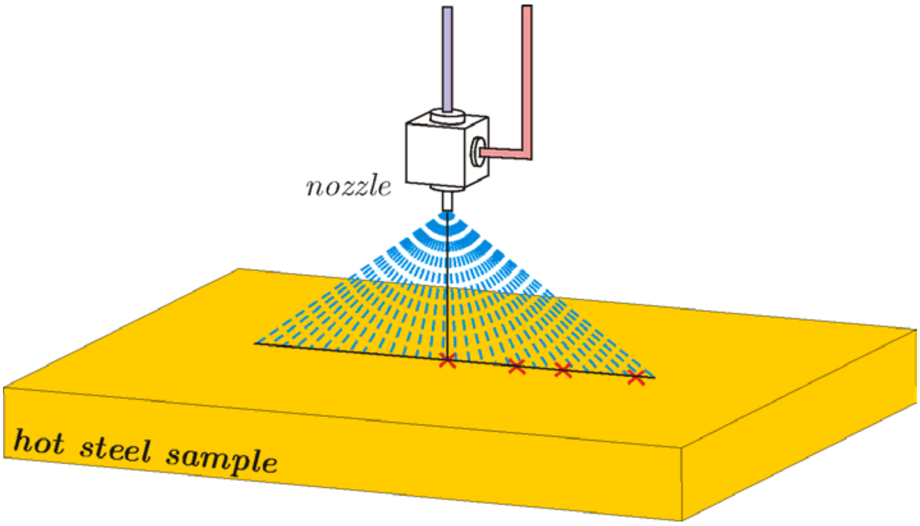

Figure 130: Measurements of heat transfer coefficients at 4 distances from the nozzle

In the transversal direction, several nozzles (up to 4) can be used to insure high cooling rate right across the slab. This configuration creates overlap of sprayed areas, as shown on Figure 131.

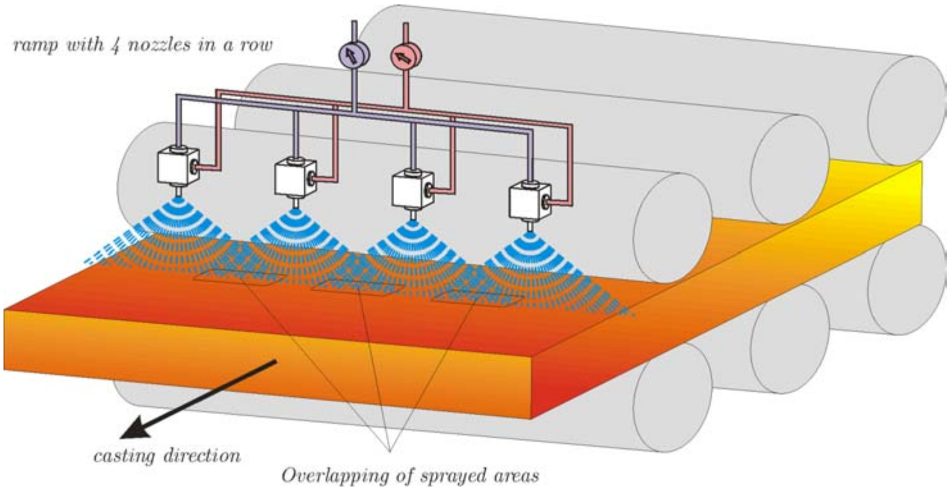

Figure 131: Ramp with four nozzles in a row and overlap of sprayed areas

In such a case, heat transfer coefficient should take into account the sum of both water flow rates in overlap zones.

Note that heat transfer coefficients have also been measured for water flow rate equal to zero. These measurements correspond approximately to zones in the shade of a roll defined on Figure 129. A complete data collection of heat transfer coefficients is thus available in the model.

2.2. Bulging control

2.2.1. Bulging with slice models

Because of ferrostatic pressure, the slab is bulging between successive rolls. The Figure 132 shows in 7 steps how a slice bulges from one pair of rolls to the next in the caster:

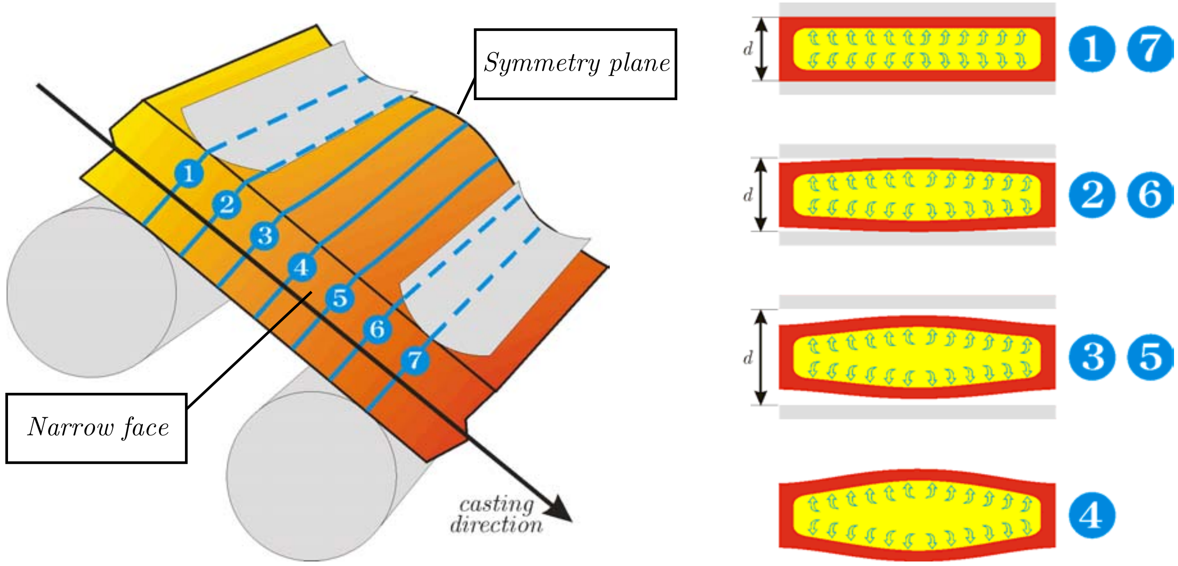

Figure 132: Bulging of the slice between two successive pairs of rolls

- When the slice is at the level of the axes of the first pair, the slice is gripped between the rolls (1). The thickness of the slice is equal to the aperture between the two rolls. This distance is the reference for bulging evaluation, which is equal to zero in this position.

- Then, while the slice is going further in the caster (2), the apparent distance *d* between the rolls becomes higher. In fact, this distance *d* is measured between the intersections of both rolls with the plane of the slice. Since slab corners are less hot and thus more rigid, but also because of the "frame" shape of the solidified shell, bulging is larger in the middle of wide faces, where contact is maintained, while contact is quickly lost close to the edges of the slab (in the corners).
- After a given time, contact between slab and rolls is lost all around the slice (3). Bulging is not limited by the rolls anymore, but by the material behaviour.
- Maximum bulging in reached in (4), not necessarily at mid-distance between the two pairs. This maximum is limited by the shell behaviour in the casting direction.
- The presence of the next pair enforce the bulging to decrease (5) and the contact occur in (6), starting from the middle of wide faces and finally expanding to the whole faces (7)

A classical 2D "slice" model is not able to predict such a bulging. Even the 2D½ approach cannot do that. The reason is the lack of shear stress in the out-of-plane direction. The absence of such a stress does not allow transmitting shearing force, which is of prime importance. Considering a vertical slice in the vertical plane of symmetry of the caster - ! not in the same axes than the modelled slice – see Figure 133:

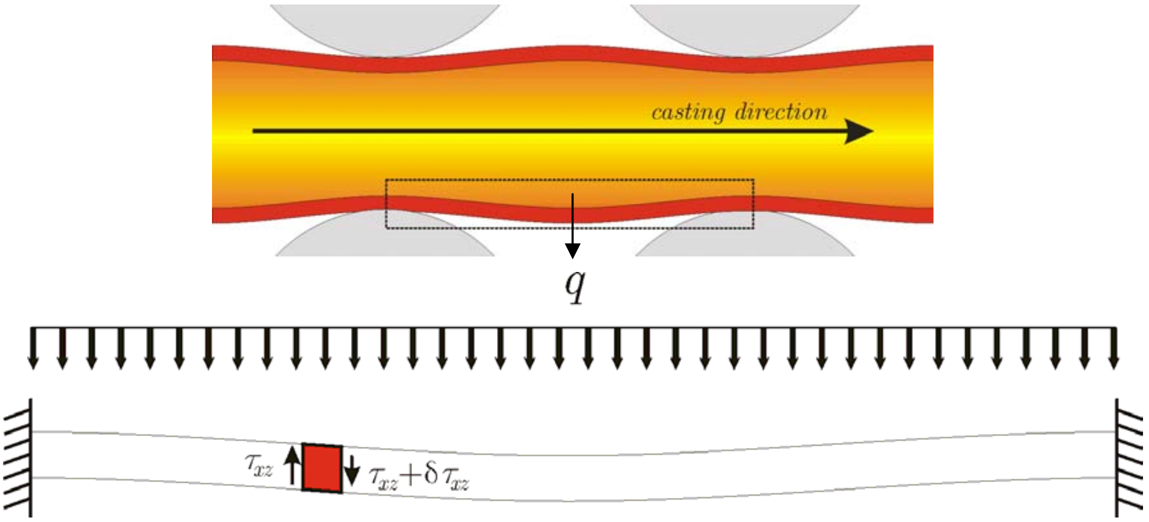

Figure 133: Shear force transmission in the casting direction

The solidified shell under ferrostatic pressure bulges and its deflection is analogous to the one of a beam clamped at both extremities and under uniformly loaded.

In lack of transmission of shear stresses, each slice (perpendicular to casting direction) bulges independently of the behaviour of the previous and the next slice, giving globally a bulging the type of is:

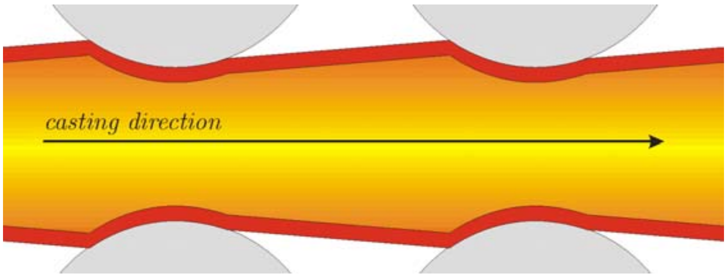

Figure 134: Bulging of the slice in lack of shear stress in casting direction

The problem of slice models is thus the lack of transmission of shear force from one slice to the next, what could be introduced, but also from the next slice, what is unknown. The first results obtained with the model were completely wrong, with bulging 10 to 100 times too large. A solution had to be found.

3D models allow modelling such bulging, but they are more CPU time expensive. Continuing with the 2D½, the following solution has been tested.

2.2.2. *Bulging based on elastic plates theory*

Consider the slab in lack of rolls: it bulges freely, like a tube under pressure. The bulging would be similar to the one pictured on Figure 135. Each wide face is bulging more or less like a plate clamped along two opposite edges and uniformly loaded is deflecting – see Figure 136.

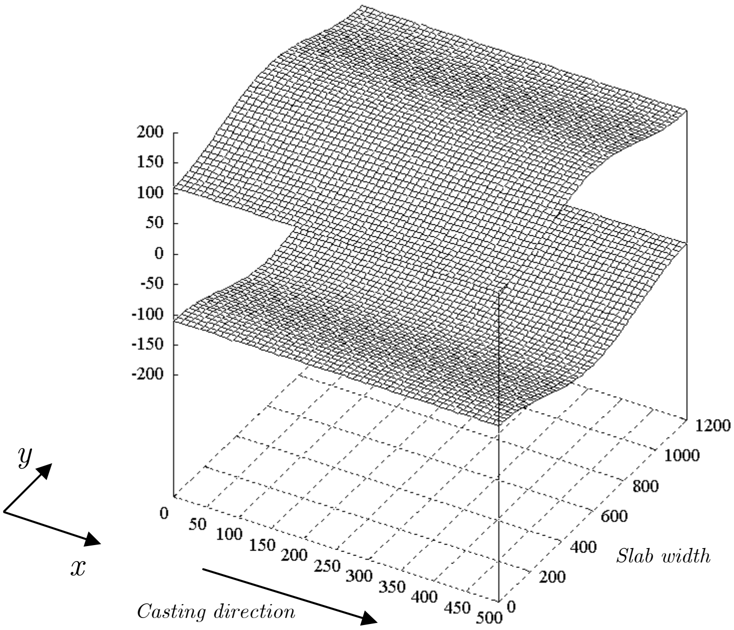

Figure 135: Wide faces of a portion of slab bulging without rolls

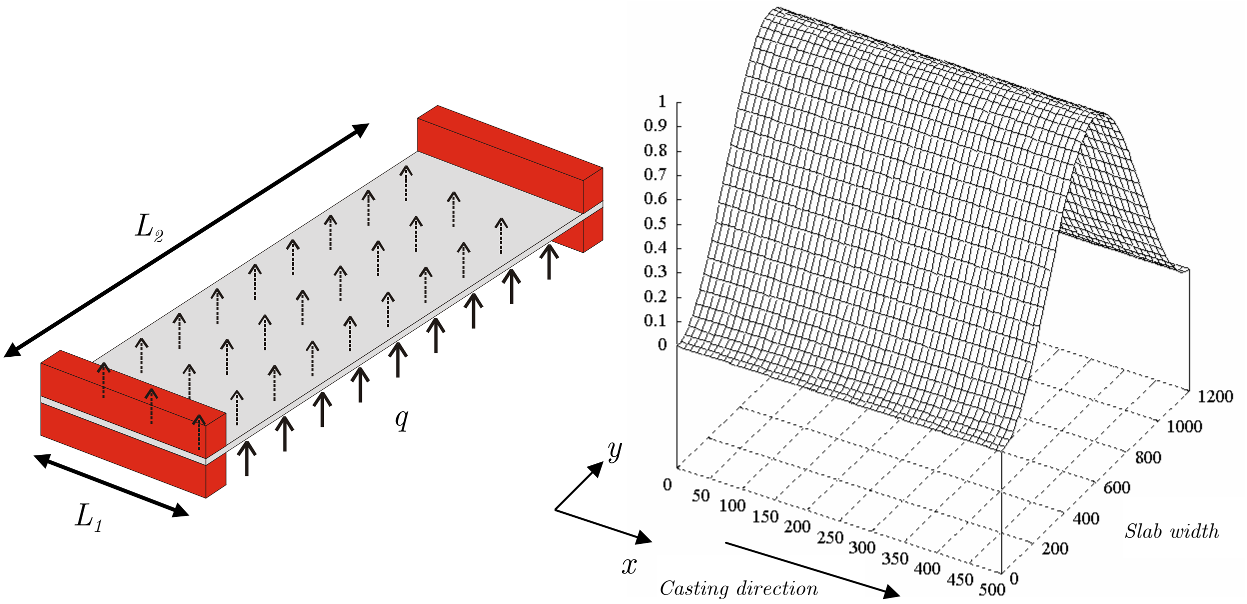

Figure 136: Deflection of a uniformly loaded plate clamped along two opposite edges

Assuming elastic linear behaviour of the plate, the deflection $w_1(y)$ of such a plate is given by:

$$w_1(y) = \frac{qL_2^4}{\pi^4 \dfrac{Eh^3}{1-\nu^2}} 1.5 \left[1-\cos\left(\frac{2\pi y}{L_2}\right)\right] \tag{307}$$

where q is the uniform loading, E elastic modulus, ν Poisson's coefficient, h the thickness of the plate and L_2 the span of the plate between clamped edges (corresponding to slab width). This corresponds approximately to the bulging of the slab with slice models (shear stress τ_{xz} being equal to zero), except that the no-penetration of slab in the rolls limits the bulging as follows:

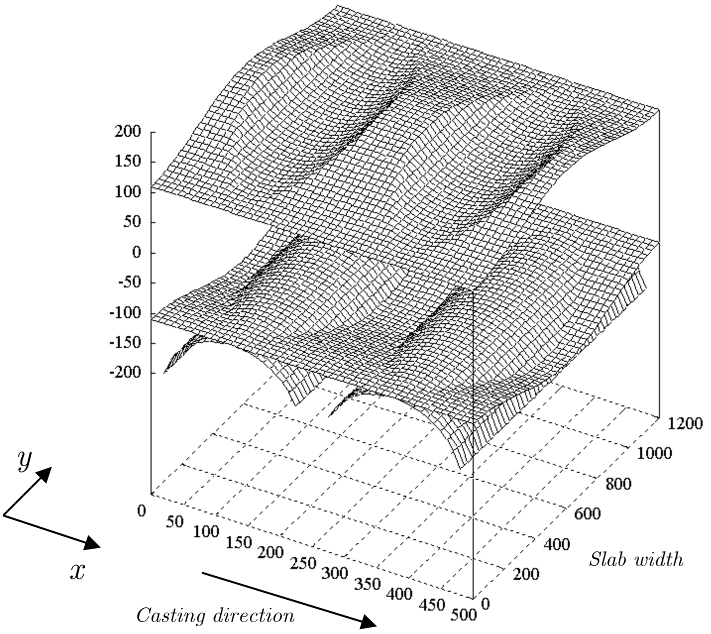

Figure 137: Bulging with slice models, only limited by the no-penetration in rolls

Actually, the bulging of the slab corresponds rather to the deflection of uniformly loaded plate clamped along its four edges:

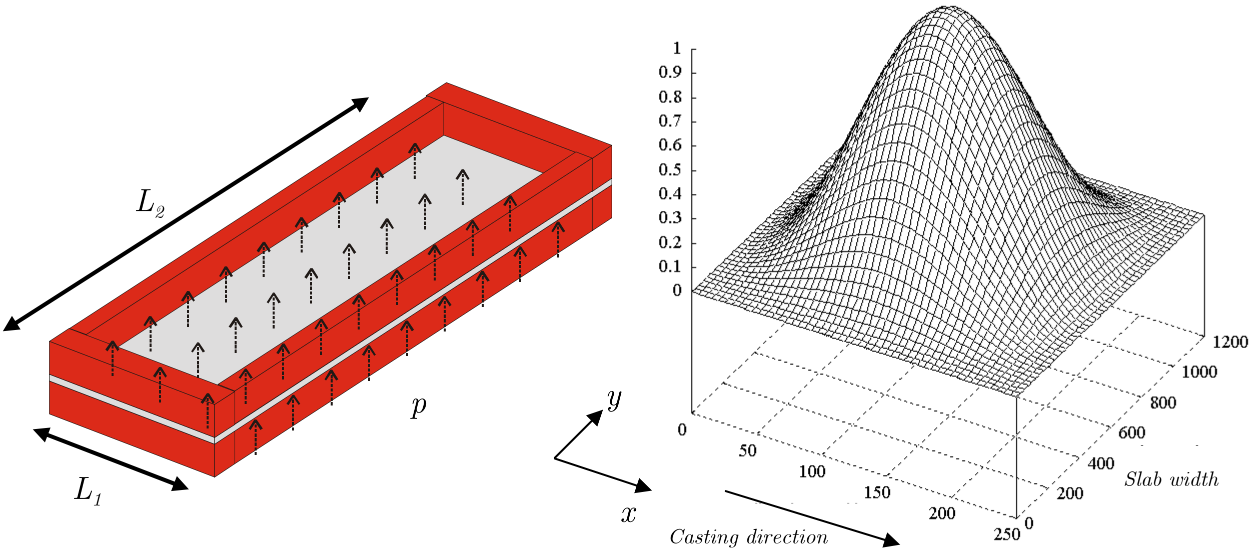

Figure 138: Deflection of a uniformly loaded plate clamped along its four edges

In such a case, shear stress τ_{xz} is not equal to zero. Assuming again linear elasticity, the deflection $w_2(x,y)$ of such a plate is:

$$w_2(x,y) = \frac{pL_2^4}{\pi^4 \dfrac{Eh^3}{1-\nu^2}} \frac{1}{\left(\dfrac{L_2}{L_1}\right)^4 + \dfrac{2}{3}\left(\dfrac{L_2}{L_1}\right)^2 + 1} \left[1 - \cos\left(\frac{2.\pi.x}{L_1}\right)\right]\left[1 - \cos\left(\frac{2.\pi.y}{L_2}\right)\right] \tag{308}$$

where p is the uniform loading, E elastic modulus, ν Poisson's coefficient, h the thickness of the plate and L_1 and L_2 are spans respectively along x and y directions (casting direction and width of the slab). If the bulging could follow such a shape, and taking into account the no-penetration condition, it would be something like:

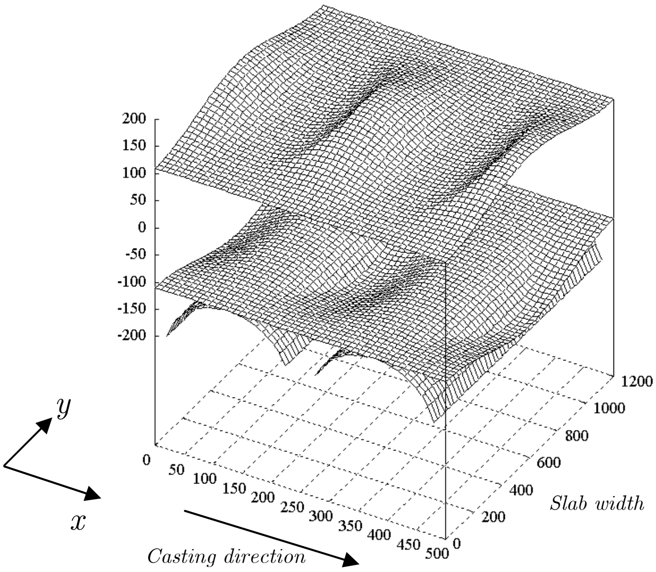

Figure 139: Wide faces of a portion of slab bulging with rolls and shear stress

A quick computation of maximum bulging with typical parameters in continuous casting can be operated with relations (307) and (308). Considering:

- $p = q = p_f = 0.2\mathrm{N/mm^2}$ (equivalent to about 3m of fluid pressure)
- $E = 10\mathrm{GPa}$ (corresponding to a temperature in the range of 1300-1400°C)
- $\nu = 0.3$
- $h = 30\mathrm{mm}$
- $L_1 = 250\mathrm{mm}$
- $L_2 = 1200\mathrm{mm}$

The maximum deflections (bulging) would be:

$$\begin{cases} w_1\left(\dfrac{L_2}{2}\right) \simeq 40\mathrm{mm} \\ w_2\left(\dfrac{L_1}{2},\dfrac{L_2}{2}\right) \simeq 0.1\mathrm{mm} \end{cases} \tag{309}$$

This proves that if the shear stress is not taken into account, the maximum deflection can be several magnitudes larger than it should be (here: 400 times).

To reduce bulging obtained with the slice model, it was necessary to introduce an additional force, which could simulate the application of shear force. The evaluation of such a force is not trivial. However, the result is rather well known: the force should lead to obtain a bulging similar to the one defined by relation (308). To do so, springs have been introduced in the model, for each node on the wide faces. The stiffness of the springs is added to the stiffness of the solidified shell, so that the bulging under ferrostatic pressure is reduced since the effort is partly balanced by the springs and the solidified shell:

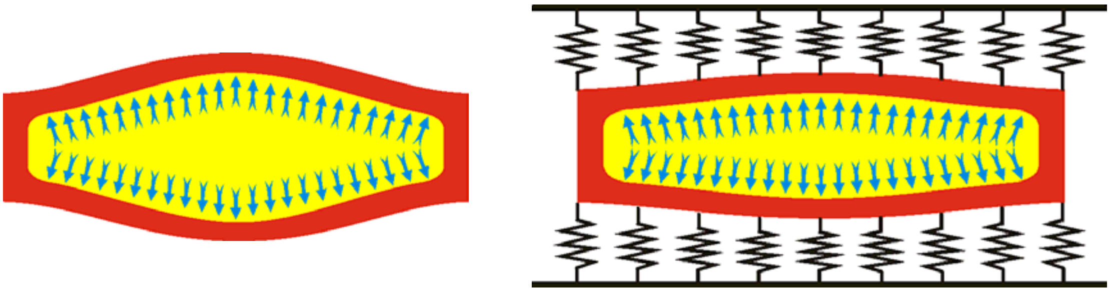

Figure 140: Reduction of slice bulging under ferrostatic pressure – without springs (on the left) and with springs (on the right)

Since the model remains a slice model, the bulging is given by relation (307). However, because of the introduction of springs, only a part of the ferrostatic pressure p_f is applied on the solidified shell, this part q being equal to:

$$q = p_f - f \tag{310}$$

where f is the force in the springs (per unit surface). The applied force q being reduced, the bulging $w_1(y)$ is also reduced and the higher the stiffness of the springs is, the lower the bulging is.

Now considering that the stiffness of the springs is varying in time (so with respect to casting direction), the loading part q also becomes a function of time, or x:

$$q(x) = p_f - f(x) \tag{311}$$

which means that the bulging varies also with respect to casting direction:

$$w_1(x,y) = \frac{q(x)L_2^4}{\pi^4 \dfrac{Eh^3}{1-\nu^2}} 1.5 \left[1 - \cos\left(\frac{2\pi y}{L_2}\right)\right] \tag{312}$$

That way, the bulging has always the shape of a cosine curve, but the amplitude of the "wave" can be modified with the stiffness of the springs.

Now, to obtain a bulging equivalent to relation (308), the value of the pressure *q(x)* can be computed thanks to the equality:

$$w_1(q,x,y) = w_2\left(p_f,x,y\right) \tag{313}$$

or

$$\frac{q(x)L_2^4}{\pi^4 \dfrac{Eh^3}{1-\nu^2}} 1.5 \left[1 - \cos\left(\frac{2\pi y}{L_2}\right)\right] = \frac{p_f L_2^4}{\pi^4 \dfrac{Eh^3}{1-\nu^2}} \frac{\left[1 - \cos\left(\dfrac{2.\pi.x}{L_1}\right)\right]\left[1 - \cos\left(\dfrac{2.\pi.y}{L_2}\right)\right]}{\left(\dfrac{L_2}{L_1}\right)^4 + \dfrac{2}{3}\left(\dfrac{L_2}{L_1}\right)^2 + 1} \tag{314}$$

$$\leftrightarrow \qquad q(x) = \frac{p_f}{1.5} \frac{1 - \cos\left(\dfrac{2.\pi.x}{L_1}\right)}{\left(\dfrac{L_2}{L_1}\right)^4 + \dfrac{2}{3}\left(\dfrac{L_2}{L_1}\right)^2 + 1} \tag{315}$$

The relation (315) defines the load *q(x)* that must be applied to the slice model in order to obtain a bulging equivalent to a 3D model, the bulging of which would be given by relation (308).

To obtain such a load *q(x)*, the springs must balance an effort given by:

$$f(x) = p_f - q(x) \tag{316}$$

In other respect, the elongation of the springs w_3 is equal to the bulging of the slab:

$$w_1(q,x,y) = w_2\left(p_f,x,y\right) = w_3(f,x,y) \tag{317}$$

So the stiffness of the springs k must be equal to:

$$\begin{aligned} k(x,y) &= \frac{f(x)}{w_3(f,x,y)} = \frac{p_f - q(x)}{w_1(q,x,y)} = \frac{\dfrac{p_f}{q(x)} - 1}{\dfrac{L_2^4}{\pi^4 \dfrac{Eh^3}{1-\nu^2}} 1.5\left[1-\cos\left(\dfrac{2\pi y}{L_2}\right)\right]} \\ &= \left[1.5\frac{\left(\dfrac{L_2}{L_1}\right)^4 + \dfrac{2}{3}\left(\dfrac{L_2}{L_1}\right)^2 + 1}{1-\cos\left(\dfrac{2\pi x}{L_1}\right)} - 1\right]\frac{\pi^4 \dfrac{Eh^3}{1-\nu^2}}{1.5L_2^4\left[1-\cos\left(\dfrac{2\pi y}{L_2}\right)\right]} \end{aligned} \tag{318}$$

2.2.3. <u>Extension of the method</u>

In the previous section, a rather simple method has been introduced to control the bulging of the slab. Thanks to the introduction of springs and controlling their stiffness, it is possible to impose a slice to bulge following a given surface equation – relation (308).

Using this approach, the maximum bulging do not correspond exactly to the one observed on the caster. In fact, it would be utopian to believe that the bulging follows the equation of an elastic plate: the material is not elastic (but rather viscoplastic with creep effect), temperature (thus material behaviour) is not uniform towards the shell thickness, and ferrostatic pressure is not constant from one roll to the next one. Therefore, it was not surprising to obtain bulging quite different from the real one. However:

- the shape of bulging is much closer to the real one than with the "simple" slice models (without springs);
- an amplification factor can be applied to the spring stiffness to fit the maximum bulging on a reference value (from measurement on the caster or from a bulging model).

In the present application, these reference values have been computed by IRSID. The input data are: the ferrostatic pressure, the roll pitch (distance between two successive contacts with the rolls), the thickness of the solidified shell, the surface temperature, the Young's modulus, the consistency and the sensibility to strain and strain rate of the material. The maximum bulging according to the casting conditions is represented on Figure 141.

Obviously, any other surface equation than relation (308) can be supplied to the model. Such a relation can be found with analytical or numerical models. Literature supplies many examples of study of bulging in many different conditions and under different assumptions [KAN97,REN98,HA01,TOY02].

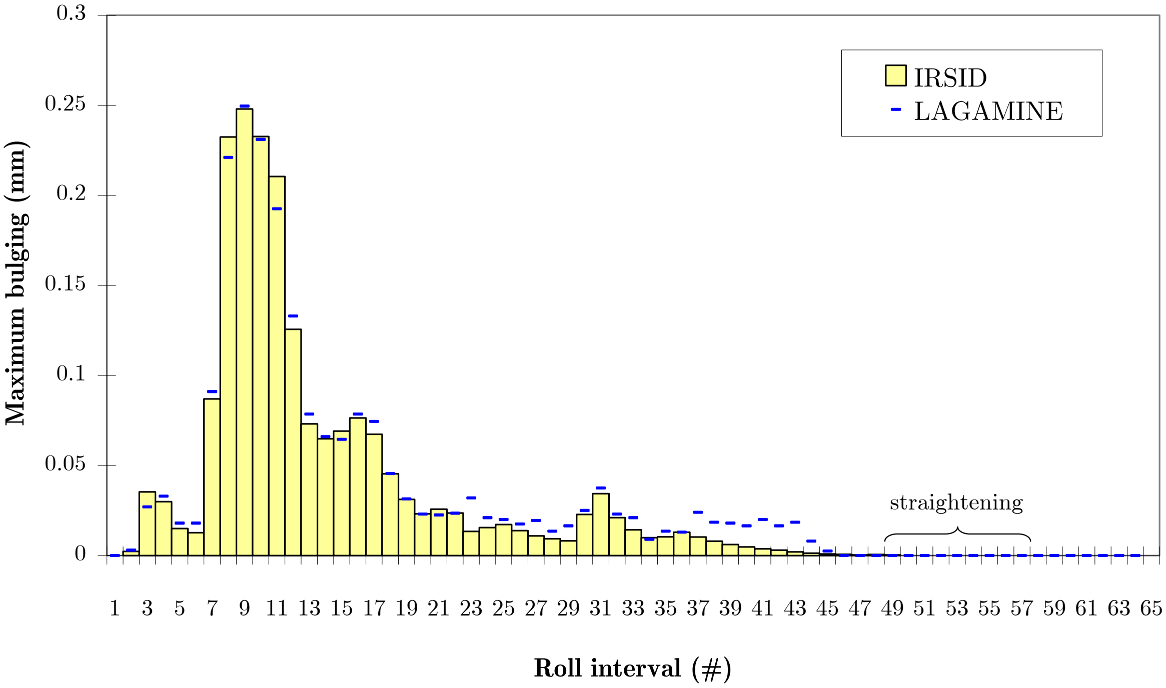

Figure 141: Maximum bulging of the slab for each roll interval in the caster – Comparison IRSID model (input data) and result with LAGAMINE model

2.3. Extraction force

2.3.1. Evaluation of extraction force: coupled approach

As already explained in section III.1.3.1, there are two contributions δR_1 and δR_2 to the global resisting force δR in the caster.

To determine δR_1, one only has to multiply the adequate friction coefficient by the effort δF_1 of the slab on the rolls due to bulging. This can be obtained by the integration of contact pressure. However, the introduction of springs (see previous section VI.2.2) strongly modifies the contact pressure, which becomes equal to zero. Instead of contact pressure, one can use efforts in the springs where the contact is assumed to occur, but this is not trivial.

For the second contribution δR_2, another difficulty comes about: as already mentioned, during bending (or straightening) the slab is similar to a hyperstatic beam on many fixations (87 pairs of rolls + mould). Moreover, the slab is not elastic and not homogenous: its properties varying along the caster, but also in a given slice (liquid in the centre, solidified on the perimeter).

Despite these problems, an attempt of evaluation of resisting force has been carried out. The following assumptions have been considered:

- For δR_1 computation, a contact area of 10mm along casting direction have been assumed (cf. Figure 142), so that the contact force δF_1 is given by:

$$\delta F_1 = \sum_{contact} F_{springs} \tag{319}$$

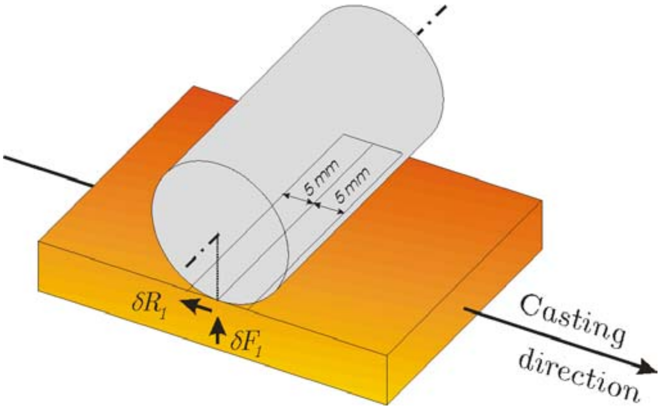

Figure 142: Assumed contact zone for computation of δF_1

- For δR_2, which depends of δF_2, the behaviour of the slab has been compared to a beam with plastic hinges (cf. Figure 143). In such a beam, one can consider that:

$$\delta F_2 = \frac{\delta M_2}{L} \tag{320}$$

  where L is the distance between pair of rolls $\#i$ and $\#i{+}1$ and δM_2 the bending moment at the level of pair $\#i$, which is the resultant of the longitudinal stresses σ_{zz} multiplied by the distance y to neutral axis:

$$\delta M_2^{(i)} = \int_{slice} \sigma_{zz} y \mathrm{d}s \tag{321}$$

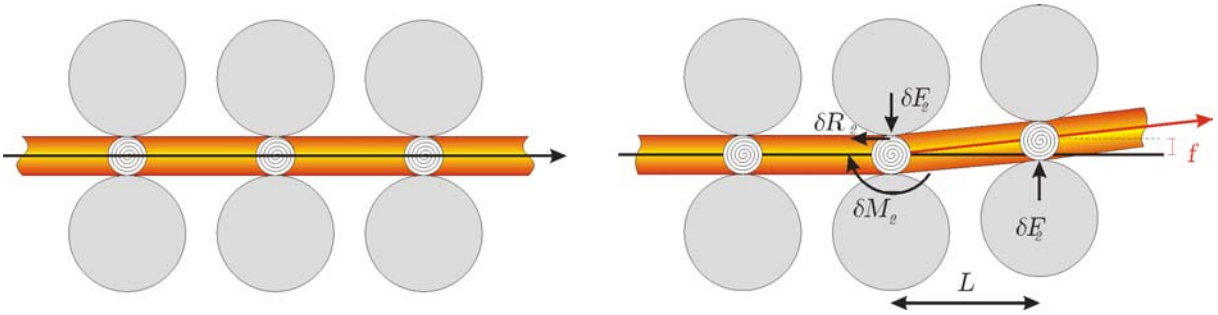

Figure 143: Bending of beam with plastic hinges

Summing these contributions and integrating the resisting force, it is thus possible to apply this external force on first degree of freedom of the generalized plane strain state. This force is added to the integration of the out-of-plane stresses σ_{zz} computed in the Norton-Hoff mechanical constitutive law and the equilibrium equation provides the thickness of the slice (cf. section III.1).

According to the assumption of distribution of work among extracting rolls (cf. III.1.3.2), the extracting force is set equal to zero when a pair of extracting rolls is reached.

2.3.2. Curves of extraction force from the caster manufacturer: uncoupled approach

Some curves of extraction force from the caster manufacturer are available. The first one (Figure 144 – continuous curve) represents the cumulated resisting force in normal conditions. The way to read this curve is the following: each pair of rolls contributes to the resisting force. The addition of each contribution from the first pair gives a cumulated resisting force, which increases step by step. For example, considering all the pairs up to 20m from the free surface, the total resisting force is 60t. The total resisting force can be read at the end of the curve: about 70t. That means that the total extraction force, which is distributed in several points of the caster (extracting rolls), must be equal to 70t.

In other respects, on the same figure, a discontinuous curve represents the potential extraction force of the caster. Each step of this curve corresponds to the maximum extraction force that an extracting roll can provide to the system. At the end of the caster, the continuous curve must be below the discontinuous one. Otherwise, the slab would be locked in the caster, the maximum extraction force (about 175t) being less than the resisting force.

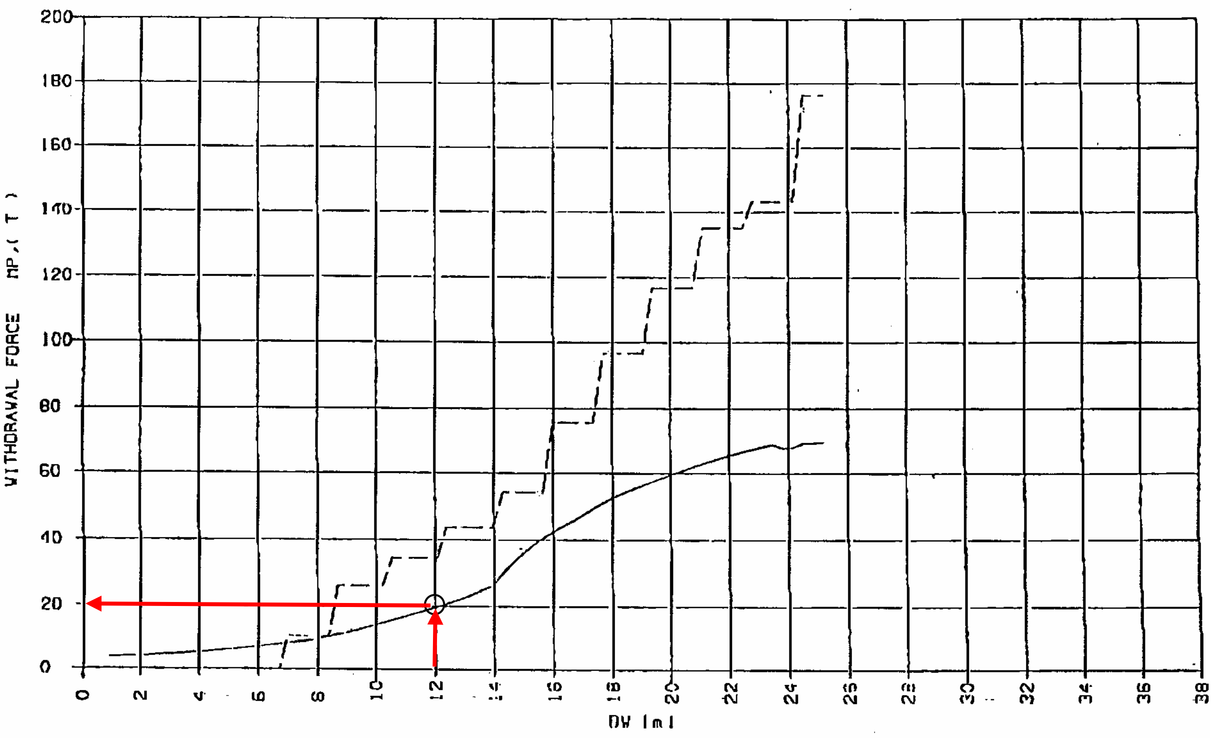

Figure 144: Cumulated resisting force in normal conditions (continuous curve) and total potential of extraction force (discontinuous curve)
– From caster manufacturer –

The effective longitudinal effort in the slab is equal to the cumulated resisting force minus the cumulated extracting force: it increases at each roll step and decreases when an extracting roll is reached. Another curve from caster manufacturer is available: this one shows the effective longitudinal effort in the slab in normal conditions (see Figure 145). It is equivalent to the continuous curve of Figure 144 (cumulated resisting force), except some decreasing steps corresponding to every extracting rolls.

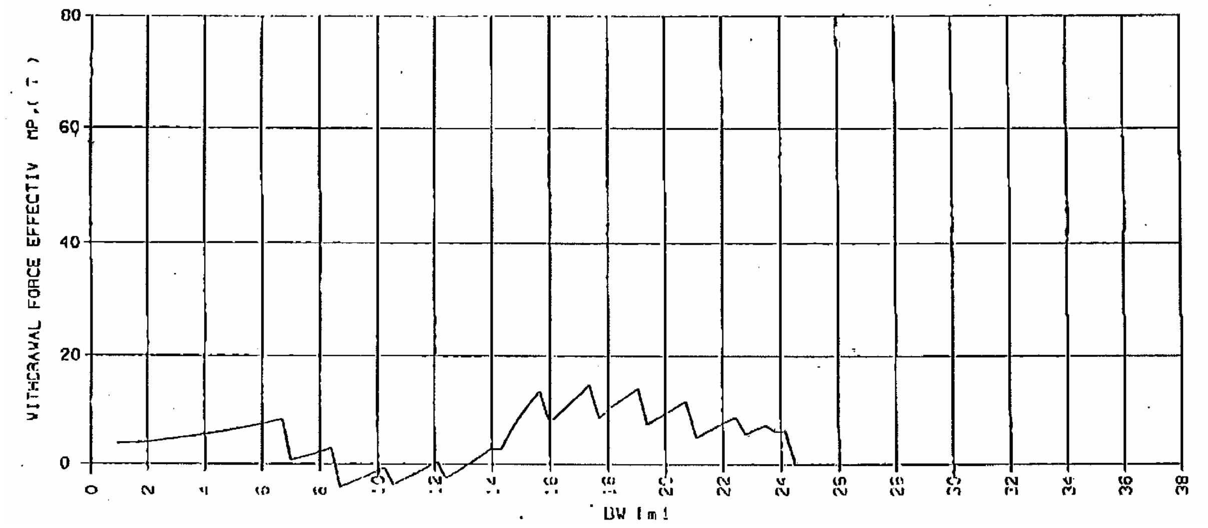

Figure 145: Effective longitudinal effort in the slab in normal conditions
– From caster manufacturer –

The amplitude of the step is equal to the extraction effort. It is thus possible to measure on this curve the extraction effort of each pair, as shown on Figure 146.

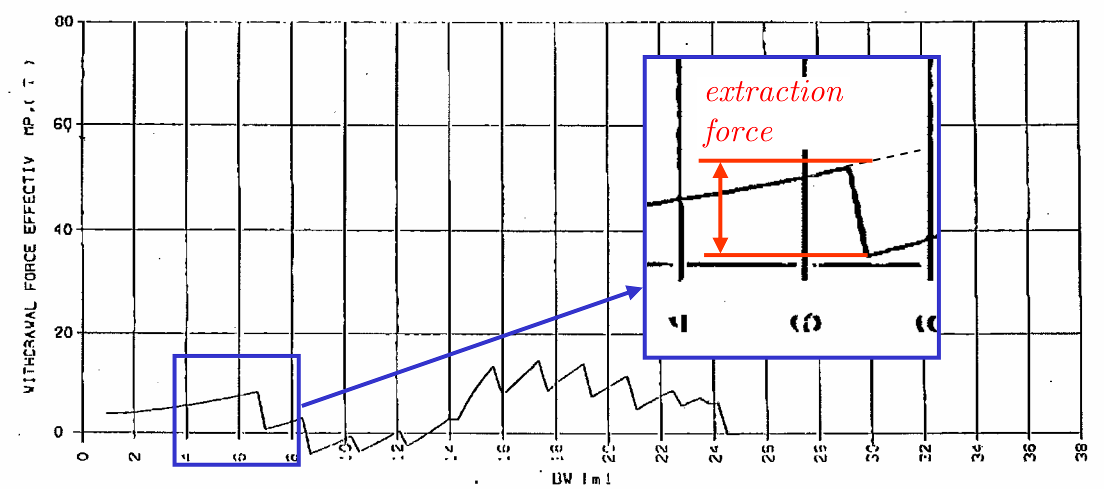

Figure 146: Measurement of extraction effort made by pair #26

This approach is qualified of "uncoupled" approach at the opposite of the previous one (section VI.2.3.1). In fact, the in-plane forces δF_1 and δF_2 are computed in both approaches, but only the first one couples the value of δR_1 and δR_2 to in-plane forces, while the second one consider imposed value (from the curves of the caster manufacturer).

2.3.3. Which curve to use?

On one hand, curves from manufacturer are very practical, because it is possible to apply directly in the model the effective longitudinal effort from these curves. However, they are available only in standard casting conditions, i.e. without any local defect.

On the other hand, the methodology presented above to evaluate the effective longitudinal effort rests on some assumptions that can lead to discussion. Moreover, the obtained values are coupled to the behaviour of the slice in its plane, so that computing time and convergence path are longer.

When manufacturer curves are available, they can be considered as input data. Otherwise, coupled approach has to be used. So in the following results, only uncoupled approach has been used, except for roll misalignment: in that case both approaches have been necessary to evaluate the effect of such type of defect (see details in section VI.4.3.1).

2.3.4. Weight of the slab

Actually, the resisting force R is balanced by driving forces: up till now, only force applied by extracting rolls F has been considered, but the weight of the slab W is a second driving force. One can write:

$$R = F + W \tag{322}$$

According "coupled" approach above (section VI.2.3.1), the longitudinal force applied in the model derives directly from the resisting force. Thus, this assumes that driving forces are balancing R, whatever these forces could be.

At the opposite, in the "uncoupled" approach (VI.2.3.2), when the curves of caster manufacturer are used, the applied force F corresponds only to what these curves represent: they are based on measurements of the electric power supplied to the caster. So they only represent one part of driving forces, the missing part precisely being the weight of the slab W. In such a case the weight is neglected.

What to think about this? In the lower part of the caster (and notably in straightening zone), the slab is (almost) horizontal and it is supported by the rolls. The weight of the slab is thus (almost) in the plane of the slice and it does not affect the value of the longitudinal loading of the slab, which is a major factor in the transverse cracking.

In the upper part of the caster, the weight is corresponding to casting direction (vertical). However, since the slab is bulging, it is also supported on the rolls, as shown on Figure 147. Considering the slab to be divided in sub-sections supported by two rolls, the maximum longitudinal tensile stress would be obtained considering each sub-section to be suspended.

In such a case, the maximum longitudinal loading is equal to the weight of the sub-section dW. A rough magnitude of dW can be obtained by:

$$W_{per\ meter} = \rho_{mean}.S = 7.5\frac{t}{m^3}\times 1{,}2m\times 0{,}220m \simeq 2\frac{t}{m} \tag{323}$$

which represents the weight of one meter of slab. In the upper part of the caster, typical length of such a sub-section is about 200 to 275mm. Thus the magnitude of the weight of a subsection (and thus of the maximum driving force *W)* could be from 0,4t to 0,55t, which is slight enough to be neglected with respect to longitudinal loading in this part of the caster (about 5t, i.e. 10 times the weight of a sub-section – cf. curves from manufacturer, cf. Figure 145).

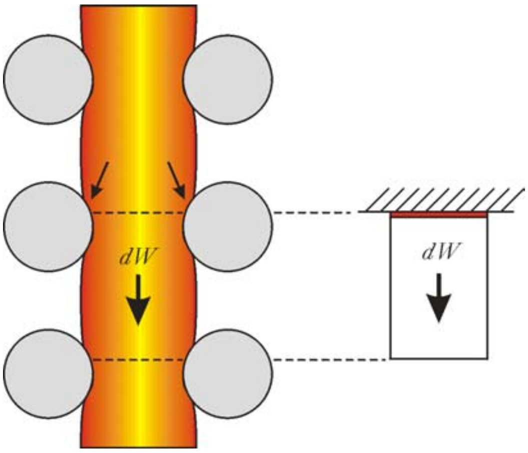

Figure 147: Transmission of weight to supporting rolls

2.4. Definition of indexes relative to risk of transverse cracking

In order to make an objective comparison between different simulations, it has been necessary to define indicators of risk of transverse cracking. They are not criteria, since no critical value is available, but their value increases with the risk of transverse cracking so that it possible to have a qualitative appreciation of the mechanical state of the slab in different situations.

According to the objective of the study (cf. I.2.2), the model only focuses on the surface transverse cracks, which generally appear in the corners. Two mechanical elements can generate such cracks: longitudinal stress σ_{zz} and longitudinal strain rate $\dot{\varepsilon}_{zz}$.

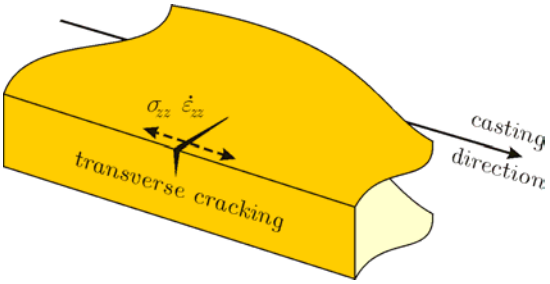

Figure 148: Longitudinal stress and strain rate, generators of transverse cracks

Two indexes have been applied: they have been provided by IRSID and they combine both metallurgical and mechanical unfavourable aspects. They are established on the following bases:

- indexes are positives if mechanical state is favourable to opening of the transverse cracks – equal to zero otherwise;
- indexes are significant when the material is characterized by low potential of deformation without cracking, i.e. when the ductility of the material is low (this gap of ductility occurs for temperatures between 800°C and 950°C for the studied steel);
- the higher the indexes are, the higher the risk is.

According to these assumptions, a first index I_1 has been defined as follows:

$$I_1 = \begin{cases} \max\left(0, \sigma_{zz}\right) & \text{if } 800°\text{C} < T < 950°\text{C} \\ 0 & \text{otherwise} \end{cases} \tag{324}$$

According to this definition, I_1 is equal to zero when the temperature is out of low ductility range and when the longitudinal stress is negative (compression). At the opposite, if the temperature corresponds to low ductility range and the slab is in longitudinal tensile state, the indicator is equal to the value of this tensile stress: the higher the stress is, the higher the risk of cracking is.

In the same way, a second index I_2 based on longitudinal strain rate has been defined:

$$I_2 = \begin{cases} \max\left(0, \dot{\varepsilon}_{zz}\right) & \text{if } 800°\text{C} < T < 950°\text{C} \\ 0 & \text{otherwise} \end{cases} \tag{325}$$

The same discussion can be hold about the value of I_2. Note that longitudinal strain rate has been preferred to longitudinal strain, since the latter is a cumulative value and do not necessarily take into account sudden and local variation of longitudinal state.

2.5. Modelling of the liquid behaviour

The same assumptions as in the first industrial application have been formulated for the behaviour of the liquid. One can refer to section V.1.6 for further details.

3. *Reference case: casting in standard conditions – no local defect*

3.1. Initial conditions

The computation starts at the exit of the mould. At this level, the slice is assumed to have the exactly the shape of the mould: a perfectly rectangular section.

Neither initial stress nor strain is introduced. That is not exactly correct, but since bending and straightening are critical zones to study, one can expect that initial stresses and strains do not influence substantially the results.

At the opposite, a non-trivial initial temperature field has to be introduced. To do so, a pure 2D thermal calculation has been performed on the slice, assuming a constant heat extraction coefficient while going trough the mould. The value of this coefficient is a mean value in the mould and it has been fit to get surface temperature and solidification fronts – solidus and liquidus – at the right position, this information being provided by measurements and other models already validated.

3.2. Evolution of the slab surface temperature

To check the validity of the thermal model, there is a reference curve obtained for the same caster with a 1D thermal finite difference model developed by CRM. This curve represents the evolution through the caster of the temperature at the extrados mid-face:

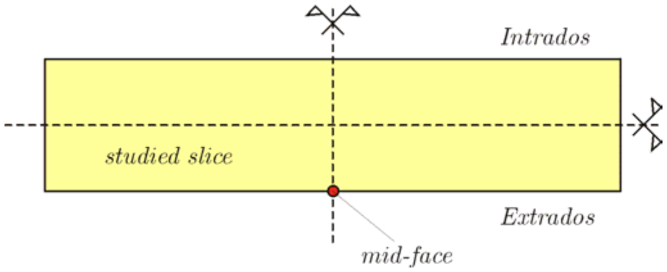

Figure 149: Slab section and mid-face point on extrados face

This reference curve has been validated by some measurements and the corresponding result obtained with the LAGAMINE model is shown both with reference (CRM) curve on Figure 150.

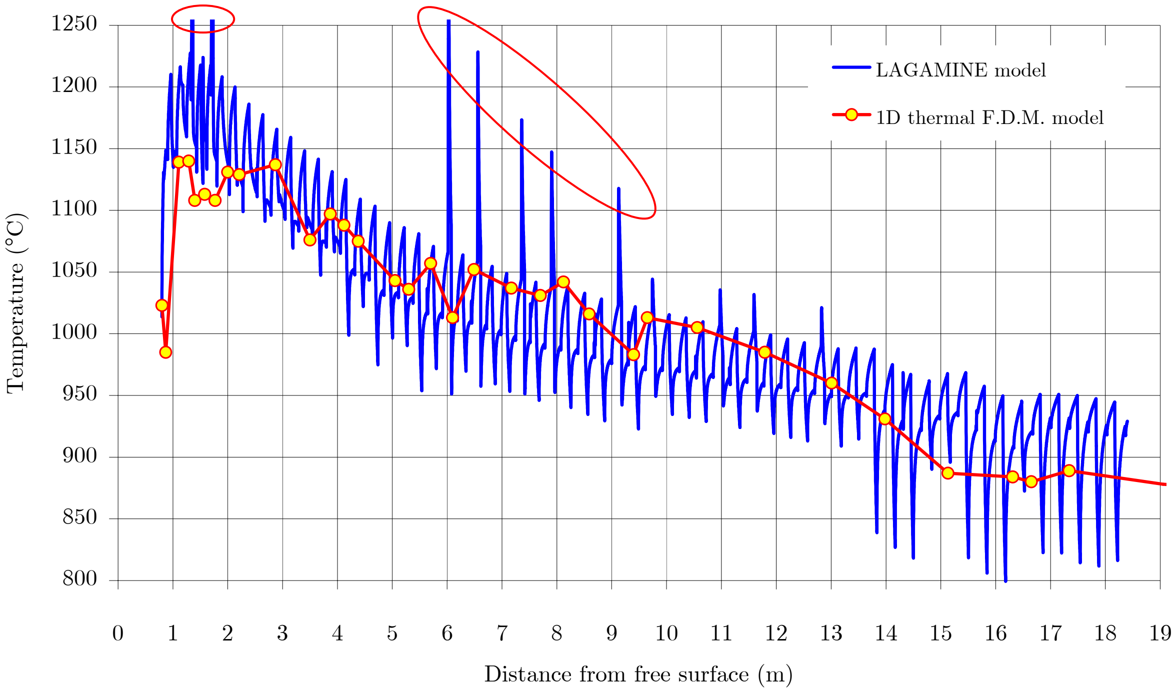

Figure 150: Evolution of surface temperature at the middle of extrados wide face

Globally, the two curves are following the same path: first, the temperature is rising (the heat flux above the mould is lower than in the mould, thus the liquid core tends to reheat slab surface), then it globally decreases.

The main difference between the two curves is the number of points of calculation. On CRM curve, each point is distant of its neighbours from 0.2m to 1m. That means that between two calculations, different types of heat transfer zones can occur (contact, radiation, water sprays…). In a way, this curve represents a mean temperature over a part of the caster. At the opposite, LAGAMINE model includes many calculations for each zone (typically one point each time step or 5mm in the casting direction). It allows thus modelling sharp variations in heat transfer coefficients and the temperature oscillates according to high and lower coefficients.

Note that on Figure 150, some peaks are appearing (circled in red). They correspond to the well-known effect of numerical thermal shock which can occur when an important variation in the studied domain occurs, such as a sharp variation of heat transfer coefficient. In such a case, the effect of the perturbation (variation of temperature) propagates like a wave from the surface to the internal domain. The wave propagation is a transient phenomenon, which is characterized by a given propagation velocity (linked to the thermal diffusivity of the material). If the time step used for the thermal analysis is too small, the wave does not reach enough points of integrations and the solution is a temperature fields which do not match physical behaviour of the material: temperature oscillations in space.

To counteract this problem, two simple solutions exit: to use longer time step and/or smaller finite element. Both solutions allow the wave reaching more integration points over the time step. The first one however cannot be extended excessively, otherwise, long time steps lead to long displacements of the slice in the casting direction. The other solution (smaller finite elements) is also limited, but essentially by the capacities of the computers. CPU time and number of finite elements is not in linear relation.

A trial has been performed at the beginning of the model development to compare the actual mesh with a more refined one (1574 elements instead of 594 – see). The comparison of both mechanical and thermal response of the model allowed concluding that they are almost equal in both cases, except in the very vicinity of numerical thermal shocks. The Figure 151 presents the temperature at the middle of extrados wide face obtained with the refined mesh. This curve is equivalent to Figure 150, but the heat transfer coefficients were not yet correctly defined, hence the slight difference with Figure 150. Because of CPU time, the refined mesh (which needed 80-90 hours of computation time) has not been chosen and the present mesh has been maintained (15-20 hours).

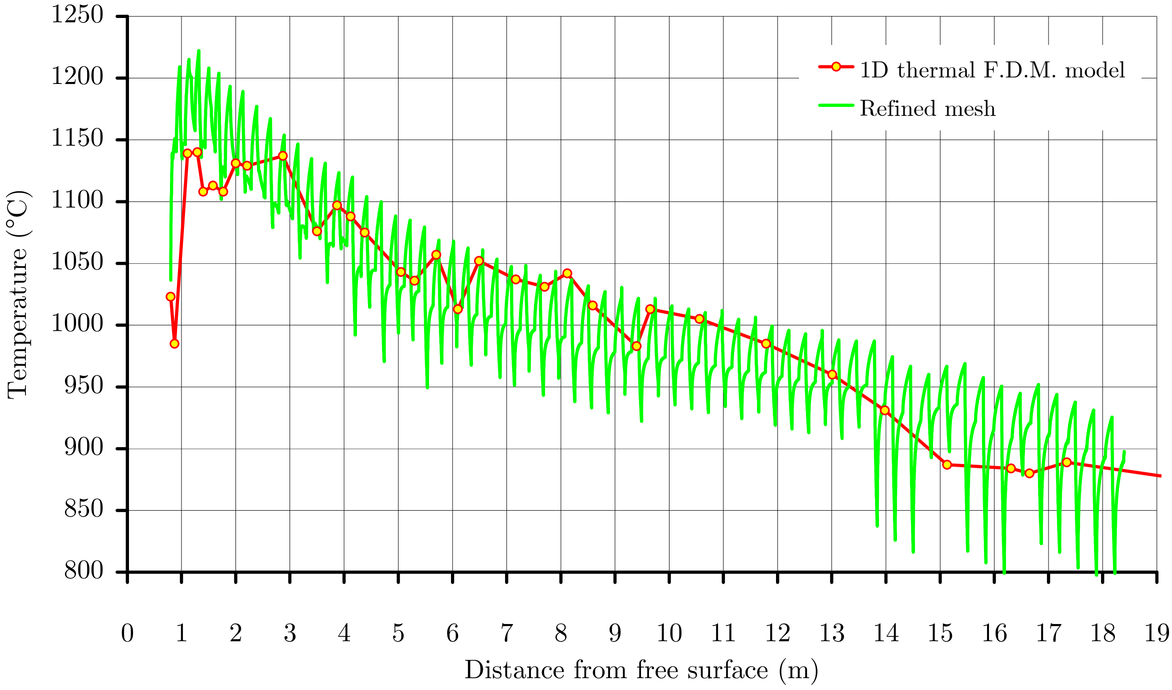

Figure 151: Evolution of surface temperature at the middle of extrados wide face obtained with the refined mesh

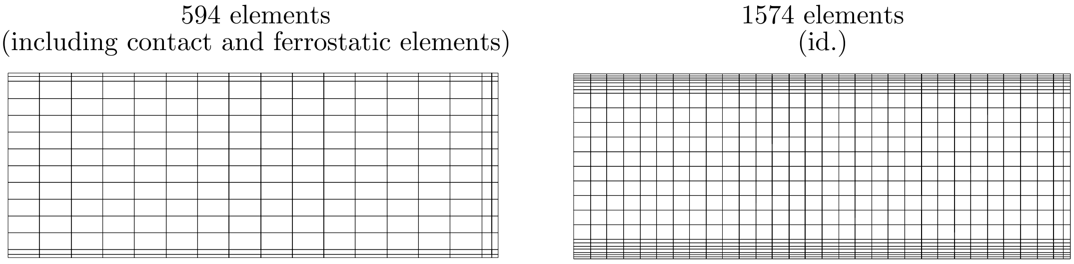

Figure 152: Comparison between used mesh (left) and a more refined one (right)

Other solutions exist to avoid numerical thermal shocks keeping the same mesh and time step. Recently, Aliaga made a review of these techniques [ALI00]. However such methods require non-trivial modifications of the finite element code and they have not been implemented for this reason.

Note that the slice model does not take into account heat transfers in the casting direction (3rd dimension). That means that when the heat transfer coefficient presents sudden and large variations (for example when the contact with a roll occur or when the slice enters in a sprayed zone), the surface temperature varies in proportion: this variation can be higher than 100°C in a fraction of a second. In reality, the longitudinal heat transfer (along casting direction) diffuses the effect of variation of this coefficient and one can expect to measure smoother temperature variations. However, some modelling and temperature measurements on slab casting have been performed by Patrick et al. [PAT00] as pictured on Figure 153. It seems that such variations in temperature can be observed in practical cases. However, they depend very much on the casting conditions and especially on the water flow cooling rate.

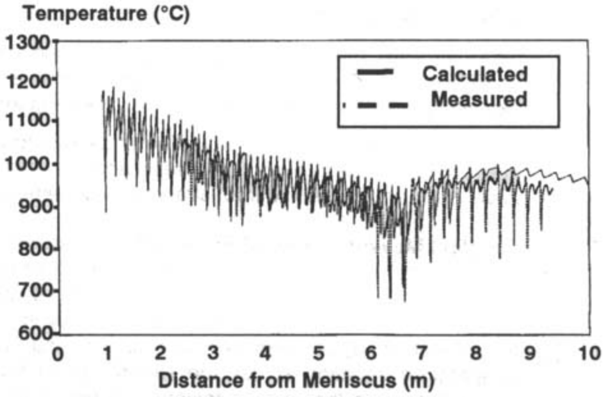

Figure 153: Measured and calculated surface temperature in [**PAT00**]

The Figure 154 shows slab temperature on its surface (intrados, extrados and narrow faces). Colours correspond to the range of assumed low ductility defined in VI.2.3.4: green colours are used for temperatures over 950°C, blue colours correspond to temperatures below 800°C and other coloration (from violet to light yellow) are used for temperatures corresponding to low ductility (from 800°C to 950 °C).

Low ductility zones are underlined on Figure 155 where they appear in red. According to this figure, they are located in the corner of the slab (continuously along casting direction). In the central two third of the slab, low ductility zones alternates with safe zones, which correspond to temperatures higher than the 950°C top limit (cf. Figure 154).

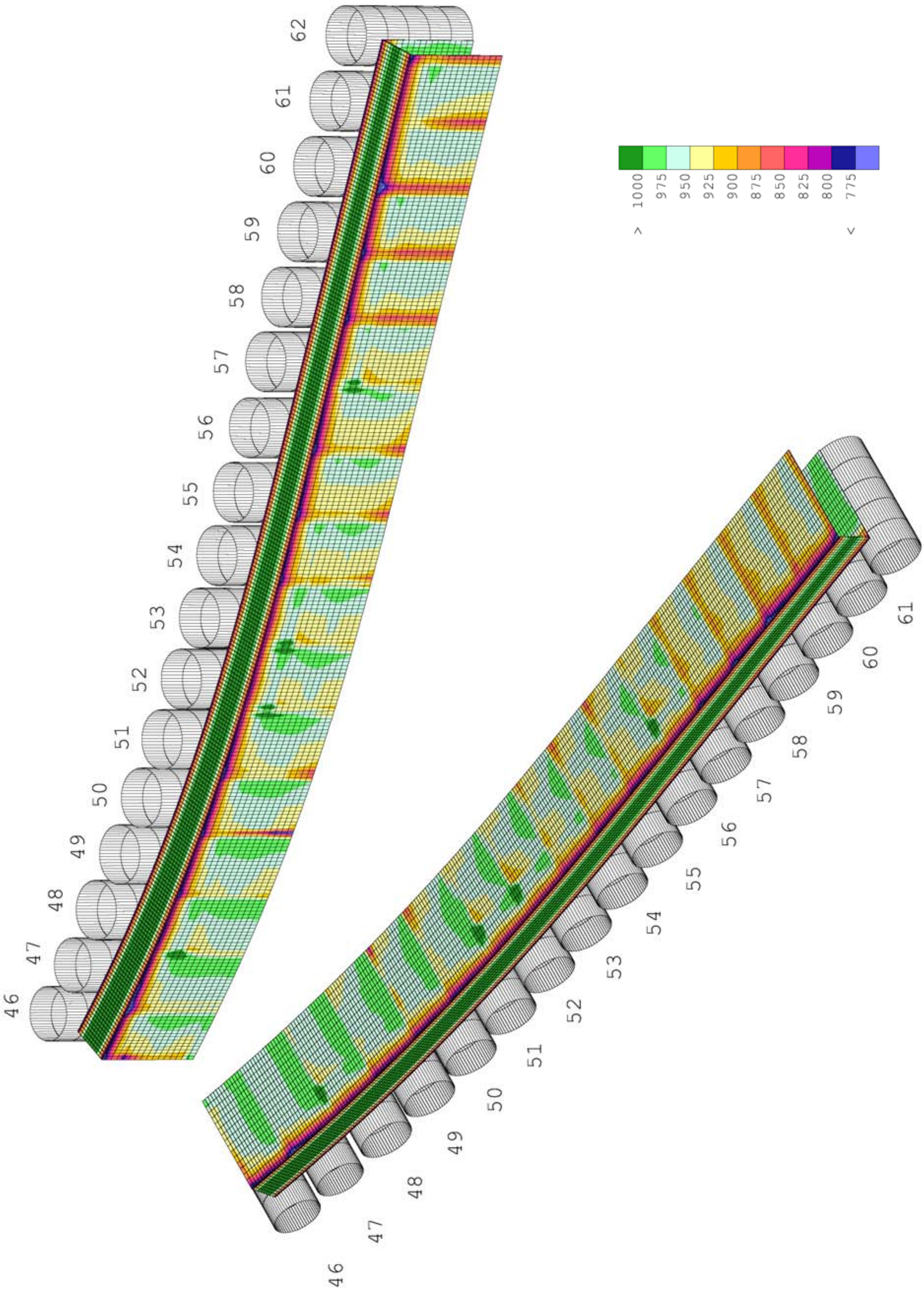

Figure 154: Slab surface temperature (°C) – Reference case

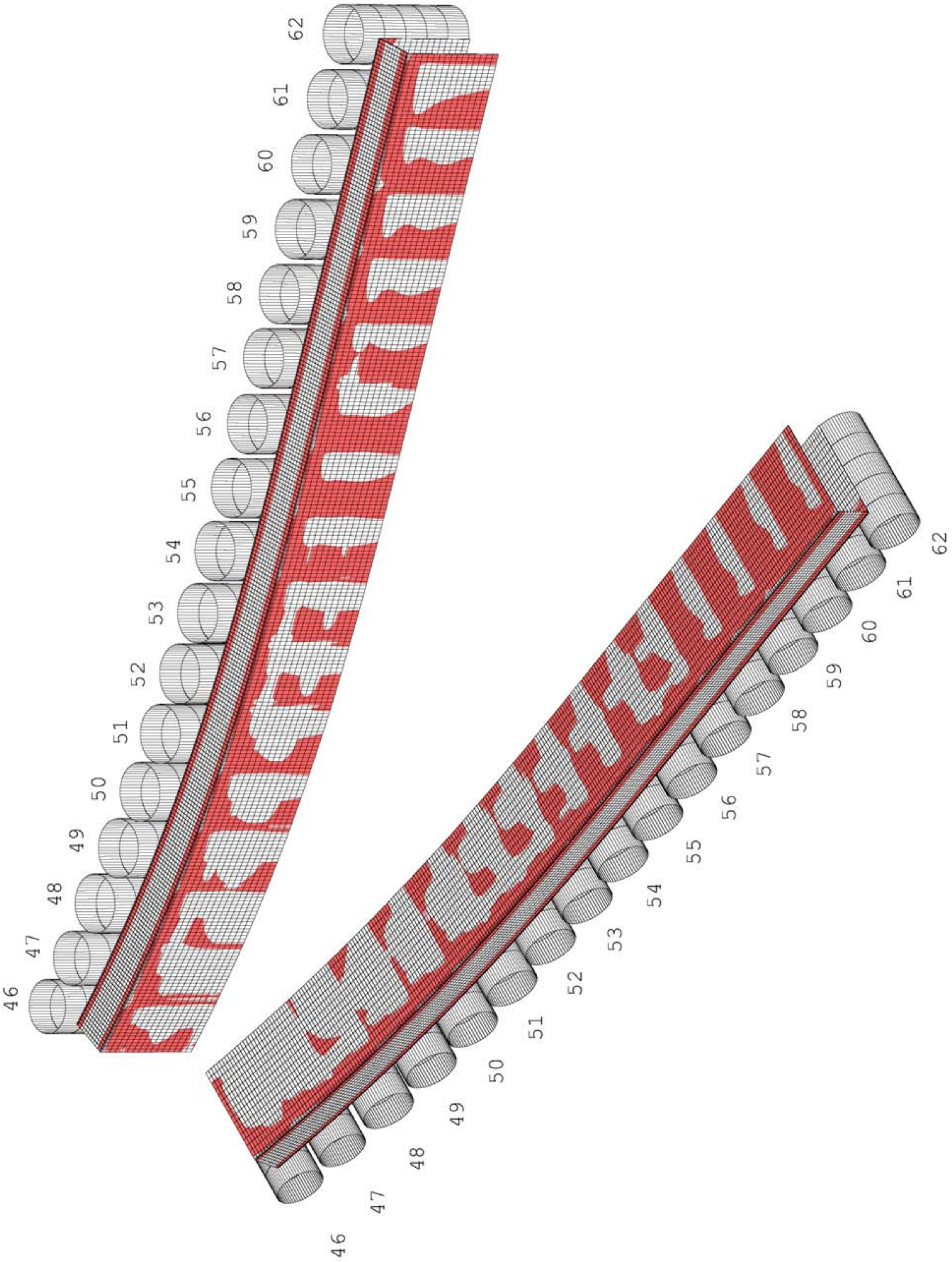

Figure 155: Low ductility zones (in red) on the slab surface – Reference case

3.3. Evolution of the thickness of the modelled slice

The model describes the evolution of a slice perpendicular to the casting direction. As already mentioned, generalized plane strain state allows to model out-of-plane stresses and strains. The following section deals with the evolution of the computed thickness of the slice while going through the caster.

At the beginning of the simulation (bottom of the mould), the thickness of the slice is equal to one and uniform. The initial degrees of freedom of generalized plane strain state are equal to:

$$\begin{cases} \alpha_0 = 1 \\ \alpha_1 = 0 \\ \alpha_2 = 0 \end{cases} \tag{326}$$

Then, thickness of the slice varies, because of thermal shrinkage, application of the extracting force and bending/straightening of the slab, the last two actions generating a different thickness on both wide faces of the slab (intrados and extrados).

Three particular points are observed here: there are located along the symmetry vertical plane, two being on the surface (one on each wide face of the slab), and the third one being at the centre of the slice (corresponding to the casting axis) – see Figure 156 and Figure 157.

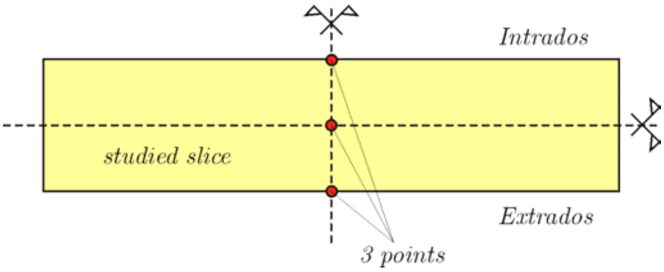

Figure 156: Position of the 3 points in the slice where thickness evolution is observed

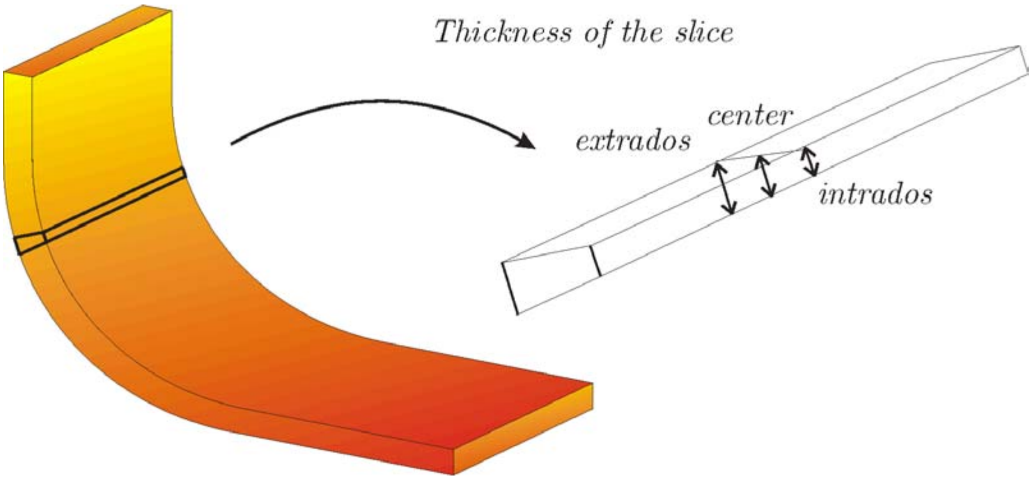

Figure 157: Thickness of the slice

The results for reference case are shown on Figure 158: three curves corresponding to the three particular points represent the thickness of the slice vs. the position of the slice in the caster from the free surface (meniscus).

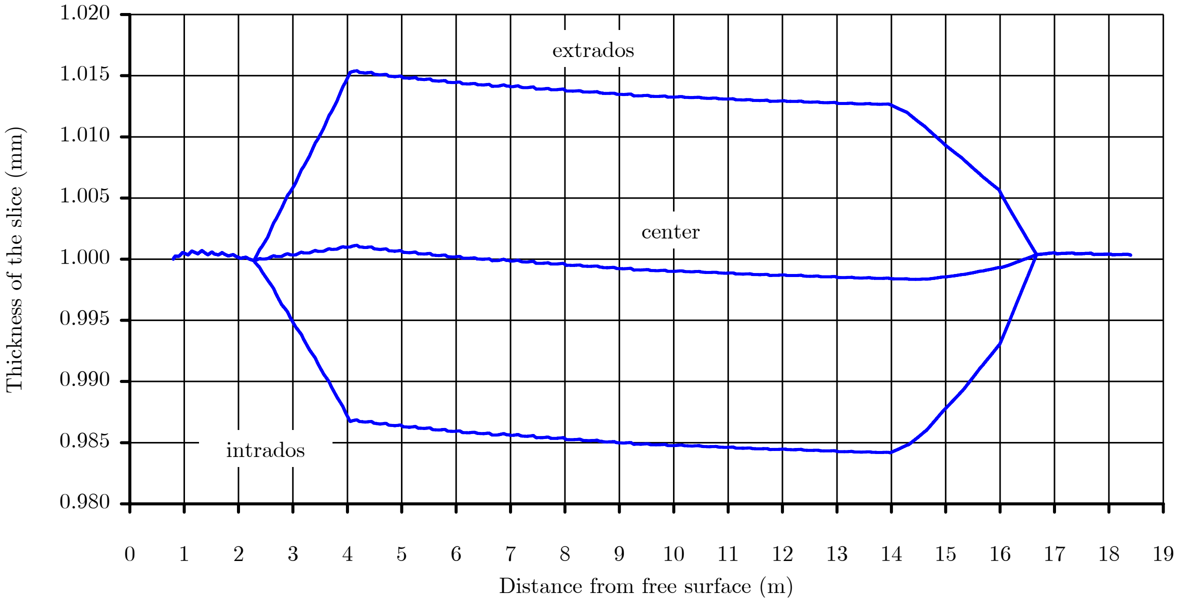

Figure 158: Evolution of the thickness of the slice – Reference case

The analysis of Figure 158 is the following:

- In a first time, the three curves are superposed: the thickness is uniform. This corresponds to the vertical part of the caster, just below the mould and before bending. The curves start at 0.8m corresponding to the active height of the mould. Then, the thickness is slightly increasing: this is due to the increase of temperature in the solidified shell and the consequent thermal expansion when exiting of the mould. Small oscillations are visible: they correspond to water spray cooling zones, where the temperature decreases dramatically. So, oscillations can be though to be linked to thermal strains. However, these oscillations are quite negligible when compared with the thickness variations further in the caster.
- At abscise of about 2.3m bending begins: the three curves are diverging. Thickness of the slice measured on the extrados face is increasing, this face being in extension and thus under longitudinal tensile state. At the same time, thickness on the intrados face is decreasing corresponding to compression state.

  Neutral axis corresponds to constant thickness during bending. It is not precisely located, however the thickness computed in the centre of the slice is almost constant, even is slightly increasing. That means that neutral axis is located between the centre and the intrados face, but close to the centre.
- A third part corresponds to the constant curvature of the caster: the three curves are "parallel" up to 14m from the free surface. Globally, thickness is decreasing, as temperature does (cf. Figure 150). Small oscillations are still visible.
- From 14m to about 16.5m, the three curves are converging, the thickness becoming identical again for the three observed points: this is straightening. During this operation, the variation of thickness get quicker at the end, meaning

that straightening is progressive, being soft at the beginning and harder at the end.

- Final thickness of the slice is about 1.001mm, which corresponds to a longitudinal strain equal to 10^{-3}.

Since thickness of the slice is linked to longitudinal strain of the slab, the variation of thickness (thus slope of the curves on Figure 158) is a measure of longitudinal strain rate. From the previous analysis, it appears that the most critical zone is located on the intrados face at the end of straightening. The slope is in fact the largest in this part of the curve. This is in agreement with industrial observations and is confirmed by indexes values in the following section.

Note that in a first assumption, the neutral axis was fixed and placed on the intrados face during bending and on the extrados face during straightening. This assumption was based on the fact that oscillation marks do not seem to go closer during these operations. The result corresponding to the Figure 158 with this assumption is pictured on Figure 159.

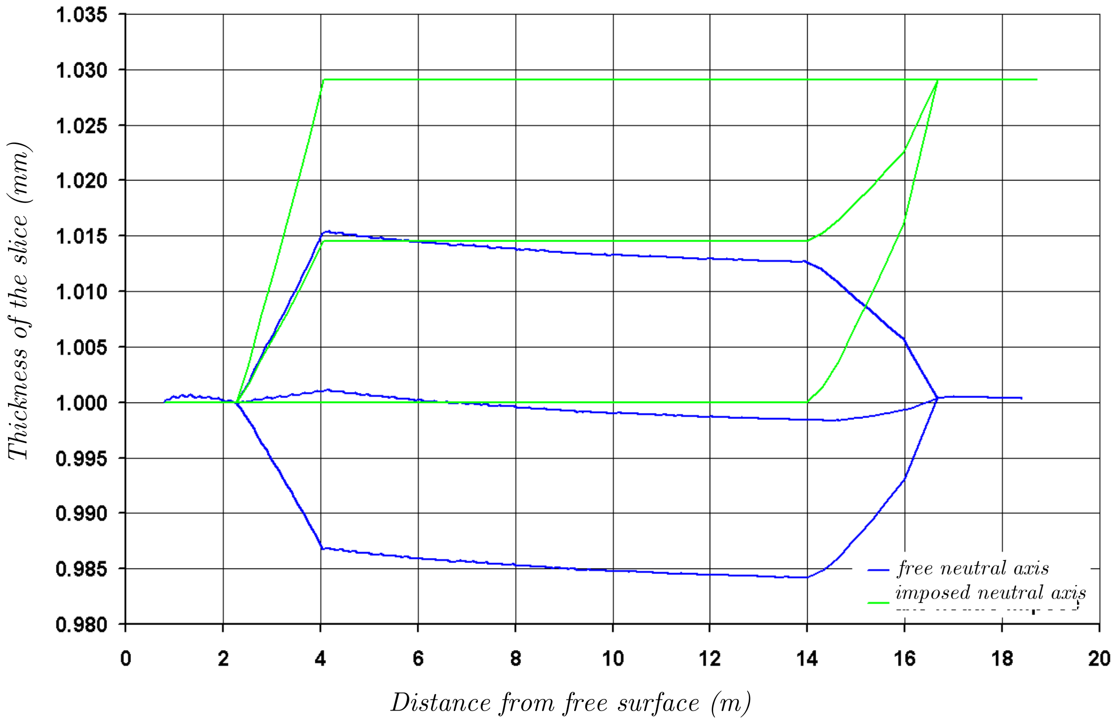

Figure 159: Evolution of the thickness of the slice when imposing neutral axis on the intrados face during bending and on the extrados face during straightening

This assumption led to longitudinal strain much higher at the end of the simulation, after straightening (almost 3%). Moreover, the integration of the longitudinal stresses σ_{zz} balanced an extraction force 4 times higher than the extraction force indicated by the curves from the caster manufacturer, meaning that the elongation was too large.

In other respects, when the neutral axis is fixed as well as the radius of curvature of the caster, there is no more degree of freedom on the generalized plane strain state (cf. section III.1.4). The longitudinal strain and strain rate were thus imposed.

3.4. Indexes of transversal cracking

Figure 160 and Figure 161 show the risk of transversal cracking according to both indexes defined in section VI.2.3.4. The coloration is similar: white zones correspond to indexes equal to zero, while other colours are used to indicate progressive increasing of risk of transverse cracking.

The first index I_1 (linked to longitudinal stress – see Figure 160) shows that the risk is almost inexistent on extrados surface: during straightening, this face is under longitudinal compression. At the opposite, longitudinal tensile stresses are observed on intrados face, the maximum being located in the corner at the end of straightening (between pairs of rolls #55 and #57). The maximum value of index I_1 is equal to 41.1 MPa.

The second index I_2 (linked to longitudinal elongation rate – see Figure 161) gives similar indications: highest risk on the intrados surface, in the corner, at the end of straightening. The maximum value is equal to 22.10^{-5} s^{-1}. This is in good agreement with the first indicator, but also with on-site observations.

3.5. Reference case in bending zone

Even if the most critical zone was expected during straightening, the model allowed checking if bending is less critical. Extrados face is indeed in tensile state during bending, it is necessary to verify that indexes values are lower than in the straightening zone.

Figure 162 to Figure 165 are showing the results from the exit of the mould up to three rolls after the end of bending. Low ductility zones (Figure 163) are in the corner, since surface temperature almost always over 1000°C. A horizontal red line appears at the surface between rolls #5 and #6. This one has to be ignored since it clearly corresponds to a numerical thermal shock (see Figure 162).

As a consequence, indexes are positive only on a very limited part of the slab surface. Once again, almost nothing happens on the face in compression (this time intrados face), while the indexes are maxima in the corner of the extrados face, at the end of bending:

- maximum $I_1 = 26.7$ MPa (vs. 41.1 MPa at the end of the straightening)
- maximum $I_2 = 18\ 10^{-5}$ s^{-1} (vs. $22\ 10^{-5}$ s^{-1} at the end of the straightening)

Both indexes show lower values than in straightening zones, so bending is less critical: if there is no transverse cracking during straightening in normal conditions (no defect), there cannot be transverse cracking in any way during bending.

These results are in good agreement with observation on slabs: generally, transverse cracks have been observed on the intrados face.

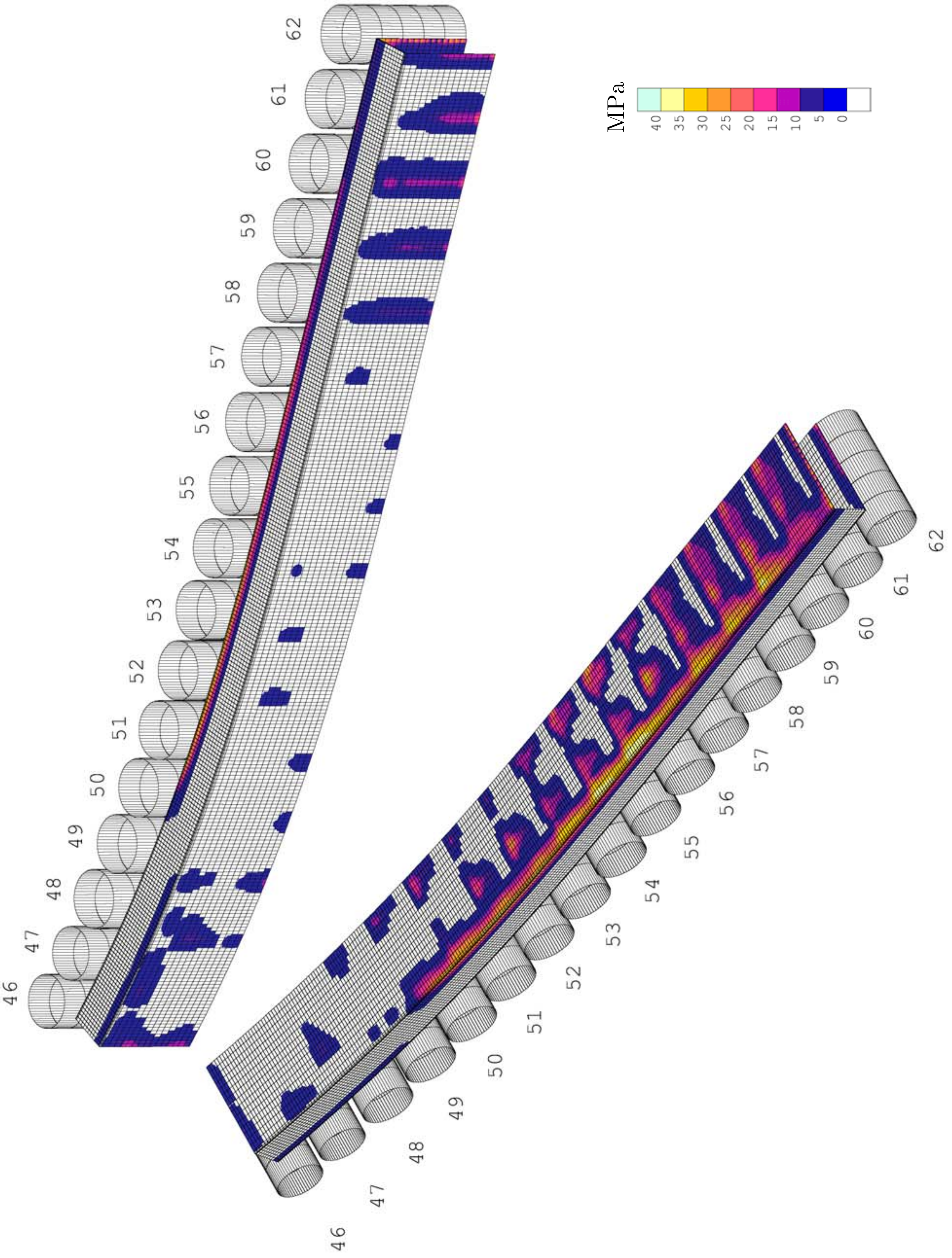

Figure 160: Risk of transversal cracking according to index I_1 – Reference case

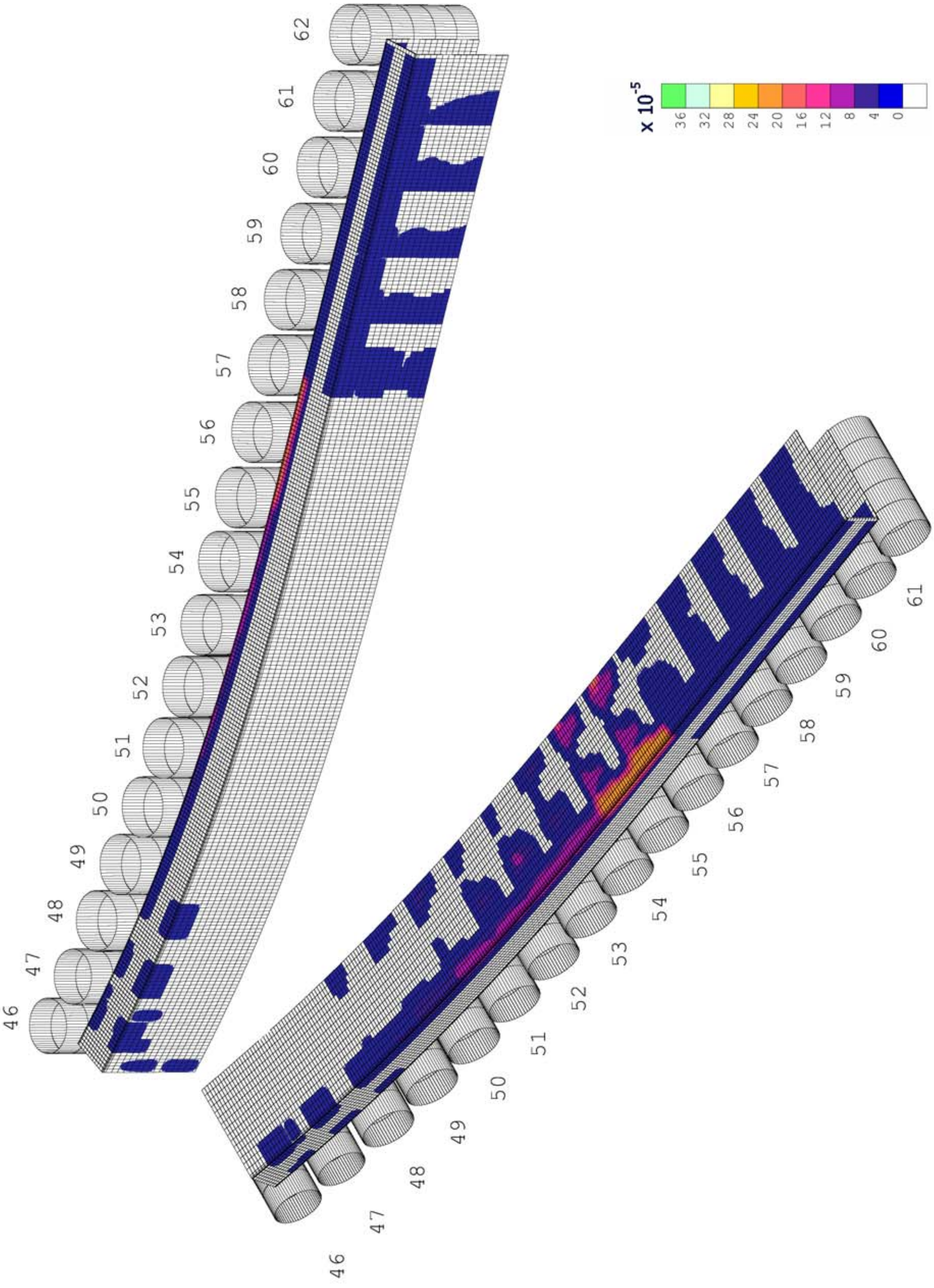

Figure 161: Risk of transversal cracking according to index I_2 – Reference case

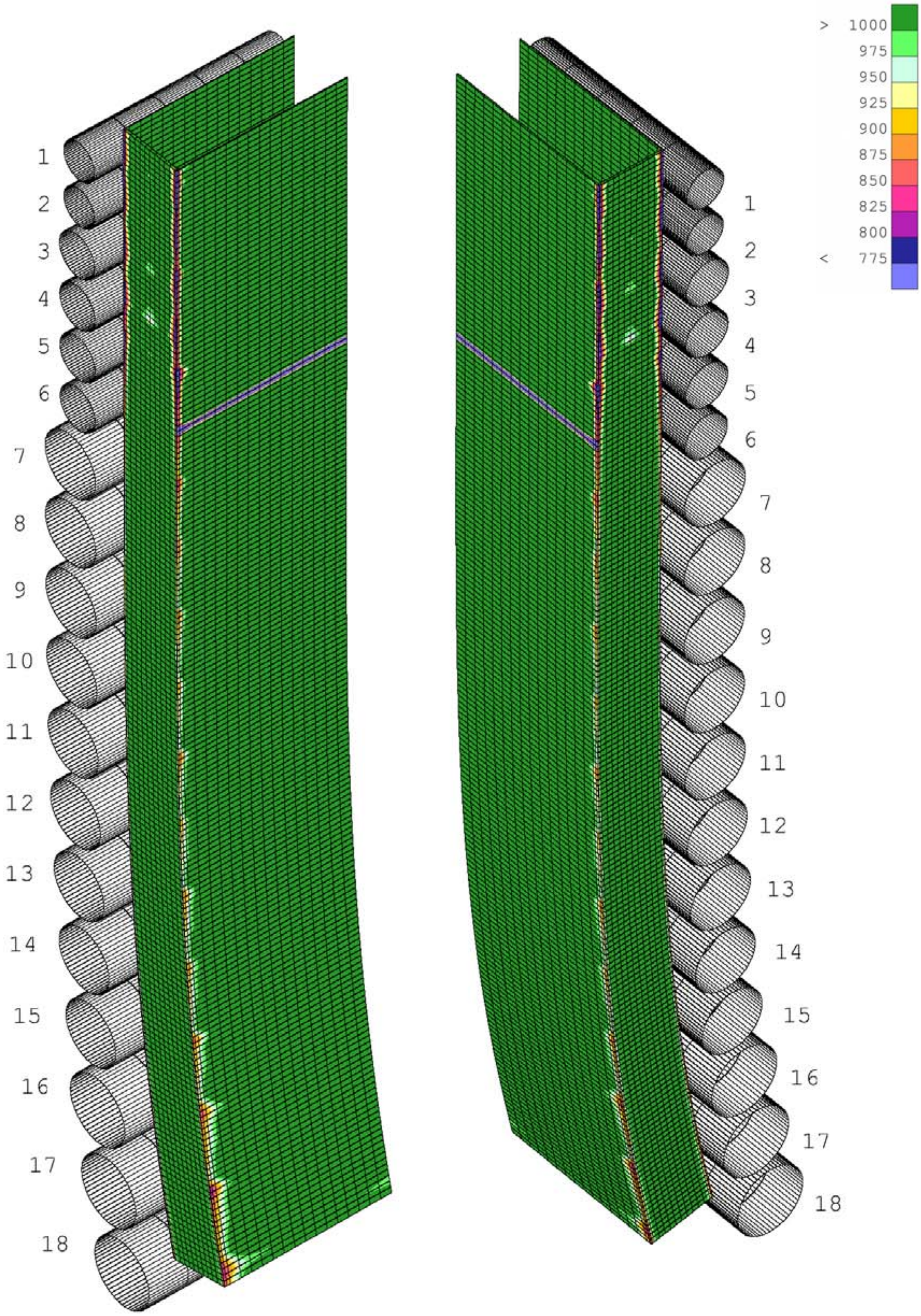

Figure 162: Slab surface temperature (°C)
Reference case in bending zone

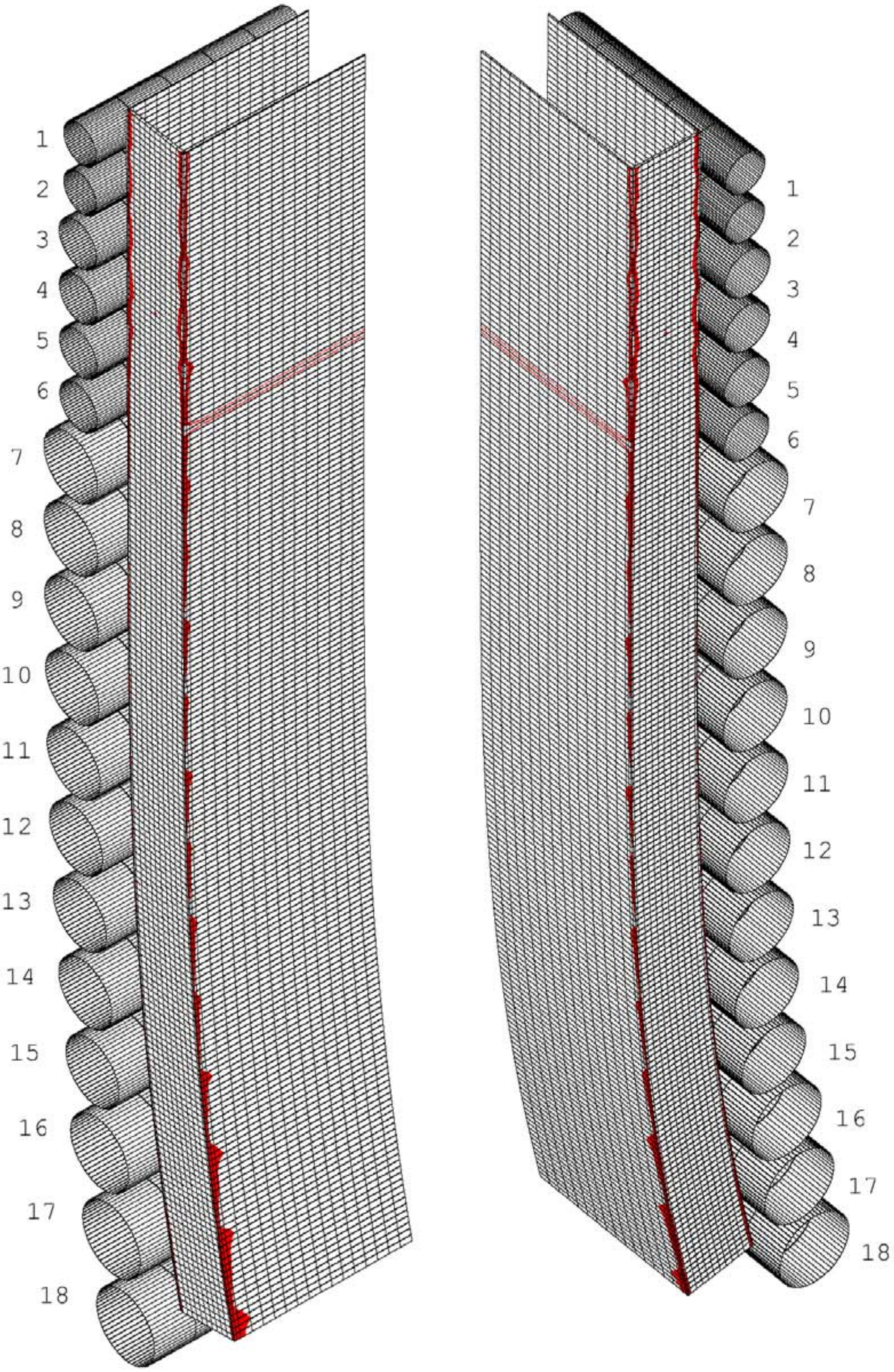

***Figure 163: Low ductility zones (in red) on the slab surface
Reference case in bending zone***

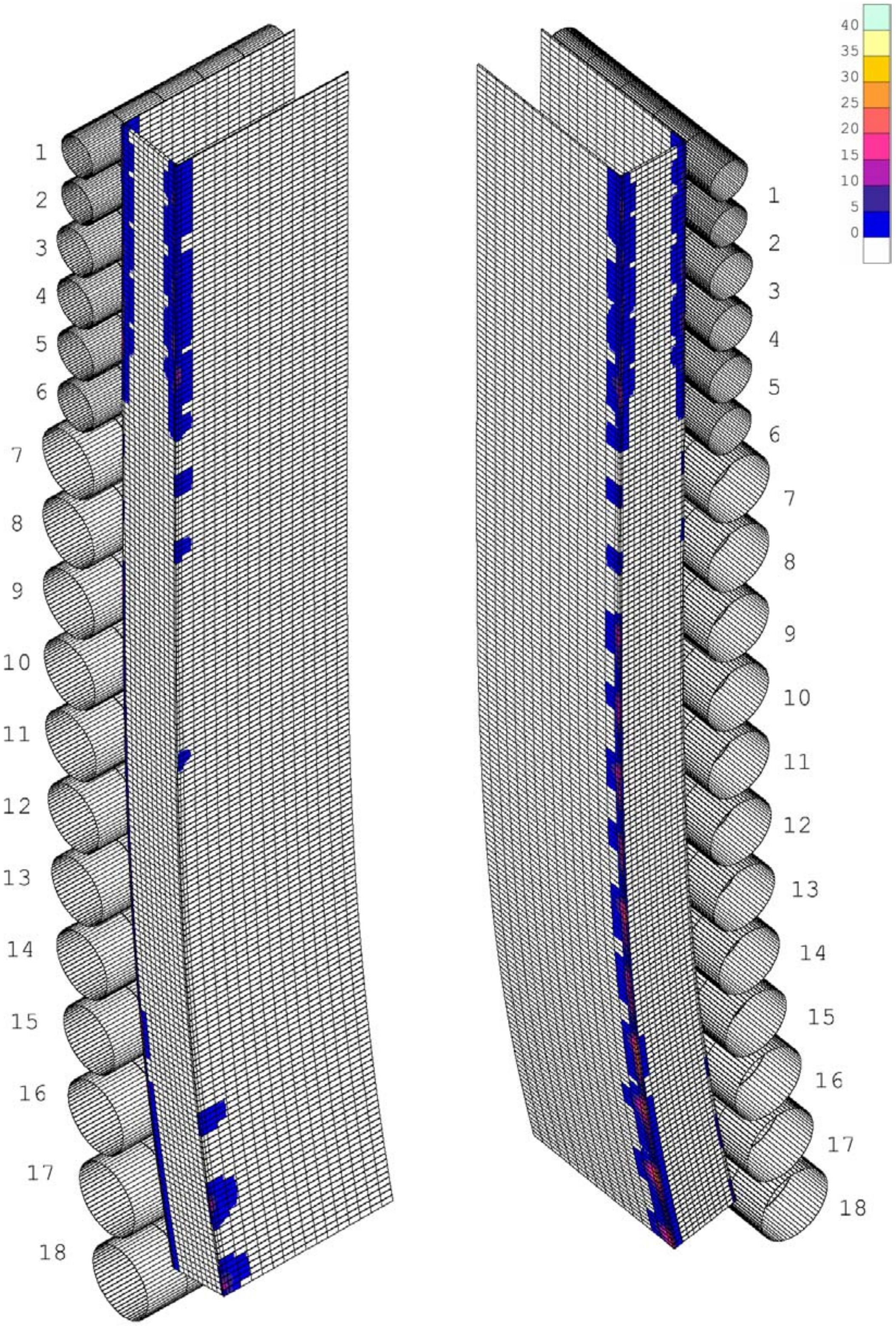

Figure 164: Risk of transversal cracking according to index I_1
Reference case in bending zone

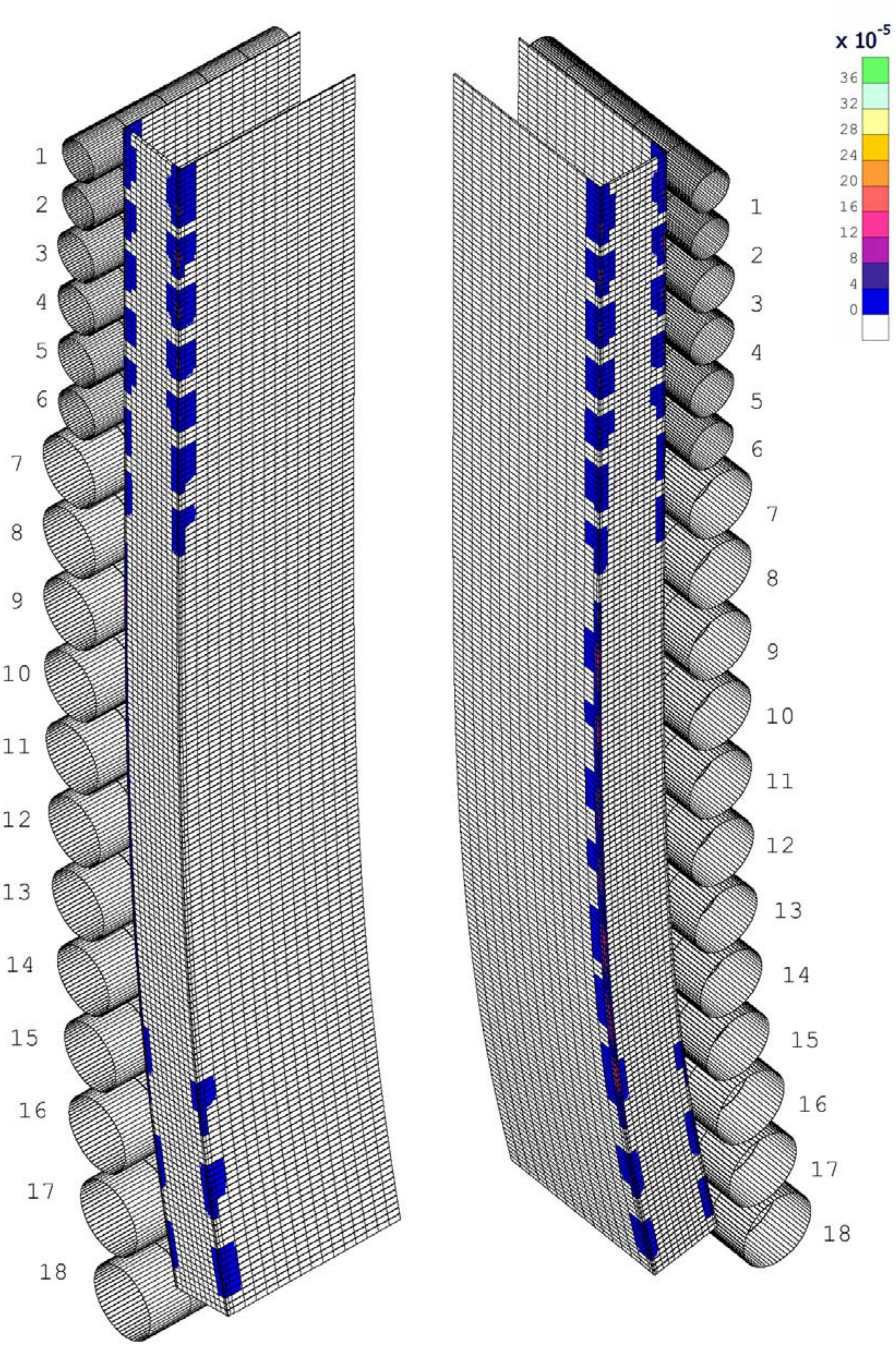

Figure 165: Risk of transversal cracking according to index I_2
Reference case in bending zone

4. Comparative study of local defects

4.1. Partial blockage of nozzles: local reduction of cooling rate

4.1.1. Definition of the local defect

The first local defect that is modelled is a reduction of water flow in one cooling circuit, which affect several ramps of nozzles both on extrados and intrados faces. The perturbed cooling circuit is positioned at the beginning of straightening, between rolls #47 and #52. The rate of water flow is reduced to 66% of the nominal value.

This is probably the simplest defect to model, since only water flow has to be changed, taking care of the non-linearity between heat transfer coefficients and water flow.

4.1.2. Effect on the surface temperature

A direct consequence of this defect should be an increase of surface temperature. This is confirmed by the model, as shown on Figure 167 and Figure 168.

As it clearly appears, the area concerned by the defect present a higher temperature on both faces. Temperature is often maintained over 950°C (green colours), while it was between 900°C and 950°C (orange-yellow) in the reference case. The temperature on a large part of slab surface is thus out of the critical range used in calculation of the risk of transverse cracking as defined above. It is particularly visible on Figure 169 and Figure 170.

The effect of such a defect is thus favourable. However, the effect is limited in time (no more effect after rolls #54) and limited to the central two third of the surface.

4.1.3. Effect on thickness of the slice

The reduction of water flow to 66% of nominal value in a short part of the caster cannot modify significantly the global mechanical state of the slab. The increase of temperature is quite slight and it concerns only a very superficial zone of the slab. That means that the subsequent thermal strain – that induced by the temperature variation with respect to reference case – cannot modify hardly the global state of the slab. Concerning the thickness of the slice, the Figure 166 confirms this.

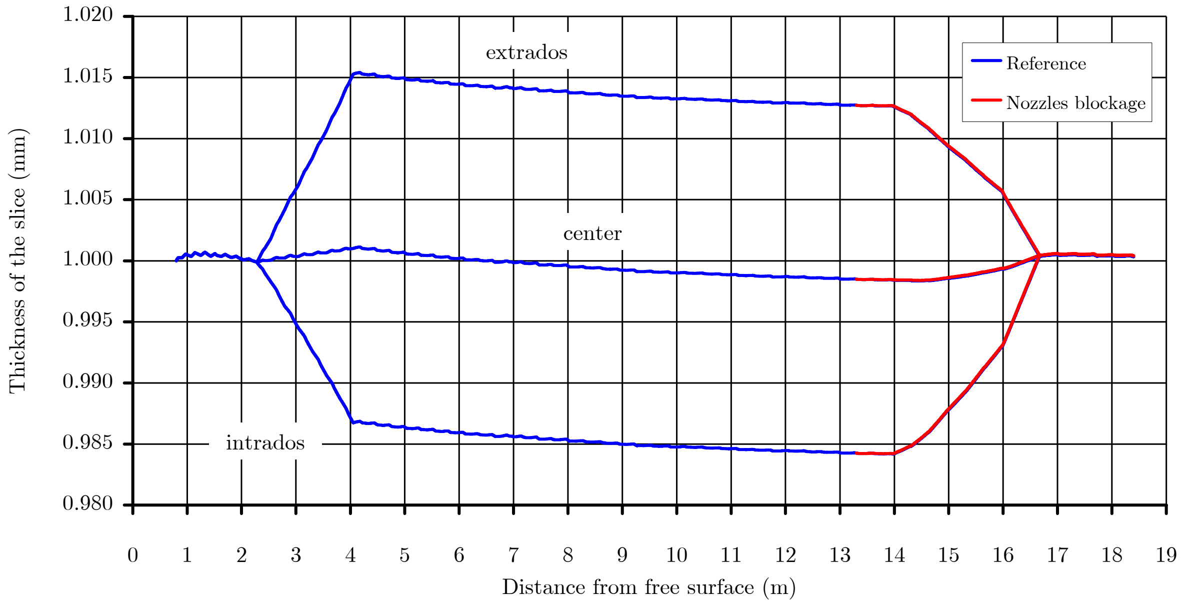

Figure 166: Effect of partial blockage of nozzles on thickness of the slice

4.1.4. Effect on risk of transverse cracking

As mentioned in the previous section, reduction of water flow has an effect only on thermal state, not on mechanical one. Consequently, the only difference between reference case and perturbed system in terms of indexes of transverse cracking can be attributed to the only modification of surface temperature.

That means that some critical zones disappear (cf. Figure 169 and Figure 170), but where the temperature criterion remains verified, the mechanical state does not change and both longitudinal stress and strain rate are identical to their value in the reference case.

This is visible on Figure 171 and Figure 172, which show the indexes I_1 and I_2 on the intrados face (nothing special appearing on the extrados face). Some critical zones disappear with reduction of water flow, however the most critical ones remain and the maximum values are identical.

4.1.5. Conclusion

The reduction of water flow has almost exclusively an effect on slab surface temperature. This effect goes in the right way, increasing the temperature over the 950°C limit of low ductility. This effect is limited in time and the defect could be more efficient if located closer to the most critical zone (end of straightening instead of beginning).

However, only the two central third of the surface are affected and there is no effect on the slab corners where the highest indexes of risk of transverse cracking are observed. So the effectiveness of such a measure to reduce transverse cracking is not established.

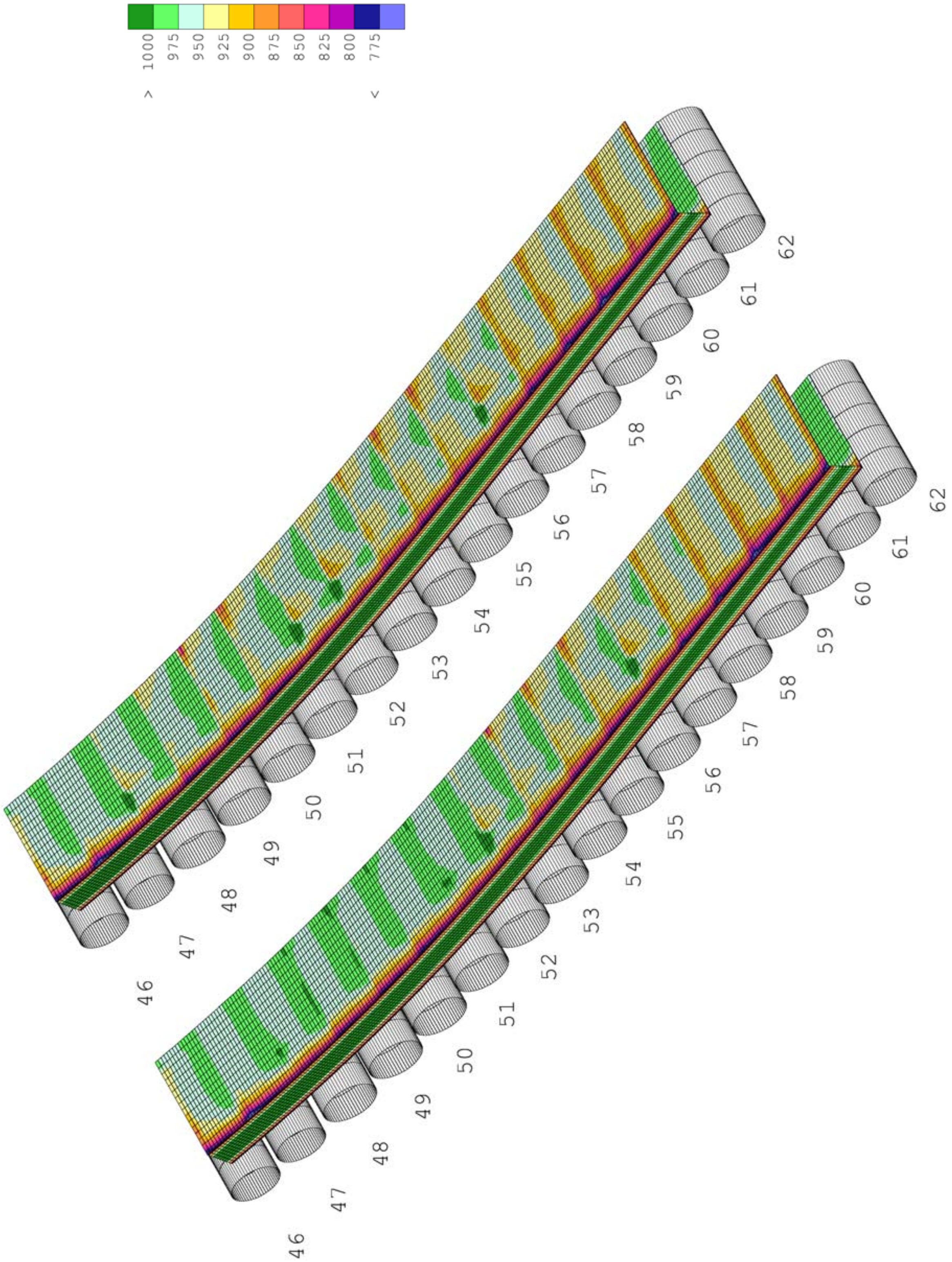

Figure 167: Effect of partial blockage of nozzles on slab surface temperature (Intrados face)

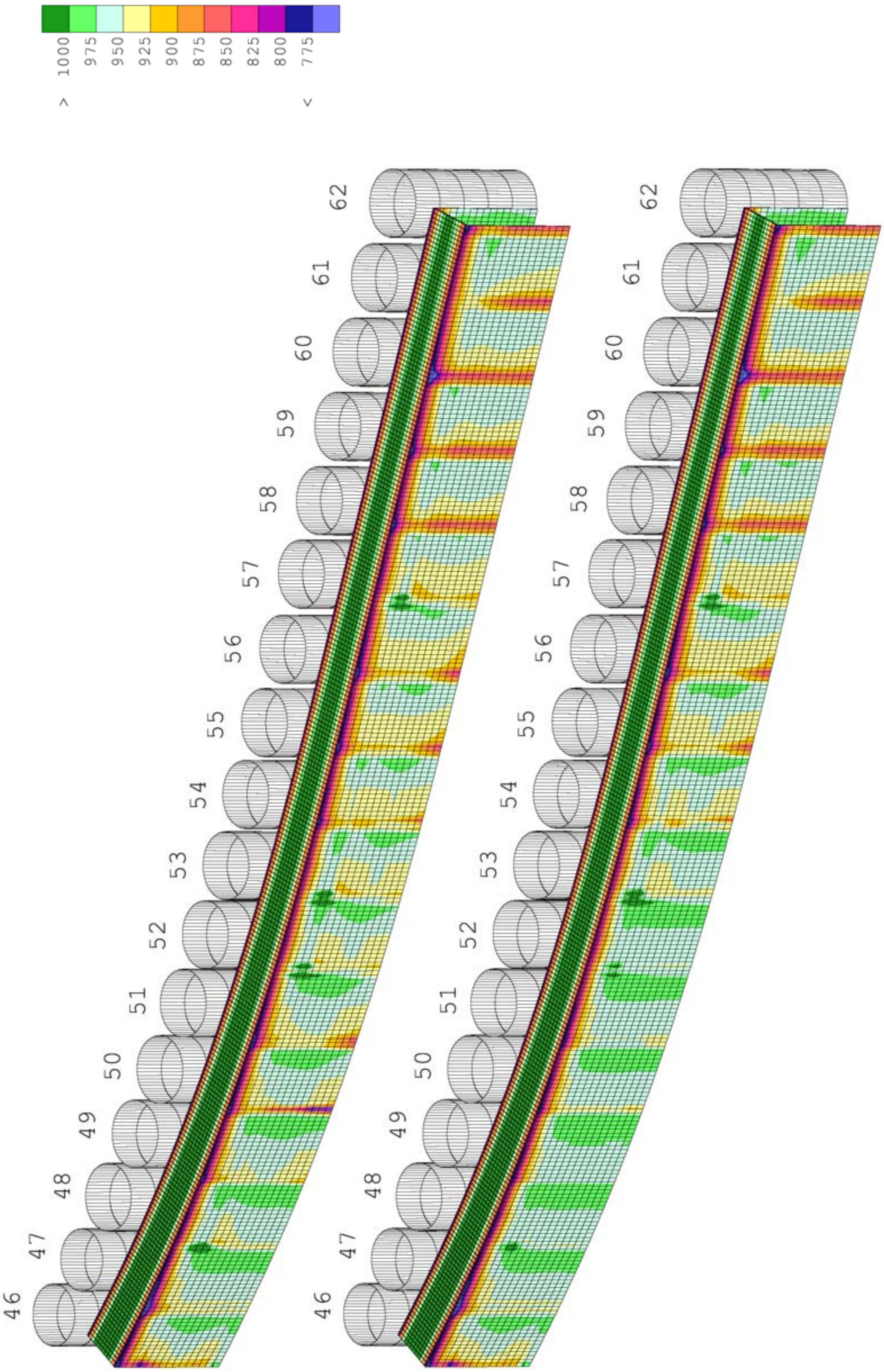

Figure 168: Effect of partial blockage of nozzles on slab surface temperature (Extrados face)

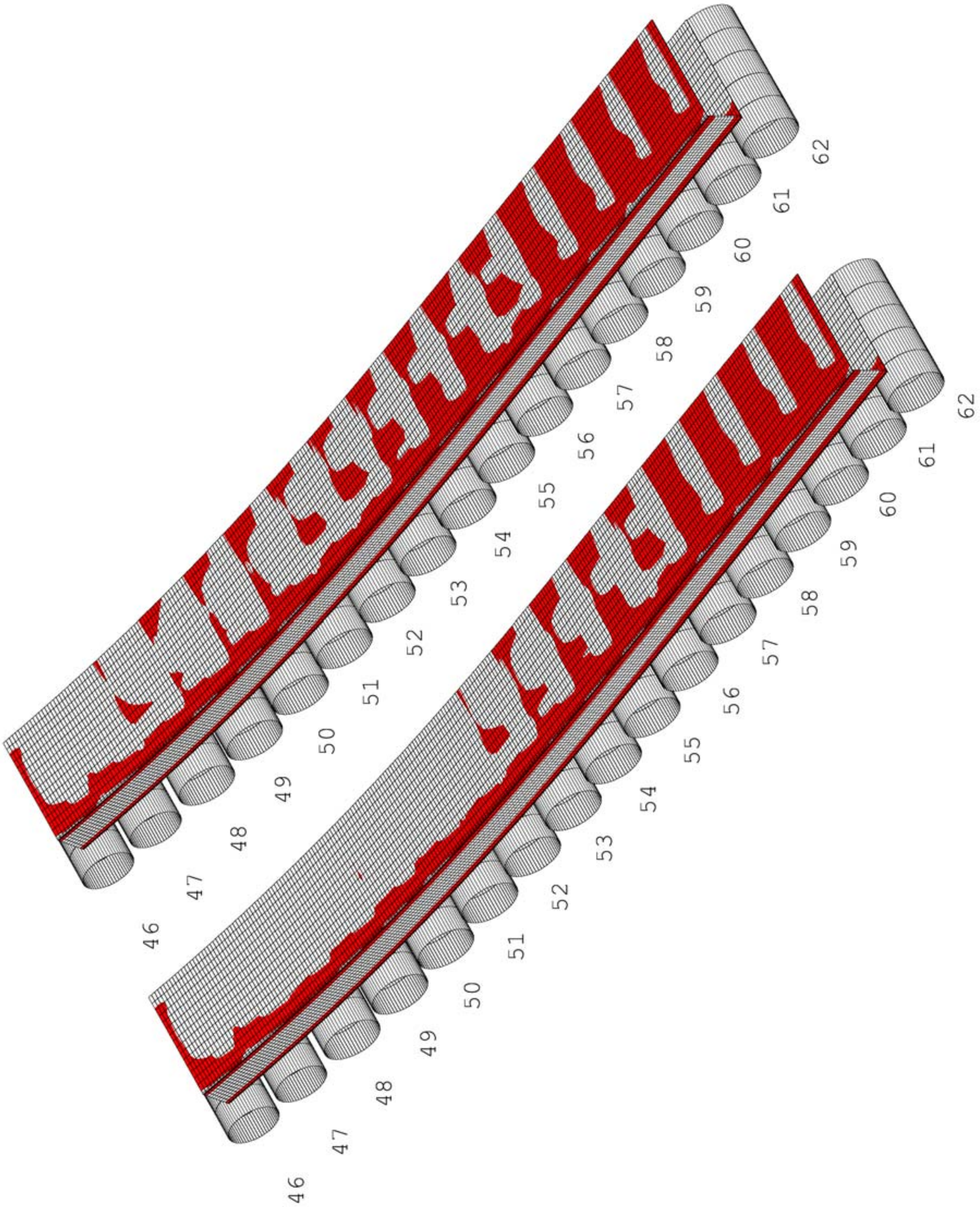

Figure 169: Effect of partial blockage of nozzles on low ductility zones (Intrados face)

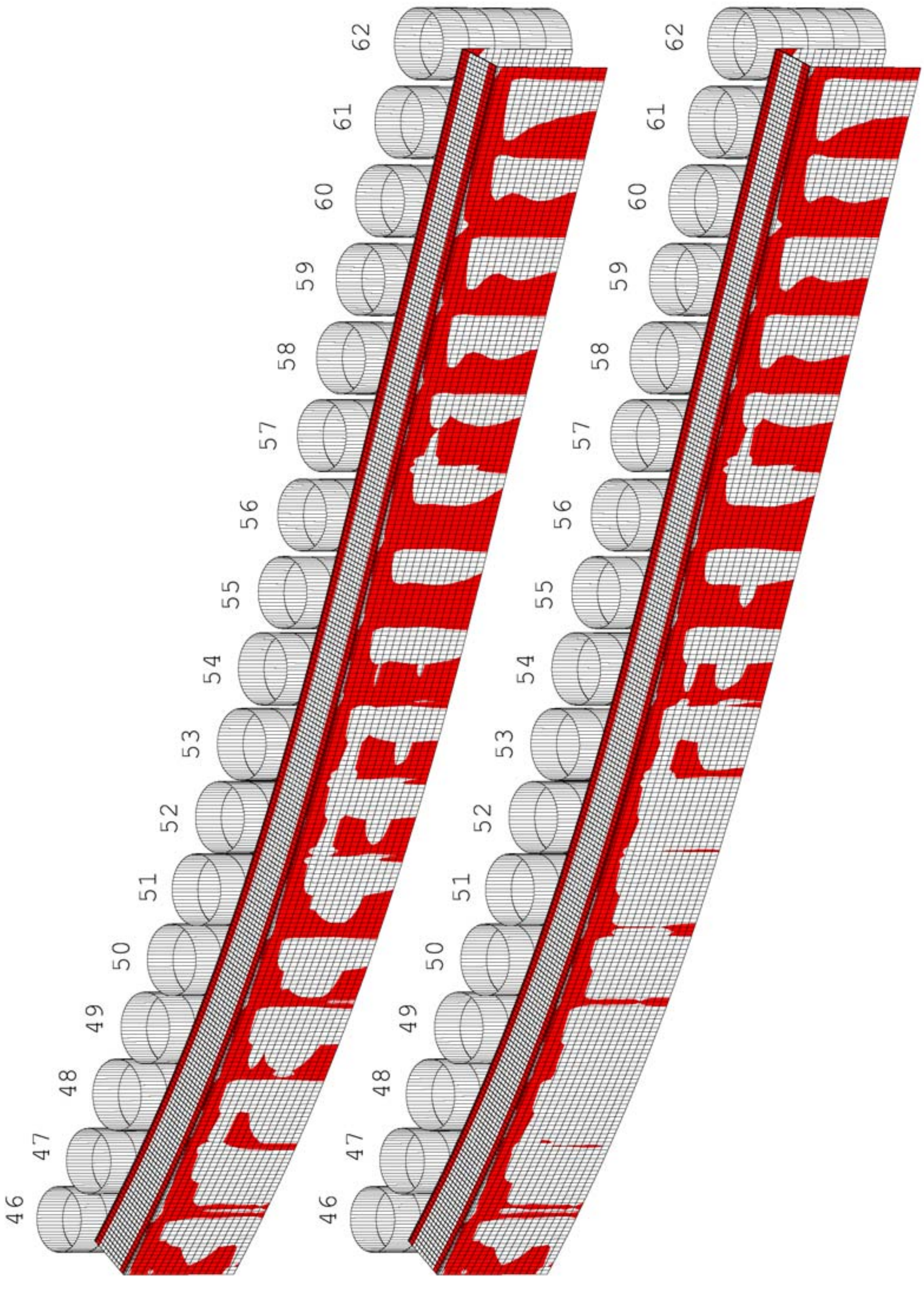

Figure 170: Effect of partial blockage of nozzles on low ductility zones (Extrados face)

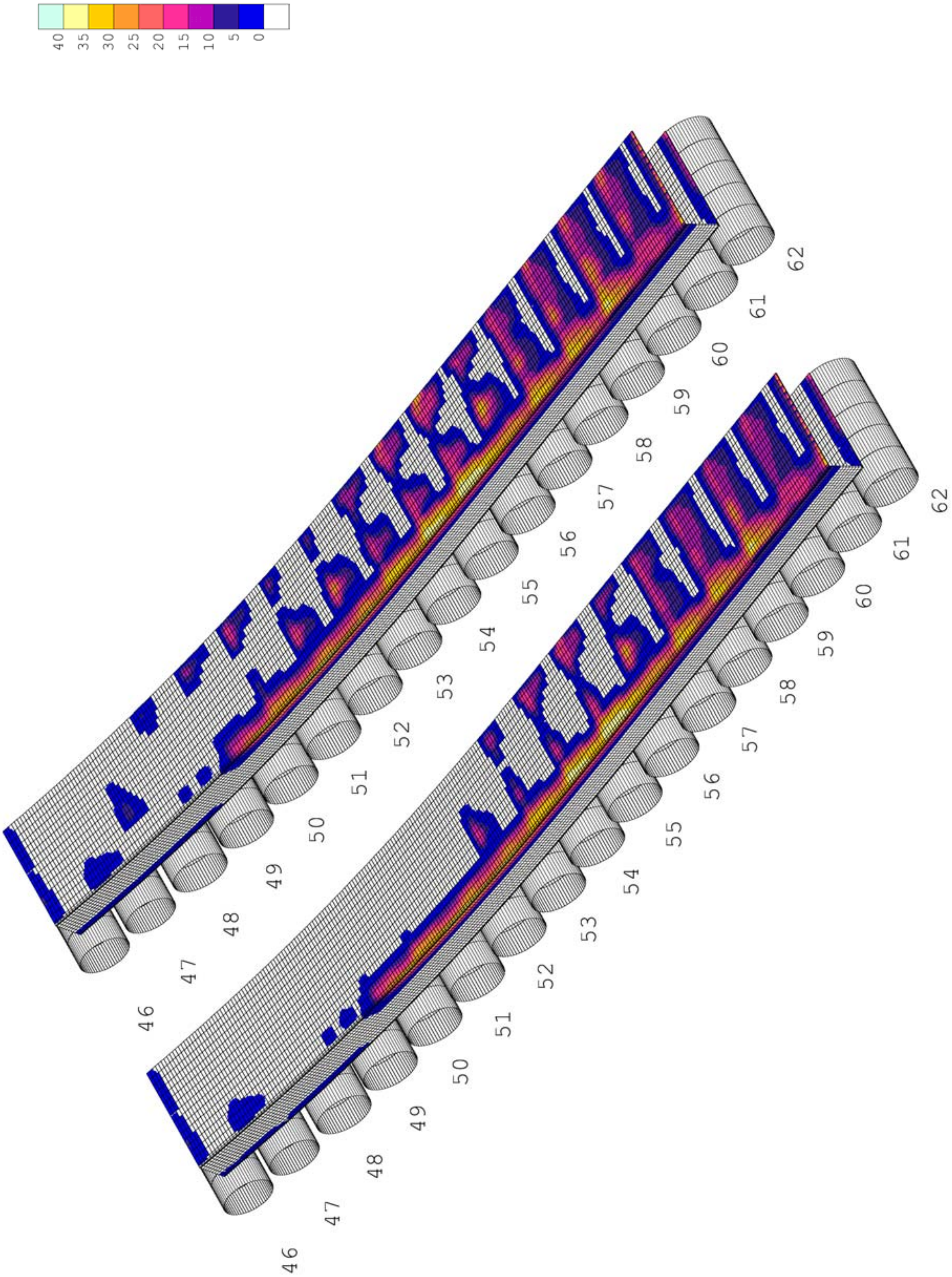

Figure 171: Effect of partial blockage of nozzles on risk of transverse cracking according to index I_1 (Intrados face)

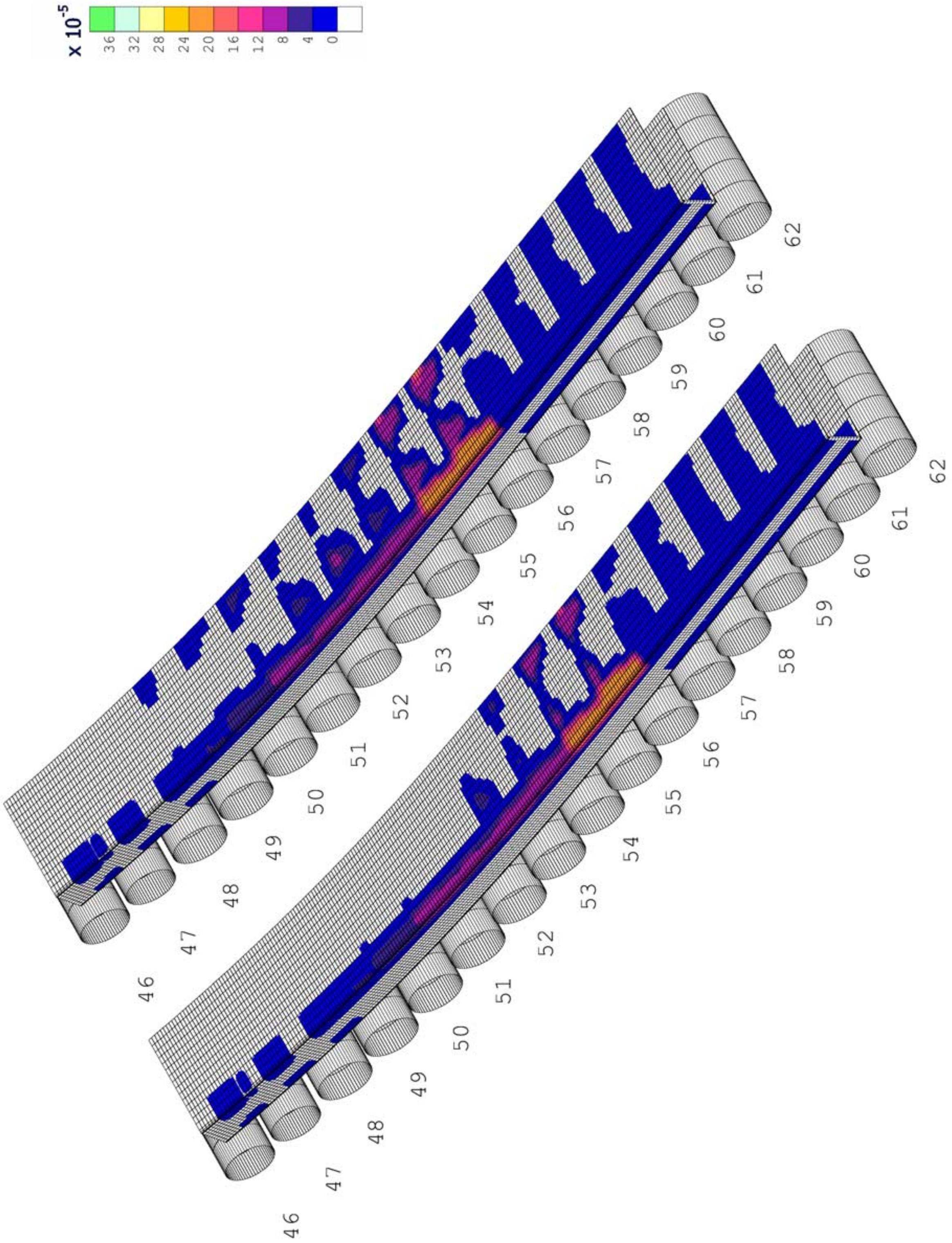

Figure 172: Effect of partial blockage of nozzles on risk of transverse cracking according to index I_2 (Intrados face)

4.2. Locking of pairs of rolls

4.2.1. Definition of the local defect

When a pair of rolls is locking, the slab starts to slide on it and the extracting force must increase to maintain constant casting speed. In such a case, the friction coefficient at the roll axis becomes infinite (the roll is locked) and obviously higher than friction coefficient between the slab and the roll. As already mentioned in section III.1.3.1, the increment of resisting force is given by:

$$\delta R = \mu_{strand-roll} \delta F \tag{327}$$

The ratio of friction coefficients is equal to:

$$\frac{\mu_{strand-roll}}{\mu_{axis}} = \frac{0.30}{0.015} = 20 \tag{328}$$

so that the increase of resisting force for each locked pair of rolls should be 20 times the one measured on free pair of rolls.

Practically, the following methodology has been applied to model locked pairs in the model. The basic curve of extracting force remains the one of the caster manufacturer, but the step corresponding to locked rolls are multiplied by 20, according to relations (327) and (328).

Two different cases have been studied:

5. the only pair #48 has been locked, this pair being in constant curvature zone;
6. pairs #48 and #52 are locked, the latter being in the straightening zone.

The cumulated resisting force becomes in both cases the following one:

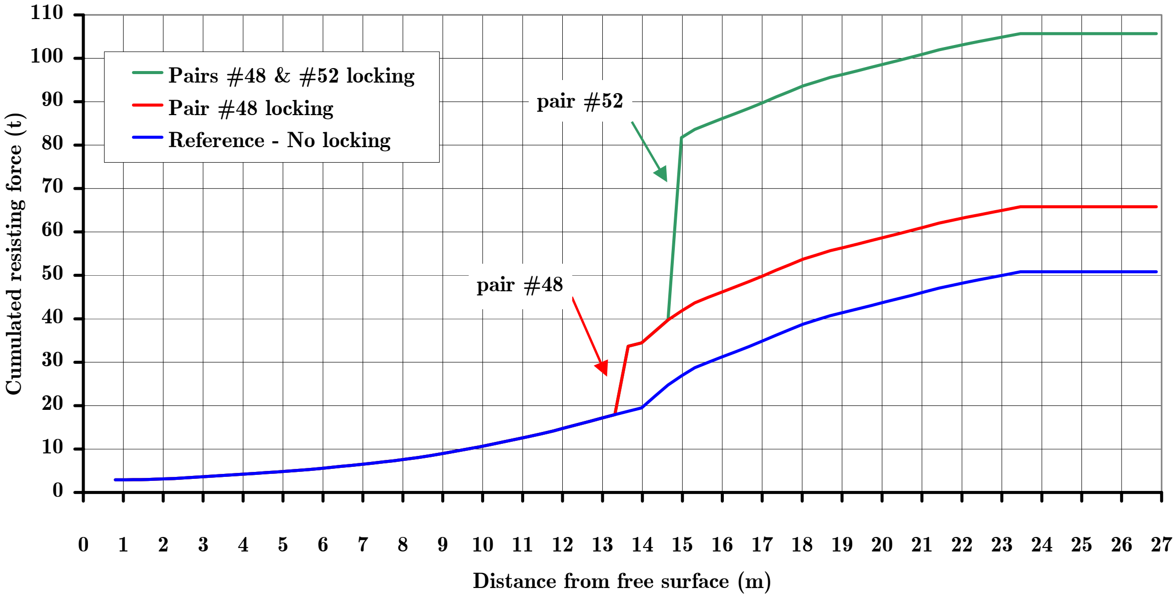

Figure 173: Cumulated resisting force in case of rolls locking

An important difference can already be mentioned: in case of locking in the straightening zone (pair #52), the increase of resisting force is much higher (almost 3 times) than for locking of rolls in the constant curvature zone. The reason is the double contribution in resisting force in straightening zone: bulging and straightening.

The increase of resisting force has to be compensated by an increase of work made by extracting rolls. Several assumptions can be made again concerning the distribution of additional work among extracting rolls. When the pair #48 is locked, 15 additional tons of resisting force have to be balanced by the increase of electrical power of the caster. Two pairs of extracting rolls are in the vicinity of pair #48: that are pairs #44 (above) and #50 (below). The most unfavourable assumption has been adopted: the one considering that preceding motorised pairs do not make any additional work. Otherwise, they would decrease the longitudinal effort. At the opposite, considering that the only pair #50 makes the additional work, the longitudinal effort increases by 15t in tensile state.

Another practical aspect has been taken into account: the maximum power of each extracting rolls, which can be expressed as limitation in terms of extracting force. The caster manufacturer provides the maximum extracting force for each pair, so that the remaining potential of extraction can be deduced for the reference case:

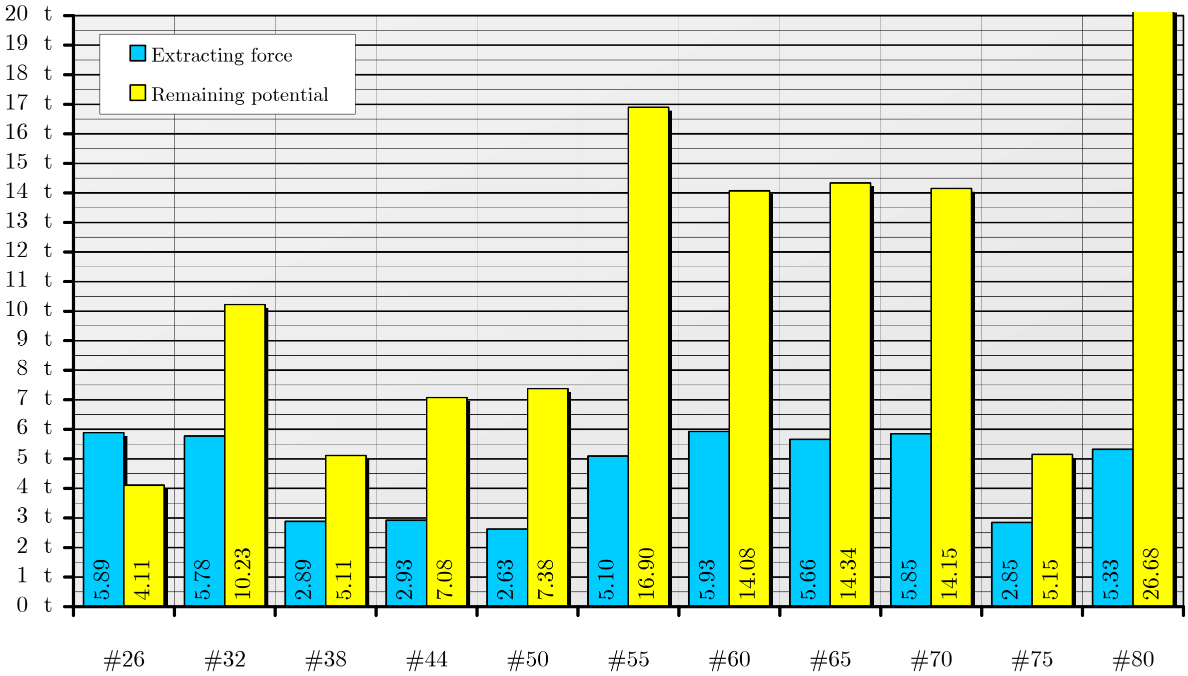

Figure 174: Distribution of extracting force and remaining potential of extraction – Reference case

In case of pair #48 locking, the 15 additional tons cannot be balanced by the increase of work made by pair #50, because this one only have 7.38t of potential additional extracting force. That means that another extracting pair has to make additional work too. To maintain the most unfavourable assumption, the pair #55 has to do. So that in case of pair #48 locking, the distribution of extracting force becomes:

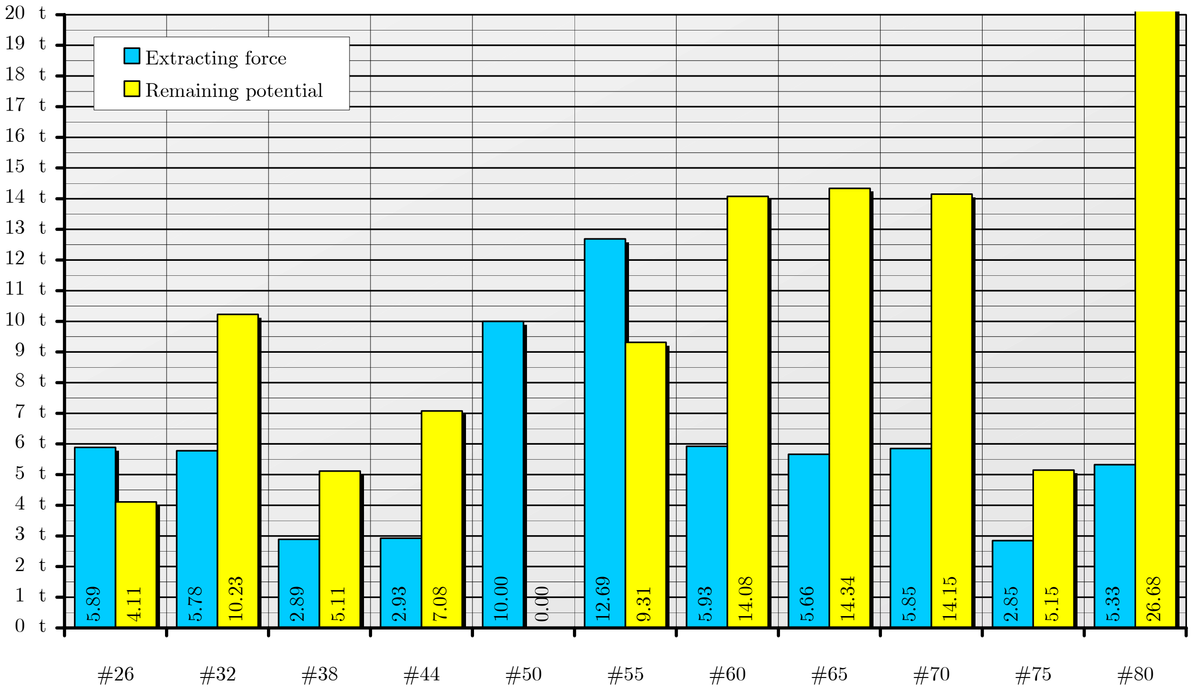

Figure 175: Distribution of extracting force and remaining potential of extraction – Locking of pair of rolls #48

In case of pairs #48 and #52 locking (second studied case of locking), several extracting pairs have to work at 100% of their nominal maximum power to balance the increase of resisting force. The extracting force is thus distributed as follows:

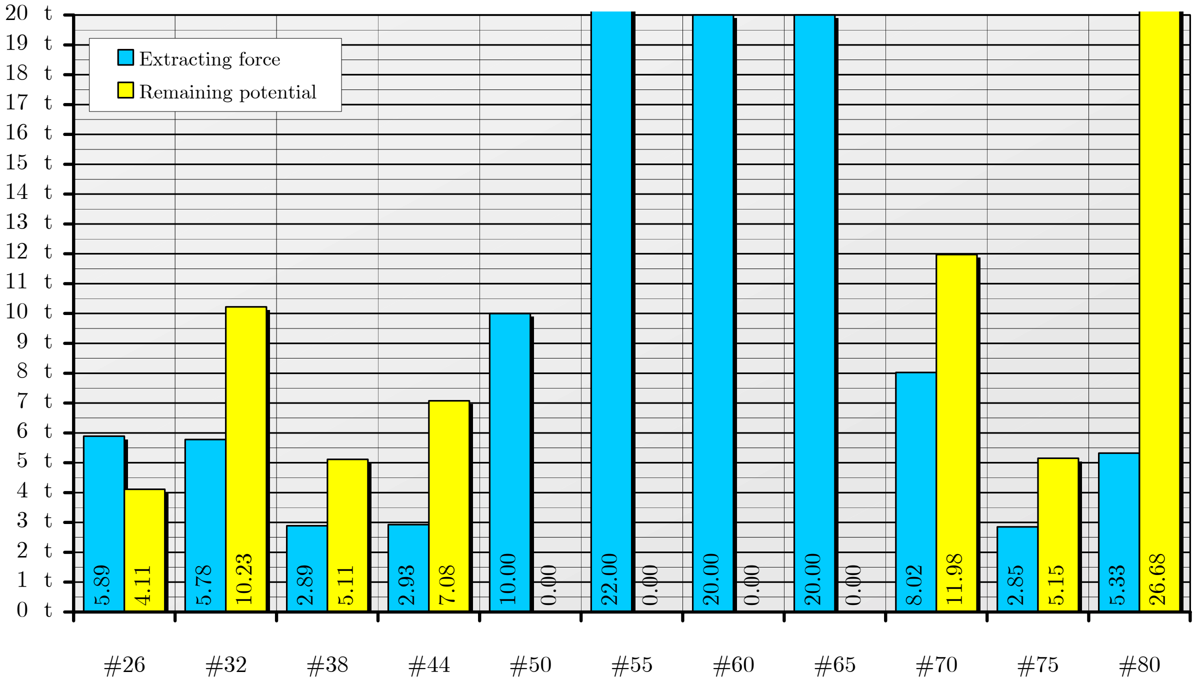

Figure 176: Distribution of extracting force and remaining potential of extraction – Locking of pairs of rolls #48 and #52

From previous considerations, the effective longitudinal effort can be deduced in case of locking(s):

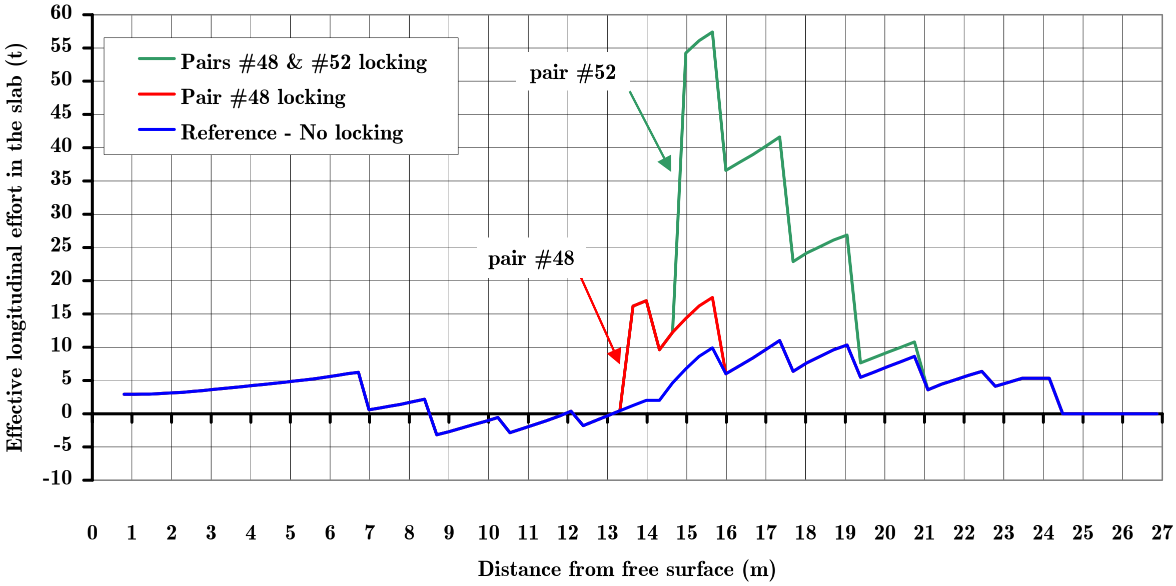

Figure 177: Effective longitudinal effort in the slab

4.2.2. Effect on the surface temperature

Locking of one or two pairs of rolls cannot influence thermal behaviour of the slab. Only friction can indeed generate heating of slab surface in contact with rolls. However, heat amount generated by such frictional effect is negligible with respect to amount of heat contained in the solidifying slab. So long as no difference can be observed in surface temperature between reference and locking cases, the same low ductility zones are visible at the slab surface.

4.2.3. Effect on thickness of the slice

Locking of one or two pairs of rolls, and subsequent rising in resisting force, tends to increase the longitudinal tensile state of the slab and thus a thicker slice, as shown on Figure 178.

This increasing is sensible for pair #48 locking, but much more important for pair #52 locking. In this last case, the slice after straightening is about 0.4% thicker than in the reference case.

In other respect, as mentioned in the analysis of the reference case (cf. section VI.3.3), the slope of the curves on Figure 178 are good indicators of longitudinal strain rate. It already seems that locking of pair #52 provokes higher strain rates, so that the risk of transverse cracking is more important in such a case and still located at the end of straightening.

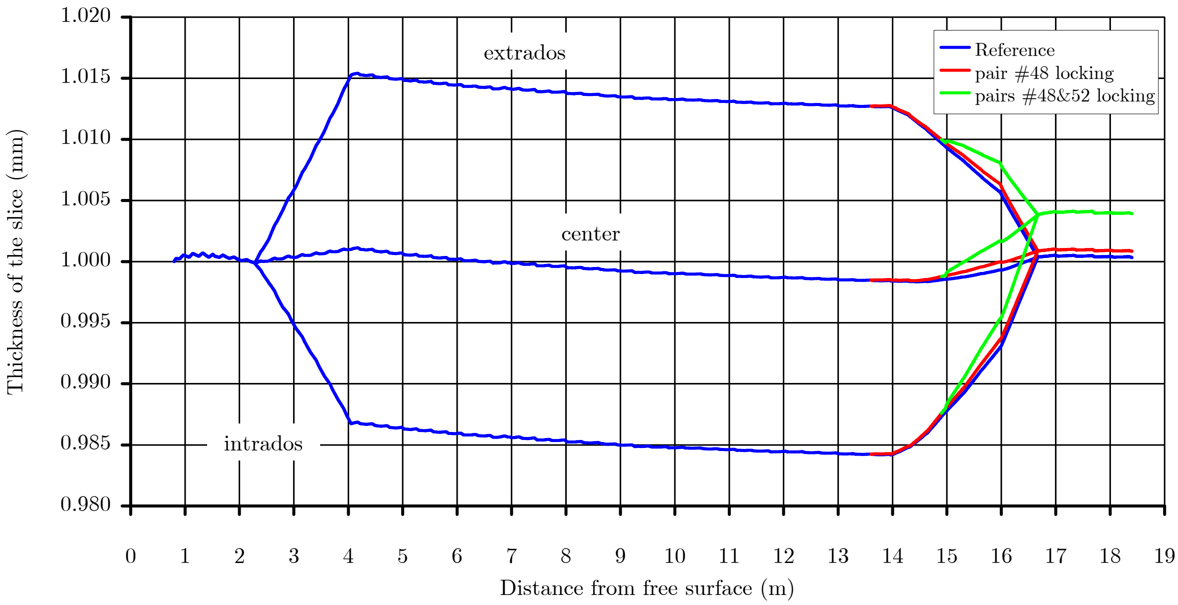

Figure 178: Effect of locking of one or two pairs of rolls on thickness of the slice

4.2.4. *Effect on risk of transverse cracking*

When only pair #48 is locked, first index I_1 does not vary so much: a few critical zones are in expansion, corresponding to area where longitudinal stress goes from compression to tensile state. The maximum risk is still located in the same zone – slab corner, intrados face and end of straightening – the maximum value of I_1 being very close to the value of the maximum in reference case (41.3MPa vs. 41.1MPa, less than 1% of difference). According to these observations (visible on Figure 179), locking of the pair #48 is unfavourable, but very slightly.

For two pairs of rolls including #52, which is in straightening zone, the influence is quite harder with a maximum index equal to 43.0MPa (+5%). This increase is more significant. In other respects, the maximum risk is again located at the same place (see Figure 179).

The second index gives almost the same conclusions (cf. Figure 180): locking of pair #48 has no influence on the index value I_2 (max. 22 10^{-5} s^{-1}, identical to reference), while locking of the both pairs #48 and #52 induces maximum value of 30 10^{-5} s^{-1}, which is 35% higher than the reference.

The Figure 181 shows the effect of rolls locking on the risk of transverse cracking on the extrados face. It must be noted that the locking of pair #52 generates a so high increasing of longitudinal effort in the slab that longitudinal stress becomes locally in tensile state (pair #52). However, compression comes back at the next pair. In other respect, the maximum on the extrados face remains quite low (15 10^{-5} s^{-1}) with respect to maximum values on intrados.

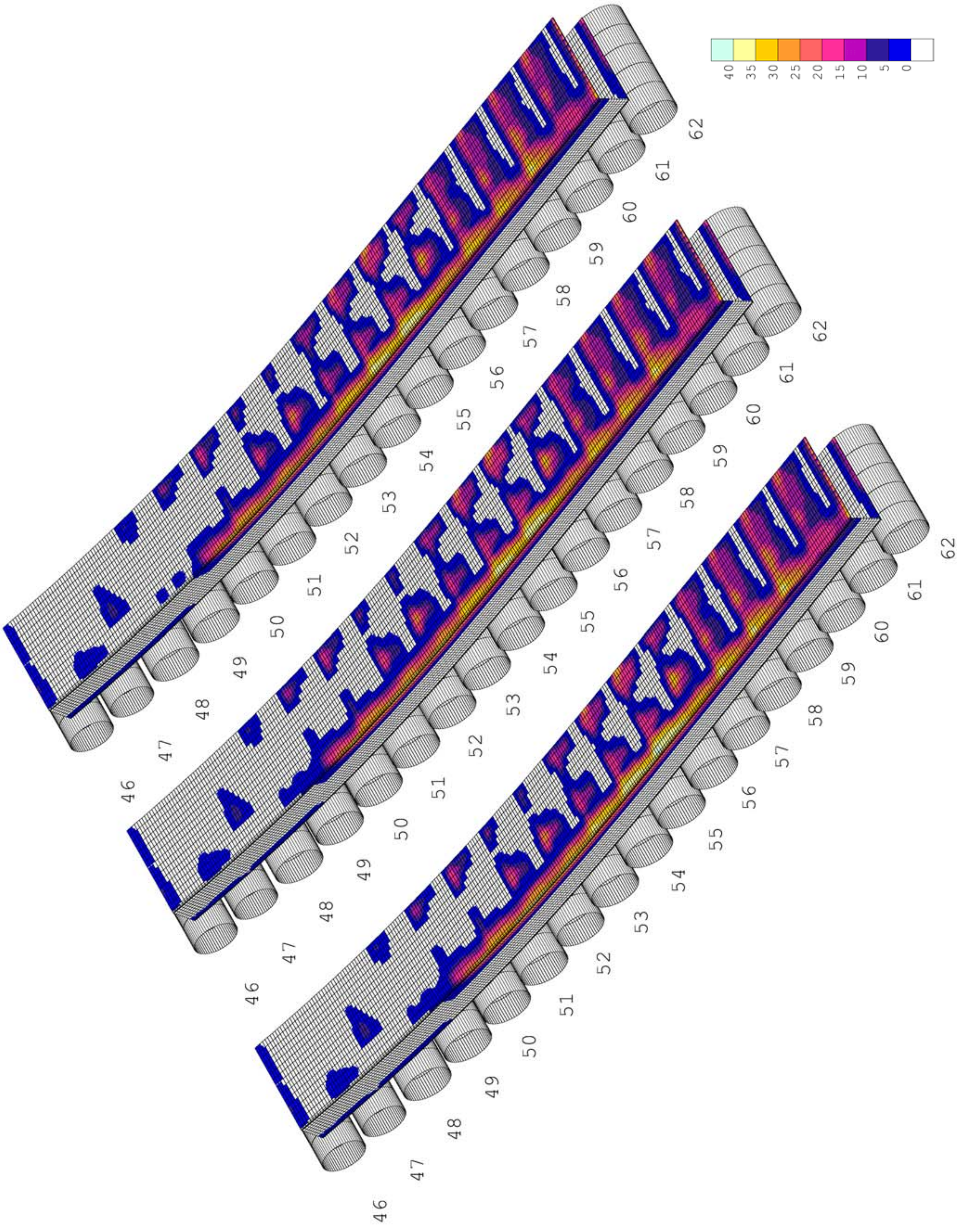

Figure 179: Effect of locking of one or two pairs of rolls on risk of transverse cracking according to index I_1 (Intrados face)

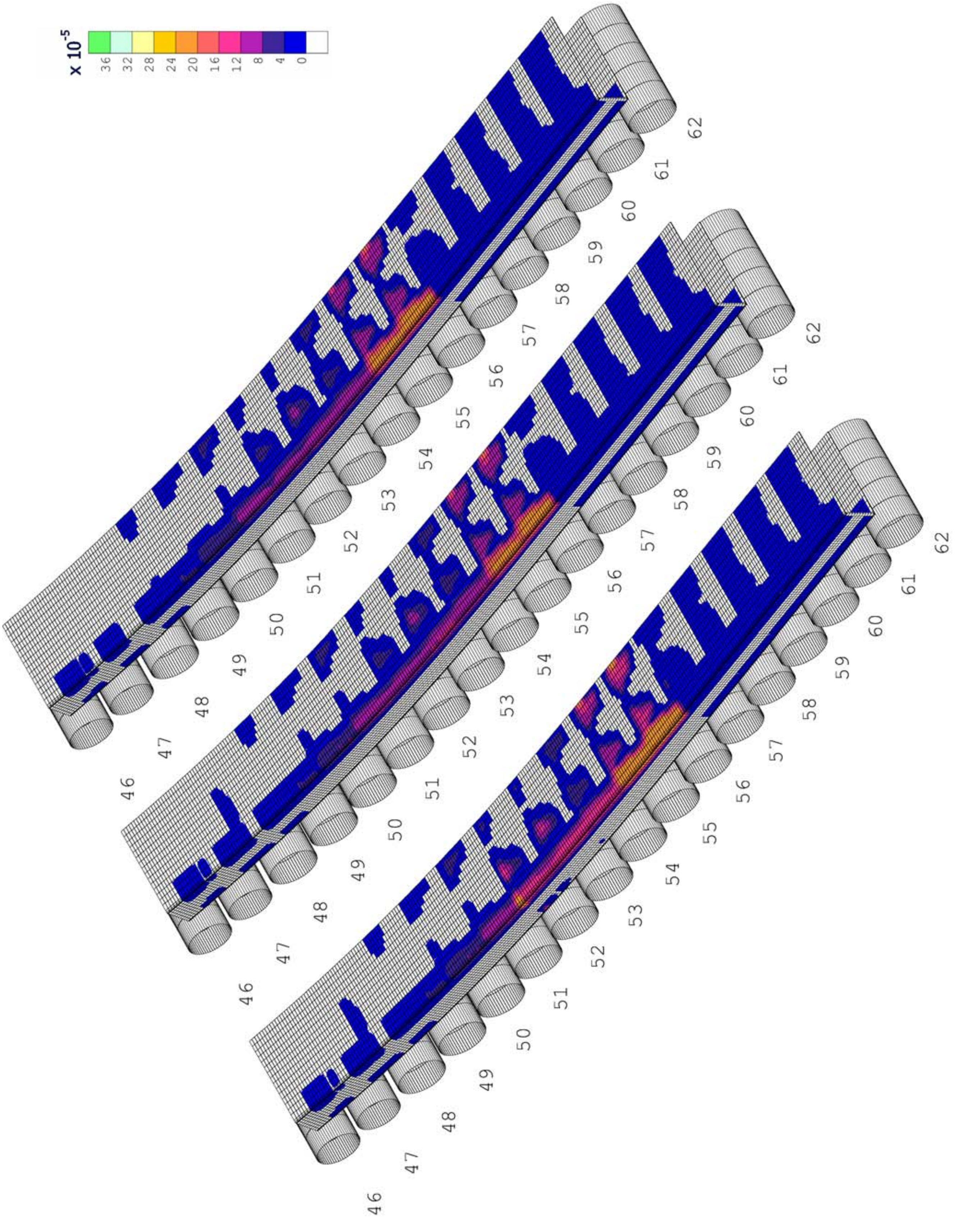

Figure 180: Effect of locking of one or two pairs of rolls on risk of transverse cracking according to index I_2 (Intrados face)

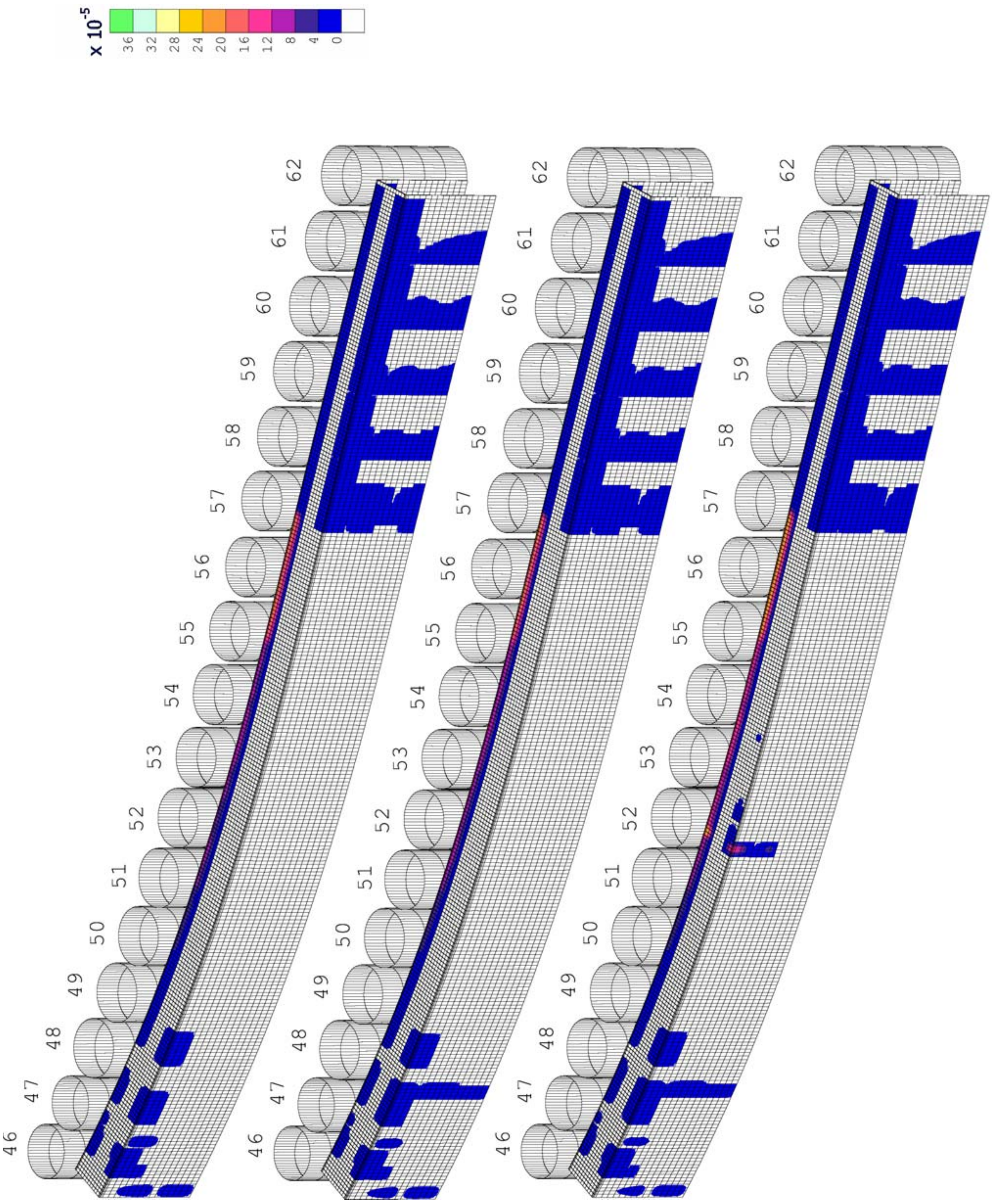

Figure 181: Effect of locking of one or two pairs of rolls on risk of transverse cracking according to index I_2 (Extrados face)

4.3. Misalignment of one pair of rolls

4.3.1. Definition of the local defect

The modelled defect is a misalignment of the pair of rolls #48. The amplitude of the misalignment is 2mm perpendicularly to the casting axis towards the centre of curvature of the caster:

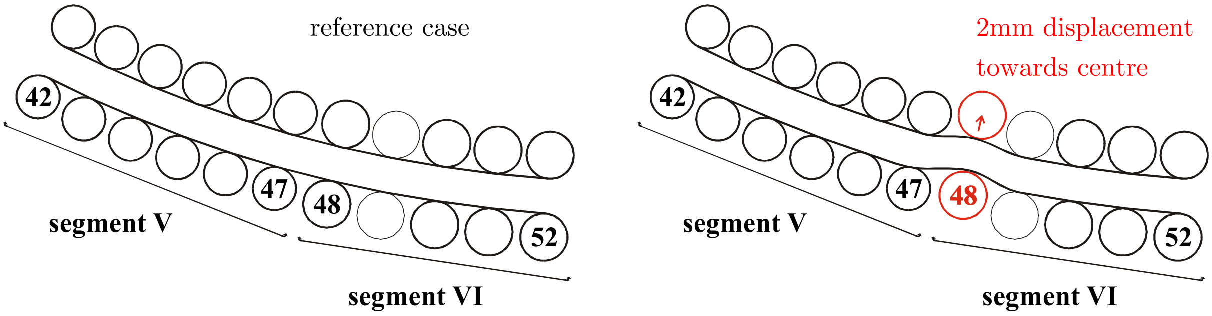

Figure 182: Misalignment introduced in the model

Further to this displacement, an important modification is introduced in the geometry of the caster. The curvature is hardly modified, even if the displacement may appear slight with respect to dimensions of the caster.

In fact, a succession of local bending/straightening/bending is created as illustrated on this figure:

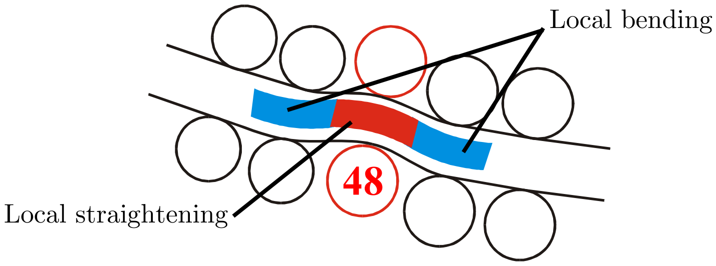

Figure 183: Succession of local bending/straightening/bending due to misalignment

After having computed the new position of rolls of pair #48, it is possible to evaluate the new radii of curvature, taking care to modify those of pairs #47, #48 and #49.

New radii are calculated assuming that three successive rolls A, B and C are defining a triangle. The radius of curvature measured at the level of roll B is given by the radius of the circle drawn round the triangle (see Figure 184 on the right).

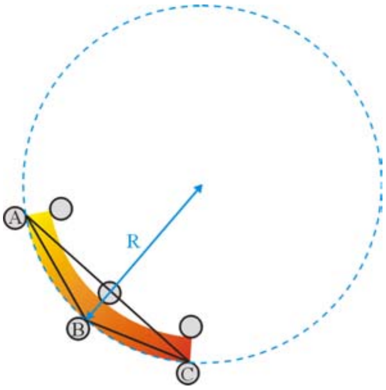

Figure 184: Circle drawn round the triangle made of three successive rolls

If a, b and c are the length of the edges of the triangle (respectively opposed to A, B and C vertexes), the radius R of the circle drawn round the triangle is given by:

$$R = \frac{abc}{4S} \tag{329}$$

where S is the surface area of the triangle.

The radius of curvature becomes:

Radius of pair:	#46	#47	#48	#49	#50
Reference case	8 006 mm	8 006 mm	8 006 mm	8 006 mm	8 400 mm
Misalignment	8 006 mm	6 984 mm	11 130 mm	7 159 mm	8 400 mm

This is the first important modification in the model.

The second one concerns the extracting force. Due to local bending and straightening, the resisting force increases significantly, the problem being to determine how much. With the previous defect, an assumption of friction coefficient has been enough to determine a multiplicative factor for resisting increment at the level of locked pairs of rolls. No such assumption can be made for roll misalignment. However, as mentioned in section VI.2.3, it is possible to evaluate the extraction force in a coupled way. This computation has been performed with and without roll misalignment and the difference between the extraction forces in both cases is about 5.5t which progressively appear starting form the roll misalignment.

Since the curves of the caster manufacturer have been used for other defects modelling – and to ensure a correct comparison of the results with current defect – the 5.5t difference has been "translated" on the manufacturer curves. To do so, it has been observed that the slope ratio between "coupled" curve and the manufacturer one is about 0.45 around pair #48. That means that the increment of resisting/extraction force calculated in the coupled way is about 45% the value given by the manufacturer. Such a ratio has been applied to the progressive additional 5.5t due to roll misalignment, the cumulated resisting force becoming:

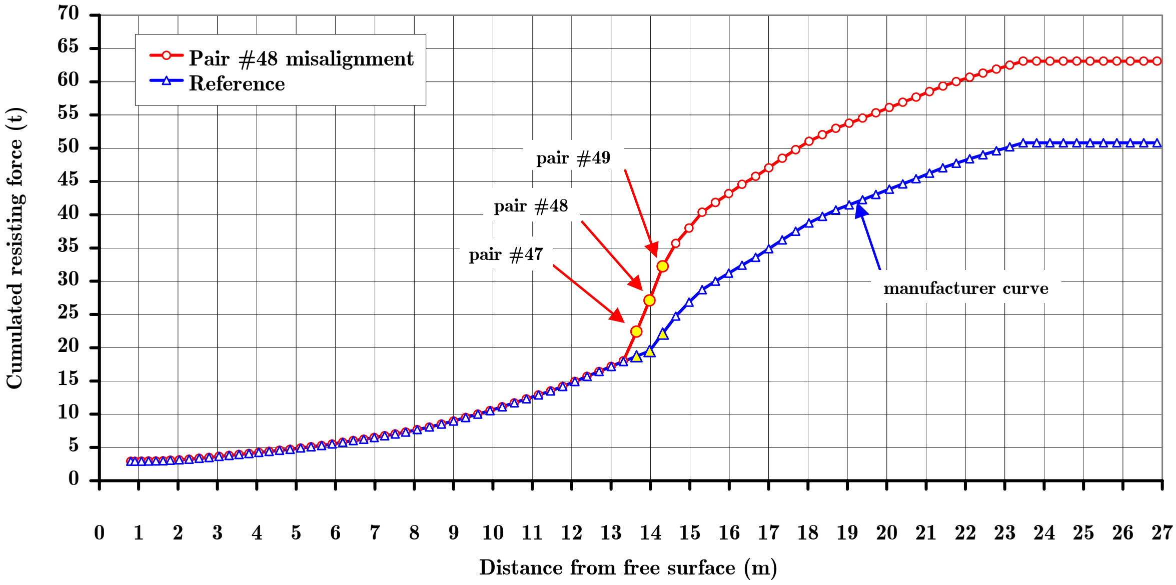

Figure 185: Cumulated resisting force in case of pair #48 misalignment

The global increasing of resisting force is finally about 12t, which is almost the same amplitude than in case of locking of pair #48. Here again, this increasing is higher than the remaining potential of extracting force of the pair #50, so that pair #55 has to make additional work too (see Figure 186).

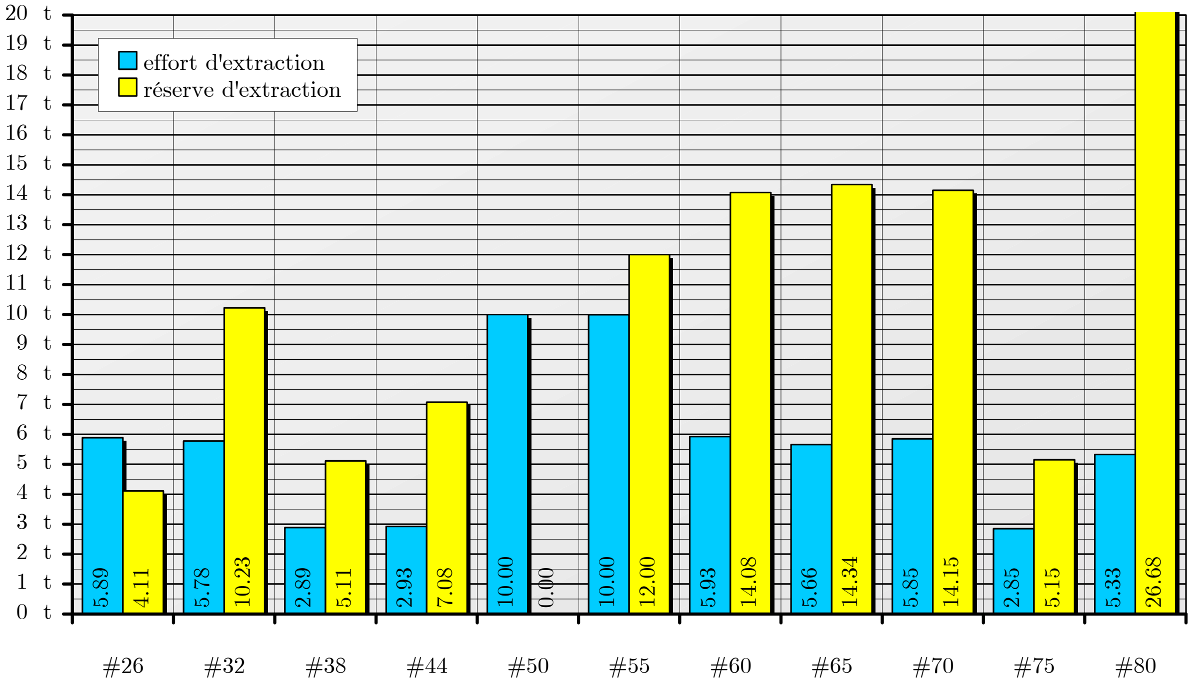

Figure 186: Distribution of extracting force and remaining potential of extraction – Misalignment of pair of rolls #48

And the effective longitudinal effort is:

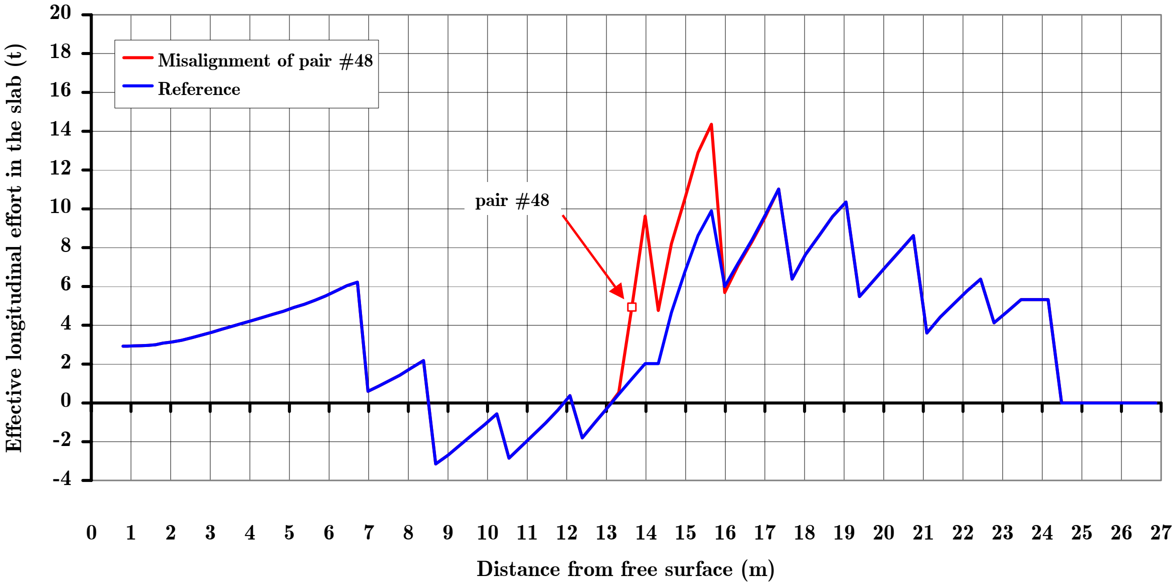

Figure 187: Effective longitudinal effort in the slab

4.3.2. Effect on the surface temperature

The same analysis (and conclusion) as for rolls locking can be made for rolls misalignment about the effect on temperature. Same surface temperatures generate the same low ductility zones with or without this type of defect.

4.3.3. Effect on thickness of the slice

Study of evolution of the slice thickness remains interesting. As pictured on Figure 188, local bending and straightening create important variations of thickness and the slopes of the curves are similar to the slope of the global straightening of the slab (the "normal" one). It is even higher during the local straightening on the intrados face and during the second local bending on the extrados face.

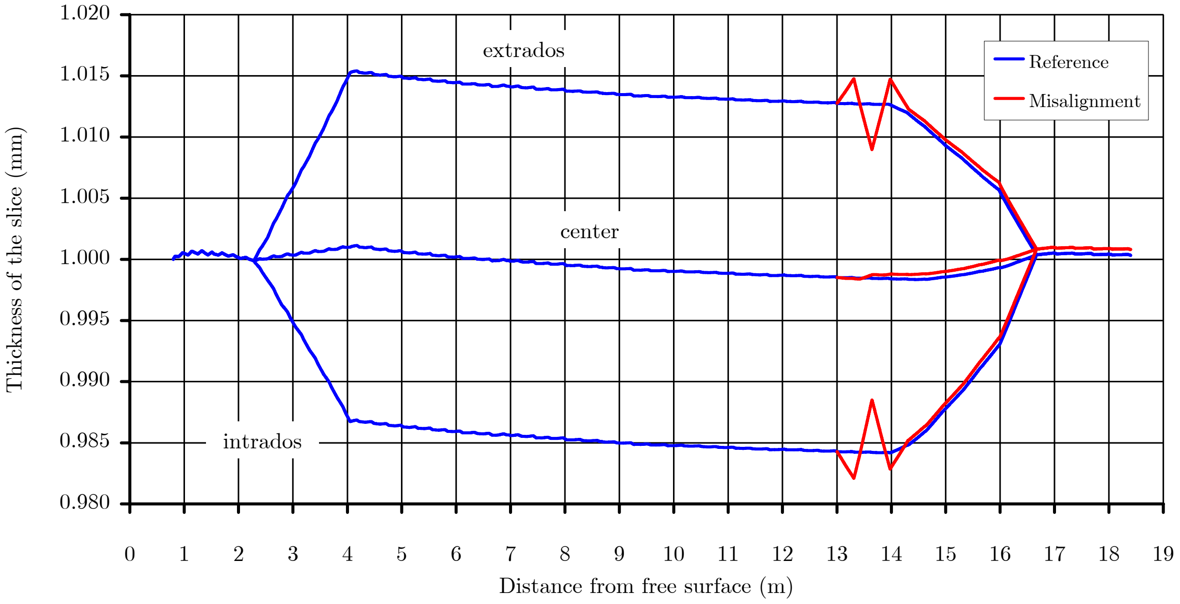

Figure 188: Effect misalignment of one pair of rolls on thickness of the slice

From these observations, one can expect to attempt high values of second index I_2 of risk of transverse cracking.

4.3.4. Effect on risk of transverse cracking

From Figure 189 to Figure 192, the risk of transverse cracking is shown for both indexes I_1 and I_2 and for both faces of the slab (intrados and extrados).

The defect of 2mm misalignment seems to generate higher risk of transverse cracking as the following curves indicate. In other respect, the maximum risk is located around the defect (in the vicinity of pair #48).

The maximum index I_1 on the intrados face is 46MPa (+12% with respect to reference), but it reaches 49.5 MPa on the extrados, which is the global maximum value.

Concerning the second index, I_2 reaches 40 10^{-5} s^{-1} on intrados face during the local straightening due to misalignment, which is almost the double of the maximum value in the reference case. On the extrados face, the maximum reaches 33 10^{-5} s^{-1} corresponding to the second local bending.

Thus both indexes are showing very large increase of the risk of transverse cracking in case of 2mm rolls misalignment.

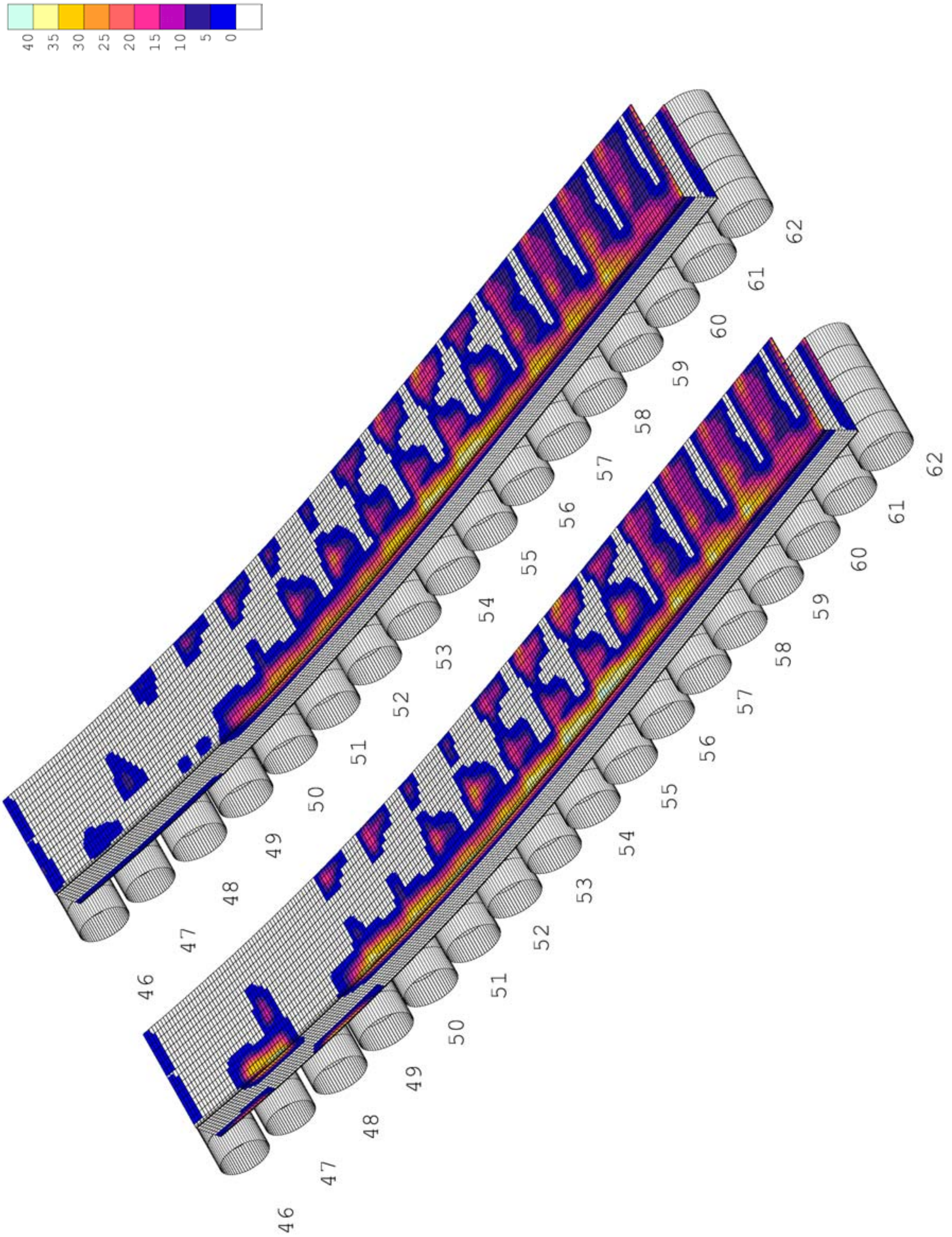

Figure 189: Effect of misalignment of one pair of rolls on risk of transverse cracking according to index I_1 (Intrados face)

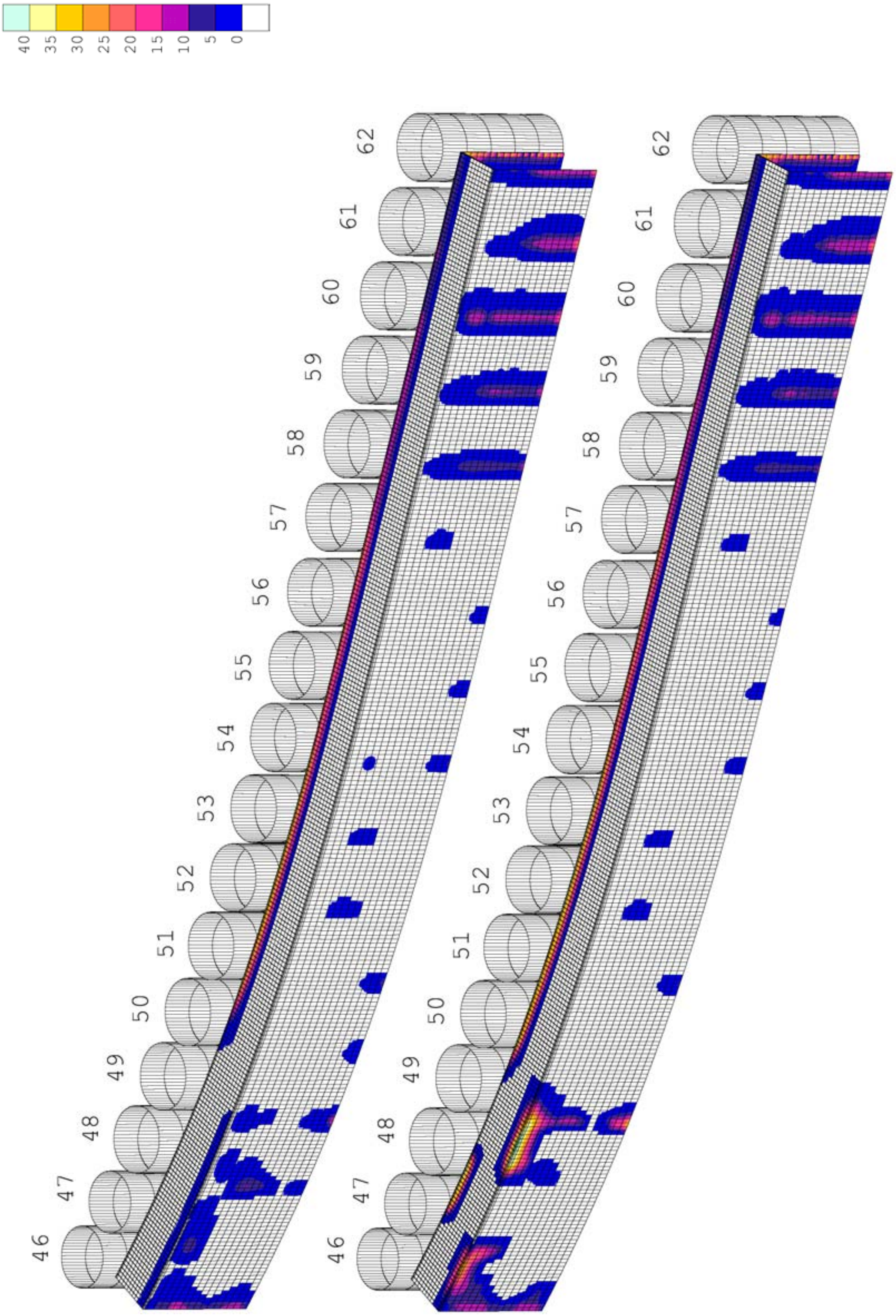

Figure 190: Effect of misalignment of one pair of rolls on risk of transverse cracking according to index I_1 (Extrados face)

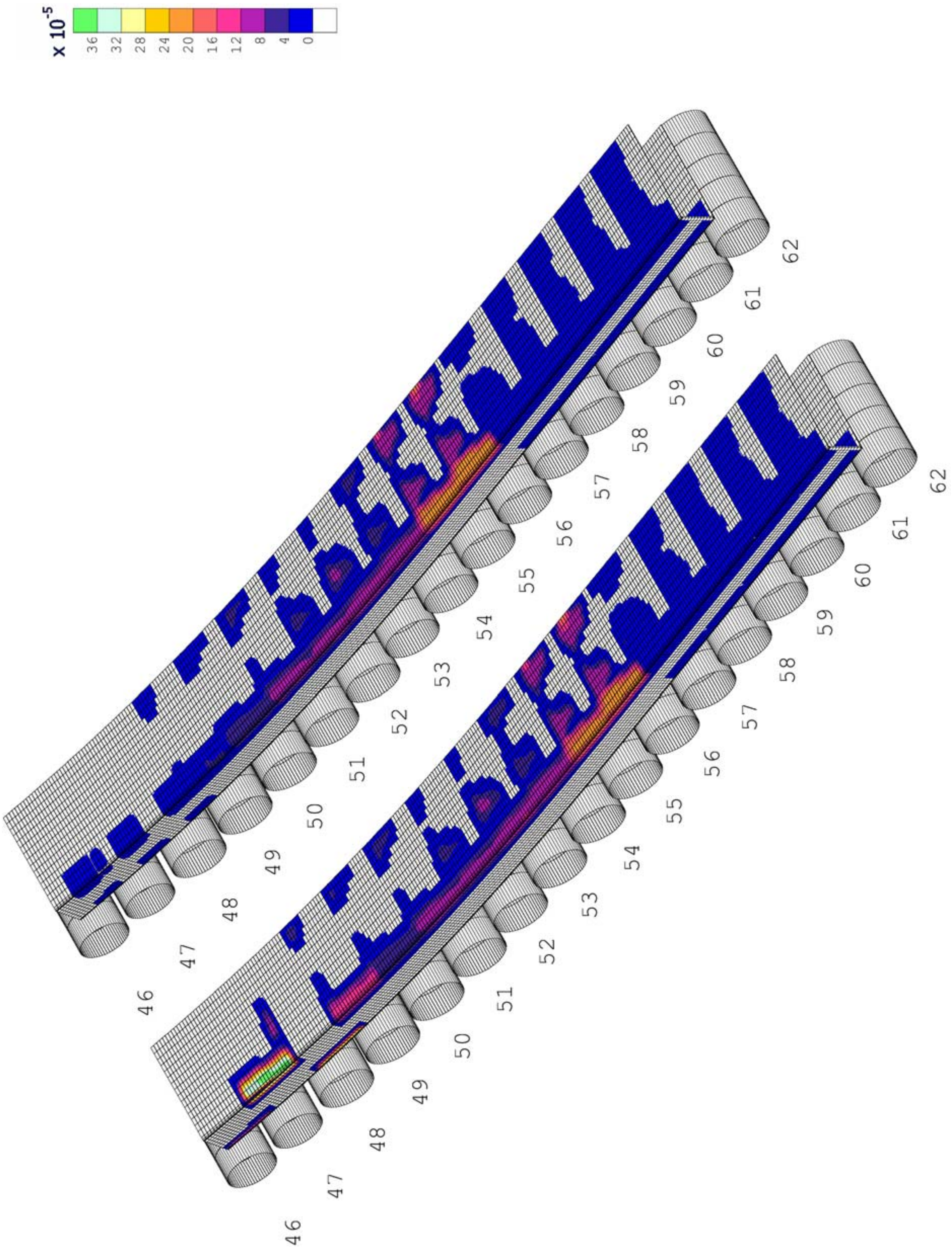

Figure 191: Effect of misalignment of one pair of rolls on risk of transverse cracking according to index I_2 (Intrados face)

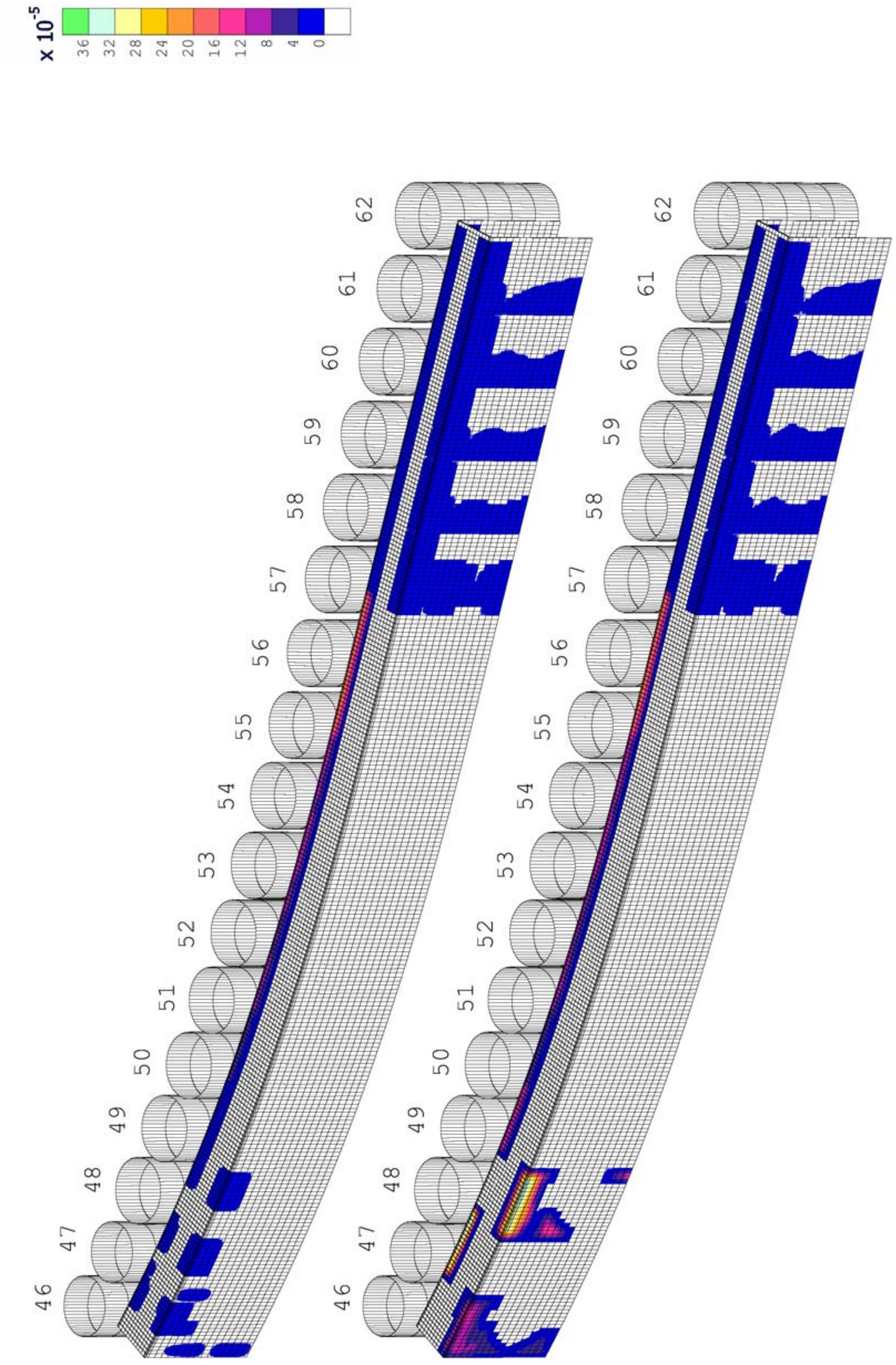

Figure 192: Effect of misalignment of one pair of rolls on risk of transverse cracking according to index I_2 (Extrados face)

5. Discussion

The objective of this industrial application was the comparison of different local defects in the caster and their consequences in terms of risk of transverse cracks formation. The detailed analysis of the results and their industrial exploitation remain the property of the industrial partner and they are not discussed in the thesis. However, from the post-research discussion, it clearly appeared that the results were in good agreement with reality.

From the mechanical point of view, the model demonstrates the aptitude of the generalized plane strain state to model bending and straightening in a slice model: respect of the curvature of the caster, application of an extracting force and position of neutral axis determined by equilibrium equations.

The control of bulging constitutes an important factor to correctly model the behaviour of the slab with such a type of slice model. The introduction of springs has been an important stage in the development of the model. An improvement could be the introduction of a coupled computation of the maximum bulging for each roll span.

VII. Conclusion and perspectives

VII. Conclusion and perspectives

During the last six years, a thermo-mechanical model of continuous casting has been developed. The construction of this model has been based according to two main constraints:

- The numerical framework: the developments have been implemented in the finite element code LAGAMINE and they are thus adopting the same main assumptions (thermo-mechanical modelling, lagrangian approach and thus no fluid flow modelling); in other respects, a 2D½ approach has been chosen, because of the large CPU time requirement of 3D models, which were not conceivable with current computers.
- The objectives: the developments have been performed in order to bring answers to the requests made by industrial partners on the subject. In the first application, the objective was not to optimize of the mould taper, but to provide to the research team of the industrial partner a numerical tool able to model the behaviour of the solid shell in the mould. In the second application, the requirements concerned the thermo-mechanical state of a slab during bending and straightening of the slab and more especially the effect of local defects on the risk of transverse cracks formation.

To reach the present configuration, many developments have been carried out in the finite element code, which had never been used for material modelling with success at so high temperatures. A unified mechanical constitutive law for steel at very high temperature has been implemented to model steel behaviour from liquid to solid phase.

A specific thermo-mechanical contact element has been developed to taken into account friction in the out-of-plane direction as well as varying thermal boundary conditions: a progressive variation of heat transfer coefficient depending on the gap size in the mould and a very complete definition of this coefficient in secondary cooling, according to water spray cooling rate.

A ferrostatic pressure element has been inserted in the LAGAMINE code.

The generalized plane strain state has also been plainly exploited with new extensions applying an external force corresponding extracting force and leaving neutral axis to settle according to equilibrium equations.

A special attention has been drawn to slab bulging with an efficient addition of springs.

The staggered time-stepping scheme is also an important feature of the model since it allowed performing the complete simulation of both applications without problem while a completely coupled thermo-mechanical analysis would have been impossible with the size of the elements used in the finite element mesh.

Globally, the results have been discussed and validated by numerous debates with industrial partners and particularly with engineers who are daily confronted with the casting problem. A close collaboration with Bourdouxhe, Labory and Hubsch from ProfilARBED Recherche has been fruitful in the first industrial application. For the second one, a real industrial team gathering people from IRSID, CDAM and the factory have coached the project.

The potential improvements to be brought to the model might be:

- A more accurate definition of the initial temperature field at the meniscus level, introducing a decreasing temperature gradient from the centre of the slice to the surface, where the temperature should already be close to the solidus from the meniscus level.
- The integration in the LAGAMINE code of a bulging model coupled to the present model.
- The development or the integration of other indexes (or criteria) relative to the low ductility and/or internal cracks formation at the liquid/solid interface.

The model can be applied in other casting conditions: these modifications can be voluntary (casting speed, steel grade, cooling rate…) or the consequence of defects (such as roll locking, roll misalignment…).

The model can also be applied to other caster without too many modifications. Now that the most important part of the work has been done (development of the constitutive law and the specific elements), changing the geometry or the cast material only requires some adaptations in the model (identification of the material behaviour, modification of the caster geometry, positioning of sprays and flow rate, definition of casting speed, computation new maximum bulging for each roll span, introduction of an extraction force compatible with the caster and the product…). In fact, a first other application has begun a few months ago with a model of copper semi-continuous casting.

The model supplies thermal and mechanical evolutions of the slice and these results are also exploitable by other models:

- a first attempt of automatic optimization of the mould taper has already been driven in the framework of a graduating thesis [MIE93];
- another Ph.D. thesis is in progress, focussing on the prediction of cracks at the grain scale: the present "macroscopic" model gives the loading (stress, strain and temperature fields) to apply to a mesoscopic cell defined in that other (future-) thesis, which allows examining the link between some metallurgy aspects (grain size, alloying elements), stress state and transverse crack formation [REM02,CAS03].

Thus, besides some potential improvement of the model itself, other models can be based on the present one or its results, ensuring some interesting perspectives.

VIII. Appendix: analytical developments

VIII. Appendix: analytical developments

1. *Implicit time integration of Norton-Hoff law*

To simplify notations, time step is noted Δt, but it is identical to Δt_{AB}. Starting from relation (181):

$$\underline{A} \cdot \Delta\underline{\hat{\sigma}} = \underline{F} \tag{330}$$

with

$$\Delta\underline{\hat{\sigma}} = \begin{Bmatrix} \Delta\hat{\sigma}_{11} \\ \Delta\hat{\sigma}_{22} \\ \Delta\hat{\sigma}_{12} \\ \Delta\hat{\sigma}_{33} \end{Bmatrix} \tag{331}$$

$$\underline{A} = \begin{bmatrix}
1 - \left.\frac{\partial g_{11}}{\partial \hat{\sigma}_{11}}\right|_A \theta\Delta t & -\left.\frac{\partial g_{11}}{\partial \hat{\sigma}_{22}}\right|_A \theta\Delta t & -\left.\frac{\partial g_{11}}{\partial \hat{\sigma}_{12}}\right|_A \theta\Delta t & -\left.\frac{\partial g_{11}}{\partial \hat{\sigma}_{33}}\right|_A \theta\Delta t \\
-\left.\frac{\partial g_{22}}{\partial \hat{\sigma}_{11}}\right|_A \theta\Delta t & 1 - \left.\frac{\partial g_{22}}{\partial \hat{\sigma}_{22}}\right|_A \theta\Delta t & -\left.\frac{\partial g_{22}}{\partial \hat{\sigma}_{12}}\right|_A \theta\Delta t & -\left.\frac{\partial g_{22}}{\partial \hat{\sigma}_{33}}\right|_A \theta\Delta t \\
-\left.\frac{\partial g_{12}}{\partial \hat{\sigma}_{11}}\right|_A \theta\Delta t & -\left.\frac{\partial g_{12}}{\partial \hat{\sigma}_{22}}\right|_A \theta\Delta t & 1 - \left.\frac{\partial g_{12}}{\partial \hat{\sigma}_{12}}\right|_A \theta\Delta t & -\left.\frac{\partial g_{12}}{\partial \hat{\sigma}_{33}}\right|_A \theta\Delta t \\
-\left.\frac{\partial g_{33}}{\partial \hat{\sigma}_{11}}\right|_A \theta\Delta t & -\left.\frac{\partial g_{33}}{\partial \hat{\sigma}_{22}}\right|_A \theta\Delta t & -\left.\frac{\partial g_{33}}{\partial \hat{\sigma}_{12}}\right|_A \theta\Delta t & 1 - \left.\frac{\partial g_{33}}{\partial \hat{\sigma}_{33}}\right|_A \theta\Delta t
\end{bmatrix} \tag{332}$$

$$\underline{F} = \begin{Bmatrix}
\left(f_{11}|_A + g_{11}|_A \right) + \left(\left.\frac{\partial f_{11}}{\partial T}\right|_A + \left.\frac{\partial g_{11}}{\partial T}\right|_A \right)\theta\Delta T + \left.\frac{\partial g_{11}}{\partial \overline{\varepsilon}^{vp}}\right|_A \theta\Delta\overline{\varepsilon}^{vp} \\
\left(f_{22}|_A + g_{22}|_A \right) + \left(\left.\frac{\partial f_{22}}{\partial T}\right|_A + \left.\frac{\partial g_{22}}{\partial T}\right|_A \right)\theta\Delta T + \left.\frac{\partial g_{22}}{\partial \overline{\varepsilon}^{vp}}\right|_A \theta\Delta\overline{\varepsilon}^{vp} \\
\left(f_{12}|_A + g_{12}|_A \right) + \left(\left.\frac{\partial f_{12}}{\partial T}\right|_A + \left.\frac{\partial g_{12}}{\partial T}\right|_A \right)\theta\Delta T + \left.\frac{\partial g_{12}}{\partial \overline{\varepsilon}^{vp}}\right|_A \theta\Delta\overline{\varepsilon}^{vp} \\
\left(f_{33}|_A + g_{33}|_A \right) + \left(\left.\frac{\partial f_{33}}{\partial T}\right|_A + \left.\frac{\partial g_{33}}{\partial T}\right|_A \right)\theta\Delta T + \left.\frac{\partial g_{33}}{\partial \overline{\varepsilon}^{vp}}\right|_A \theta\Delta\overline{\varepsilon}^{vp}
\end{Bmatrix} \Delta t \tag{333}$$

where

$$\begin{cases} \underline{f}(T(t)) = 2G\hat{\dot{\underline{\varepsilon}}}^{tot} \\ \\ \underline{g}(\underline{\hat{\sigma}}(t), \overline{\varepsilon}^{vp}(t), T(t)) = \dfrac{1}{G}\dfrac{\partial G}{\partial T}\underline{\hat{\sigma}}\dot{T} - G\dfrac{(-J_2)^{p_5}\, e^{\frac{p_1}{p_3}\overline{\varepsilon}^{vp}}}{(K_0 p_2)^{\frac{1}{p_3}}(\overline{\varepsilon}^{vp})^{\frac{p_4}{p_3}}}\underline{\hat{\sigma}} \end{cases} \tag{334}$$

Hence:

$$\begin{aligned} F_{11} &= (f_{11}|_A + g_{11}|_A).\Delta t + \left(\left.\frac{\partial f_{11}}{\partial T}\right|_A + \left.\frac{\partial g_{11}}{\partial T}\right|_A\right)\theta\Delta T.\Delta t + \left.\frac{\partial g_{11}}{\partial \overline{\varepsilon}^{vp}}\right|_A \theta\Delta\overline{\varepsilon}^{vp}\Delta t \\ &= 2G\Delta t.\hat{\dot{\varepsilon}}_{11}^{tot} + 2\frac{\partial G}{\partial T}\theta\Delta T.\Delta t.\hat{\dot{\varepsilon}}_{11}^{tot} + \frac{1}{G}\frac{\partial G}{\partial T}\dot{T}\Delta t.\hat{\sigma}_{11} \\ &-G\frac{(-J_2)^{p_5}\, e^{\frac{p_1}{p_3}\overline{\varepsilon}^{vp}}}{(K_0 p_2)^{\frac{1}{p_3}}(\overline{\varepsilon}^{vp})^{\frac{p_4}{p_3}}}\Delta t.\hat{\sigma}_{11} + \frac{\partial}{\partial T}\left(\frac{1}{G}\right)\frac{\partial G}{\partial T}\dot{T}\theta\Delta T.\Delta t.\hat{\sigma}_{11} \\ &-\frac{\partial}{\partial T}\left(G\frac{(-J_2)^{p_5}\, e^{\frac{p_1}{p_3}\overline{\varepsilon}^{vp}}}{(K_0 p_2)^{\frac{1}{p_3}}(\overline{\varepsilon}^{vp})^{\frac{p_4}{p_3}}}\right)\theta\Delta T.\Delta t.\hat{\sigma}_{11} \\ &-G\frac{(-J_2)^{p_5}}{(K_0 p_2)^{\frac{1}{p_3}}}\frac{\partial}{\partial\overline{\varepsilon}^{vp}}\left(e^{\frac{p_1}{p_3}\overline{\varepsilon}^{vp}}(\overline{\varepsilon}^{vp})^{-\frac{p_4}{p_3}}\right)\theta\Delta\overline{\varepsilon}^{vp}\Delta t.\hat{\sigma}_{11} \end{aligned} \tag{335}$$

Grouping some terms:

$$\begin{aligned} F_{11} &= \left(2G\Delta t + 2\frac{\partial G}{\partial T}\theta\Delta T.\Delta t\right)\hat{\dot{\varepsilon}}_{11}^{tot} + \left\{\frac{1}{G}\frac{\partial G}{\partial T}\dot{T}\Delta t\right. \\ &-G\frac{(-J_2)^{p_5}\, e^{\frac{p_1}{p_3}\overline{\varepsilon}^{vp}}}{(K_0 p_2)^{\frac{1}{p_3}}(\overline{\varepsilon}^{vp})^{\frac{p_4}{p_3}}}\Delta t - \frac{1}{G^2}\left(\frac{\partial G}{\partial T}\right)^2\dot{T}\theta\Delta T.\Delta t \\ &-\frac{\partial}{\partial T}\left(G\frac{(-J_2)^{p_5}\, e^{\frac{p_1}{p_3}\overline{\varepsilon}^{vp}}}{(K_0 p_2)^{\frac{1}{p_3}}(\overline{\varepsilon}^{vp})^{\frac{p_4}{p_3}}}\right)\theta\Delta T.\Delta t \\ &\left.-G\frac{(-J_2)^{p_5}}{(K_0 p_2)^{\frac{1}{p_3}}}\frac{\partial}{\partial\overline{\varepsilon}^{vp}}\left(e^{\frac{p_1}{p_3}\overline{\varepsilon}^{vp}}(\overline{\varepsilon}^{vp})^{-\frac{p_4}{p_3}}\right)\theta\Delta\overline{\varepsilon}^{vp}\Delta t\right\}\hat{\sigma}_{11} \\ &= \mu\hat{\dot{\varepsilon}}_{11}^{tot} + \eta\hat{\sigma}_{11} \end{aligned} \tag{336}$$

assuming

$$\mu = 2G\Delta t + 2\frac{\partial G}{\partial T}\theta\Delta T.\Delta t \tag{337}$$

$$
\begin{aligned}
\eta = {} & \frac{1}{G}\frac{\partial G}{\partial T}\dot{T}\Delta t - G\frac{(-J_2)^{p_5}\, e^{\frac{p_1}{p_3}\overline{\varepsilon}^{vp}}}{(K_0p_2)^{\frac{1}{p_3}}\,(\overline{\varepsilon}^{vp})^{\frac{p_4}{p_3}}}\Delta t - \frac{1}{G^2}\left(\frac{\partial G}{\partial T}\right)^2\dot{T}\theta\Delta T.\Delta t \\
& -\frac{\partial}{\partial T}\left(G\frac{(-J_2)^{p_5}\, e^{\frac{p_1}{p_3}\overline{\varepsilon}^{vp}}}{(K_0p_2)^{\frac{1}{p_3}}\,(\overline{\varepsilon}^{vp})^{\frac{p_4}{p_3}}}\right)\theta\Delta T.\Delta t \\
& -G\frac{(-J_2)^{p_5}}{(K_0p_2)^{\frac{1}{p_3}}}\frac{\partial}{\partial\overline{\varepsilon}^{vp}}\left(e^{\frac{p_1}{p_3}\overline{\varepsilon}^{vp}}\,(\overline{\varepsilon}^{vp})^{-\frac{p_4}{p_3}}\right)\theta\Delta\overline{\varepsilon}^{vp}\Delta t
\end{aligned}
\tag{338}
$$

Computing the derivatives appearing in η:

$$
\begin{aligned}
\frac{\partial}{\partial T}\left(G\frac{(-J_2)^{p_5}\, e^{\frac{p_1}{p_3}\overline{\varepsilon}^{vp}}}{(K_0p_2)^{\frac{1}{p_3}}\,(\overline{\varepsilon}^{vp})^{\frac{p_4}{p_3}}}\right) = {} & \frac{\partial G}{\partial T}\frac{(-J_2)^{p_5}\, e^{\frac{p_1}{p_3}\overline{\varepsilon}^{vp}}}{(K_0p_2)^{\frac{1}{p_3}}\,(\overline{\varepsilon}^{vp})^{\frac{p_4}{p_3}}} \\
& +G\frac{e^{\frac{p_1}{p_3}\overline{\varepsilon}^{vp}}}{(K_0p_2)^{\frac{1}{p_3}}\,(\overline{\varepsilon}^{vp})^{\frac{p_4}{p_3}}}\frac{\partial}{\partial T}\left((-J_2)^{p_5}\right) \\
& +G\frac{(-J_2)^{p_5}}{(K_0p_2)^{\frac{1}{p_3}}\,(\overline{\varepsilon}^{vp})^{\frac{p_4}{p_3}}}\frac{\partial}{\partial T}\left(e^{\frac{p_1}{p_3}\overline{\varepsilon}^{vp}}\right) \\
& +G\frac{(-J_2)^{p_5}\, e^{\frac{p_1}{p_3}\overline{\varepsilon}^{vp}}}{(\overline{\varepsilon}^{vp})^{\frac{p_4}{p_3}}}\frac{\partial}{\partial T}\left((K_0p_2)^{-\frac{1}{p_3}}\right) \\
& +G\frac{(-J_2)^{p_5}\, e^{\frac{p_1}{p_3}\overline{\varepsilon}^{vp}}}{(K_0p_2)^{\frac{1}{p_3}}}\frac{\partial}{\partial T}\left((\overline{\varepsilon}^{vp})^{-\frac{p_4}{p_3}}\right) \\
= {} & \frac{\partial G}{\partial T}\frac{(-J_2)^{p_5}\, e^{\frac{p_1}{p_3}\overline{\varepsilon}^{vp}}}{(K_0p_2)^{\frac{1}{p_3}}\,(\overline{\varepsilon}^{vp})^{\frac{p_4}{p_3}}} \\
& +G\frac{e^{\frac{p_1}{p_3}\overline{\varepsilon}^{vp}}}{(K_0p_2)^{\frac{1}{p_3}}\,(\overline{\varepsilon}^{vp})^{\frac{p_4}{p_3}}}(-J_2)^{p_5}\frac{\partial p_5}{\partial T}\ln(-J_2) \\
& +G\frac{(-J_2)^{p_5}}{(K_0p_2)^{\frac{1}{p_3}}\,(\overline{\varepsilon}^{vp})^{\frac{p_4}{p_3}}}e^{\frac{p_1}{p_3}\overline{\varepsilon}^{vp}}\left(\frac{\partial p_1}{\partial T}-\frac{p_1}{p_3}\frac{\partial p_3}{\partial T}\right)\frac{\overline{\varepsilon}^{vp}}{p_3} \\
& -G\frac{(-J_2)^{p_5}\, e^{\frac{p_1}{p_3}\overline{\varepsilon}^{vp}}}{(\overline{\varepsilon}^{vp})^{\frac{p_4}{p_3}}}\frac{1}{(K_0p_2)^{\frac{1}{p_3}}}\frac{\partial}{\partial T}\left(\frac{\ln(K_0p_2)}{p_3}\right) \\
& -G\frac{(-J_2)^{p_5}\, e^{\frac{p_1}{p_3}\overline{\varepsilon}^{vp}}}{(K_0p_2)^{\frac{1}{p_3}}}\frac{1}{(\overline{\varepsilon}^{vp})^{\frac{p_4}{p_3}}}\frac{\partial}{\partial T}\left(\frac{p_4}{p_3}\ln(\overline{\varepsilon}^{vp})\right)
\end{aligned}
\tag{339}
$$

Let

$$\lambda = \frac{(-J_2)^{p_5}\, e^{\frac{p_1}{p_3}\overline{\varepsilon}}}{(K_0 p_2)^{\frac{1}{p_3}}\, \overline{\varepsilon}^{\frac{p_4}{p_3}}} \tag{340}$$

Relation (339) becomes

$$\begin{aligned}
\frac{\partial}{\partial T}(G\lambda) &= \frac{\partial G}{\partial T}\lambda + G\lambda\frac{\partial p_5}{\partial T}\ln(-J_2) + G\lambda\left(\frac{\partial p_1}{\partial T} - \frac{p_1}{p_3}\frac{\partial p_3}{\partial T}\right)\frac{\overline{\varepsilon}^{vp}}{p_3} \\
&\quad -G\lambda\frac{\partial}{\partial T}\left(\frac{\ln(K_0 p_2)}{p_3}\right) - G\lambda\frac{\partial}{\partial T}\left(\frac{p_4}{p_3}\ln(\overline{\varepsilon}^{vp})\right) \\
&= \frac{\partial G}{\partial T}\lambda + G\lambda\frac{\partial p_5}{\partial T}\ln(-J_2) + G\lambda\left(\frac{\partial p_1}{\partial T} - \frac{p_1}{p_3}\frac{\partial p_3}{\partial T}\right)\frac{\overline{\varepsilon}^{vp}}{p_3} \\
&\quad -G\lambda\frac{1}{p_3}\left(\frac{1}{K_0 p_2}\left(\frac{\partial K_0}{\partial T}p_2 + K_0\frac{\partial p_2}{\partial T}\right) - \ln(K_0 p_2)\frac{1}{p_3}\frac{\partial p_3}{\partial T}\right) \\
&\quad -G\lambda\left(\frac{\partial p_4}{\partial T} - \frac{\partial p_3}{\partial T}\frac{p_4}{p_3}\right)\frac{1}{p_3}\ln(\overline{\varepsilon}^{vp})
\end{aligned} \tag{341}$$

The second derivative in η is:

$$\begin{aligned}
\frac{\partial}{\partial \overline{\varepsilon}^{vp}}\left(e^{\frac{p_1}{p_3}\overline{\varepsilon}^{vp}}(\overline{\varepsilon}^{vp})^{-\frac{p_4}{p_3}}\right) &= \frac{p_1}{p_3}e^{\frac{p_1}{p_3}\overline{\varepsilon}^{vp}}(\overline{\varepsilon}^{vp})^{-\frac{p_4}{p_3}} - \frac{p_4}{p_3}e^{\frac{p_1}{p_3}\overline{\varepsilon}^{vp}}(\overline{\varepsilon}^{vp})^{-\frac{p_4}{p_3}-1} \\
&= \frac{1}{p_3}e^{\frac{p_1}{p_3}\overline{\varepsilon}^{vp}}(\overline{\varepsilon}^{vp})^{-\frac{p_4}{p_3}}\left(p_1 - \frac{p_4}{\overline{\varepsilon}}\right)
\end{aligned} \tag{342}$$

Hence, η is equal to:

$$\begin{aligned}
\eta &= \frac{1}{G}\frac{\partial G}{\partial T}\dot{T}\Delta t - G\lambda\Delta t - \frac{1}{G^2}\left(\frac{\partial G}{\partial T}\right)^2\dot{T}\theta\Delta T.\Delta t \\
&\quad -\frac{\partial G}{\partial T}\lambda\theta\Delta T.\Delta t - G\lambda\frac{\partial p_5}{\partial T}\ln(-J_2)\theta\Delta T.\Delta t \\
&\quad -G\lambda\left(\frac{\partial p_1}{\partial T} - \frac{p_1}{p_3}\frac{\partial p_3}{\partial T}\right)\frac{\overline{\varepsilon}^{vp}}{p_3}\theta\Delta T.\Delta t \\
&\quad +G\lambda\frac{1}{p_3}\left(\frac{1}{K_0.p_2}\left(\frac{\partial K_0}{\partial T}p_2 + K_0\frac{\partial p_2}{\partial T}\right) - \ln(K_0 p_2)\frac{1}{p_3}\frac{\partial p_3}{\partial T}\right)\theta\Delta T.\Delta t \\
&\quad +G\lambda\left(\frac{\partial p_4}{\partial T} - \frac{\partial p_3}{\partial T}\frac{p_4}{p_3}\right)\frac{1}{p_3}\ln(\overline{\varepsilon}^{vp})\theta\Delta T.\Delta t \\
&\quad -G\lambda\frac{1}{p_3}\left(p_1 - \frac{p_4}{\overline{\varepsilon}^{vp}}\right)\theta\Delta\overline{\varepsilon}^{vp}\Delta t
\end{aligned} \tag{343}$$

To simplify this expression, let

$$\begin{aligned}\rho = &-\frac{\partial G}{\partial T} - G\frac{\partial p_5}{\partial T}\ln(-J_2) - G\left(\frac{\partial p_1}{\partial T} - \frac{p_1}{p_3}\frac{\partial p_3}{\partial T}\right)\frac{\overline{\varepsilon}^{vp}}{p_3}\\ &+G\frac{1}{p_3}\left(\frac{1}{K_0p_2}\left(\frac{\partial K_0}{\partial T}p_2 + K_0\frac{\partial p_2}{\partial T}\right) - \ln(K_0p_2)\frac{1}{p_3}\frac{\partial p_3}{\partial T}\right)\\ &+G\left(\frac{\partial p_4}{\partial T} - \frac{\partial p_3}{\partial T}\frac{p_4}{p_3}\right)\frac{1}{p_3}\ln(\overline{\varepsilon}^{vp})\end{aligned}\tag{344}$$

So that

$$\begin{aligned}\eta = &\frac{1}{G}\frac{\partial G}{\partial T}\dot{T}\Delta t - G\lambda\Delta t - \frac{1}{G^2}\left(\frac{\partial G}{\partial T}\right)^2\dot{T}\theta\Delta T.\Delta t\\ &+\rho\lambda\theta\Delta T.\Delta t - G\lambda\frac{1}{p_3}\left(p_1 - \frac{p_4}{\overline{\varepsilon}^{vp}}\right)\theta\Delta\overline{\varepsilon}^{vp}\Delta t\end{aligned}\tag{345}$$

Computing $\underline{A}$:

$$\begin{aligned}A_{11} &= 1 - \left.\frac{\partial g_{11}}{\partial\hat{\sigma}_{11}}\right|_A\theta\Delta t = 1 - \frac{\partial}{\partial\hat{\sigma}_{11}}\left(\frac{1}{G}\frac{\partial G}{\partial T}\hat{\sigma}_{11}\dot{T} - G\frac{(-J_2)^{p_5}\,e^{\frac{p_1}{p_3}\overline{\varepsilon}^{vp}}}{(K_0p_2)^{\frac{1}{p_3}}(\overline{\varepsilon}^{vp})^{\frac{p_4}{p_3}}}\hat{\sigma}_{11}\right)\theta\Delta t\\ &= 1 - \left(\frac{1}{G}\frac{\partial G}{\partial T}\dot{T} - G\frac{(-J_2)^{p_5}\,e^{\frac{p_1}{p_3}\overline{\varepsilon}^{vp}}}{(K_0p_2)^{\frac{1}{p_3}}(\overline{\varepsilon}^{vp})^{\frac{p_4}{p_3}}}\right.\\ &\qquad\left.-G\frac{e^{\frac{p_1}{p_3}\overline{\varepsilon}^{vp}}}{(K_0p_2)^{\frac{1}{p_3}}(\overline{\varepsilon}^{vp})^{\frac{p_4}{p_3}}}\frac{\partial(-J_2)}{\partial\hat{\sigma}_{11}}p_5(-J_2)^{p_5-1}\hat{\sigma}_{11}\right)\theta\Delta t\\ &= 1 - \left(\frac{1}{G}\frac{\partial G}{\partial T}\dot{T} - G\lambda - G\lambda\hat{\sigma}_{11}\frac{p_5}{-J_2}\hat{\sigma}_{11}\right)\theta\Delta t\\ &= 1 - \frac{1}{G}\frac{\partial G}{\partial T}\dot{T}\theta\Delta t + G\lambda\theta\Delta t + G\lambda\frac{p_5}{-J_2}\hat{\sigma}_{11}\hat{\sigma}_{11}\theta\Delta t\end{aligned}\tag{346}$$

and

$$\begin{aligned}A_{12} &= -\left.\frac{\partial g_{11}}{\partial\hat{\sigma}_{22}}\right|_A\theta\Delta t = -\frac{\partial}{\partial\hat{\sigma}_{22}}\left(\frac{1}{G}\frac{\partial G}{\partial T}\hat{\sigma}_{11}\dot{T} - G\frac{(-J_2)^{p_5}\,e^{\frac{p_1}{p_3}\overline{\varepsilon}^{vp}}}{(K_0p_2)^{\frac{1}{p_3}}(\overline{\varepsilon}^{vp})^{\frac{p_4}{p_3}}}\hat{\sigma}_{11}\right)\theta\Delta t\\ &= -\left(-G\frac{e^{\frac{p_1}{p_3}\overline{\varepsilon}^{vp}}}{(K_0p_2)^{\frac{1}{p_3}}(\overline{\varepsilon}^{vp})^{\frac{p_4}{p_3}}}\frac{\partial(-J_2)}{\partial\hat{\sigma}_{22}}p_5(-J_2)^{p_5-1}\hat{\sigma}_{11}\right)\theta\Delta t\\ &= G\lambda\hat{\sigma}_{22}\frac{p_5}{-J_2}\hat{\sigma}_{11}\theta\Delta t = G\lambda\frac{p_5}{-J_2}\hat{\sigma}_{11}\hat{\sigma}_{22}\theta\Delta t\end{aligned}\tag{347}$$

Taking care of

$$\frac{\partial(-J_2)}{\partial\hat{\sigma}_{12}} = \frac{1}{2}\frac{\partial}{\partial\hat{\sigma}_{12}}(\hat{\sigma}_{11}\hat{\sigma}_{11} + \hat{\sigma}_{22}\hat{\sigma}_{22} + 2\hat{\sigma}_{12}\hat{\sigma}_{12} + \hat{\sigma}_{33}\hat{\sigma}_{33}) = 2\hat{\sigma}_{12}\tag{348}$$

then:

$$\begin{aligned}
A_{13} &= -\left.\frac{\partial g_{11}}{\partial \hat{\sigma}_{12}}\right|_A \theta\Delta t = -\frac{\partial}{\partial \hat{\sigma}_{12}}\left(\frac{1}{G}\frac{\partial G}{\partial T}\hat{\sigma}_{11}\dot{T} - G\frac{(-J_2)^{p_5}\, e^{\frac{p_1}{p_3}\bar{\varepsilon}^{vp}}}{(K_0 p_2)^{\frac{1}{p_3}}(\bar{\varepsilon}^{vp})^{\frac{p_4}{p_3}}}\hat{\sigma}_{11}\right)\theta\Delta t \\
&= -\left(-G\frac{e^{\frac{p_1}{p_3}\bar{\varepsilon}^{vp}}}{(K_0 p_2)^{\frac{1}{p_3}}(\bar{\varepsilon}^{vp})^{\frac{p_4}{p_3}}}\left(\frac{\partial(-J_2)}{\partial \hat{\sigma}_{12}}\right) p_5 (-J_2)^{p_5 - 1}\hat{\sigma}_{11}\right)\theta\Delta t \qquad (349) \\
&= G\lambda(2\hat{\sigma}_{12})\frac{p_5}{-J_2}\hat{\sigma}_{11}\theta\Delta t = G\lambda\frac{p_5}{-J_2}\theta\Delta t(2\hat{\sigma}_{12})\hat{\sigma}_{22}
\end{aligned}$$

Let

$$\begin{cases} \alpha = G\lambda\dfrac{p_5}{-J_2}\theta\Delta t \\ \beta = 1 - \dfrac{1}{G}\dfrac{\partial G}{\partial T}\dot{T}\theta\Delta t + G\lambda\theta\Delta t \end{cases} \qquad (350)$$

The system (181) becomes:

$$\begin{bmatrix} \beta + \alpha\hat{\sigma}_{11}\hat{\sigma}_{11} & \alpha\hat{\sigma}_{22}\hat{\sigma}_{11} & \alpha 2\hat{\sigma}_{12}\hat{\sigma}_{11} & \alpha\hat{\sigma}_{33}\hat{\sigma}_{11} \\ \alpha\hat{\sigma}_{11}\hat{\sigma}_{22} & \beta + \alpha\hat{\sigma}_{22}\hat{\sigma}_{22} & \alpha 2\hat{\sigma}_{12}\hat{\sigma}_{22} & \alpha\hat{\sigma}_{33}\hat{\sigma}_{22} \\ \alpha\hat{\sigma}_{11}\hat{\sigma}_{12} & \alpha\hat{\sigma}_{22}\hat{\sigma}_{12} & \beta + \alpha 2\hat{\sigma}_{12}\hat{\sigma}_{12} & \alpha\hat{\sigma}_{33}\hat{\sigma}_{12} \\ \alpha\hat{\sigma}_{11}\hat{\sigma}_{33} & \alpha\hat{\sigma}_{22}\hat{\sigma}_{33} & \alpha 2\hat{\sigma}_{12}\hat{\sigma}_{33} & \beta + \alpha\hat{\sigma}_{33}\hat{\sigma}_{33} \end{bmatrix} \begin{Bmatrix} \Delta\hat{\sigma}_{11} \\ \Delta\hat{\sigma}_{22} \\ \Delta\hat{\sigma}_{12} \\ \Delta\hat{\sigma}_{33} \end{Bmatrix} = \mu \begin{Bmatrix} \hat{\dot{\varepsilon}}_{11}^{tot} \\ \hat{\dot{\varepsilon}}_{22}^{tot} \\ \hat{\dot{\varepsilon}}_{12}^{tot} \\ \hat{\dot{\varepsilon}}_{33}^{tot} \end{Bmatrix} + \eta \begin{Bmatrix} \hat{\sigma}_{11} \\ \hat{\sigma}_{22} \\ \hat{\sigma}_{12} \\ \hat{\sigma}_{33} \end{Bmatrix} \qquad (351)$$

2. Analytical compliance matrix

In the relation (198), the dCC_1 factor is the variation of CC_1 factor in the perturbed configuration:

$$dCC_1 = d\left(\frac{\mu}{\beta}\right) = \frac{\beta d\mu - \mu d\beta}{\beta^2} \qquad (352)$$

From relation (337), μ does not depend on the velocity gradient, so that μ does not vary in perturbed configuration:

$$d\mu = 0 \qquad (353)$$

At the opposite, β is perturbed (cf. (350)) :

$$
\begin{aligned}
d\beta &= d\left(1-\frac{1}{G}\frac{\partial G}{\partial T}\dot{T}\theta\Delta t+G\lambda\theta\Delta t\right)=G\theta\Delta t.d\lambda \\
&= G\theta\Delta t.d\left(\frac{\left(-J_2\right)^{p_5}\,e^{\frac{p_1}{p_3}\overline{\varepsilon}}}{\left(K_0p_2\right)^{\frac{1}{p_3}}\,\overline{\varepsilon}^{\frac{p_4}{p_3}}}\right)=G\theta\Delta t\frac{e^{\frac{p_1}{p_3}\overline{\varepsilon}}}{\left(K_0p_2\right)^{\frac{1}{p_3}}\,\overline{\varepsilon}^{\frac{p_4}{p_3}}}d\left(\left(-J_2\right)^{p_5}\right) \\
&= G\theta\Delta t\frac{\left(-J_2\right)^{p_5}\,e^{\frac{p_1}{p_3}\overline{\varepsilon}}}{\left(K_0p_2\right)^{\frac{1}{p_3}}\,\overline{\varepsilon}^{\frac{p_4}{p_3}}}\frac{p_5}{-J_2}\frac{1}{2}d\left(\hat{\sigma}_{11}\hat{\sigma}_{11}+\hat{\sigma}_{22}\hat{\sigma}_{22}+2\hat{\sigma}_{12}\hat{\sigma}_{12}+\hat{\sigma}_{33}\hat{\sigma}_{33}\right) \\
&= G\theta\Delta t.\lambda\frac{p_5}{-J_2}\left(\hat{\sigma}_{11}d\hat{\sigma}_{11}+\hat{\sigma}_{22}d\hat{\sigma}_{22}+2\hat{\sigma}_{12}d\hat{\sigma}_{12}+\hat{\sigma}_{33}d\hat{\sigma}_{33}\right) \\
&= G\theta\Delta t.\lambda\frac{p_5}{-J_2}\left\{\hat{\sigma}_{11}\quad\hat{\sigma}_{22}\quad 2\hat{\sigma}_{12}\quad\hat{\sigma}_{33}\right\}\begin{Bmatrix} d\hat{\sigma}_{11} \\ d\hat{\sigma}_{22} \\ d\hat{\sigma}_{12} \\ d\hat{\sigma}_{33} \end{Bmatrix} \\
&= \left(G\theta\Delta t.\lambda\frac{p_5}{-J_2}\underline{a}\right)\cdot d\underline{\hat{\sigma}}=\underline{c}_{\beta}\cdot d\underline{\hat{\sigma}}
\end{aligned}
\tag{354}
$$

Hence:

$$
dCC_1=-\frac{\mu}{\beta^2}\underline{c}_{\beta}\cdot d\underline{\hat{\sigma}}=\underline{c}_{1\sigma}\cdot d\underline{\hat{\sigma}} \tag{355}
$$

For dCC_2:

$$
\begin{aligned}
dCC_2 &= d\left(-\mu\delta\underline{a}\cdot\hat{\dot{\underline{\varepsilon}}}^{tot}+\frac{\eta}{\beta}-\eta\delta\underline{a}\cdot\underline{\hat{\sigma}}\right) \\
&= -\mu\underline{a}\cdot\hat{\dot{\underline{\varepsilon}}}^{tot}d\delta-\mu\delta\hat{\dot{\underline{\varepsilon}}}^{tot}\cdot d\underline{a}-\mu\delta\underline{a}\cdot d\hat{\dot{\underline{\varepsilon}}}^{tot}+\frac{\beta d\eta-\eta d\beta}{\beta^2} \\
&\quad -\delta\underline{a}\cdot\underline{\hat{\sigma}}d\eta-\eta\underline{a}\cdot\underline{\hat{\sigma}}d\delta-\eta\delta\underline{\hat{\sigma}}\cdot d\underline{a}-\eta\delta\underline{a}\cdot d\underline{\hat{\sigma}}
\end{aligned}
\tag{356}
$$

Noting that:

$$
\begin{aligned}
d\alpha &= d\left(G\lambda\frac{p_5}{-J_2}\theta\Delta t\right)=G\frac{p_5}{-J_2}\theta\Delta t.d\lambda-G\lambda\frac{p_5}{-J_2}\theta\Delta t\frac{-1}{-J_2}d\left(-J_2\right) \\
&= G\lambda\frac{p_5}{-J_2}\theta\Delta t\frac{p_5}{-J_2}\underline{a}\cdot d\underline{\hat{\sigma}}+G\lambda\frac{p_5}{-J_2}\theta\Delta t\frac{1}{-J_2}\underline{a}\cdot d\underline{\hat{\sigma}} \\
&= \left(G\lambda\frac{p_5}{-J_2}\theta\Delta t\right)\frac{1}{-J_2}\left(p_5+1\right)\underline{a}\cdot d\underline{\hat{\sigma}}=\left(\alpha\frac{p_5+1}{-J_2}\underline{a}\right)\cdot d\underline{\hat{\sigma}}=\underline{c}_{\alpha}\cdot d\underline{\hat{\sigma}}
\end{aligned}
\tag{357}
$$

$$
d\beta=\underline{c}_{\beta}\cdot d\underline{\hat{\sigma}} \tag{358}
$$

$$d\underline{a} = \begin{Bmatrix} d\hat{\sigma}_{11} \\ d\hat{\sigma}_{22} \\ 2d\hat{\sigma}_{12} \\ d\hat{\sigma}_{33} \end{Bmatrix} = \begin{bmatrix} 1 & 0 & 0 & 0 \\ 0 & 1 & 0 & 0 \\ 0 & 0 & 2 & 0 \\ 0 & 0 & 0 & 1 \end{bmatrix} \begin{Bmatrix} d\hat{\sigma}_{11} \\ d\hat{\sigma}_{22} \\ d\hat{\sigma}_{12} \\ d\hat{\sigma}_{33} \end{Bmatrix} = \underline{Diag}\begin{pmatrix} 1 & 1 & 2 & 1 \end{pmatrix} \cdot d\underline{\hat{\sigma}} \tag{359}$$

$$d\underline{\hat{\dot{\varepsilon}}}^{tot} = \underline{MDL} \cdot d\underline{L} \tag{360}$$

$$\begin{aligned}
d\delta &= d\left(\frac{\alpha}{\beta}\frac{1}{\beta + \alpha\underline{a}\cdot\underline{\hat{\sigma}}}\right) \\
&= \frac{\beta d\alpha - \alpha d\beta}{\beta^2}\frac{1}{\beta + \alpha\underline{a}\cdot\underline{\hat{\sigma}}} - \frac{\alpha}{\beta}\frac{1}{\left(\beta + \alpha\underline{a}\cdot\underline{\hat{\sigma}}\right)^2} d\left(\beta + \alpha\underline{a}\cdot\underline{\hat{\sigma}}\right) \\
&= \frac{d\alpha}{\beta}\frac{1}{\beta + \alpha\underline{a}\cdot\underline{\hat{\sigma}}} - \frac{\alpha}{\beta^2} d\beta \frac{1}{\beta + \alpha.\underline{a}\cdot\underline{\hat{\sigma}}} \\
&\quad - \frac{\alpha}{\beta}\frac{1}{\left(\beta + \alpha\underline{a}\cdot\underline{\hat{\sigma}}\right)^2}\left(d\beta + d\alpha\underline{a}\cdot\underline{\hat{\sigma}} + \alpha d\underline{a}\cdot\underline{\hat{\sigma}} + \alpha\underline{a}\cdot d\underline{\hat{\sigma}}\right) \\
&= \left(\frac{\alpha}{\beta}\frac{1}{\beta + \alpha\underline{a}\cdot\underline{\hat{\sigma}}}\right)\frac{d\alpha}{\alpha} - \left(\frac{\alpha}{\beta}\frac{1}{\beta + \alpha\underline{a}\cdot\underline{\hat{\sigma}}}\right)\frac{d\beta}{\beta} \\
&\quad - \left(\frac{\alpha}{\beta}\frac{1}{\beta + \alpha\underline{a}\cdot\underline{\hat{\sigma}}}\right)^2 \frac{\beta}{\alpha}\left(d\beta + d\alpha\underline{a}\cdot\underline{\hat{\sigma}} + \alpha\underline{\hat{\sigma}}\cdot d\underline{a} + \alpha\underline{a}\cdot d\underline{\hat{\sigma}}\right) \\
&= \delta\frac{d\alpha}{\alpha} - \delta\frac{d\beta}{\beta} - \delta^2\frac{\beta}{\alpha}\left(d\beta + d\alpha\underline{a}\cdot\underline{\hat{\sigma}} + \alpha\underline{\hat{\sigma}}\cdot\underline{Diag}\begin{pmatrix} 1 & 1 & 2 & 1 \end{pmatrix}\cdot d\underline{\hat{\sigma}} + \alpha\underline{a}\cdot d\underline{\hat{\sigma}}\right) \\
&= \frac{\delta}{\alpha}\underline{c}_{\alpha}\cdot d\underline{\hat{\sigma}} - \frac{\delta}{\beta}\underline{c}_{\beta}\cdot d\underline{\hat{\sigma}} - \delta^2\frac{\beta}{\alpha}\underline{c}_{\beta}\cdot d\underline{\hat{\sigma}} \\
&\quad - \delta^2\frac{\beta}{\alpha}\underline{c}_{\alpha}\cdot d\underline{\hat{\sigma}}\cdot\underline{a}\cdot\underline{\hat{\sigma}} - \delta^2\beta\underline{a}\cdot d\underline{\hat{\sigma}} - \delta^2\beta\underline{a}\cdot d\underline{\hat{\sigma}} \\
&= \left(\frac{\delta}{\alpha}\underline{c}_{\alpha} - \frac{\delta}{\beta}\underline{c}_{\beta} - \delta^2\frac{\beta}{\alpha}\left(\underline{c}_{\beta} + \underline{c}_{\alpha}\cdot\underline{a}\cdot\underline{\hat{\sigma}}\right) - 2\delta^2\beta\underline{a}\right)\cdot d\underline{\hat{\sigma}} \\
&= \underline{c}_{\delta}\cdot d\underline{\hat{\sigma}}
\end{aligned} \tag{361}$$

Assuming that ρ does not vary:

$$\begin{aligned}
d\eta &= d\left(\ldots\right) \\
&= \left(-G\Delta t + \rho\theta\Delta T.\Delta t - G\frac{1}{p_3}\left(p_1 - \frac{p_4}{\overline{\varepsilon}^{vp}}\right)\overline{\dot{\varepsilon}}^{vp}\theta\Delta t^2\right)d\lambda \\
&\quad - G\lambda\frac{1}{p_3}\left(p_1 - \frac{p_4}{\overline{\varepsilon}^{vp}}\right)\theta\Delta t^2 d\overline{\dot{\varepsilon}}^{vp} \\
&= \left(C_{\eta\lambda}\lambda\frac{p_5}{-J_2}\underline{a}\right)\cdot d\underline{\hat{\sigma}} + C_{\eta\varepsilon}d\overline{\dot{\varepsilon}}^{vp} = \underline{c}_{\eta\sigma}\cdot d\underline{\hat{\sigma}} + C_{\eta\varepsilon}.d\overline{\dot{\varepsilon}}^{vp}
\end{aligned} \tag{362}$$

And that

$$\bar{\dot{\varepsilon}}^{vp} \simeq \bar{\dot{\varepsilon}}^{tot} = \sqrt{\frac{2}{3}\underline{\dot{\varepsilon}} \cdot \underline{Diag}\begin{pmatrix}1 & 1 & 2 & 1\end{pmatrix} \cdot \underline{\dot{\varepsilon}}} \tag{363}$$

Then:

$$\begin{aligned}
d\bar{\dot{\varepsilon}}^{vp} &= \frac{1}{2\bar{\dot{\varepsilon}}^{vp}}\frac{2}{3}d\left(\underline{\dot{\varepsilon}} \cdot \underline{Diag}\begin{pmatrix}1 & 1 & 2 & 1\end{pmatrix} \cdot \underline{\dot{\varepsilon}}\right) \\
&= \frac{1}{\bar{\dot{\varepsilon}}^{vp}}\frac{2}{3}.\underline{L} \cdot \begin{bmatrix}1 & 0 & 0 & 0 \\ 0 & 1 & 0 & 0 \\ 0 & 0 & \frac{1}{2} & 0 \\ 0 & 0 & \frac{1}{2} & 0 \\ 0 & 0 & 0 & 1\end{bmatrix}\begin{bmatrix}1 & 0 & 0 & 0 \\ 0 & 1 & 0 & 0 \\ 0 & 0 & 2 & 0 \\ 0 & 0 & 0 & 1\end{bmatrix}\begin{bmatrix}1 & 0 & 0 & 0 & 0 \\ 0 & 1 & 0 & 0 & 0 \\ 0 & 0 & \frac{1}{2} & \frac{1}{2} & 0 \\ 0 & 0 & 0 & 0 & 1\end{bmatrix} \cdot d\underline{L} \\
&= \frac{1}{3\bar{\dot{\varepsilon}}^{vp}}\underline{L} \cdot \begin{bmatrix}2 & 0 & 0 & 0 & 0 \\ 0 & 2 & 0 & 0 & 0 \\ 0 & 0 & 1 & 1 & 0 \\ 0 & 0 & 1 & 1 & 0 \\ 0 & 0 & 0 & 0 & 2\end{bmatrix} \cdot d\underline{L} \\
&= \frac{1}{3\bar{\dot{\varepsilon}}^{vp}}\left\{2L_{11} \quad 2L_{22} \quad L_{12} + L_{21} \quad L_{12} + L_{21} \quad 2L_{33}\right\} \cdot d\underline{L}
\end{aligned} \tag{364}$$

Hence:

$$\begin{aligned}
d\eta &= \underline{c}_{\eta\sigma} \cdot d\underline{\hat{\sigma}} + \frac{C_{\eta\varepsilon}}{3\bar{\dot{\varepsilon}}^{vp}}\left\{2L_{11} \quad 2L_{22} \quad L_{12} + L_{21} \quad L_{12} + L_{21} \quad 2L_{33}\right\} \cdot d\underline{L} \\
&= \underline{c}_{\eta\sigma} \cdot d\underline{\hat{\sigma}} + \underline{c}_{\eta L} \cdot d\underline{L}
\end{aligned} \tag{365}$$

And dCC_2 becomes:

$$\begin{aligned}
dCC_2 &= -\mu\underline{c}_{\delta} \cdot d\underline{\hat{\sigma}} \cdot \underline{a} \cdot \hat{\underline{\dot{\varepsilon}}}^{tot} - \mu\delta d\underline{a} \cdot \hat{\underline{\dot{\varepsilon}}}^{tot} - \mu\delta\underline{a} \cdot \underline{MDL} \cdot d\underline{L} \\
&\quad + \frac{1}{\beta}\underline{c}_{\eta\sigma} \cdot d\underline{\hat{\sigma}} + \frac{1}{\beta}\underline{c}_{\eta L} \cdot d\underline{L} - \frac{\eta}{\beta^2}\underline{c}_{\beta} \cdot d\underline{\hat{\sigma}} - \delta\underline{c}_{\eta\sigma} \cdot d\underline{\hat{\sigma}} \cdot \underline{a} \cdot \underline{\hat{\sigma}} \\
&\quad - \delta\underline{c}_{\eta L} \cdot d\underline{L} \cdot \underline{a} \cdot \underline{\hat{\sigma}} - \eta\underline{c}_{\delta} \cdot d\underline{\hat{\sigma}} \cdot \underline{a} \cdot \underline{\hat{\sigma}} - \eta\delta d\underline{a} \cdot \underline{\hat{\sigma}} - \eta\delta\underline{a} \cdot d\underline{\hat{\sigma}} \\
&= \left(\frac{1}{\beta}\underline{c}_{\eta L} - \mu\delta\underline{a} \cdot \underline{MDL} - \delta\underline{a} \cdot \underline{\hat{\sigma}} \cdot \underline{c}_{\eta L}\right) \cdot d\underline{L} \\
&\quad + \left(\frac{1}{\beta}\underline{c}_{\eta\sigma} - \frac{\eta}{\beta^2}\underline{c}_{\beta} - \mu\underline{a} \cdot \hat{\underline{\dot{\varepsilon}}}^{tot} \cdot \underline{c}_{\delta} - \mu\delta\hat{\underline{\dot{\varepsilon}}}^{tot} \cdot \underline{Diag}\begin{pmatrix}1 & 1 & 2 & 1\end{pmatrix}\right. \\
&\quad \left. - \delta\underline{a} \cdot \underline{\hat{\sigma}} \cdot \underline{c}_{\eta\sigma} - \eta\underline{a} \cdot \underline{\hat{\sigma}} \cdot \underline{c}_{\delta} - 2\eta\delta\underline{a}\right) \cdot d\underline{\hat{\sigma}} \\
&= \underline{c}_{2L} \cdot d\underline{L} + \underline{c}_{2\sigma} \cdot d\underline{\hat{\sigma}}
\end{aligned} \tag{366}$$

The relation (198) is thus:

$$
\begin{aligned}
d\underline{\hat{s}}_B &= dCC_1\hat{\dot{\underline{\varepsilon}}}^{tot} + CC_1 d\hat{\dot{\underline{\varepsilon}}}^{tot} + dCC_2\underline{\hat{\sigma}}_A + \left(1+CC_2\right)d\underline{\hat{\sigma}}_A \\
&= \underline{c}_{1\sigma}\cdot d\underline{\hat{\sigma}}\cdot\hat{\dot{\underline{\varepsilon}}}^{tot} + CC_1\underline{MDL}\cdot d\underline{L} + \underline{c}_{2L}\cdot d\underline{L}\cdot\underline{\hat{\sigma}}_A + \underline{c}_{2\sigma}\cdot d\underline{\hat{\sigma}}\cdot\underline{\hat{\sigma}}_A + \left(1+CC_2\right)d\underline{\hat{\sigma}}_A \\
&= \left(CC_1\underline{MDL} + \underline{\hat{\sigma}}\cdot\underline{c}_{2L}\right)\cdot d\underline{L} + \left(\hat{\dot{\underline{\varepsilon}}}^{tot}\otimes\underline{c}_{1\sigma} + \underline{\hat{\sigma}}_A\otimes\underline{c}_{2\sigma} + \left(1+CC_2\right)\underline{I}\right)\cdot d\underline{\hat{\sigma}}_A \\
&= \underline{M}_{SL}\cdot d\underline{L} + \underline{M}_{SS}\cdot d\underline{\hat{\sigma}}_A
\end{aligned}
\tag{367}
$$

And with Jaumann objective derivation:

$$
\underline{\hat{\sigma}} = \begin{Bmatrix} \hat{s}_{11} + 2\left(\omega_E\Delta t\right)\hat{s}_{12} \\ \hat{s}_{22} - 2\left(\omega_E\Delta t\right)\hat{s}_{12} \\ \hat{s}_{12} + \left(\omega_E\Delta t\right)\left(\hat{s}_{22}-\hat{s}_{11}\right) \\ \hat{s}_{33} \end{Bmatrix} = \begin{bmatrix} 1 & 0 & 2\omega_E\Delta t & 0 \\ 0 & 1 & -2\omega_E\Delta t & 0 \\ -\omega_E\Delta t & \omega_E\Delta t & 1 & 0 \\ 0 & 0 & 0 & 1 \end{bmatrix}\cdot\underline{\hat{s}}
\tag{368}
$$

and

$$
\begin{aligned}
d\underline{\hat{\sigma}}_B &= \begin{Bmatrix} d\hat{s}_{11} + 2\left(\omega_E\Delta t\right)d\hat{s}_{12} \\ d\hat{s}_{22} - 2\left(\omega_E\Delta t\right)d\hat{s}_{12} \\ d\hat{s}_{12} + \left(\omega_E\Delta t\right)\left(d\hat{s}_{22}-d\hat{s}_{11}\right) \\ d\hat{s}_{33} \end{Bmatrix} + \begin{Bmatrix} 2\left(d\omega_E\Delta t\right)\hat{s}_{12} \\ -2\left(d\omega_E\Delta t\right)\hat{s}_{12} \\ \left(d\omega_E\Delta t\right)\left(\hat{s}_{22}-\hat{s}_{11}\right) \\ 0 \end{Bmatrix} \\
&= \begin{bmatrix} 1 & 0 & 2\omega_E\Delta t & 0 \\ 0 & 1 & -2\omega_E\Delta t & 0 \\ -\omega_E\Delta t & \omega_E\Delta t & 1 & 0 \\ 0 & 0 & 0 & 1 \end{bmatrix}\begin{Bmatrix} d\hat{s}_{11} \\ d\hat{s}_{22} \\ d\hat{s}_{12} \\ d\hat{s}_{33} \end{Bmatrix} + \begin{Bmatrix} \left(dL_{12}-dL_{21}\right)\Delta t.\hat{s}_{12} \\ -\left(dL_{12}-dL_{21}\right)\Delta t.\hat{s}_{12} \\ \left(dL_{12}-dL_{21}\right)\Delta t\dfrac{\hat{s}_{22}-\hat{s}_{11}}{2} \\ 0 \end{Bmatrix} \\
&= \begin{bmatrix} 1 & 0 & 2\omega_E\Delta t & 0 \\ 0 & 1 & -2\omega_E\Delta t & 0 \\ -\omega_E\Delta t & \omega_E\Delta t & 1 & 0 \\ 0 & 0 & 0 & 1 \end{bmatrix}\begin{Bmatrix} d\hat{s}_{11} \\ d\hat{s}_{22} \\ d\hat{s}_{12} \\ d\hat{s}_{33} \end{Bmatrix} + \begin{bmatrix} 0 & 0 & \Delta t.\hat{s}_{12} & -\Delta t.\hat{s}_{12} & 0 \\ 0 & 0 & -\Delta t.\hat{s}_{12} & \Delta t.\hat{s}_{12} & 0 \\ 0 & 0 & \Delta t\dfrac{\hat{s}_{22}-\hat{s}_{11}}{2} & -\Delta t\dfrac{\hat{s}_{22}-\hat{s}_{11}}{2} & 0 \\ 0 & 0 & 0 & 0 & 0 \end{bmatrix}\begin{Bmatrix} dL_{11} \\ dL_{22} \\ dL_{12} \\ dL_{21} \\ dL_{33} \end{Bmatrix} \\
&= \underline{M}_{\sigma S}\cdot d\underline{\hat{s}} + \underline{M}_{\sigma L}\cdot d\underline{L}
\end{aligned}
\tag{369}
$$

introducing (367) in (369)

$$
\begin{aligned}
d\underline{\hat{\sigma}}_B &= \underline{M}_{\sigma S}\cdot\left(\underline{M}_{SL}\cdot d\underline{L} + \underline{M}_{SS}\cdot d\underline{\hat{\sigma}}_A\right) + \underline{M}_{\sigma L}\cdot d\underline{L} \\
&= \underline{M}_{\sigma S}\cdot\underline{M}_{SS}\cdot d\underline{\hat{\sigma}}_A + \left(\underline{M}_{\sigma S}\cdot\underline{M}_{SL} + \underline{M}_{\sigma L}\right)\cdot d\underline{L} \\
&= \underline{A}_{\sigma\sigma}\cdot d\underline{\hat{\sigma}}_A + \underline{A}_{\sigma L}\cdot d\underline{L}
\end{aligned}
\tag{370}
$$

IX. References

IX. References

[ABR96] Abratis H., Höfer F., Jünemann M., Sardemann J., Stoffel H. – *Heat transfer in continuous casting moulds when using different mould powders.* Stahl und Eisen 116, No. 9, 1996, pp.73-78

[ALI00] Aliaga C., *Simulation numérique par elements finis en 3D du comportement thermomécanique au cours du traitement thermique d'aciers: application à la trempe de pièces forgées ou coulées.* Ph.D. Thesis, Ecole Nationale Supérieure des Mines de Paris (France), 2000

[ARB] ProfilARBED source: *site of Esch-Belval mills*

[ARC] *ARCELOR: A portrait* - www.arcelor.com/anglais/html/groupe.htm

[BAK93] Bakshi I.A., Brendzy J.L., Walker N., Chandra S., Samarasekera I.V., Brimacombe J.K. – *Mould-strand interaction in continuous casting of steel billets. Part 1: Industrial trials.* Ironmaking and Steelmaking, Vol.20, No.1, 1993

[BAR91] Barber B., Leckenby B.M., Lewis B.A. – *Finite element analysis of roll misalignment during continuous casting.* Ironmaking and Steelmaking, Vol.18, No.6, 1991, pp.431-436

[BAR98] Barber B., Walmsley R., Farnsworth R. – *Influence of Strand Reduction on Bloom segregation.* Conf. on Developments in Continuous Casting of Blooms and Billets for Improved Quality and Productivity, The Institute of Materials – Steel Division, London (UK), 4th-5th February 1998

[BAR00] Barber B., Walmsley R. – *Soft Reduction of Cast Blooms.* SMAE Conference and Exhibition, Sheffield (UK), 15th-16th June 2000

[BLA87-88] Blazek K.E. – *Mold Heat Transfer During Continuous Casting. Parts I to X.* I&SM (Iron & Steelmakers), Iron & Steel Society, Sept-Oct-Nov-Dec 87 (Parts I to IV) and Jan-Feb-Mar-Apr-May-Jun 88 (Parts V to X)

[BOU86] Bourdouxhe M., Charlier R., Cescotto S. – *A finite element for thermo-mechanical problems.* Proc. 2nd Int. Conf. on Numerical Methods in Industrial Forming Processes, Mattiasson K., Samuelsson A., Wood R.D. and Zienkiewicz O.C. Eds., A.A. Balkema, Rotterdam, Netherlands, 1986, pp. 97-102

[BOU98] Bourdouxhe M., Pascon F., Habraken A.M. – *Mathematical Modelisation of Beam Blank Casting in Order to Optimise the Mould Taper.* Proc. 3rd European Conference on Continuous Casting, Madrid (Spain), 20th-23rd October 1998

[BRE93] Brendzy J.L., Bakshi I.A., Samarasekera I.V., Brimacombe J.K. – *Mould-strand interaction in continuous casting of steel billets. Part 2 Lubrication and oscillation mark formation.* Ironmaking and Steelmaking, Vol.20, No.1, 1993, pp.63-74

[BRI73] Brimacombe J.K., Weinberg F. – *Continuous Casting of Steel. Part 2: Theoretical and measured liquid pool profiles in the mould region during the continuous casting of steel.* Journal of the Iron and Steel Institute, January 1973, pp.24-33

[BRI93] Brimacombe J.K. – *Empowerment with knowledge: toward the intelligent mold for the continuous casting of steel billets.* Metallurgical Transactions B, Vol.24B, December 1993, pp.917-935

[CAS03] Castagne S., Pascon F., Blès G., Habraken A.M. – *Developments in Simulations of Continuous Casting.* Proc. 2nd Int. Conf. Thermal Process Modelling and Computer Simulation, Nancy (France), 31st March-2nd April 2003

[CES89] Cescotto S., Habraken A.M., Radu J.P., Charlier R. – *Some recent developments in computer simulation of metal forming processes.* Proc. 9th Int. Conf. on Computer Methods in Mechanics, Vol.4, Krakow (Poland), 16th-20th May 1989

[CHA87] Charlier R. – *Approche unifiée de quelques problèmes non linéaires de mécanique des milieux continus par la méthode des éléments finis.* Ph.D. Thesis, Université de Liège (Belgium), 1987

[CHA90] Charlier R., Habraken A.M. – *Numerical Modellisation of contact with friction phenomena by the finite element method.* Computers and Geotechnics 9, 1990, pp.59-72

[CHA93] Chandra S., Brimacombe J.K., Samarasekera I.V. – *Mould-strand interaction in continuous casting of steel billets. Part 3 Mould heat transfer and taper.* Ironmaking and Steelmaking, Vol.20, No.2, 1993, pp.104-112

[COH94] Coheur J.P. – *Connaissance des matériaux métalliques.* Notes de cours, Université de Liège, 1994-1995

[DIP86] Dippenaar R.J., Samarasekera I.V., Brimacombe J.K. – *Mould Taper in Continuous-Casting Billet Machines.* ISS Transactions, Vol.7, 1986, pp.31-43

[ELB95] El-Bealy M., Leskinen N., Fredriksson H. – *Simulation of cooling conditions in secondary cooling zones in continuous casting process.* Ironmaking and Steelmaking, Vol.22, No.3, 1995, pp.246-255

[FAS67] Fasiska E.J., Wagenblast H., Trans. AIME, 239, 1967, pp.1818-1820

[FIC00] Fic A., Nowak A.J., Bialecki R. – *Heat transferanalysis of the continuous casting process by the front tracking BEM.* Engineering Analysis with Boundary Elements 24, 2000, pp.215-223

[GRI93] Grisard L. – *Modélisation bidimensionnelle de la mise à forme des tôles par la méthode des éléments finis.* Ph.D. Thesis, Université de Liège (Belgium), 1995

[GRO85] Grober H., Cescotto S., Charlier R., Bourdouxhe M., Habraken A.M. – *Numerical Simulation of Metal Forming Processes.* Proc. Int. Conf. on Nonlinear Mechanics, Shanghai (China), 1985, 7p.

[HA01] Ha J.S., Cho J.R., Lee B.Y., Ha M.Y. – *Numerical analysis of secondary cooling and bulging in the continuous casting of slabs.* J. Materials Processing Technology, No.113, 2001, 257-261

[HAB89] Habraken A.M. – *Contribution à la modélisation du formage des métaux par la méthode des éléments finis.* Ph.D. Thesis, Université de Liège (Belgium), 1989

[HAB92] Habraken A.M., Bourdouxhe M. – *Coupled thermo-mechanical-metallurgical analysis during cooling of steel pieces.* European Journal of Mechanics: A/Solids, Vol.11, No.3, 1992, pp.381-402

[HAB98a] Habraken A.M., Charles J.-F., Wégria J., Cescotto S. – *Dynamic Recrystallisation during Zinc Rolling.* International Journal of Forming Processes, Vol.1, No.1, 1998, pp.53-73

[HAB98b] Habraken A.M., Cescotto S. – *Contact between deformable solids, the fully coupled approach.* Mathematical and Computer Modelling, Vol.28, No.4-8, 1998, pp.153-169

[HAB01] Habraken A.M. – *Contributions to Constitutive Laws of Metals: Micro-Macro and Damage Models. Part A: Introduction.* Thèse d'Agrégation de l'Enseignement Supérieur, Université de Liège, 2001

[HIL50] Hill R. – *The Mathematical Theory of Plasticity.* Oxford University Press, 1950

[HOF01] Hofferlin E. – *Incorporation of an accurate model of texture and strain-path induced anisotropy in simulations of sheet metal forming.* Ph.D. thesis, Katholieke Universiteit Leuven (Belgium), 2001

[HOR98] Horbach U., Kockentiedt J., Jung W. – *High-speed billet casting using a parabolic mold taper.* Metallurgical Plant and Technology International No.1, 1998, pp.74-84

[HRY91] Hrycaj P., Cescotto S., Oudin J. – *Elasto-plastic finite element analysis of unilateral contact with generalized Coulomb friction.* Engineering Computations, Vol.8, 1991, pp.291-303

[JES86] Jeschar R., Reiners U., Scholz R – *Heat transfer during water and water-air spray cooling in the secondary cooling zone of continuous casting plants.* Proc. 69th Steelmaking Conference, Washington (USA), Vol.69, April 1986, pp.511-521

[KAN97] Kanai N., Horioka S., Uehara M., Saiki H. – *Three-Dimensional Slab Deformation of Solidifying Shell at Intermediate Bearing during High Speed Continuous Casting.* Proc. Steelmaking Conference, 1997, pp.223-225

[LAI89] Laitinen E. – *On the simulation and control of the continuous casting process.* Ph.D. Thesis, Universität Jyväskylä (Finland), 1989

[LEW00] Lewis R.W., Ravindran K. – *Finite element simulation of metal casting.* Int. J. Numer. Meth. Engng. 47, 2000, pp.29-59

[LI03] Li C., Thomas B.G. – *Thermo-Mechanical Finite Element Model of Shell Behavior in the Continuous Casting of Steel.* Key Engineering Materials, Trans Tech Publications (Switzerland), Vol.233-236, 2003, pp.827-833

[LIN98] Lindorfer B., Hödl H., Mörwald K. – *Technolgical packages for high performance slab casting.* Metallurgical Plant and Technology International No.1, 1998, pp.66-72

[MAH91a] Mahapatra R.B., Brimacombe J.K., Samarasekera I.V., Walker N., Paterson E.A., Young J.D. – *Mold Behavior and Its Influence on Quality in the Continuous Casting of Steel Slabs: Part I. Industrial Trials, Mold Temperature Measurements, and Mathematical Modelling.* Metallurgical Transactions B, Vol.22B, December 1991, pp.861-874.

[MAH91b] Mahapatra R.B., Brimacombe J.K., Samarasekera I.V. – *Mold Behavior and Its Influence on Quality in the Continuous Casting of Steel Slabs: Part II. Mold Heat Transfer, Mold Flux Behavior, Formation of Oscillation Marks, Longitudinal Off-Corner Depressions, and Subsurface Cracks.* Metallurgical Transactions B, Vol.22B, December 1991, pp.875-888.

[MAN90] Männiko T. – *Convex and nonconvex duality in optimal control.* Ph.D. Thesis, Universität Jyväskylä (Finland), 1990

[MIE03] Miesse G. – *Optimisation de la conicité d'un lingotière à coulee continue.* Graduating thesis, Université de Liège (Belgium), 2003

[MIS13] von Mises R. – *Göttinger Nachrichten.* Math.-Phys. Klasse, 1913, 582

[MIY98] Miyake T., Nakayama K., Morishita M. – *Effects of Heat and Fluid Flow in Continuous Casting Molds on Solidification Shell Growth.* Kobelco Technology Review, No.21, April 1998, pp.7-13

[MIY01] Miyazawa K.-i. – *Continuous Casting of Steels in Japan.* Science and Technology of Advanced Materials 2, 2001,pp.59-65

[MIZ02] Mizukami H., Yamanaka A., Watanabe T. – *High Temperature Deformation Behavior of Peritectic Carbon Steel during Solidification.* ISIJ International (Iron and Steel Institute of Japan), Vol.42, No.9, 2002, pp.964-973

[MOI93a] Moitra A. – *Thermo-mechanical Model of Steel Shell Behavior in Continuous Slab Casting.* Ph.D. Thesis, University of Illinois, 1993

[MOI93b] Moitra A., Thomas B.G., Zhu H. – *Application of a thermo-mechanical model for steel shell behavior in continuous slab casting.* Proc. Steelmaking Conference, Dallas TX, 1993

[MÖR98] Mörwald K., Schönhuber K., Köhl R. – *Modern High Speed Casting Technology for Billet Casting.* Conf. on Developments in Continuous Casting of Blooms and Billets for Improved Quality and Productivity, The Institute of Materials – Steel Division, London (UK), 4th-5th February 1998

[MOU02] Moureaux P., Moto Mpong S., Remy M., Bouffioux C., Lecomte-Beckers J., Habraken A.M. – *Identification d'une loi thermo-elasto-viscoplastique en vue de la modélisation du laminage a chaud du cuivre.* Journal de Physique IV – Proceedings, Vol.12-Pr.11, EDP Sciences Ed., December 2002, pp.361-368

[ORO45] Orowan E. - *The Calculation of Roll Pressure in Hot and Cold Flat Rolling.* J. Inst. Mech. Eng., Feb 1944 - Discussion: Journal Dec. 1945, Proc. 152, pp.314-324

[PAS00a] Pascon F., Habraken A.M., Bourdouxhe M., Labory F. – *Modélisation des phénomènes thermomécaniques dans une lingotière de coulee continue.* Mécanique & Industries, Vol.1, No.1, Jan-Feb 2000, pp.61-70

[PAS00b] Pascon F. - *Finite element modelling of contact between the strand and the mould in continuous casting.* MS Thesis, Université de Liège, 2000

[PAS01] Pascon F., Habraken A.M., Bourdouxhe M., Labory F. – *Finite element modelling of thermo-mechanical behaviour of a steel strand in continuous casting.* Proc. 7th European Conference on Advanced Materials and Processes, Rimini (Italy), 10th-14th June 2001

[PAS02] Pascon F., Habraken A.M. – *Finite element thermomechanical model of continuous steel casting.* Proc. 7th Int. Conf. on Technology of Plasticity, Yokohama (Japan), 28th-30th October 2002, pp.1321-1326

[PAT00] Patrick B., Barber B., Brown D. – *Practical Aspects of the Design, Operation and Performance of Caster Spray Systems.* SMAE Conference and Exhibition, Sheffield (UK), 15th-16th June 2000

[RAP98] Rappaz M., Bellet M., Deville M. – *Modélisation Numérique en Science et Génie des Matériaux.* Traité des Matériaux, Vol.10, Presses Polytechniques et Universitaires Romandes, Lausanne (CH), 1998

[REN98] Ren J., Wang Z. – *Analysis of bulging and strain for continuously cast slab as thermoelastic continuous beam.* Ironmaking and Steelmaking, Vol.25, No.5, 1998, pp.394-397

[RIB79] Riboud P.V., Larrecq M., Proc. of the NOH-BOS Conference of the AIME, Detroit – March 1979

[RIC73] Richter F. – *Die wichtigsten physikalischen Eigenschaften von 52 Eisenwerkstoffen.* Stahlheisen-Sonderberichte Heft 8, Verlag Stahleisen M.B.H., Düsseldorf (Germany), 1973

[RID70] Ridley N., Stuart H., Met. Sci. J., 4, 1970, pp.219-222

[RID94] Ridolfi M.R., Thomas B.G., Della Foglia U. – *The optimization of mold taper for the Ilva-Dalmine round bloom caster.* La Revue de Métallurgie – CIT, Avril 1994, pp.609-620

[REM02] Remy M., Castagne S., Habraken A.M. – *Progress in microscopic modelling of damage in steel at high temperature.* International Journal of Forming Processes, Vol.5, No.2-3-4/2002, pp.445-455

[SCH88] F. Schlosser, *Eléments de mécanique des sols*, 276 p., Presses de l'Ecole Nationale des Ponts et Chaussées, 1988

[SHA96] Schackelford J.F. – *Introduction to Material Science for Engineers.* 4th Ed., Prentice-Hall Inc. Edt., New Jersey (USA), 1996

[SIN74] Singh S.N., Blazek K.E. – *Heat transfer and skin formation in continuous casting mold as a function of steel carbon content.* Journal of Metals, October 1974, pp.17-27

[STO90] Storkman W.R. – *Optimization of the Mold Taper Design Using Mathematical Models of Continuous Steel Slab Casting.* MS Thesis, University of Illinois, 1990

[STO99] Stone D., Thomas B.G. – *Measurement and modelling of heat transfer across interfacial mold flux layers.* Canadian Metallurgical Quarterly, Vol.38, No.5, 1999, pp.363-375

[TEK90] *Continuous casting of steel – Teräksen jatkuvavalu 1984-1989.* TEKES Finland (Technology Development Center), Seppo Louhenkilpi Ed., 1990

[THO91] Thomas B.G., Ho B. – *Spreadsheet model of Continuous Casting.* Materials Processing in the Computer Age, Voller V.R., Stachovicz M.S. and Thomas B.G. Eds., The Minerals, Metals and Materials Society, 1991

[THO02] Thomas B.G. – *Modeling for Casting and Solidification Processing. Chapter 15: Continuous casting.* Kuang-O Yu Edt., Marcel Dekker Inc., New-York (USA), 2002

[TOY02] Toyoshima S., Gotoh M., Nakayama K. – *Computational Technique for 3-Dimensional Deformation Analysis of Continuously Cast Steel Strand in Multi-Roll-Spans.* Proc. 7th Int. Conf. on Technology of Plasticity, Yokohama (Japan), 28th-30th October 2002

[VAL02] Valencia J.J., Kuang-O Y. – *Modeling for Casting and Solidification Processing. Chapter 6: Thermophysical Properties.* Kuang-O Yu Edt., Marcel Dekker Inc., New-York (USA), 2002

[WOL00] Wolff M.M. – Future *Developments in Continuous Casting Technology.* SMAE Conference and Exhibition, Sheffield (UK), 15th-16th June 2000

[WRA80] Wray P.J. – *Modeling of casting and welding processes.* pp. 245-257, 1980, Warrendale, PA, Metallurgical Society of AIME

[YU00] Yu L. – FEM *Analysis of Bulging between Rolls in Continuous Casting.* MS Thesis, University of Illinois, 2000

[ZHU96] Zhu H. – *Coupled Thermal-Mechanical Finite Element Model with Application to Initial Solidification.* Ph.D. Thesis, University of Illinois, 1996

[ZIE00] Zienkiewicz O.C., Taylor R.L. – *The Finite Element Method.* 3 vol., 5th Edition (2000), Butterworth and Heneimann Eds.